Phase tuning in transition metal pnictide CrAs

Zur Erlangung des akademischen Grades eines

Doktors der NATURWISSENSCHAFTEN (Dr. rer. nat)

von der KIT-Fakultät für Physik des
Karlsruher Instituts für Technologie (KIT)
angenommene

Dissertation

von
M. Sc. Paolo Battistoni

Tag der mündlichen Prüfung: 22.05.2026
1. Referent: Prof. Dr. Matthieu Le Tacon
2. Referent: PD Dr. Frank Weber

Abstract

In unconventional superconductors, electronic and structural degrees of freedom are strongly intertwined and play a key role in stabilizing ordered phases outside the superconducting state, with also direct implications for superconductivity. A detailed understanding of these interactions is therefore crucial for clarifying the underlying mechanism of unconventional superconductivity.
In this thesis, the unconventional superconductor chromium arsenide (CrAs) was chosen as a model system due to its strong coupling between magnetic order and lattice degrees of freedom. CrAs exhibits an anomalous magnetoelastic effect across its first-order magnetostructural transition, which is progressively suppressed under applied pressure as magnetic order disappears and superconductivity emerges. Suppression of magnetic order in CrAs by applied pressure is accompanied by signatures associated with quantum critical behavior. When the same magnetic instability is suppressed through phosphorus substitution in $CrAs_{1-x}P_x$ similar quantum critical signatures are observed, even though superconductivity remains absent. In this context, previous work on the interplay between competing orders in CrAs has primarily addressed the coexistence between magnetic and superconducting phases at low temperatures. By contrast, phase coexistence at higher temperatures - between magnetically ordered and non-magnetic phases - has received significantly less attention in both pure and phosphorus-substituted CrAs, despite the potential influence of proximity to a quantum critical regime. Investigating phase coexistence within the normal state is therefore highly relevant for probing how the interplay between magnetic, structural, and electronic degrees of freedom may influence the emergence of superconductivity. On this basis, this thesis focused on the study of phase coexistence through the structural and lattice response, examining its relation to the magnetostructural transition and its evolution under external control parameters such as hydrostatic pressure and chemical substitution, using Raman spectroscopy and Transmission Electron Microscopy (TEM).

In this thesis, high quality single crystals of CrAs and phosphorus-substituted $CrAs_{1-x}P_x$ were grown and characterized by powder X-ray diffraction and magnetometry measurements. Raman spectroscopy performed on single crystals revealed that phase coexistence in CrAs-based systems is intrinsically local. Phase coexistence was directly tracked through the simultaneous observation of two distinct A_g phonon modes, associated with the high temperature non-magnetic and low temperature magnetically ordered phases. Raman mapping further revealed strongly position dependent spectra, consistent with a temperature dependent domain reconfiguration dynamics, with some regions retaining signatures of phase coexistence down to the lowest temperatures.
Under hydrostatic pressure on pure CrAs, Raman measurements showed a progressive suppression of previously reported linewidth anomalies, confirming their magnetoelastic nature. In addition, Raman measurements showed evidence for a previously reported low pressure transition around 0.2-0.3 GPa. In phosphorus-substituted $CrAs_{1-x}P_x$, the magnetostructural transition was similarly suppressed, while enhanced phonon linewidths pointed to the important role of disorder, indicating a clear deviation from the analogy between chemical and hydrostatic pressure.
TEM provided direct real-space evidence that phase coexistence occurs on nanometric length scales and, when combined with Raman spectroscopy, offered a complementary perspective on how the coexistence evolves across different tuning parameters. In phosphorus-substituted samples, the coexistence can

organize into stripe-like configurations, pointing to a more complex coupling between magnetic, structural, and electronic degrees of freedom.

Zusammenfassung

In unkonventionellen Supraleitern sind elektronische und strukturelle Freiheitsgrade stark miteinander verflochten und spielen eine Schlüsselrolle bei der Stabilisierung geordneter nicht-supraleitender Phasen, was auch direkte Auswirkungen auf die Supraleitung hat. Ein detailliertes Verständnis dieser Wechselwirkungen ist daher entscheidend für die Aufklärung des zugrunde liegenden Mechanismus der unkonventionellen Supraleitung.
In dieser Arbeit wurde der unkonventionelle Supraleiter Chromarsenid (CrAs) aufgrund seiner starken Kopplung zwischen magnetischer Ordnung und Gitterfreiheitsgraden als Modellsystem gewählt. CrAs zeigt einen anomalen magnetoelastischen Effekt bei seinem magnetostrukturellen Übergang erster Ordnung, der unter Druck zunehmend unterdrückt wird, wobei die magnetische Ordnung verschwindet und Supraleitung auftritt. Die Unterdrückung der magnetischen Ordnung in CrAs durch Druck geht mit Anzeichen einher, die mit quantenkritischem Verhalten assoziiert sind. Wenn dieselbe magnetische Instabilität durch Phosphorsubstitution in $CrAs_{1-x}P_x$ unterdrückt wird, werden ähnliche quantenkritische Anzeichen beobachtet, obwohl keine Supraleitung auftritt. In diesem Zusammenhang haben sich frühere Arbeiten zum Wechselspiel zwischen konkurrierenden Ordnungen in CrAs in erster Linie mit der Koexistenz von magnetischen und supraleitenden Phasen bei niedrigen Temperaturen befasst. Im Gegensatz dazu hat die Phasenkoexistenz bei höheren Temperaturen – zwischen magnetisch geordneten und nichtmagnetischen Phasen – sowohl bei reinem als auch bei phosphorsubstituiertem CrAs deutlich weniger Beachtung gefunden, trotz des potenziellen Einflusses der Nähe zu einem quantenkritischen Regime. Die Untersuchung der Phasenkoexistenz im Normalzustand ist daher von großer Bedeutung, um zu erforschen, wie das Zusammenspiel zwischen magnetischen, strukturellen und elektronischen Freiheitsgraden die Entstehung von Supraleitung beeinflussen kann. Auf dieser Grundlage konzentrierte sich diese Arbeit auf die Untersuchung der Phasenkoexistenz anhand der Struktur- und Gitterantwort und untersuchte deren Zusammenhang mit dem magnetostrukturellen Übergang und dessen Entwicklung unter externen Kontrollparametern wie hydrostatischem Druck und chemischer Substitution unter Verwendung von Raman-Spektroskopie und Transmissionselektronenmikroskopie (TEM).

In dieser Arbeit wurden hochwertige Einkristalle aus CrAs und phosphorsubstituiertem $CrAs_{1-x}P_x$ gezüchtet und mittels Pulver-Röntgendiffraktometrie und Magnetometrie charakterisiert. Die an den Einkristallen durchgeführte Raman-Spektroskopie ergab, dass die Phasenkoexistenz in CrAs-basierten Systemen intrinsisch lokal ist. Die Phasenkoexistenz wurde durch die gleichzeitige Beobachtung von zwei unterscheidbaren A_g-Phononenmoden, die mit der nichtmagnetischen Hochtemperaturphase und der magnetisch geordneten Niedrigtemperaturphase assoziiert sind, direkt verfolgt. Die Raman-Kartierung ergab darüber hinaus stark positionsabhängige Spektren, was mit einer temperaturabhängigen Dynamik der Domänenkonfiguration übereinstimmt, wobei einige Bereiche bis zu den niedrigsten Temperaturen Anzeichen einer Phasenkoexistenz aufweisen.
Unter hydrostatischem Druck auf reinem CrAs zeigten Raman-Messungen eine fortschreitende Unterdrückung der zuvor berichteten Anomalien der Linienbreite, was deren magnetoelastische Natur bestätigt. Darüber hinaus lieferten Raman-Messungen Hinweise auf einen zuvor berichteten Niederdruckübergang bei etwa 0,2–0,3 GPa. In phosphorsubstituiertem $CrAs_{1-x}P_x$ wurde der magnetostrukturelle Übergang ebenfalls unterdrückt, während erhöhte Phononenlinienbreiten auf die wichtige Rolle von Unordnung hinwiesen und eine deutliche Abweichung von der Analogie zwischen chemischem und

hydrostatischem Druck zeigten. TEM lieferte direkte Realraum-Beweise dafür, dass Phasenkoexistenz auf nanometrischen Längenskalen auftritt, und bot in Kombination mit Raman-Spektroskopie eine ergänzende Perspektive darauf, wie sich die Koexistenz über verschiedene Abstimmungsparameter hinweg entwickelt. In phosphorsubstituierten Proben kann sich die Koexistenz zu streifenartigen Konfigurationen organisieren, was auf eine komplexere Kopplung zwischen magnetischen, strukturellen und elektronischen Freiheitsgraden hindeutet.

Contents

1. Introduction

Superconductivity is a remarkable phase of matter that has attracted long standing interest, both because of its potential applications and because it reflects the emergence of collective electronic behavior. While conventional superconductivity can be successfully described within the well established theoretical framework of electron-phonon coupling (BCS theory) [1, 2], the discovery of unconventional superconductors has revealed a much more complex phenomenology, in which multiple electronic and structural degrees of freedom are often strongly intertwined [3, 4].
In many unconventional superconductors, the normal state from which superconductivity emerges is characterized by competing or coexisting electronic orders, and numerous studies have shown that the coupling between electronic and lattice degrees of freedom plays an important role in shaping the phase diagram [5, 6]. Materials in which magnetism, lattice distortions and electronic properties are strongly coupled therefore provide a particularly fertile ground for investigating the mechanisms underlying unconventional superconductivity.

In this context, chromium arsenide (CrAs) and chemically substituted CrAs-based systems represent appealing platforms for investigating the strong interplay between magnetism, lattice distortions and electronic properties. CrAs exhibits a low-temperature antiferromagnetic phase, commonly described in terms of helimagnetic order, together with a pronounced coupling between magnetic order and lattice degrees of freedom. This coupling is evidenced by an exceptionally large structural anomaly at the magnetostructural transition, involving an expansion of the crystallographic b axis by approximately 4% and of the unit-cell volume by about 2%, while the crystal symmetry remains unchanged [7, 8]. Upon the application of external pressure, the magnetic order is progressively suppressed and superconductivity emerges once long-range magnetism is fully destabilized. Chemical substitution provides an additional tuning parameter to modify this balance of competing phases, offering a complementary approach to pressure tuning that has been comparatively less explored. In particular, the substitution of phosphorus for arsenic has been shown to suppress magnetic order in a manner qualitatively similar to the application of external pressure, while not inducing superconductivity [7]. Tuning this magnetic instability, either by external pressure or chemical substitution, has been suggested to bring the CrAs system in proximity to a quantum critical regime, with potential consequences for the electronic properties beyond the superconducting phase itself [7, 9].

Within this broader context, previous studies have reported the existence of a two-phase region at low temperatures and moderate pressures, in which magnetic and superconducting phases coexist [9, 10]. Despite extensive investigations of the magnetic and superconducting states of CrAs, comparatively little attention has been devoted to the onset of phase coexistence at higher temperatures and to its evolution as a function of physical or chemical tuning parameters. In particular, the implications of phase coexistence for the structural response and lattice dynamics of CrAs-based systems, especially in the vicinity of a putative quantum critical regime, remain largely unexplored.
The aim of this thesis is to address these open questions by investigating the lattice dynamics and structural responses of pure and phosphorus-doped CrAs under different external conditions, with a particular focus on the nature, locality, and evolution of phase coexistence.

Chapter 2 provides the physical background for this thesis. It introduces the crystal and magnetic structure of CrAs, the nature of the magnetostructural transition and its evolution under external pressure and chemical substitution. The discussion also addresses the suppression of magnetic order and the emergence of superconductivity, including their relation to quantum criticality, electronic structure models and phase coexistence. This framework provides the context for the experimental investigations presented in the following chapters.

Chapter 3 describes the synthesis and characterization of CrAs and phosphorus-doped CrAs. It presents the preparation of polycrystalline samples and the growth of single crystals, followed by a structural characterization and a compositional analysis based on powder X-ray diffraction. Magnetization measurements are also used to probe the magnetic response of the doped compounds and to establish a comparison with pressure-dependent results reported in the literature.

Chapter 4 presents the main experimental results of this thesis and focuses on the lattice dynamics and structural responses of pure and phosphorus-doped CrAs. After a brief introduction to the relevant aspects of Raman scattering and a description of the experimental configurations used at ambient and high pressure, Raman measurements are used to investigate the magnetostructural transition and phase coexistence in pure CrAs, its evolution under applied pressure and the effects of phosphorus substitution. To further explore the local nature of phase coexistence, a complementary approach combining spatially resolved Raman spectroscopy with transmission electron microscopy is developed. The chapter then extends the investigation to the nanometric length scale through transmission electron microscopy, including the preparation of TEM lamellae and diffraction-based measurements, providing new complementary insight into the local nature of phase coexistence.

Chapter 5 presents a summary of the main results of this thesis, together with an outlook on possible directions for future work.

Supplementary information related to various topics discussed in this thesis is provided in **Appendices A–D**.

2. Structural, magnetic and electronic properties of CrAs

The family of 3d intermetallic pnictides and chalcogenides has been the focus of growing research interest owing to their diverse structural and magnetic properties, together with their strong response to external parameters such as temperature, pressure, magnetic field and chemical substitution [11]. Within this broad class of materials, CrAs has emerged as a model system for studying the connection between helimagnetic order and superconductivity, since both are strongly tied to the underlying structural degrees of freedom and can be tuned directly through their modification. This sensitivity gives rise to a complex interplay between magnetic, structural and superconducting phases, resulting in a rich phase diagram that provides a valuable perspective on the physics of unconventional superconductors [12, 13, 14].

2.1. Overview on CrAs

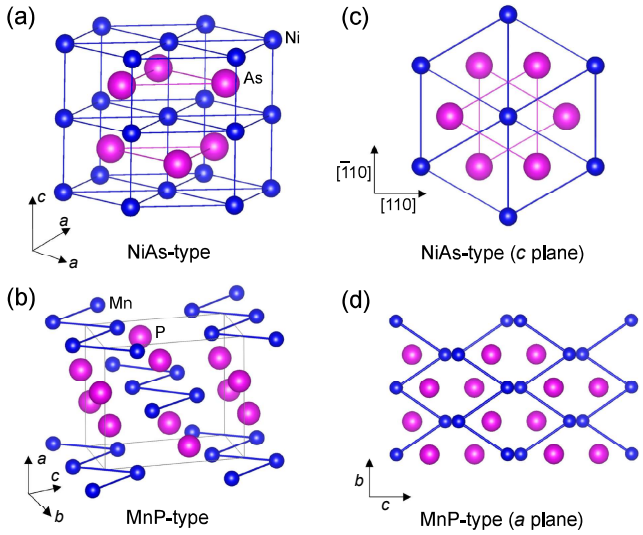

Figure 2.1.: (a) Crystal structure of the NiAs-type phase (hexagonal, $P6_3/mmc$) and (b) the MnP-type phase (orthorhombic, $Pnma$). (c) Projection of the NiAs-type structure along the c axis and (d) projection of the MnP-type structure along the a axis. Although these projections correspond to equivalent planes in the two structure types, the distortion along the c axis in the MnP-type structure leads to increased anisotropy in the Mn-P distances. Figure from [15].

A large number of binary transition-metal compounds adopt the NiAs-type structure (space group $P6_3/mmc$) or one of its lower symmetry derivatives. Among these distorted variants is the orthorhombic MnP-type structure (space group $Pnma$), which is commonly found in the transition metal pnictides. In some of these compounds - including CrAs - the NiAs and MnP arrangements are linked through a structural transition [11, 16].

Although CrAs adopts the MnP-type structure at ambient conditions, the structural relationship to the higher symmetry NiAs phase remains relevant. Fig. 2.1 shows the comparison between the MnP and NiAs structures. In the hexagonal phase, the transition-metal atoms arrange themselves in a uniform triangular lattice, when viewed along the c axis. However, in the MnP-type structure, the projection along the orthorhombic a axis - geometrically equivalent to the NiAs c axis view - shows that this arrangement becomes distorted, forming zigzag chains of Cr atoms. This distortion produces non-uniform Cr-As and Cr-Cr distances, which are essential for the magnetic interactions and the overall magnetic properties of CrAs [11, 16].

In the MnP-type structure, each Cr atom is coordinated by six As atoms in a distorted $[Cr(As)_6]$ octahedral environment, while each As atom is coordinated by six Cr atoms, forming a distorted trigonal prism. These coordination polyhedra constitute the fundamental local building blocks of the lattice and stack in a characteristic pattern along the three crystallographic axes [17, 18]. The distortions of these polyhedra originate from the symmetry lowering structural transition connecting the high temperature NiAs-type structure to the orthorhombic MnP-type structure. This transformation proceeds through the group-subgroup sequence $P6_3/mmc \rightarrow Cmcm \rightarrow Pnma$ where the intermediate $Cmcm$ phase ("ortho-hexagonal") retains certain features of the hexagonal parent structure while being a fully orthorhombic lattice [16]. A more comprehensive description of this structural pathway and the associated atomic displacements can be found in the work of Eich et al. [18, 16]. For the purpose of the following discussion, it is sufficient to emphasize that the MnP-type structure emerges from a symmetry reduction of the NiAs lattice and that the corresponding distortions manifest directly in the Cr-As coordination geometry.

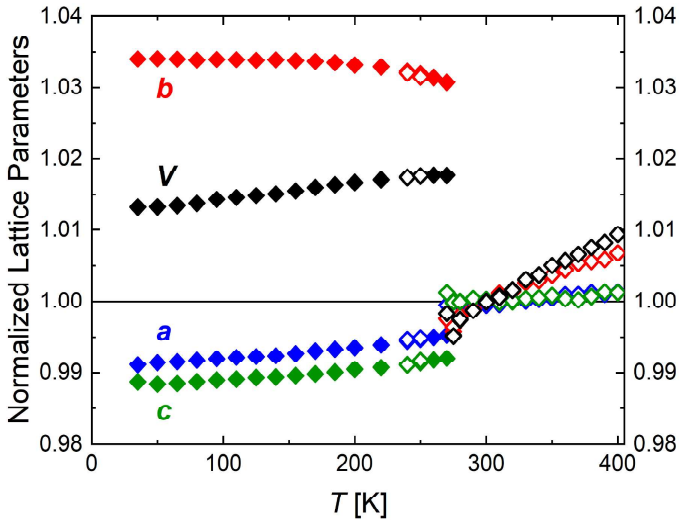

Figure 2.2.: Temperature dependence of the CrAs lattice parameters and unit cell volume at ambient pressure, normalized to their room temperature values. Figure adapted from [18].

Upon cooling to $T_N \approx 265$ K, CrAs undergoes a first-order magnetic transition that is accompanied by an isostructural phase transition, namely, a change in lattice parameters without any modification of the crystallographic symmetry [13, 14]. The structural behavior of CrAs has been investigated in numerous diffraction studies spanning a wide range of temperatures and pressures[1].

[1] A detailed overview of the structural work on CrAs can be found in [13, 14, 15, 16].

These studies consistently showed that no symmetry change occurs in CrAs up to 9.5 GPa at room temperature [18], nor at cryogenic temperatures under pressures up to 1 GPa [19, 20, 7]. Fig. 2.2 shows the temperature and pressure dependence of the CrAs lattice, normalized to their values at ambient conditions, as reported by Eich et al. [18]. Upon cooling at ambient pressure through T_N, the lattice parameters exhibit large and abrupt discontinuities, which are consistently reported in the literature, $\Delta a/a \approx -0.5\%$, $\Delta b/b \approx 3.5\%$, $\Delta c/c \approx -0.9\%$ and $\Delta V/V \approx 2.2\%$ [13, 14]. This anomalous behavior of the lattice, particularly the pronounced increase of the b axis, is a clear indication of the presence of a strong magnetoelastic coupling in CrAs, a feature already noted in the early studies of the 1970s when its magnetic structure was first resolved [21, 22, 23].

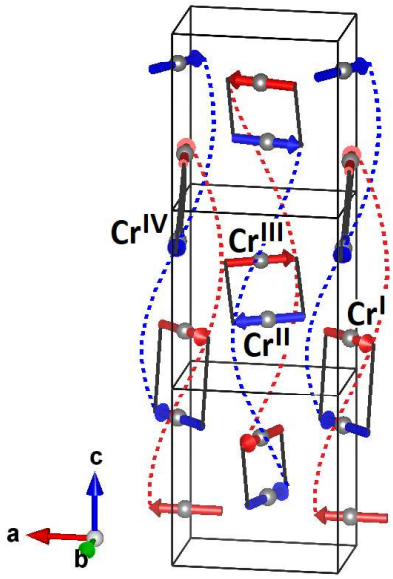

Figure 2.3.: Scheme of the helical magnetic structure of CrAs along the c axis. The two in-phase helical pairs are highlighted by the red (CrI-CrIII) and blue (CrII-CrIV) dashed curved lines, with the corresponding spins indicated. Black lines mark the antiparallel alignments between the nearest-neighbor spin pairs (CrI-CrIV and CrII-CrIII). Figure from [16].

Below T_N, CrAs orders magnetically into an incommensurate double helical structure with the spins lying in the ab plane and an ordered moment of approximately 1.7 μ_B at low temperature. Fig. 2.3 shows a schematic depiction of this magnetic structure, adapted from [16]. The two helices propagate along the c axis with the same propagation vector $\mathbf{k} = (0, 0, k_c)$, where $k_c \approx 0.381$ at T_N and decreases to $k_c \approx 0.356$ at 4 K [13, 14]. The term "double helical" reflects the fact that the four Cr atoms in the unit cell form two spin pairs with fixed relative phases. Following the notation used in Fig. 2.3, the angle between the CrI-CrII and CrIII-CrIV is approximately $-100°$, while the rotation between CrI-CrIV and CrII-CrIII is around 180° [19, 20]. This magnetic arrangement is connected to the structural features of the MnP-type lattice, where the zigzag chains of Cr atoms and the non-uniform Cr-Cr distances give rise to competing exchange pathways.

Different studies arrived at the observed double helical order using different microscopic models. In some works, the helical structure is reproduced using only a classical Heisenberg exchange interaction framework [7, 24], while others introduce additional antisymmetric terms, such as Dzyaloshinskii-Moriya interactions, to account for specific features of the magnetic order[2] [19, 20, 25]. Moreover, the microscopic description of the magnetic ground state is not fully settled.
A recent neutron diffraction study on single crystal CrAs by Eich et al. showed that the conventional double helical model does not reproduce all magnetic satellite intensities. Their refinement shows that the magnetic structure is neither a pure helix, with the normal of the spin-rotation plane parallel to c^*, nor a pure cycloid, where this normal is perpendicular to c^*. Instead, their analysis shows that the spin rotation planes are tilted by a finite angle $0° < \theta < 90°$ with respect to c^* [26]. This new microscopic model leads to a larger refined magnetic moment of the Cr atoms, around $3.2 - 3.6\ \mu_B$, rather than the generally accepted $1.7\ \mu_B$ [26]. Therefore, further investigations on the microscopic magnetic structure of CrAs are still required.

2.1.1. Pressure dependence of CrAs

To understand the emergence of such a complicated magnetic structure, early work focused on the strong coupling between the lattice and the magnetic ordering in CrAs. Studies by Kallel et al. and Zavadskiĭ et al. proposed that the helical magnetic order below T_N originates from an electronic transition from itinerant states to localized ones. According to this model, the normal thermal contraction of the lattice upon cooling reduces the Cr-Cr distances, increasing the electron repulsion and leading to the abrupt expansion of the b axis at T_N [22, 27]. Zavadskiĭ et al. further reported that applying physical pressure lowers and ultimately suppresses the magnetostructural transition, which is attributed to a pressure-induced enhancement of the electron itineracy [27]. A more detailed discussion of this model is provided in Sec. 2.1.3.

More recently, new neutron diffraction, NMR and μSR measurements have significantly refined our understanding of how the helimagnetic order in CrAs evolves under pressure. However, the emerging picture is far from consistent, as the reported pressure dependence of both the magnetic propagation vector and the ordered moment varies greatly depending on the sample form and on the experimental technique [13, 14]. For polycrystalline samples, Keller et al. observed a strong suppression of the ordered moment - reduced to about 25% of its ambient pressure value at 0.7 GPa - while the propagation vector remains essentially unchanged [19]. In their measurements, the magnetic order disappears completely at around 0.7 GPa. Khasanov et al. similarly reported that the ordered moment decreases to about 85% of the original value, likewise locating the disappearance of magnetic order near 0.7 GPa [10]. In contrast, Shen et al. reported a qualitatively different behavior: a rotation of the helical plane from ab to ac accompanied by an abrupt decrease of the propagation vector at around 0.6 GPa. Their data show only a modest reduction of the magnetic moment (to approximately 85% at 0.6 GPa), with magnetic order persisting until approximately 0.9 GPa. However, both the proposed spin reorientation and the sudden change in the propagation vector remain unconfirmed by any later studies [20].

[2] Further discussion of these interaction models is provided in Sec. 4.1.3.2 and D.

Single crystal measurements present a different scenario. Kotegawa et al. found that the magnetic order disappears above 0.74 GPa, in broad agreement with the critical pressures reported by Keller and Khasanov, though they did not provide quantitative estimates of the ordered moment [28]. Matsuda et al. reported a moderate pressure dependence of the propagation vector - stronger than that observed by Keller et al. but far less drastic than that of Shen et al. - along with a substantial reduction of the ordered moment to roughly 65% of its ambient pressure value and found that magnetic order persists up to approximately 0.9 GPa [7].

A more consistent picture emerges when considering the structural degrees of freedom. Regardless of the differences reported in the magnetic behavior, all diffraction studies agree that the lattice parameters respond to pressure in a similar manner [13, 14, 15]. In particular, the b axis displays a pronounced anisotropic compressibility while also showing a characteristic relative expansion, $\Delta b/b$, at the magnetic transition. Some of these $\Delta b/b$ values are listed in Tab. 2.1. In this context, it is worth mentioning the room temperature measurement of Yu et al., who reported an isostructural transition at approximately 0.35 GPa associated with a decrease of the b axis by about -0.9%. This anomaly has not been observed again in later diffraction measurements. The interpretation proposed by Yu et al., based on a modification of the model of Zavadskiĭ et al., will be discussed in Sec. 2.1.3. Viewed collectively, the data identify the b axis as the structural parameter most directly responsive to and shaped by the application of pressure [13, 14, 15].

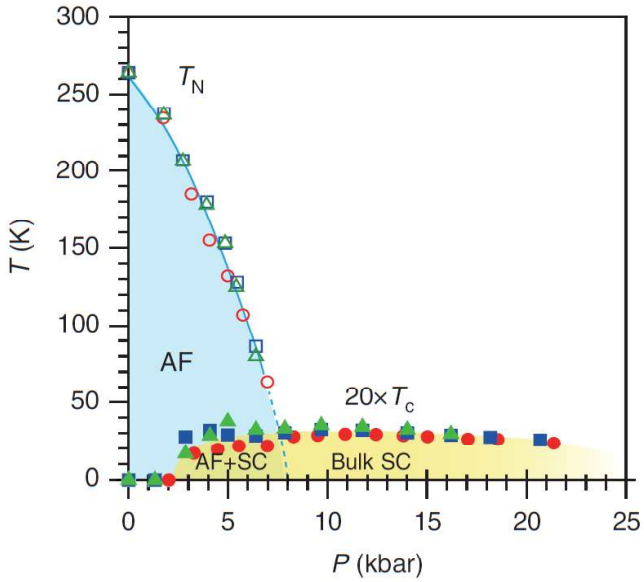

Figure 2.4.: Temperature-pressure phase diagram of CrAs single crystals, showing the helical antiferromagnetic phase (AF), the superconducting region (SC) and their corresponding transition temperatures T_N and T_c. For clarity, the T_c values have been scaled by a factor of 20. The red circles, blue squares and green triangles correspond to three independent samples with residual resistivity ratios (RRR) of 240, 327 and 250, respectively. Adapted from [9].

Upon the partial suppression of the helimagnetic phase, CrAs enters a superconducting state under pressure. As shown in Fig. 2.4, superconductivity is observed only once the long range magnetic order has been sufficiently weakened, forming a dome with a maximum transition temperature of 2 K at 1 GPa, which extends up to several gigapascals [13, 14].

The superconducting transition was first reported by Wu et al. and Kotegawa et al., on single crystals grown using Sn flux [9, 29]. The superconducting phase appears to be strongly dependent on sample quality. In particular, only high quality single crystals with a high residual resistivity ratio (RRR), typically above 100, exhibit a sharp and complete superconducting transition under pressure [9, 29, 30]. The sensitivity to disorder together with the proximity of the superconducting dome to the magnetic phase are often regarded as indications of unconventional pairing. In addition, the presence of a coexistence region between approximately 0.3 and 0.7 GPa, where the helimagnetic order and superconductivity are simultaneously present in different parts of the sample, together with the reported increase of the magnetic susceptibility in the paramagnetic phase - similarly found in several iron-based superconductors (see Sec. 3.3.1) - reinforces the unconventional nature of the pairing, possibly mediated by magnetic fluctuations [13, 14]. This is consistent with the NMR results of Kotegawa et al., who reported the absence of a Hebel-Slichter coherence peak in $1/T_1$ below T_c [28]. A complementary result comes from the angle dependence measurements of the critical field H_{c2} by Guo et al., who reported a pronounced in-plane anisotropy of the upper critical field under pressure suggesting an odd-parity, possibly triplet, pairing state [31].
Interestingly, μSR measurements by Khasanov et al. - performed on polycrystalline CrAs - reported that the zero-temperature superfluid density scales with T_c as $\rho \approx T_c^{3.2}$. This power law is closer to that expected for a fully gapped BCS superconductor, rather than to the nearly linear scaling commonly observed in unconventional systems [10]. This discrepancy mirrors the differences discussed previously between the polycrystalline and single crystal measurements of the helimagnetic phase [19, 20, 7]. Therefore, it is plausible that the superconducting properties are similarly sensitive to sample form, leaving the nature of the pairing mechanism in CrAs still unresolved.

2.1.2. Doping dependence of CrAs

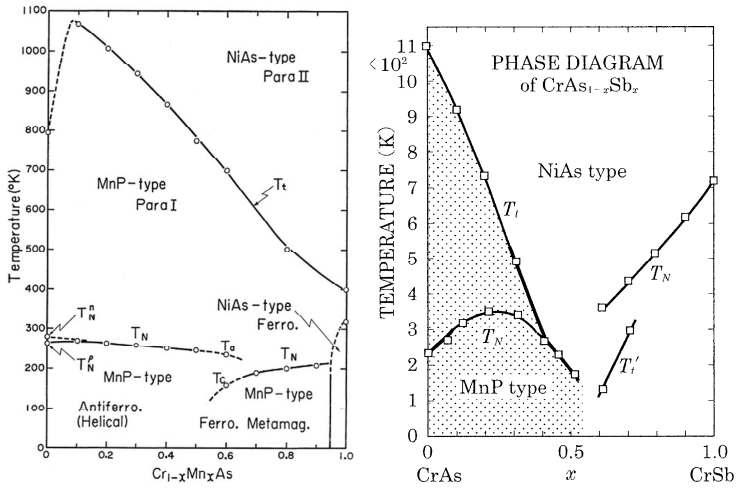

Figure 2.5.: Left: $Cr_{1-x}Mn_xAs$ magnetic phase diagram. Right: $CrAs_{1-x}Sb_x$ magnetic phase diagram. Figure adapted from [13].

In contrast to physical pressure - which primarily suppresses the magnetic order - chemical substitution provides an alternative route that perturbs the lattice and the magnetic interactions in qualitatively different ways. Substitutions on both the transition-metal site and the pnictogen site were investigated. Notable examples include Cr replacement with Mn [23, 32, 33, 34] or Al [35] and P or Sb substitution with As [7, 36, 37, 38, 39]. Fig. 2.5 shows the magnetic phase diagram of $Cr_{1-x}Mn_xAs$ and $CrAs_{1-x}Sb_x$.

The phase diagrams become progressively more complex and in both systems the magnetostructural transition temperature increases for small substitution levels. The Mn doping introduces an additional magnetic cation that perturbs the Cr magnetic sublattice, leading to a sequence of magnetic phases within the MnP-type structure before approaching the ferromagnetic state of MnAs [11, 13]. In contrast, low Sb substitution - similarly to P doping - introduces only a weak disturbance to the Cr sublattice[3] yet still influences the structural and magnetic properties. At approximately $x \approx 0.5$, the magnetic order changes from the helical state to a collinear antiferromagnetic phase, accompanied by a transition to the NiAs-type structure [11, 13]. While the hydrostatic pressure suppresses the magnetic order in CrAs, the two chemical substitutions discussed so far act differently. Although both modify the structural parameters and even enhance T_N at low concentrations, their primary effect is a change in the magnetic ground state. Notably, MnAs is a ferromagnet known for its strong magnetocaloric response [40], while the collinear antiferromagnet CrSb has recently been identified as an altermagnet [41]. Overall, these findings reflect the continued relevance of this family of compounds[4].

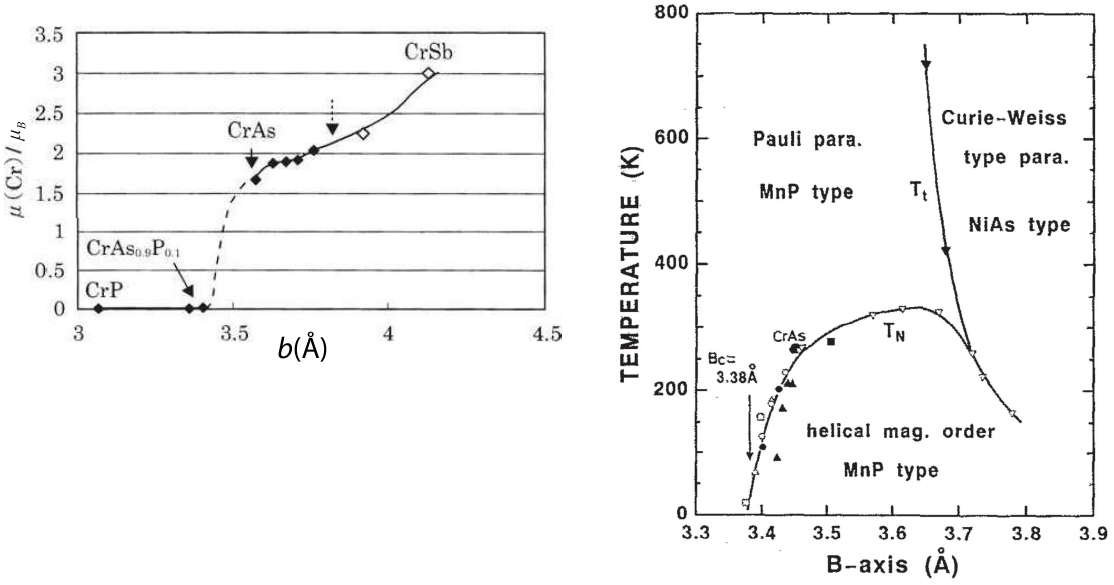

Figure 2.6.: Left: Relation between the magnetic moment per Cr atom, in CrPn compounds, and the b axis length at 4.2K. Filled symbols correspond to the MnP-type structure, while open symbols indicate the NiAs-type structure. Figure adapted from [11] Right: T_N of $Cr_{1-x}M_xAs$ (with M = Ti, Mn, Fe, Co, Ni) and $CrAs_{1-x}Pn_x$ (with Pn = P,Sb) plotted as a function of the b axis length. Symbols: Ti (solid triangle), Mn (solid square), Fe (open triangle), Co (open circle), Ni (solid circle), P (open square) and Sb (inverted triangle). Figure adapted from [38] .

By contrast, the effect of isovalent P substitution is much closer to that of hydrostatic pressure. Earlier studies by Selte et al., Suzuki et al. and Kanaya et al. showed that replacing As with P leads to a strong shrinking of the lattice - mostly on the b axis - resulting in a complete suppression of magnetic order around $x \approx 0.05$[5] [7, 36, 38, 39].

[3] Sb and P are non magnetic and isovalent with As [13].

[4] To the best of our knowledge, two theoretical studies have examined whether CrAs could be an altermagnet. Fakhredine et al. predicted altermagnetic behavior only for a hypothetical C-type collinear antiferromagnetic configuration, which is not realized experimentally [42]. Beida et al. proposed that altermagnetism may appear in the high temperature NiAs-type phase. However, this structure is metastable (stable only above ≈ 1170K) and no experimental data exist so far regarding its magnetic ordering [43]

[5] Variability in the critical concentration, particularly in older studies, is likely due to sample quality issues. Further discussion is provided on Sec. 3.1.3.

Compound	b_{RT} **(Å)**	$\Delta b/b$ **(at** T_N **)**	T_N
CrAs - 0 GPa	3.46	3.5%	265 K [7]
CrAs - 0.69 GPa	3.41	5%	130 K [7]
CrAs - 1.2 GPa	3.39		[7]
CrAs - 9.5 GPa	3.23		[18]
$CrAs_{0.9}Sb_{0.1}$	3.57		320 K [37]
$Cr_{0.9}Mn_{0.1}As$	3.50	2.1%	280 K [38]
$Cr_{0.993}Al_{0.007}As$	3.48		275 K [35]
$Cr_{0.98}Ni_{0.02}As$	3.45	4.3%	200 K [38]
$CrAs_{0.965}P_{0.035}$	3.43	4.7%	180 K [7]
$CrAs_{0.95}P_{0.05}$	3.41		[7]
CrP	3.11		[39]

Table 2.1.: Summary of the room temperature b lattice parameter (b_{RT}), relative jump $\Delta b/b$ at the transition and T_N for selected CrAs-based compound, including both chemically subsituted samples and pure CrAs under pressure. Missing entries reflect either the suppression of the transition (as in high pressure or highly P doped CrAs) or the absence of the relevant information in the original publication ($\Delta b/b$ for Sb substitution). References are listed row by row.

This strong sensitivity of the b parameter reinforces the picture of a pronounced magnetoelastic coupling in CrAs. This behavior was further highlighted by Suzuki et al. who performed a systematic study of various chemical substitutions on both the Cr and As sites. By correlating T_N of the doped compounds with their room temperature b lattice parameter, they identified a critical parameter $b_c \approx 3.38$ Å below which the incommensurate double helical phase does not stabilize, regardless of the specific dopant [38]. Fig. 2.6 summarizes the stability of the magnetic ground state as a function of the b axis length. The dependence of the ordered Cr moment on the low temperature b parameter in the CrPn compounds, together with the variation of T_N with the room temperature b parameter in the doped Cr-M-Pn systems, clearly shows that the chemical substitution primarily tunes the magnetic properties through its effect on the lattice [11, 13, 38]. This provides a clear justification for describing such substitutions as a form of chemical pressure. Introducing atoms with a smaller covalent radius reduces the unit cell volume and moves the system through the structural-magnetic boundary, in close analogy to external hydrostatic pressure.

On the other hand, substituting atoms with a larger covalent radius expands the lattice - negative pressure - and increases T_N [13]. Suzuki et al. reported that the relative jump $\Delta b/b$ at the transition becomes larger at T_N, as the magnetic order gets partially suppressed, consistent with the observed trend in the more recent single crystal and polycrystalline diffraction studies on pure CrAs under pressure. In contrast $\Delta b/b$ decreases when T_N is enhanced by substitutions with larger atoms [19, 20, 7, 38]. A summary of the b lattice parameter values at room temperature[6], together with the relative jump $\Delta b/b$ at the transition and the corresponding T_N for selected CrAs-based compound are listed in Tab. 2.1. Among all investigated substitutions, P doping most closely mimics the effect of physical pressure. Replacing As with the smaller P atom contracts the lattice and suppresses the helical magnetic order without stabilizing any alternative magnetic phase [7].

[6]Combining the study by Suzuki et al. with more recent diffraction work, the critical paramater separating the helical magnetic order from paramagnetic one should be constrained at $b_c = 3.40 \pm 0.01$ Å.

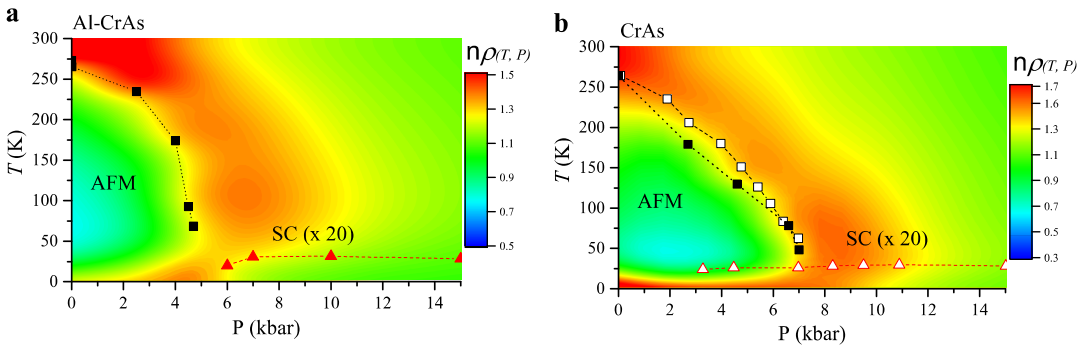

Figure 2.7.: Normalized isothermal resistivity of Al-doped CrAs (a) and pure CrAs (b) as a function of temperature and pressure. For each temperature, the resistivity is normalized by its value at the highest measured pressure (2.41 GPa for Al-CrAs and 2.25 GPa for CrAs), providing a common reference in the paramagnetic phase. Solid squares and triangles mark the transition temperatures T_N and T_c, while open symbols indicate corresponding values taken from Wu et al.[9]. For visibility, T_c is multiplied by 20. AFM and SC denote the antiferromagnetic and superconducting phases, respectively. Adapated from [35]

Given the strong analogy between pressure and phosphorus substitution in suppressing the helimagnetic phase, a natural question is whether P doping can also induce superconductivity in the same way that physical pressure does. Matsuda et al. measured the resistivity of several $CrAs_{1-x}P_x$single crystals across different doping levels. They confirmed that the magnetostructural transition is suppressed at a relatively low concentration, around $x \approx 0.05$, consistent with previous reports. However, no superconductivity was detected in any of their samples [7]. The doped crystals exhibited relatively large residual resistivities, $\rho_0 \approx$ 40-70 $\mu\Omega$ cm, corresponding to a RRR of only 6-9. Matsuda et al. attributed this to chemical disorder and/or strain introduced by the substitution. As discussed previously, superconductivity in CrAs is obtained in the single crystals only with RRR values in the order of 100 or more. In this sense, the absence of superconductivity in P doped samples is consistent with the strong disorder sensitivity of the pressure-induced superconduting phase [7, 9].

The only doped system in which superconductivity has been reported is Al-substituted CrAs, with $x \approx 0.7\%$, studied by Park et al. Unlike isovalent P doping, which acts primarily through structural contraction, Al substitution changes the carrier concentration and introduces disorder, reducing the RRR to values around 30. Despite this, superconductivity can still be induced under pressure, forming a dome that emerges around 0.6 GPa and reaches its maximum near 1 GPa, where the reported T_c is approximately the same as in pure CrAs [35]. Fig. 2.7 compares the temperature-pressure phase diagrams of Al-doped CrAs and pure CrAs. The contour maps display the normalized isothermal resistivity, normalized by its value at the highest measured pressure, 2.41 GPa for Al-CrAs and 2.25 GPa for CrAs, respectively. This reveals the evolution of the normal state resistivity across pressure and temperature, highlighting how magnetic scattering develops and how the helimagnetic phase is suppressed in the two systems. Although the b lattice parameter and the ambient pressure T_N increase - consistent with the negative pressure trend outlined previously, see Tab. 2.1 - the magnetic transition collapses much more rapidly under applied pressure in the Al-doped compound.

The helimagnetic order disappears around 0.45 GPa, compared to the 0.7-1.0 GPa in pure CrAs. This behavior can't be explained by lattice effects alone and instead points to changes in the electronic structure arising from carrier doping [35]. In pure CrAs, the normalized resistivity exhibits a broad and pronounced enhancement that stretches up to the vicinity of the superconducting dome, showing that the strong magnetic scattering persists almost up to the onset of superconductivity. In Al-doped CrAs, the corresponding enhancement is narrower and stops at much lower pressures, suggesting that the magnetic fluctuations are significantly reduced when superconductivity appears [35].

This fast suppression of magnetism suggests that the superconducting dome in Al-doped CrAs becomes effectively detached from the potential quantum critical point. This deviation from the pure compound and from the negative pressure picture suggests that the formation of Cooper pairs in Al-doped CrAs is not mediated solely - or perhaps not at all - by critical magnetic fluctuations [35].

2.1.3. Electronic structure and band model of CrAs

The structural and magnetic properties of CrAs have been interpreted within the phenomenological band model introduced by Boller et al. and later refined by Zavadskiĭ et al. [22, 27]. This framework has been widely used to explain the behavior of CrAs under temperature and applied pressure [17, 18]. In this model, the properties of CrAs are attributed to a reconfiguration of the electronic structure associated with a transition of electrons from an itinerant state above T_N to a localized state below T_N [27]. The approach assumes that both Cr and As are trivalent and that covalent Cr-As bonding together with direct Cr-Cr interactions governs the electronic density of states near the Fermi energy. The former has been confirmed experimentally by Pan et al. through X-ray absorption spectroscopy measurements [25], while the latter is supported by first principles studies [44, 45, 46].

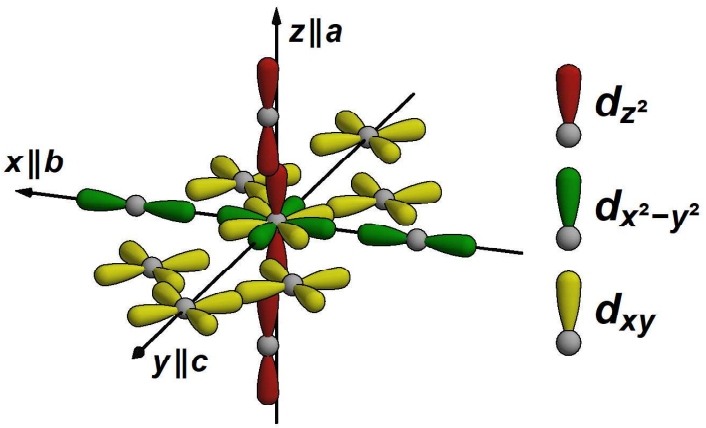

Figure 2.8.: Orientation of the Cr 3*d* orbitals in CrAs following the notation of Boller et al. Only Cr atoms are shown. Figure from [16].

Fig. 2.8 shows the orientation of the Cr 3*d* orbitals in the MnP-type structure of CrAs. Following the notation introduced by Boller et al., the crystallographic axes are chosen such that $x \parallel b$, $y \parallel c$ and $z \parallel a$ [22, 27]. Within the distorted octahedral environment formed by the surrounding As atoms, the Cr^{3+} states are subject to a crystal-field splitting that separates the 3d orbitals into a lower energy t_{2g} set and a higher energy set e_g. In this crystallographic coordinate system, the t_{2g} state corresponds to the $(d_{z^2}, d_{x^2-y^2}, d_{xy})$ orbitals, while the e_g states are formed by (d_{xz}, d_{yz}) orbitals. Within this convention, the d_{z^2} orbital is oriented along the a-axis toward the nearest Cr neighbor, the d_{xy} orbital lies in the bc-plane toward nearest Cr neighbors, and the $d_{x^2-y^2}$ orbital is oriented along the b-axis toward the next-nearest Cr neighbor along that direction. The d_{xz} and d_{yz} orbitals point toward neighboring As atoms [22]. The construction of this scheme relies on the analysis of how Cr 3*d* orbitals align within the crystal lattice and interact with neighboring atoms, in relation to the Mott critical distance R_C, which describes the crossover from itinerant to localized electronic states. For Cr-Cr distances R_C was estimated to be 3.18 Å[22, 27].

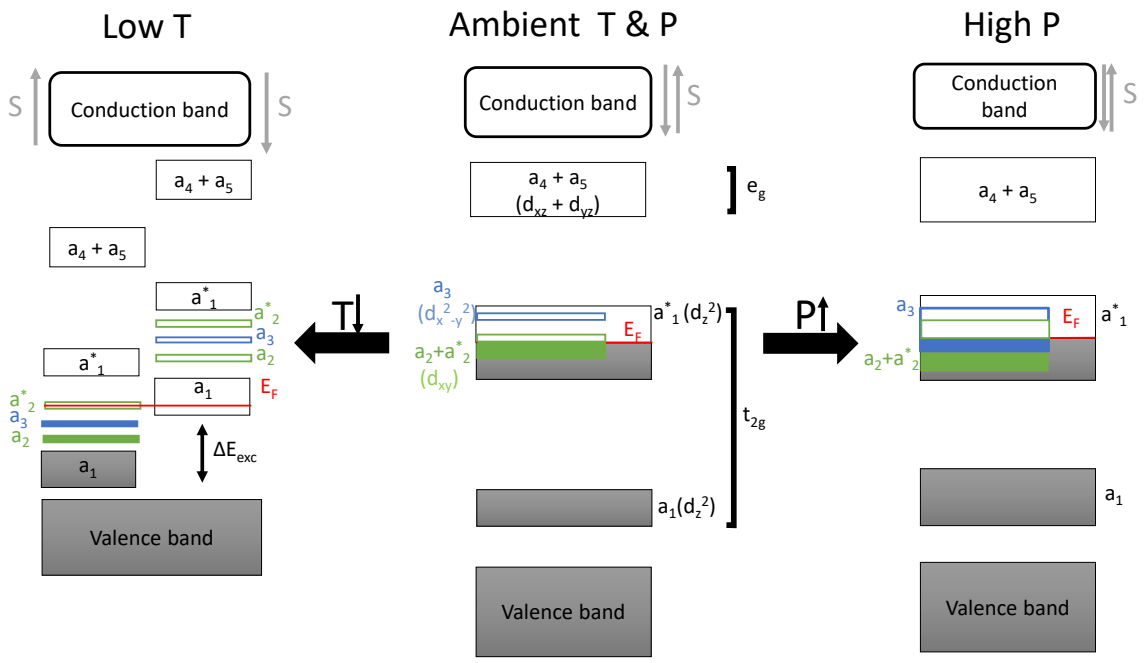

Figure 2.9.: Schematic representation of the CrAs band structure and its evolution with temperature and pressure. The three panels compare the electronic structure in the low-temperature helimagnetic phase at ambient pressure (left), under ambient conditions (center), and at room temperature under high pressure (right). In the helimagnetic phase, the Cr 3*d*-derived bands exhibit an exchange splitting with the spin channels indicated by gray arrows. The labeling of the bonding and antibonding bands (a_i and a_i^*) follows the notation discussed in the main text. Image adapted from [17, 27].

Fig. 2.9 shows a schematic representation of the band structure of CrAs, constructed on the basis of the phenomenological model introduced by Boller *et al.* and further developed by Zavadskiĭ *et al.* [22, 27]. To remain consistent with the notation adopted in this framework, the same band labeling scheme is used in the following discussion. Within this scheme, the bonding and antibonding bands originating from the directional overlap of Cr 3*d* orbitals are denoted by a_i and a_i^*, respectively. The bands a_1 and a_1^* are predominantly derived from the d_{z^2} orbital, a_2 and a_2^* from the d_{xy} orbital, and a_3 and a_3^* from the $d_{x^2-y^2}$ orbital. These states originate from direct Cr–Cr interactions and form the subset of bands whose energetic position and degree of localization are governed by the corresponding Cr–Cr distances relative to the Mott critical distance R_C. In contrast, the d_{xz} and d_{yz} orbitals, labeled a_4 and a_5 within this notation, are oriented toward neighboring As atoms and therefore hybridize strongly with As *p* states. Consequently, they do not form well-defined bonding–antibonding pairs but instead give rise to a single broad band, commonly referred to as the combined $a_4 + a_5$ band. This band lies far from the Fermi energy and plays only a secondary role in the magnetic instability at T_N.

The behavior at T_N results from the a_3 band - initially unoccupied because the Cr-Cr separation along the *b* axis exceeds R_C - crossing the Fermi energy, upon cooling. Because this Cr-Cr distance remains larger than the Mott critical value, the electrons that start to populate a_3 states retain a partially localized character, which enhances Coulomb repulsion along the *b* axis, leading to an abrupt increase of approximately 4% of the *b*-axis detected in diffraction studies. Moreover, as the Cr-Cr distances within the *bc*-plane approach R_C, band narrowing enhances electronic localization and promotes band magnetism, explaining the appearance of magnetic moment in the Cr atom[7].

[7]This leads to a lifting of degeneracy due to the intra-atomic exchange energy ΔE_{exc} [27].

The pressure dependence of the CrAs band structure has been investigated via DFT calculations by Yu et al. and Autieri et al., revealing an overall broadening of the electronic bands with increasing pressure, driven by the reduction of Cr-Cr interatomic distances [17, 47]. Although the Cr-Cr distance associated with the a_3 orbital orientation remains larger than the Mott critical distance R_C even under applied pressure [18], the pressure-induced increase in bandwidth reduces the degree of localization of the a_3 states. Yu et al. further showed that the electronic charge density is intrinsically lower along the b axis, compared to the other lattice parameters, and that its gradient decreases with pressure [17]. This flattening of the charge distribution, together with the band broadening, indicates an enhanced electronic itinerancy along the b. As a result, when the a_3 band intersects the Fermi level in the pressure range 0.2-0.3 GPa - according to the schematic band picture of Yu et al. - it does so in an itinerant regime, enabling the pronounced collapse of the b axis [17]. In Yu et al. diffraction data, this anomaly manifests as an abrupt decrease of the b axis of approximately -1%, corresponding to an equivalent -1% decrease in the unit cell volume, within the 0.2-0.3 GPa pressure range. However, this pressure-induced isostructural transition has not been reproduced in further studies and its underlying mechanism is still not fully understood.

The same pressure-dependent band structure considerations can be extended to the doped $CrAs_{1-x}P_x$ system. Phosphorus substitution is isovalent, leaving the Cr^{3+} electronic configuration, while exerting a chemical pressure effect that mimics the reduction of lattice parameters induced by physical pressure. The resulting enhancement of band broadening, due to the shorter Cr-Cr distances, is also supported by first principles calculations on CrP by Ito et al. [44]. This band structure framework provides the basis for interpreting the structural evolution induced by phosphorus substitution and for comparing its effects with those of applied pressure in the following sections.

2.2. Quantum criticality in CrAs

A quantum critical point (QCP) is a continuous phase transition occurring at absolute zero temperature and is accessed by tuning a nonthermal parameter, such as pressure, chemical substitution or magnetic field [48, 49]. Unlike classical phase transitions, which are driven by thermal fluctuations, quantum phase transitions are governed by zero-point quantum fluctuations. These quantum fluctuations are not confined to the point $T = 0$ as they spread upward in temperature and shape the physical properties over an extended region of the phase diagram [48, 49].

In many correlated electron systems - such as heavy-fermions, cuprates and iron pnictides - unconventional superconductivity often emerges in proximity to a magnetically ordered phase whose transition temperature is continuously suppressed to zero. This empirical observation has led to the idea that quantum critical fluctuations themselves play a central role in the formation of Cooper pairs, making them a fundamental ingredient for unconventional superconductivity [48, 49].
Based on the observation that the helimagnetic transition in CrAs can be completely suppressed by the application of pressure, the existence of a QCP has been proposed for this compound [7, 9, 29].Several studies have reported that the resistivity of CrAs under pressure exhibits clear deviations from the Fermi liquid behavior as the helimagnetic phase is suppressed. In particular, the exponent n in the expression $\rho(T) = \rho_0 + AT^n$ decreases from the Fermi-liquid value $n = 2$ toward $n \approx 1.5$, around P_c, while the A coefficient - obtained from fixed $n = 2$ fits - shows a pronounced enhancement near the critical pressure [7, 9, 29].

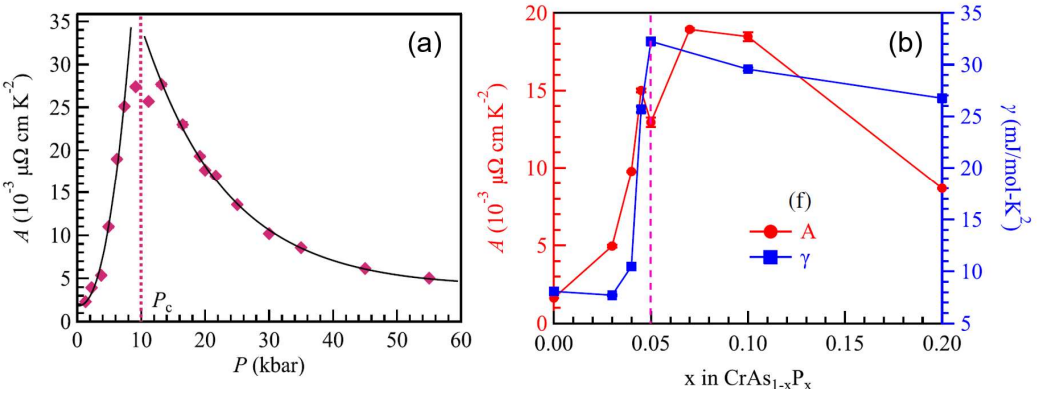

Figure 2.10.: (a) Pressure dependence of the T^2 coefficient A in pure CrAs, showing a pronounced enhancement near the critical pressure $P_c \approx 1$ GPa. (b) Chemical pressure dependence of the T^2 coefficient A and the electronic specific-heat coefficient γ for $CrAs_{1-x}P_x$. Both quantities exhibit a strong increase near the critical concentration x_c. Figure adapted from [7].

Fig. 2.10 shows the comparison between the signatures of quantum criticality in pure CrAs single crystals and in $CrAs_{1-x}P_x$ single crystals, as reported by Matsuda et al. [7]. At the critical concentration $x_c \approx 0.05$, where helimagnetism disappears, the exponent in the doped sample also approaches $n \approx 1.5$ together with the increase in both A and the electronic specific-heat coefficient γ increase significantly. These features are commonly associated with the vicinity of a magnetic quantum critical point, since the reduction of n toward non Fermi liquid values together with the enhancement of $A \propto (m^*/m_0)$ and γ reflects the growing quasiparticle scattering and effective mass expected as magnetic fluctuations soften toward zero temperature [48, 49]. These parallels show that P substitution specifically acts as an effective chemical pressure, driving CrAs through a similar magnetic instability as physical pressure.

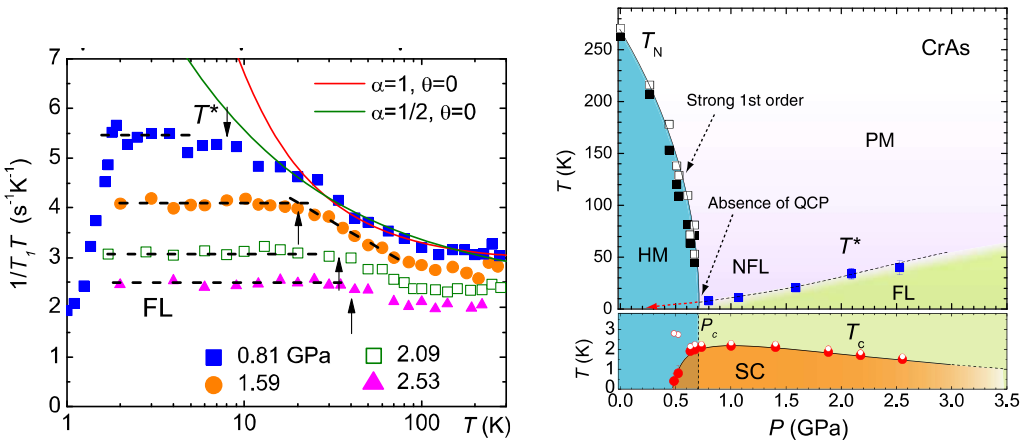

Figure 2.11.: Left: Temperature dependence of $1/T_1T$ in the paramgnetic state. The increase upon cooling indicates the onset of magnetic fluctuations. At low temperatures, $1/T_1T$ deviates from the expected divergence at a QCP. The characteristic temperature T^* is obtained from the intersection of the low and high temperature extrapolations. Right: Pressure-temperature phase diagram of CrAs. Although no QCP is present at P_c, the extrapolation of T^* (red arrow) suggest that a QCP may be hidden in the first-order helimagnetic phase. Figure adapted from [30].

To further probe whether these transport signatures truly correspond to a magnetic quantum critical point, Kotegawa et al. performed NMR measurements under pressure. Their $1/T_1T$ data, summarized in Fig. 2.11 show a clear enhancement upon cooling from about 100 K down to 10-20 K for all pressures above 0.7 GPa.

This behavior is consistent with the growth of low energy antiferromagnetic fluctuations and, at first glance, supports the quantum critical interpretation supported by resistivity data [28, 29]. However, at lower temperatures, the $1/T_1T$ deviates from the divergence expected near a magnetic QCP - observed in several iron-based superconductors [50] - and instead crosses over into a Fermi liquid regime [28]. The lack of critical fluctuations in $1/T_1T$, together with the strong first-order character maintained by the helimagnetic transition, led Kotegawa et al. to conclude that no QCP is realized at the pressure where helimagnetism disappears. At the same time, the increase of $1/T_1T$ upon cooling in the paramagnetic phase - especially just above the critical pressure region - reflects growth of magnetic fluctuations, until a Fermi liquid regime is recovered at lower temperatures. The characteristic crossover temperature T^*, defined by this recovery, decreases with pressure but remains finite at the critical pressure (see Fig. 2.11). Extrapolating T^* to zero would place, potentially, the QCP near approximately 0.2 GPa [30]. In this view, CrAs would host a QCP at low pressure, but the first-order nature of the helimagnetic transition would prevent the system from reaching it, effectively masking the QCP.

It is worth noting that the pressure phase diagram reported for CrAs already exhibit noticeable sample dependent differences. The phase diagrams reported by Wu et al. and Matsuda et al. are consistent with one another, while they deviate from the one reported by Kotegawa et al. In particular, Matsuda et al. place the complete suppression of the magnetic order around 1 GPa, while both Wu et al. and Kotegawa et al. locate it near 0.7 GPa (see Fig. 2.4 and 2.11). Nevertheless, both Wu et al. and Matsuda et al. observe a coexistence region between helimagnetism and superconductivity, extending roughly from 0.3 GPa up to their respective P_c (0.7 GPa for Wu et al. and 1 GPa for Matsuda et al.), while Kotegawa et al. report the onset of superconductivity only from 0.5 GPa, coexisting with magnetism until 0.7 GPa[8] [7, 9, 29]. A similar discrepancy appears in the analysis of the A coefficient. In Matsuda's data, the enhancement of A peaks near their critical pressure of 1 GPa - see Fig. 2.10 - while in Kotegawa's data the maximum occurs around 0.7 GPa [29]. These shifts reflect the same underlying sensitivity to sample quality and residual resistivity and they suggest that the question of whether CrAs actually hosts a QCP - or only exhibits quantum critical like signatures - may depend strongly on specific sample factors.

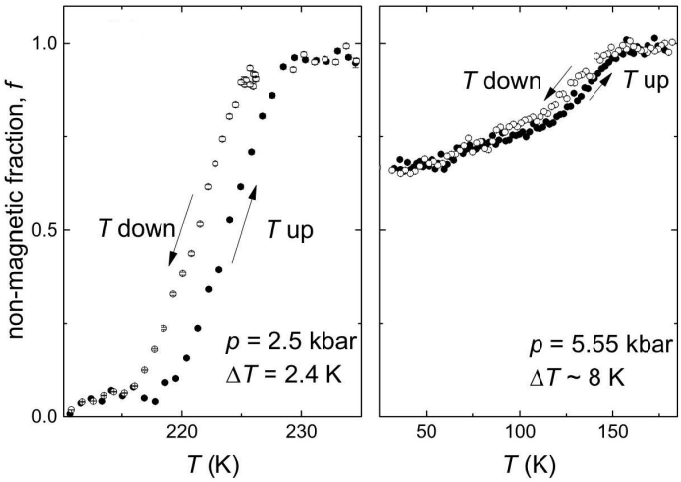

Figure 2.12.: Non-magnetic volume fraction of CrAs as a function of temperature and pressure, extracted from μSR. The curves labeled *T down* and *T up* correspond to cooling and warming cycles, respectively. The hysteresis ΔT associated with the first-order transition is marked in each panel. Adapted from [10].

[8] Moreover, Kotegawa et al. themselves remark that the superconducting transition temperatures of their samples differ from those reported by Wu et al. [29].

All recent studies agree that the magnetostructural transition in CrAs remains strongly first order under pressure [7, 9, 29]. The clearest signatures of the first-order character are the phase separation and the hysteresis. Fig. 2.12 shows the non-magnetic volume fraction as a function of temperature and pressure, extracted by the μSR data by Khasanov et al. [10]. Approximately above 0.3 GPa, the sample develops coexisting magnetic and non-magnetic regions in the temperature range between T_N and T_c, while at lower pressures the transition produces a fully magnetic volume fraction immediately after T_N[9] [10]. Hysteresis provides the other clear manifestation of the first order nature of the transition. In Fig. 2.11, the hysteresis of the magnetostructural transition appears as the offset between the T_N values determined via transport measurements upon cooling (solid black squares) and warming (open squares). Although the width of the hysteresis varies with pressure - narrowing above approximately 0.6 GPa - it remains finite all the way up to the disappearance of helimagnetism [29]. Comparable hysteretic behavior is also visible in diffraction measurements (see [7]) and in the μSR estimate of the non-magnetic volume fraction (see Fig. 2.12) [10]. Despite the quantitative width of the hysteresis varies between experiments and techniques, its persistence is robust and indicates that the transition never change toward the continuous limit required for the appearance of a genuine QCP.

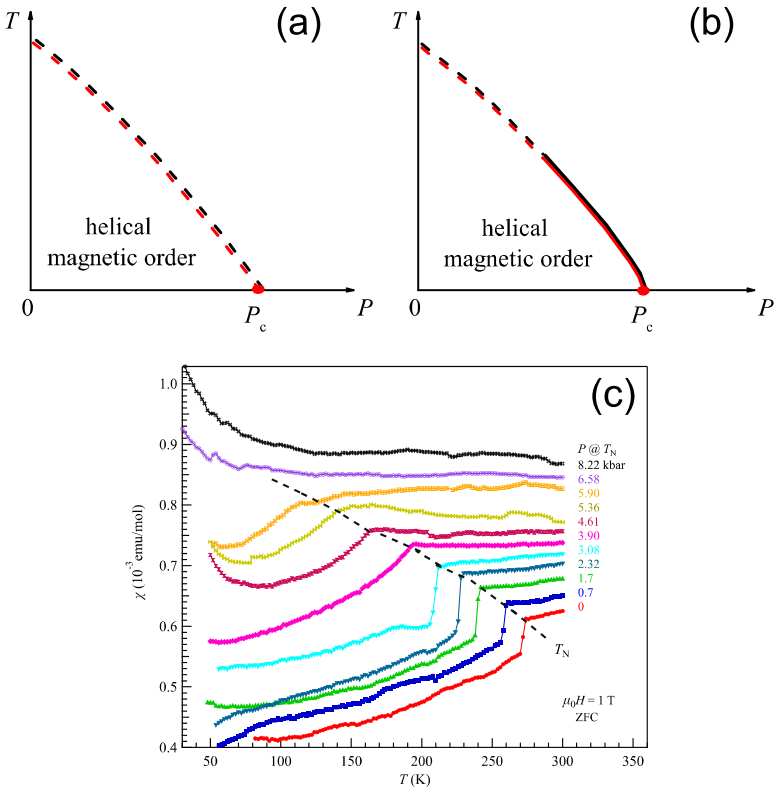

Figure 2.13.: (a,b) Schematic representation of the structural (black) and magnetic (red) phase transition in CrAs under pressure, which remain coupled at all pressures. Dashed lines indicate first order. With increasing pressure they may either remain first order (a) or evolve toward second-order (b). (c) Temperature dependence of the magnetic susceptibility in CrAs single crystals under pressures up to 8 kbar (0.8 GPa). Curves are shifted vertically for clarity. Adapted from [7].

A theoretical framework that helps interpret these observations was developed by Matsuda et al., who examined the nature of the magnetostructural transition in CrAs and its evolution under pressure.

[9] Their measurements were performed on polycrystalline CrAs, therefore the usual caveats regarding sample form and quality apply.

Using a phenomenological free energy functional containing a term proportional to the product of the unit cell volume change and the square of the magnetic order parameter, they show that magnetic and structural orders necessarily emerge together and retain either the same first or second-order character allowed by the model, as shown in Fig. 2.13 [7]. In order to extend this description toward zero temperature, Matsuda et al. incorporate the dynamics of the helimagnetic order parameter and the damping that arises from its coupling to the increasingly itinerant electrons under pressure[10]. Within this formulation, the magnetic phase transition can evolve toward a quasisecond-order character - namely, with almost no discontinuity - even though the structural component of the transition remains first order, as confirmed by the diffraction measurements of Matsuda et al. [7]. This behavior is reflected in the magnetic susceptibility of pure CrAs under pressure - shown in Fig. 2.13 - where, above 0.3 GPa, the sharp jump associated with the first-order transition is replaced by a smooth cusp-like anomaly that broadens progressively with increasing pressure [7]. Even though the magnetostructural transition remains first order, the phenomenological model suggests that the progressive softening of the magnetic response under pressure could be a sign that the system is being brought increasingly close to a magnetic QCP. Therefore, even if quantitative differences between the phase diagrams obtained by different groups remain, the model provides a unified interpretation in which the magnetic transition becomes progressively softer while the structural discontinuity persists. Within this scenario, quantum critical like signatures - such as the increase of both the A and γ coefficients near P_c or x_c- can develop even in the absence of a strictly continuous transition [7].

2.3. Phase coexistence in CrAs

Under applied pressure, CrAs enters a regime where the first-order magnetostructural AFM-PM transition produces a macroscopic coexistence of helimagnetic and non-magnetic regions (see Fig. 2.12). μSR and NMR/NQR measurements have established that superconductivity develops within this non-magnetic volume fraction, so that, in the coexistence regime below P_c, the superconducting and antiferromagnetic phases occupy spatially separated regions of the sample [10, 28, 30]. This section reviews the experimental evidence for phase coexistence in CrAs and discusses the conditions under which it becomes observable, highlighting the limitations of existing structural probes and motivating the need for complementary approaches. Since the AFM-PM transition is magnetostructural and retains its first-order character up to the QCP [7], any reduction of the antiferromagnetic phase must be accompanied by the discontinuous changes in the lattice parameters - with regions displaying either the high temperature or the low temperature lattice parameters, shown in Sec. 2.1 - and by the formation of structural domains. Although several studies have reported clear evidence of such coexistence in both pure CrAs under pressure and in various doped compounds [7, 22, 34, 38, 51], the structural dynamics associated with the coexistence region - particularly how the competing lattice responses evolve with temperature or pressure - have not been systematically investigated. Given that this phase separation appears at temperatures well above T_c, understanding these aspects may provide additional insights into the interplay between superconductivity and the structural degrees of freedom in a rich phase diagram such as that of unconventional superconductor CrAs.

[10] As discussed in Sec. 2.1.1, the application of pressure was proposed to broaden the electronic bands of CrAs, enhancing itineracy [27].

The temperature range over which the phase coexistence is observed, as well as the temperature at which it becomes detectable, appears to depend on the synthesis conditions and sample characteristics [22, 38, 51]. This dependence may account for the discrepancy reported across different studies. Notably, no signature of coexistence has been reported in CrAs single crystal at ambient pressure near T_N [18, 7], while it has been observed in polycrystalline CrAs, under similar conditions [22, 51][11]. Similarly, no signatures of coexistence has been reported in doped CrAs single crystals [7], although several polycrystalline doped compounds - with doping occurring both on the transition metal or pnictide site - do show clear evidence of the coexistence [34, 38]. To make sense of these contrasting results, it is necessary to consider the experimental conditions under which coexistence is observable and the limitations that may affects its visibility. Under applied pressure, coexistence has been detected in CrAs single crystal by Matsuda et al. and Kotegawa et al. [7, 28][12], as well as in polycrystalline samples by Khasanov et al. and Keller et al. [19, 10][13].

The absence of any observable signature of the phase coexistence in the recent ambient pressure studies on CrAs single crystals, could therefore be linked to the very sharp transition. Detecting the coexistence would require stabilizing the sample temperature close to T_N, with an offset smaller than 5 K, which is a level of temperature control that is often not implemented in these studies. The way coexistence would manifest itself in a single crystal diffraction experiment would be as additional Bragg reflections associated with the emerging structural phase. These reflections would appear near the position expected for the monophase structure - since the two phases are isostructural - but slightly shifted due to the difference in lattice parameters. Their relative intensities would reflect the volume fraction of the emerging phase. The mismatch between the lattice parameters of the coexisting domains would introduce internal stress and create grain boundaries, leading to further splitting of the Bragg reflections[14]. For small volume fractions, these additional reflections may become so weak, broadened or overlapping with the main peaks that they could be dismissed as strain related artifacts or mosaicity, making coexistence difficult to identify unambiguously. A particularly illustrative example of these inconsistencies is provided by the neutron diffraction study of Matsuda et al., which compares directly pure CrAs under pressure with ambient pressure $CrAs_{1-x}P_x$[7] .

Fig. 2.14 shows the temperature dependence of b lattice parameter of CrAs and $CrAs_{1-x}P_x$single crystals, obtained via neutron diffraction, reported by Matsuda et al. [7]. The phase coexistence is observed in undoped CrAs under pressure, while it is absent in the doped $CrAs_{1-x}P_x$single crystal samples. Matsuda et al. attribute this difference to possible pressure inhomogeneity within the pressure cell. However, the study does not specify the sequence of pressure and thermal cycles and it remains unclear whether the same sample was subjected to repeated crossing of the transition. The cracking induced by the abrupt change in the lattice parameters - see Sec. 3.1.3 - could in principle generate mechanically isolated regions which would prevent the transition from completing, locally.

[11] Notably, both Boller et al. and Hu et al. display different T_N values from the one accepted in literature.

[12] Kotegawa et al. probed coexistence via NMR/NQR, not directly reporting the lattice parameters

[13] While these studies do not report directly the lattice parameter they show evidence of competition between magnetism and superconductivity via μSR and neutron diffraction.

[14] Fig. 3.3, taken from [18], displays few unindexed Bragg reflections. Although the authors do not discuss the nature of these additional reflections, it is plausible that they could originate from a small fraction of the sample showing the coexistence.

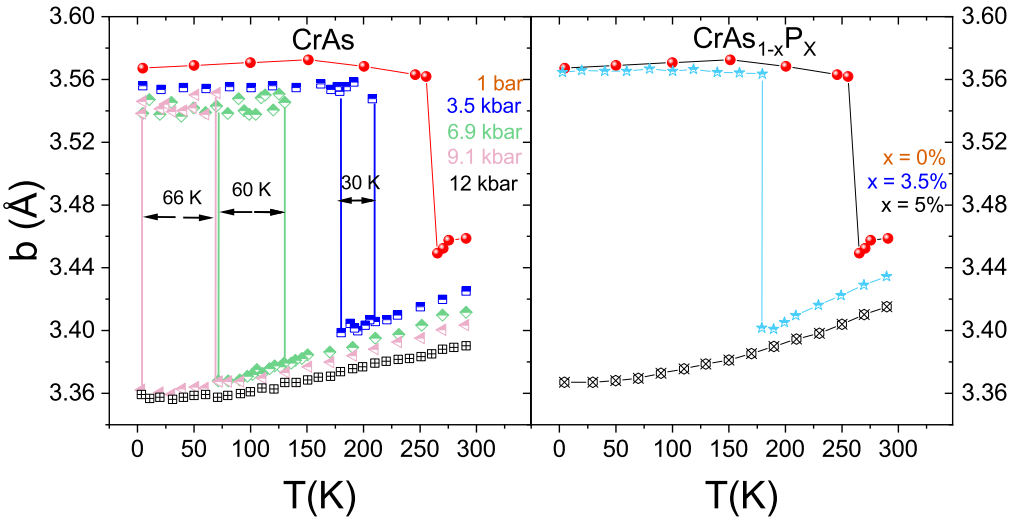

Figure 2.14.: Temperature dependence of the b lattice parameter of CrAs under physical pressure (left) and chemical pressure (right). The regions between the two solid lines represent the temperature range over which the two-phase coexistence is observed, with the corresponding width written. Data digitized from [7].

Interestingly, in the work of Matsuda et al., the coexistence is primarily detected through the b lattice parameter, while the earlier studies by Boller [22] and Suzuki et al. [34, 38] also reported signatures of coexistence in the a and c axes. This difference likely arises because the c-axis data in Matsuda's work are significantly noisier and display only subtle variations at the transition, making it difficult to clearly identify the two phases. Such noise levels are not present in polycrystalline diffraction studies, such as those by Boller, Suzuki, or even Shen et al. [20], where no coexistence is detected, as the averaging over many randomly oriented grains results in more accurate and stable lattice parameters. Therefore, the anomalous relative change of the b lattice parameters at the transition makes it a particularly reliable probe for identifying phase coexistence in single crystal sample. Still, such mechanically trapped domains would not explain the systematic pressure-dependent onset and disappearance of the phase coexistence reported for CrAs. This suggests that the effect is more likely intrinsic to the material itself, rather than being due to pressure inhomogeneities.

To the best of our knowledge, no studies are currently available on the lattice dynamics of $CrAs_{1-x}P_x$ single crystals. Such investigations could help clarify whether the absence of phase coexistence observed by Matsuda et al. in their doped samples reflects an intrinsic difference between chemically and physically pressurized CrAs, or whether it is a consequence of extrinsic factors. This unresolved discrepancy highlights the need for an independent probe of the structural response in $CrAs_{1-x}P_x$ single crystals, capable of detecting subtle lattice distortions or phase coexistence even when diffraction signatures become weak or experimentally ambiguous. Raman spectroscopy is particularly well suited for this purpose. Its sensitivity to lattice dynamics, symmetry changes and phonon anomalies makes it an excellent probe of magnetostructural transitions and the potential phase coexistence.

Taken together, the literature reviewed in this chapter highlights the central role of the lattice in the physics of CrAs and its evolution under both physical and chemical pressure. While previous studies have already examined the lattice dynamics and its coupling to magnetism in pure CrAs [52, 8] the behavior of the doped system remains largely unexplored. In particular, the absence of phase coexistence in $CrAs_{1-x}P_x$ single crystals reported in recent studies raises the question of whether chemical pressure truly reproduces the effects of applied pressure at the level of the structural response and whether the coexistence regime itself plays any role in the emergence of superconductivity.

In this thesis, we address this gap by performing a systematic Raman study on high quality $CrAs_{1-x}P_x$ single crystals and by comparing their response to that of pure CrAs under pressure. This comparison will allow us to assess the extent to which chemical pressure reproduces the effects of physical pressure and to determine whether the structural and magnetic phenomena observed in undoped CrAs persist in the doped regime. In the following chapters, we describe the sample preparation and characterization of $CrAs_{1-x}P_x$ single crystals and present a detailed report of the experimental results from Raman scattering measurements on both pure CrAs single crystals under pressure and $CrAs_{1-x}P_x$ single crystals.

3. Sample preparation and characterization

The investigation of lattice dynamics and structural response in $CrAs_{1-x}P_x$ requires single crystals with a well defined composition and high structural quality. In this chapter, we describe the synthesis procedures used to grow $CrAs_{1-x}P_x$, together with the characterization methods employed to assess their stoichiometry, homogeneity and crystallographic quality. Particular attention is given to the evolution of lattice parameters with phosphorus substitution, which allows us to quantify the effects of chemical pressure and establish a reliable basis for comparing the doped samples with pure CrAs under pressure.

3.1. Crystal growth

Single Crystals of $CrAs_{1-x}P_x$ were grown in collaboration with Dr. Amir-Abbas Haghighirad. The Sn-flux method was chosen for crystal growth, as described in [52, 53]. Growth of $CrAs_{1-x}P_x$ from elemental sources is challenging due to the lower solubility of P in Sn compared to arsenic. To overcome this, a two-step approach was employed: first, the synthesis of the polycrystalline precursors of $CrAs_{1-x}P_x$, as described in [39, 38], which were then used for the flux growth.

3.1.1. Polycrystalline material

For the synthesis of polycrystalline $CrAs_{1-x}P_x$ precursors, the phosphorus concentration of 20% and 25% were chosen[1]. The elementary educts of chromium Cr (Alfa Aesar, powder, 99:99%), arsenic As (chemPUR, flakes, 99:999%), red phosphorus P (chemPUR, flakes, 99:999%) and tin Sn (Alfa Aesar, shot, 99:99%) were handled inside of Argon glovebox. The stoichiometry of the educts of $CrAs_{1-x}P_x$ is reported in Tab. 3.1 and 3.2. The material was inserted in an alumina (Al_2O_3) crucible inside a quartz ampule. The ampule was then connected to a turbo pump and sealed in a vacuum, with $p \approx 10^{-6}$ mbar, with the help of a oxy-hydrogen flame. The synthesis process was guided with the following reaction equation from [54, 39] where the time written in the round brackets represents the dwelling time.

	m(g)	M(g/mol)	Ratio
Cr	5	51.996	1
As	5.764	74.922	0.8
P	0.596	30.974	0.2

Table 3.1.: Stoichiometric composition of $CrAs_{1-x}P_x$ precursor material, with $x = 20\%$. The table presents the mass (m), molar mass (M), and molar ratio of the constituent elements (Cr, As, and P) for the synthesis.

[1]The concentration of $x = 0\%, 3\%, 5\%, 10\%$, both polycrystalline and single crystals were previously synthesized in the bachelor's thesis of Urs Strobel [54].

	m(g)	M(g/mol)	Ratio
Cr	4	51.996	1
As	4.323	74.922	0.75
P	0.596	30.974	0.25

Table 3.2.: Stoichiometric composition of $CrAs_{1-x}P_x$ precursor material, with $x = 25\%$. The table presents the mass (m), molar mass (M), and molar ratio of the constituent elements (Cr, As, and P) for the synthesis.

Material	Nominal m(g)	1st Sintering m(g)	2nd Sintering m(g)
$CrAs_{0.80}P_{0.20}$	11.360	11.272	11.164
$CrAs_{0.75}P_{0.25}$	8.919	8.778	8.721

Table 3.3.: Mass variation of $CrAs_{1-x}P_x$ samples during the sintering process. The table presents the nominal mass (m) of the starting material, followed by the measured mass after the first and second sintering steps, indicating material loss during processing.

$$\mathrm{RT} \xrightarrow{50^\circ C/h} 300^\circ C\,(72\mathrm{h}) \xrightarrow{50^\circ C/h} 600^\circ C\,(72\mathrm{h}) \xrightarrow{50^\circ C/h} 800^\circ C\,(168\mathrm{h}) \xrightarrow{-100^\circ C/h} \mathrm{RT} \tag{3.1}$$

After this initial synthesis, the obtained polycrystalline material was removed from the crucible and finely ground using a mortar and pestle, to ensure better homogeneity. To improve crystallinity and phase purity, the sample was first reweighed to check for any material loss and then transferred into a new quartz ampule for a second sintering process, described by the following reaction equation.

$$\mathrm{RT} \xrightarrow{50^\circ C/h} 800^\circ C\,(48\mathrm{h}) \xrightarrow{-200^\circ C/h} \mathrm{RT} \tag{3.2}$$

A slight mass loss was observed during the sintering process, documented on Tab. 3.3, due to material adhesion on the walls of the crucible and the ampule.

3.1.2. Single crystal

The Sn-flux method was chosen for the growth of $CrAs_{1-x}P_x$ single crystals, as detailed in [52]. Tin (Sn) was selected as the flux material due to its low vapor pressure and its low melting point [54, 55]. The former minimizes the risk of ampule explosions during growth; the latter ensures that the growth process operates at low temperatures [2], preventing the formation of the high-temperature hexagonal phase of the Cr-As system [36, 57]. The $CrAs_{1-x}P_x$precursor was mixed with tin in a 1:15 molar ratio ($CrAs_{1-x}P_x$:Sn), with the exact quantities detailed in Tab. 3.4 and 3.5. The preparation involved layering the materials in an alumina (Al_2O_3) crucible in the following arrangement: half of the tin was placed at the bottom, followed by $CrAs_{1-x}P_x$precursor, and then the remaining tin. This setup ensures complete coverage of the precursor during the flux growth process, for a better diffusion. The crucible was sealed within a quartz ampule, which was evacuated to $p \approx 10^{-6}$ mbar using a turbo pump and sealed with an oxy-propane flame.

The synthesis process followed the reaction equation 3.3, with the times in parentheses representing the dwelling periods. The $CrAs_{1-x}P_x$precursor fully dissolves into the molten tin upon reaching

[2] Compared to other crystal growth method like melt growth [56]

	m(g)	M(g/mol)	Ratio
$CrAs_{0.80}P_{0.20}$	2.733	118.128	1
Sn	41.193	118.710	15

Table 3.4.: Mass, molar mass, and molar ratio of $CrAs_{0.80}P_{0.20}$ and Sn used in the flux growth process. The table presents the ratio employed for crystal growth, where tin (Sn) serves as the flux.

	m(g)	M(g/mol)	Ratio
$CrAs_{0.75}P_{0.25}$	2.609	115.931	1
Sn	40.071	118.710	15

Table 3.5.: Mass, molar mass, and molar ratio of $CrAs_{0.75}P_{0.25}$ and Sn used in the flux growth process. The table presents the ratio employed for crystal growth, where tin (Sn) serves as the flux.

the maximum temperature of 850°C and then gets cooled down - at the rate of 0.5°C/h - to achieve supersaturation and nucleation [56].

$$\mathrm{RT} \xrightarrow{50°C/h} 650°C\,(10\mathrm{h}) \xrightarrow{50°C/h} 850°C\,(10\mathrm{h}) \xrightarrow{-0.5°C/h} 600°C\,(10\mathrm{h}) \xrightarrow{-100°C/h} \mathrm{RT} \tag{3.3}$$

After cooling to room temperature, the solidified solution - consisting of a mixture of crystals and tin flux - was extracted and transferred onto a ceramic plate. Single crystals were separated from the flux using a 30% diluted nitric acid (HNO_3) solution as an etching agent. Etching was performed by applying a few drops on the sample, while monitoring the reaction under a microscope. The reaction was halted by diluting the mixture with deionized water once the crystals were freed from the flux. To ensure complete flux removal, the crystals were then immersed in a diluted nitric acid solution and deionized water and subjected to ultrasonic treatment in a glass beaker.
Fig 3.1 shows representative $CrAs_{0.75}P_{25}$ single crystals obtained in this study. The crystal exhibit a pseudohexagonal habitus with a needle-like morphology. Laue diffraction measurements confirm the that long axis of the needles aligns with the crystallographic *a*-axis, in agreement with the growth of the parent compound [7, 8]. The crystals present shiny, well defined surfaces without visible defects, consistent with high structural quality. Typical dimensions are displayed in Fig. 3.2, where the crystal sizes of order $2 \times 0.7 \times 0.7\ mm^3$ are common for the $x_{nom} = 25\%$ batch.

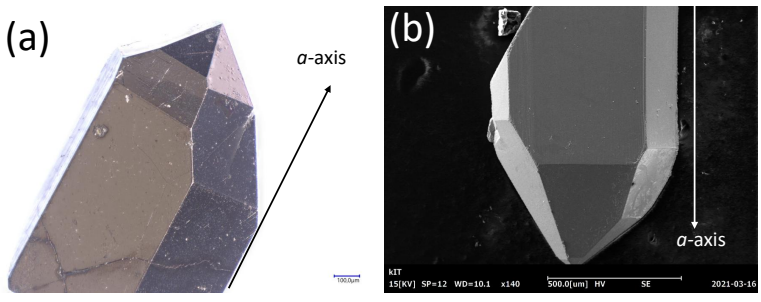

Figure 3.1.: (a) Optical microscope image of a $CrAs_{1-x}P_x$ single crystal with $x_{nom} = 25\%$. Black arrow indicates the orientation of the *a*-axis. (b) Scanning Electron Microscope (SEM) image of a different $CrAs_{1-x}P_x$ single crystal with $x_{nom} = 25\%$. White arrow indicates the orientation of *a*-axis.

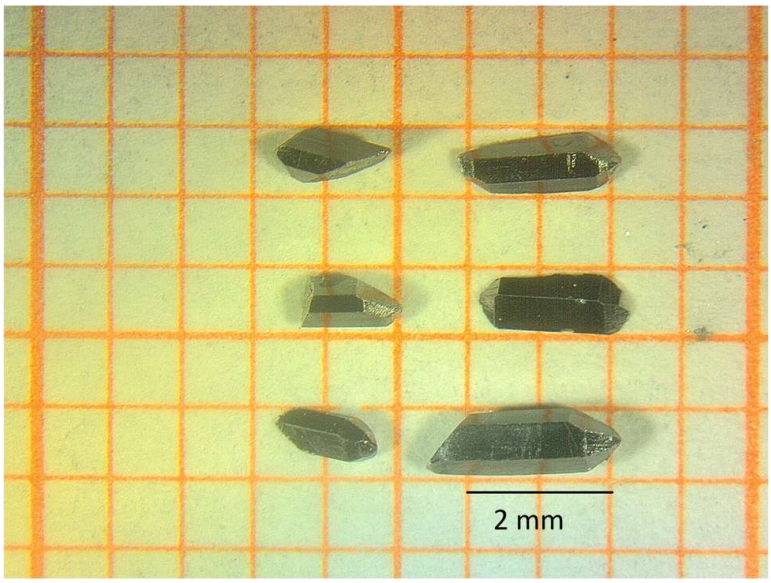

Figure 3.2.: Grown crystals of $CrAs_{0.75}P_{0.25}$ with the typical size.

Compared to pure CrAs - where crystals may reach up to $5 \times 0.5 \times 0.7$ mm [52] - the crystals grown here are significantly smaller. This reduction in size correlates with increasing phosphorus concentration [54], suggesting that the phosphorus substitution modifies the growth dynamics, potentially by altering the solubility of the constituents in the Sn flux and, consequently, the supersaturation conditions during growth [56]. A higher nucleation density naturally leads to a larger number of small crystals. In addition, the reaction scheme used in Eq. 3.3 may not fully account for the diffusion processes required for the efficient crystal growth in the presence of phosphorus, making the system more sensitive to parameters such as the cooling rate and dwelling time.

The batch with $x_{nom} = 20\%$ yielded only a few single crystals with sub-milligram masses and inadequate dimensions for physical property measurements (see Sec. A and B). This limited yield and small crystal size may be due to unfavorable temperature profile, in the reaction equation, or insufficient supersaturation during the crystallization process, both of which are critical parameters in flux growth methods [56]. Given these limitations, the present study is going to focus on the $CrAs_{1-x}P_x$ batch with $x_{nom} = 25\%$ as it yielded larger and higher quality crystals. Optimizing these growth conditions, particularly the cooling profile and flux composition, will likely be necessary to counteract the size reduction and improve both the dimensions and the quality of phosphorus doped crystals.

3.1.3. Twin domain structure

The pseudohexagonal habit observed in these crystals originates from the high temperature hexagonal NiAs-type phase (see Sec. 2.1), which possesses threefold rotational symmetry. When the structure transforms into the orthorhombic MnP-type, this symmetry is lost, giving rise to three equivalent orthorhombic twin domains related by 120° rotations about the *a*-axis as shown in Fig. 3.3 [16].

Fig. 3.4 (a) and (b) shows the attempt of twin domain detection in $CrAs_{1-x}P_x$ single crystals with the use of optically polarized light. The color contrast clearly shows the presence of twin domains with sharp boundaries, all aligned along the *a* axis. Twinning is detectable in all the synthesized $CrAs_{1-x}P_x$ single crystals, with the distribution and arrangement of the twin domains varying on different facets of the same single crystal [54].

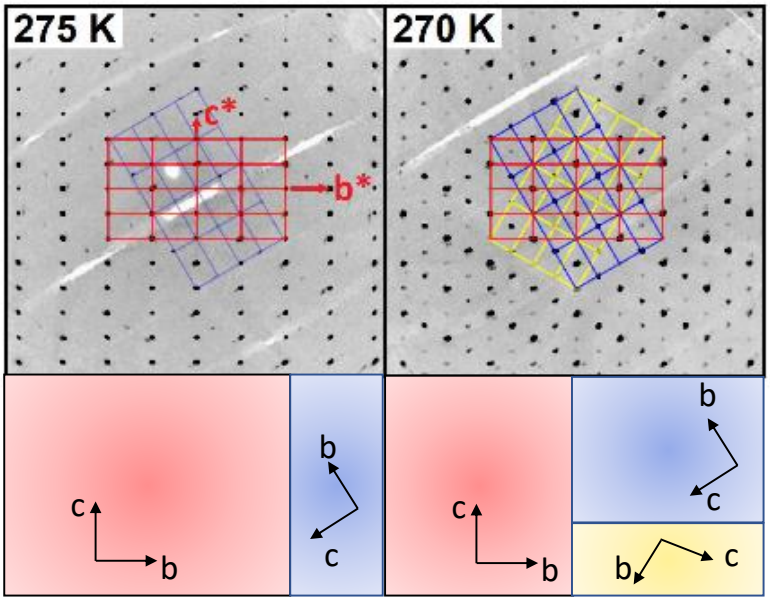

Figure 3.3.: Reconstructed reciprocal space of CrAs at 275 K (left) and 270 K (right), showing the three principal twin orientations used for indexing. Below: schematic real space representation of the corresponding twin domain configuration at the two temperatures. The relative domain fractions illustrate the evolution of twin populations across the magnetic transition, as discussed in the main text. Top panels adapted from [18].

Previous studies on CrAs [18, 58] have reported an inhomogeneous distribution of orthorhombic twin domains, typically with one dominant orientation. However, upon cooling through the magnetic transition at T_N, the domain populations change significantly populations. The same behavior is observed in $CrAs_{1-x}P_x$ single crystals. Fig. 3.4 (c) and (d) shows the same facet of a $CrAs_{1-x}P_x$ single crystal, under a polarization microscope, before and after being cooled with liquid nitrogen. The effect of cooling, and therefore the crossing of T_N, is evidenced by the formation of surface cracks, due to the abrupt expansion of the unit cell, and a change in the domain distribution. In particular, one of the previously dominant domain weakens, while new sharp boundaries are formed. The transition induced domain rearrangement is inhomogeneous across the crystal, as it varies from facets to facets, on the same single crystal [54].

Both Eich et al. and Grzechnik et al. have shown that this rearrangement of the twin domain population in CrAs originates from the evolution of the lattice parameters at the magnetic transition. As the system crosses T_N, the axial ratio c/b - which characterizes the distortion of the orthorhombic MnP-type phase relative to the hexagonal or ortho-hexagonal configuration, where $c/b = \sqrt{3}$ - evolves from values larger than $\sqrt{3}$ to value smaller than $\sqrt{3}$ [18, 58]. This crossing of the hexagonal value suggests that the structure briefly approaches the ortho-hexagonal *Cmcm* arrangement. In this framework, the loss of pseudo-threefold rotational symmetry acts as the twinning element, explaining why the domain configuration changes abruptly at T_N [18, 58].
Grzechnik et al. further identified this transition in CrAs as the first example of an anti-isostructural phase transition. In this case, the material transforms between two structures with identical orthorhombic symmetry (*Pnma*) but with opposite distortions relative to the parent hexagonal lattice [58]. This is reflected both in the axial ratios - $c/b < \sqrt{3}$ in the antiferromagnetic phase and $c/b > \sqrt{3}$ in the high temperature phase - and in the atomic position, which lie closer to the hexagonal values in the antiferromagnetic phase [58]. Moreover, this rearrangement is independent on applied pressure in CrAs, while it seems to depend on the temperature rate on the cooling rate during the transition [18, 58].

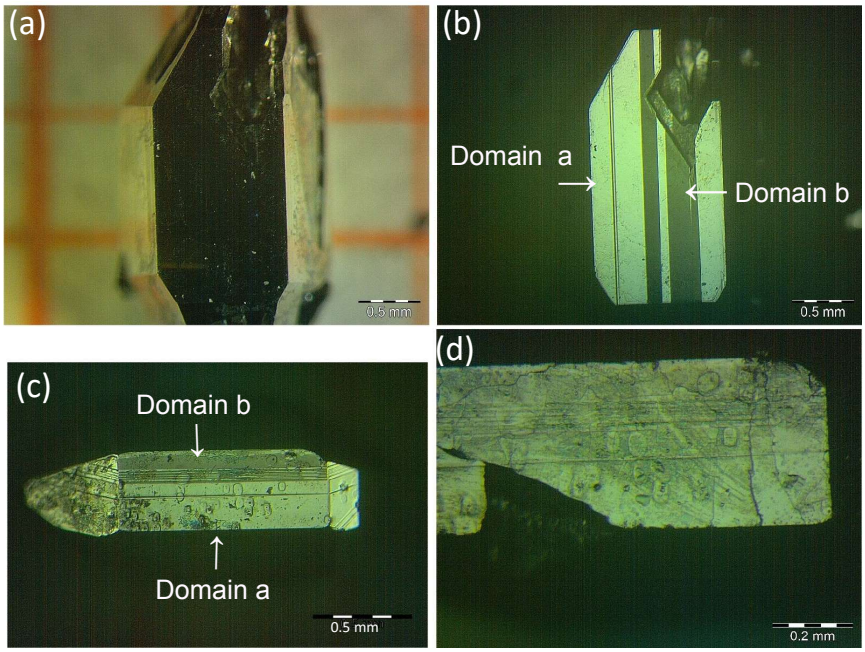

Figure 3.4.: (a-b) $CrAs_{0.97}P_{0.03}$ single crystals with unpolarized light and polarized light, respectively. (c-d) $CrAs_{0.95}P_{0.05}$ single crystals under polarized light at room temperature and below T_N, respectively. Figure adapted from [54].

P-doping (%)	T_t(K)
0	1173 ± 20
5%	1230 ± 50
10%	1270 ± 50
20%	1350 ± 50

Table 3.6.: MnP-to-NiAs structural transition temperatures in $CrAs_{1-x}P_x$, based on X-ray diffraction data from [36].

The same structural mechanism likely drives the domain reconfiguration observed in our $CrAs_{1-x}P_x$ single crystals. Since the formation and rearrangement of twin domains are associated with how the system approaches the MnP-NiAs structural boundary (see Sec. 2.1), the thermal history during crystal growth becomes a key factor in determining the final domain structure. In CrAs, the MnP to NiAs structural transition occurs at approximately $T_t = 1173$ K [16, 8]. Previous studies have shown that the chemical composition in CrPn compounds (where Pn denotes a pnictogen element) affects the structural transition temperature T_t. Venkatraman et al. reported that substituting As atoms with antimony (Sb) atoms or selenium (Se) atoms lowers T_t [57]. In contrast, Selte et al. reported that replacing As atoms with P atoms increases T_t [36, 59], with values reported in Tab. 3.6.

The temperature profiles used in our growth protocol - for both the polycrystalline and single crystal steps - remain well below the transition temperatures reported in literature (Tab. 3.6) and below the temperatures employed in previous flux growths studies (Tab. 3.7).

Method	Detail	Comment
Sn flux 1 (Kotegawa et al.)	CrAs:Sn = 1 : 10 1050 °C (2h) $\xrightarrow{-5°C/h}$ 600 °C	Multi-domain crystals tend to be formed
Sn flux 2 (Kotegawa et al.)	CrAs:Sn = 1 : 20 880 °C (2h) $\xrightarrow{-1°C/h}$ 500 °C	Mono-domain crystals tend to be formed
This study	800°C (168h) $\xrightarrow{-100°C/h}$ RT 800°C (48h) $\xrightarrow{-200°C/h}$ RT	Polycrystalline 1st Sintering (3.1) Polycrystalline 2nd Sintering (3.2)
This study	CrAs/$CrAs_{1-x}P_x$:Sn = 1 : 15 850°C (10h) $\xrightarrow{-0.5°C/h}$ 600°C	Multi-domain crystals

Table 3.7.: Comparison of single crystal growth protocols of CrAs and $CrAs_{1-x}P_x$, as reported in this study and by Kotegawa et al. Tab. adapted from [30].

Although the values reported by Selte et al. exhibit significant uncertainties and may not fully capture the effect of phosphorus substitution on T_t[3], this alone does not account for the absence of monodomain crystals in our samples, since our synthesis temperatures are already considerably lower than those employed by Kotegawa et al. (Tab. 3.7). In their study, the authors demonstrated that the formation of monodomain or multidomain CrAs single crystals depends strongly on whether the growth temperature crosses T_t. Crystals grown above T_t exhibit multiple domains, while those grown below it are monodomain. A difference which lead to different properties of CrAs single crystals, including the onset of superconductivity [30]. The fact that none of our crystals are monodomain, despite being synthetized at lower temperatures, suggest that additional factors - such as the amount of Sn, the cooling rate or the dwelling time - play an important role in determining the final domain structure of CrAs and $CrAs_{1-x}P_x$ single crystals.

3.2. X-ray diffraction and elemental analysis

For the systematic characterization of the synthesized $CrAs_{1-x}P_x$ single crystals, powder X-ray diffraction (PXRD) and energy-dispersive X-ray spectroscopy (EDX) were employed. PXRD was used to determine and refine the crystal structures, providing quantitative information on lattice parameters and their evolution as a function of Phosphorus doping. EDX offered accurate elemental analysis, confirming the chemical composition and homogeneity of the samples. All measurements were conducted in collaboration with Dr. Amir-Abbas Haghighirad and Dr. Michael Merz.

Powder X-ray Diffraction (PXRD) is a widely used technique for characterizing crystalline materials. By analyzing the diffraction pattern arising from the constructive interference of X-rays scattered by sets of parallel atomic planes (hkl) within the crystal lattice, PXRD provides valuable insights into the crystal structure, phase composition, and lattice parameters of a sample.

[3]Wu et al. report a T_t of 800 K for CrAs; however, they do not provide supporting evidence for this value, and it appears inconsistent with the more recent findings in [16].

The condition for this constructive interference is described by the Bragg equation:

$$n\lambda = 2d_{hkl} \sin \theta_{hkl} \tag{3.4}$$

where $2d_{hkl} \sin \theta_{hkl}$[4] represents the total path difference between the mirror reflected wavefront, as shown in Fig. 3.5 , n is the diffraction order and λ is the X-ray wavelength [60].

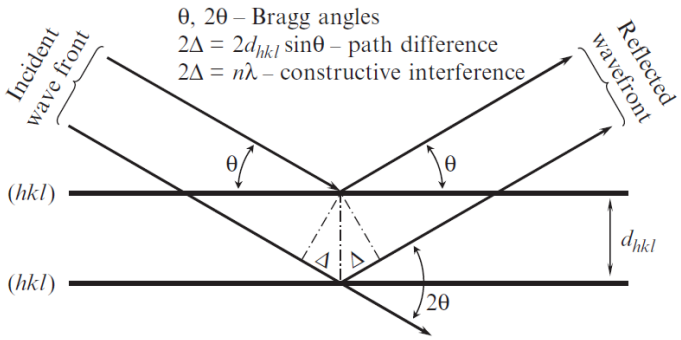

Figure 3.5.: Depiction of Bragg's law from [60].

A diffraction pattern model is often used for determining the crystal structure, typically by adjusting the model of an already known structure, similar to the material under investigation, to fit the observed the diffraction data. In this study, the refinement was performed using the Rietveld method, implemented with the GSAS-II software [61]. The Rietveld refinement is a least square method used to adjust the expected model of a crystal structure to observed data by tuning lattice parameters $(a, b, c, \alpha, \beta, \gamma)$, peak profiles parameters[5], atomic positions (x, y, z) and temperature factors. A more detailed explanation on the Rietveld refinement can be found in [60].

3.2.1. Powder X-ray diffraction on Phosphorus-doped samples

For the Cr-As system, a full structure solution investigation is not necessary as the crystal structure has been studied extensively and all the information have been inserted into crystallographic databases. For the purpose of this work, we are going to employ data entries for $CrAs_{1-x}P_x$ from the ICSD database.[6] [62]. The PXRD experiments were conducted on a STOE Stadi P machine, with the X-rays generated using a Molybdenum tube emitting the Kα_1 line at a wavelength of 0.70926 Å. The experimental setup employed the transmission geometry (pseudo-Guinier configuration) using the monochromatic Mo Kα_1 radiation. $CrAs_{1-x}P_x$ single crystals were ground to powder in a mortar to achieve a grain size around 10 μm. The resulting powder is then placed onto a mylar foil greased with a thin layer of Rotisilon silicone grease, with a mylar second foil placed on top to seal the sample. This assembly is then positioned in the sample holder.

[4] d is the interplanar spacing, and θ is the diffraction angle.

[5] Voigt or psuedoVoigt function are commonly used for Rietveld refinement [60].

[6] The CIF file used for the Rietveld refinement are ICSD-195015 for CrAs from [19] and ICSD-603360 for $CrAs_{1-x}P_x$ from [38]

The sample holder rotates at half the angular velocity of the detector to maintain proper alignment and to enhance statistical accuracy, the sample was continuously rotated during measurements. Diffraction patterns were recorded over a 2θ range from 5° to 55° with steps of 0.015°.

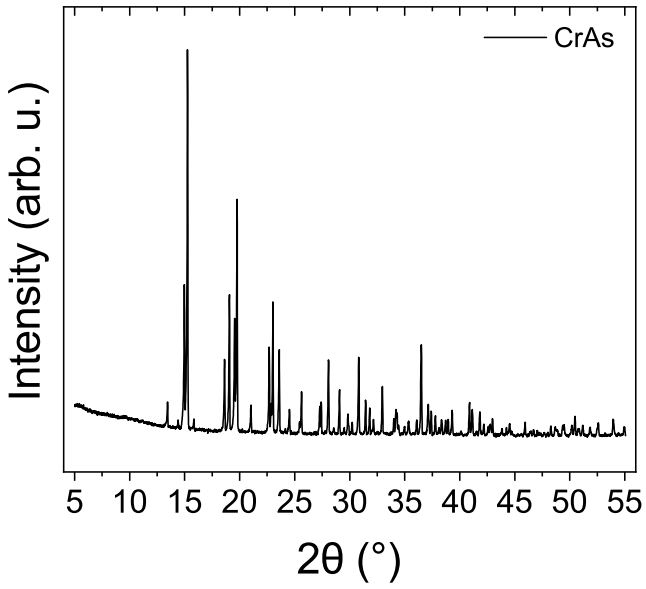

Figure 3.6.: PXRD diffractogram of a crushed CrAs single crystal

Fig. 3.6 shows a PXRD diffractogram of a typical crystalline sample, displaying characteristic peaks corresponding to specific crystallographic planes. Before performing the Rietveld refinement for structure determination, the background of the diffraction pattern is fitted using polynomial functions. The reflection profiles are modeled using pseudo-Voigt functions, which are linear combinations of Gaussian and Lorentzian functions. During the refinement process for doped $CrAs_{1-x}P_x$crushed single crystals, constraints are applied to equate the atomic positions of arsenic and phosphorus, as phosphorus substitutes arsenic sites. Differing positions would yield unphysical results, as the refinement would otherwise adjust parameters to minimize discrepancies between observed data and the calculated model.

Fig. 3.7 and 3.8 show the PXRD data for $CrAs_{1-x}P_x$ crushed single crystals with $x_{nom} = 0\%, 25\%$, respectively. For the undoped CrAs (Fig. 3.7) all 163 expected reflections from the model were succesfully indexed, with low residual values obtained from the Rietveld refinement, indicating a high quality grown crystals. The PXRD diffractograms of the doped single crystals (Fig. 3.8 and figures in Appendix B) exhibit a few unindexed reflections (5 out of 168) despite also showing low R-factors in the Rietveld refinement. Given that the undoped samples, prepared under identical conditions, did not exhibit such anomalies, we can rule out sample preparation mistakes. These additional reflections may originate from either secondary phases introduced through impurities or a crystallographic structure not accounted in the current structural model. Notably, the available diffraction data for $CrAs_{1-x}P_x$in crystallographic databases are based on polycrystalline PXRD from the work of [39, 36, 38]. This may not reflect the quality of the single crystal synthetized in this study, accounting for the discrepancies observed in our PXRD diffractograms.

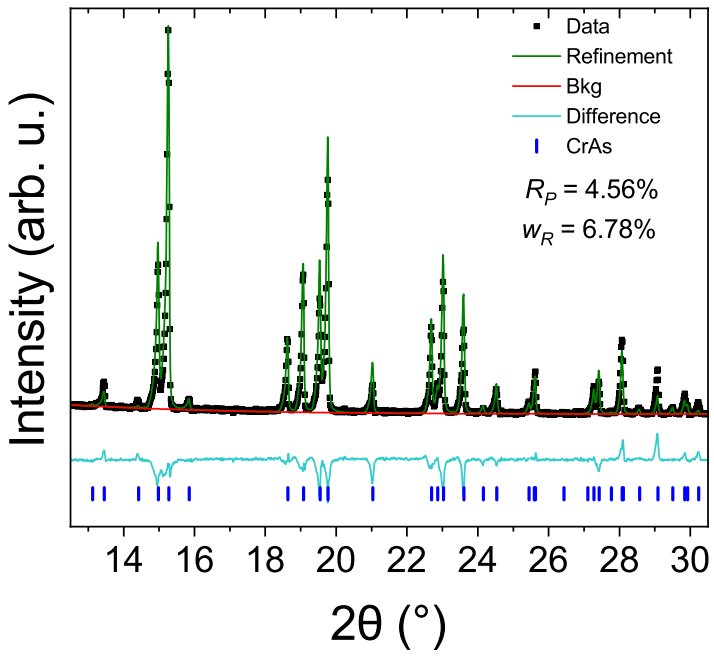

Figure 3.7.: Selected region of PXRD refinement for crushed CrAs single crystals at ambient conditions. Measured diffraction patterns (dots) are shown alongside the calculated profiles (solid lines). The difference curve (shown as gray lines) highlights the discrepancies between the observed and calculated intensities. Tick marks indicate the positions of expected Bragg reflections.

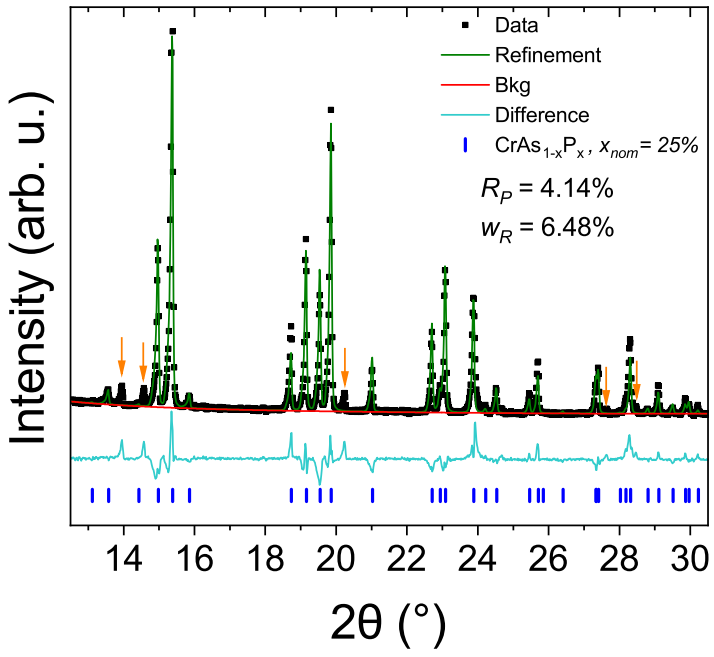

Figure 3.8.: Selected region of PXRD refinement for crushed $CrAs_{1-x}P_x$ single crystals with x_{nom} = 25% at ambient conditions. Measured diffraction patterns (dots) are shown alongside the calculated profiles (solid lines). The difference curve (shown as gray lines) highlights the discrepancies between the observed and calculated intensities. Tick marks indicate the positions of expected Bragg reflections. Orange arrows indicate the unindexed reflections.

3.2.2. Determination of Phosphorus content from PXRD

Rietveld refinement allows the site occupancy to be treated as a refinable parameter, allowing, in principle, a determination of the actual doping concentration in our samples [60]. Table 3.8 presents partial result of the Rietveld refinement of $CrAs_{1-x}P_x$ crushed single crystals at ambient conditions[7]. The refined phosphorus concentrations x_{ref} show a clear discrepancy with the established correlation between phosphorus content and b lattice parameter reported in the literature [36, 39]. Similarly to applied pressure, phosphorus substitution decreases the unit cell volume, predominantly affecting the b lattice parameter highlighting its critical role in CrAs phase diagram as its correlates with the weakening of the magnetic phase [7, 36, 39]. Therefore, it is highly unlikely for a single crystal with a lower refined phosphorus concentration to exhibit a smaller b lattice parameter compared to a sample with higher refined phosphorus content. Moreover, samples with $x_{nom} = 3\%$ and 10% display a x_{ref} higher than the nominal values. These inconsistencies indicate that x_{ref} can't be considered a reliable parameter. The refined occupancy is particularly sensitive to the quality of the peak profile fitting - as other structural parameters [60] - and as shown in Fig. 3.7 and 3.8, the peak shapes are not always well reproduced. This imperfect profile matching affects directly the accuracy of the refined site occupancies and therefore of the extracted doping concentrations, providing a natural explanation for the observed inconsistencies.

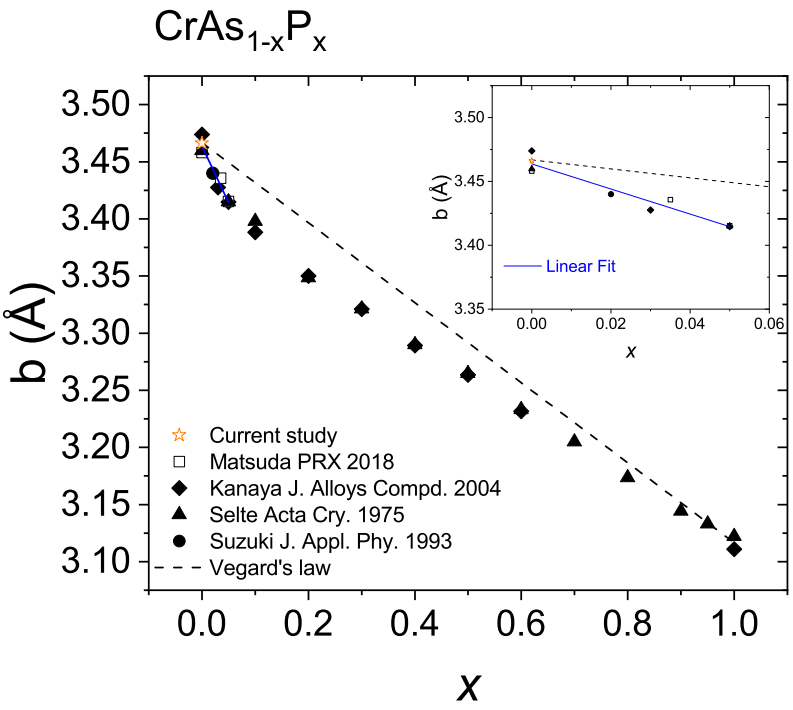

Figure 3.9.: Doping dependence of the b lattice parameter for $CrAs_{1-x}P_x$from [7, 39, 36, 38]. Open symbols and filled symbols are for single crystals and polycrystalline samples, respectively. The dashed line represents the expected trend following Vegard's law. In the inset, focused view of the doping dependence of the b lattice parameter in the range $0 \leq x \leq 0.05$. The blue line represent the best linear fit between all the data, in the range $0 \leq x \leq 0.05$.

[7]The complete table of results, along with the corresponding batch identification numbers, can be found in Sec B.

x_{nom}	0%	3%	5%	10%	13%	20%	25%
x_{ref}	0%	5.6%	4.4%	15.4%	3.2%	4.6%	4.1%
x_{eff}	0%	0.7% ± 0.1	0.9% ± 0.1	2.7% ± 0.2	1.9% ± 0.2	1.8% ± 0.2	3.8% ± 0.3
b(Å)	3.46624(10)	3.45651(10)	3.45464(10)	3.43696(5)	3.44472(10)	3.446052(25)	3.42595(10)

Table 3.8.: Nominal composition x_{nom}, refined phosphorus concentration x_{ref}, effective concentration x_{eff} obtained from the literature $b(x)$ correlation and b lattice parameters for $CrAs_{1-x}P_x$ crushed single crystals at ambient conditions.

Given the relative robustness of lattice parameter refinement compared to site occupancies - which are more strongly affected by the quality of the peak profile fit - and the well-documented behavior of the b lattice parameter in the Cr-As system under both applied and chemical pressure [13, 16, 7], we can extract the doping concentration from the trend of b lattice parameter obtained through Rietveld refinement[8]. Fig. 3.9 aggregates all available literature data for $CrAs_{1-x}P_x$, both polycrystalline and single crystals. Notably, data from Kanaya et al. and Selte et al. exhibit deviations from Vegard's law [9] resulting in two linear regimes: one for $0 \leq x \leq 0.05$ and another for $0.1 \leq x \leq 1$. By examining the b lattice parameters in table 3.8, we can limit ourselves to the linear region of $0 \leq x \leq 0.05$ as highlighted in the inset in Fig. 3.9. Data from [7, 36, 39] were fitted alongside the data from this study for the CrAs parent compound. The optimal linear fit, depicted by the blue line, serves as an estimated *b(x)* lattice parameter trend as a function of doping. The uncertainties associated were calculated through error propagation methods applied to this linear fit. The results are written in table 3.8.

To validate the phosphorus concentration inferred from PXRD, Energy-dispersive X-ray (EDX) spectroscopy measurements were carried out on representative single crystals from selected batches. All examined batches show a difference between surface and bulk phosphorus concentrations. Among them, the $x_{nom} = 10\%$ and $x_{nom} = 25\%$ batches exhibit the most pronounced surface-bulk differences and will therefore be the only ones discussed in detail in the next section. The effects of phosphorus doping on the crystal structure are discussed in more detail in a later section. The remaining batches follow similar trends and will be summarized later in the chapter.

3.2.3. Determination of Phosphorus content from EDX

EDX is an experimental technique frequently used for the elemental analysis and chemical characterization. In this method, a sample is irradiated with a beam of accelerated electrons. Inelastic scattering occurs due to the interaction between the incoming electrons and the bound electrons, leading to ionization of the atoms. To return to their ground state, the atoms emit characteristic x-rays, with the energy of each photon corresponding to the difference in energy between the two orbitals involved in the transition, making it unique to the specific element [66].
For the EDX analysis the $CrAs_{1-x}P_x$samples were characterized via EDX spectroscopy using a COXEN EM-30plus electron microscope equipped with an Oxford Silicon-Drift-Detector (SDD) and a AZtec-LiveLite-software package. To compare the surface and interior composition, the single crystals were sectioned using a wire saw, enabling EDX analysis both on the facet surface and on a cross-sectional area of the same crystal. The corresponding measurements for the $x_{nom} = 10\%$ sample are shown in Appendix A.

[8] A similar approach, for different materials can be also found in [63, 64]

[9] Vegard's law is an empirical relationship stating that the lattice parameter of a solid solution is a weighted mean of its constituents' lattice parameters at the same temperature [65]

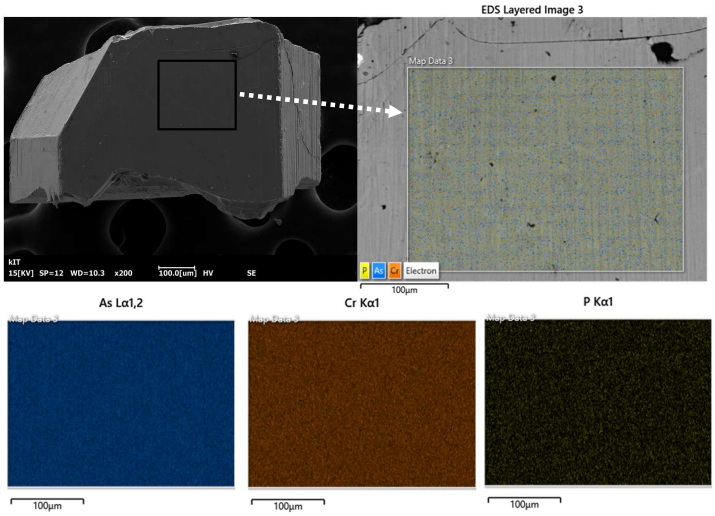

Figure 3.10.: Electron microscope image of the $x_{nom} = 25\%$ $CrAs_{1-x}P_x$ single crystal facet aligned along the a-axis. The highlighted region marks the area analyzed for elemental composition via EDX, shown with corresponding relative elemental maps.

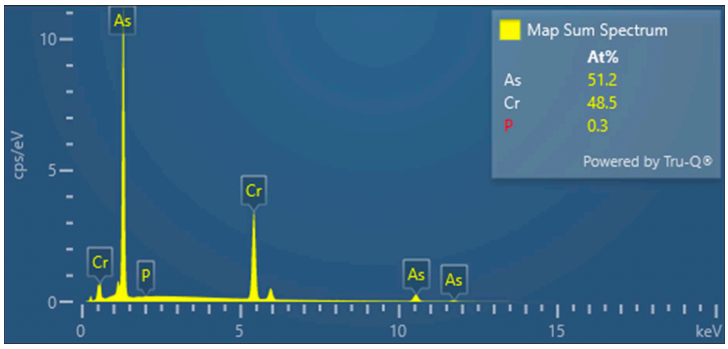

Figure 3.11.: EDX spectrum of the $x_{nom} = 25\%$ $CrAs_{1-x}P_x$ single crystal facet. In the inset, the atomic percentage of the detected elements are shown.

Fig 3.10 shows the electron microscope image of a facet of the $x_{nom} = 25\%$ $CrAs_{1-x}P_x$ single crystal. The area examined in the mapping mode of the AZtec software reveals a homogeneous distribution of all the elements involved in the crystal growth. This is evidenced by the uniform color contrast observed in the elemental maps, each corresponding to the spatial distribution of a specific element. The atomic percentages extracted from the EDX spectrum, reported in Fig. 3.11, give approximately 51% for As atoms, 48% for Cr atoms and 0.3% for P atoms at the facet surface. The phosphorus concentration at the surface was estimated from the relative P and As contents according to $x = \frac{[P]}{[P]+[As]}$ giving a value of approximately 0.6% for the analyzed facet.

The Cr:As stoichiometry deviates slightly from the ideal 1:1 ratio. However, this deviation can reasonably be attributed to the experimental uncertainty of the EDX measurement. By contrast, the phosphorus concentration measured at the crystal surface is notably lower than the value inferred from the doping dependence of the b lattice parameter behavior discussed previously. This surface to bulk discrepancy may be due to growth conditions or acid etching during sample preparation. To further investigate this discrepancy, EDX measurements were also performed on a cross-section of the same $CrAs_{1-x}P_x$ single crystal, as shown in Fig. 3.12. In this case, the Cr:As ratio still shows a slight deviation from the ideal 1:1 but unlike the facet, there is an excess of chromium atoms (51%) rather than arsenic ones (45%).

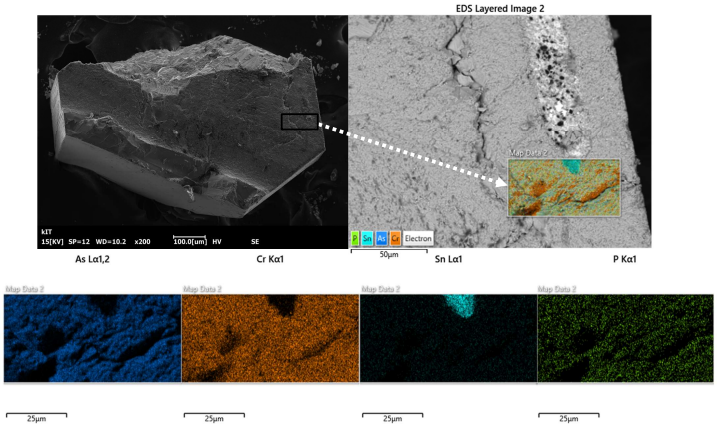

Figure 3.12.: Cross-sectional electron microscope image of $CrAs_{1-x}P_x$ single crystal, with the a-axis oriented out of plane. The highlighted region indicates the area analyzed for elemental composition using EDX, accompanied by relative elemental maps.

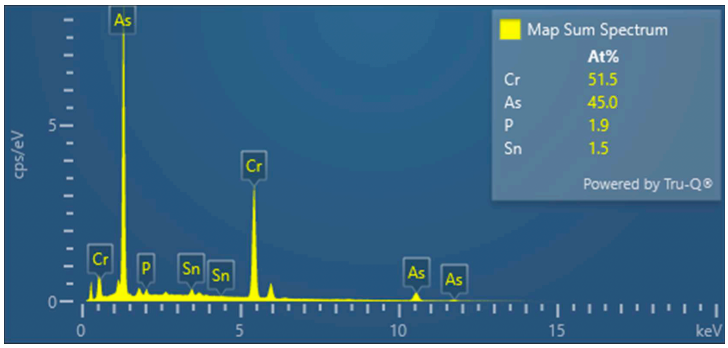

Figure 3.13.: EDX spectrum of the cross-sectional of $CrAs_{1-x}P_x$ single crystal facet. In the inset, the atomic percentage of the detected elements are shown.

The dark regions observed in the elemental map correspond to cracks or holes present on the cross-section. These regions also show the presence of tin, confirming the occurrence of flux penetration during crystal growth. In the tin-containing areas, signals from both Cr and As are absent, while phosphorus remains detectable, suggesting a possible interaction between tin and phosphorus. Such an additional phase could potentially account for the additional reflections observed in Sec. 3.2.1. However, the absence of similar reflections in pure CrAs remains an open question.
Fig 3.13 shows the atomic percentage extracted from EDX spectrum of the crystal cross-section, revealing a higher phosphorus concentration in the bulk and yielding an estimated value of approximately 4% when calculated from the relative P and As contents. For clarity, phosphorus concentrations estimated from EDX measurements at the crystal surface will be denoted as x_{sur} in the following. Interestingly, two batches exhibit the opposite concentration gradient, with a higher phosphorus content at the surface than in the crystal interior. For the $x_{nom} = 10\%$ batch, shown in Fig. A.2 and Fig. A.3, the surface concentration reaches $x_{sur} \approx 4.5\%$, while the concentration inferred from the cross-sectional EDX analysis is approximately 2.5%. A similar surface-enriched profile is also observed in the $x_{nom} = 13\%$ batch (not shown here), where the surface concentration reaches $x_{sur} \approx 3.2\%$. For the $x_{nom} = 20\%$ batch, due to the poor quality and limited amount of material, a surface EDX measurement was not performed and the corresponding x_{sur} value is therefore not reported.

The EDX measurements therefore indicate that the phosphorus distribution in $CrAs_{1-x}P_x$ single crystals is not uniform and can vary between the as-grown crystal surface and the crystal interior. While surface-sensitive EDX measurements reveal pronounced concentration gradients, the phosphorus content measured on crystal cross-sections is, for the sample investigated here, consistent with the effective concentration x_{eff} inferred independently from the doping dependence of the b lattice parameter. This consistency supports the use of x_{eff} as a practical descriptor of the phosphorus content of the crystals. Accordingly, unless otherwise specified, the phosphorus concentration of the $CrAs_{1-x}P_x$ single crystals will be reported using the effective value x_{eff} throughout this thesis. For clarity, in figures and plots this quantity will be denoted simply as x.

3.3. Effects of Phosphorus doping

With the effective phosphorus concentrations established through the combined PXRD and EDX analysis of Sec. 3.2.3, the physical consequences of chemical substitution can be examined. Replacing arsenic with phosphorus influences both the magnetic phase and crystal structure of CrAs in a comparable way to the effects of applied physical pressure. The comparison between these two tuning paths - chemical substitution and external pressure - is presented in the following subsections, together with the evolution of magnetic susceptibility and structural parameters as a function of doping.

3.3.1. Effects of Phosphorus doping on magnetic susceptibility

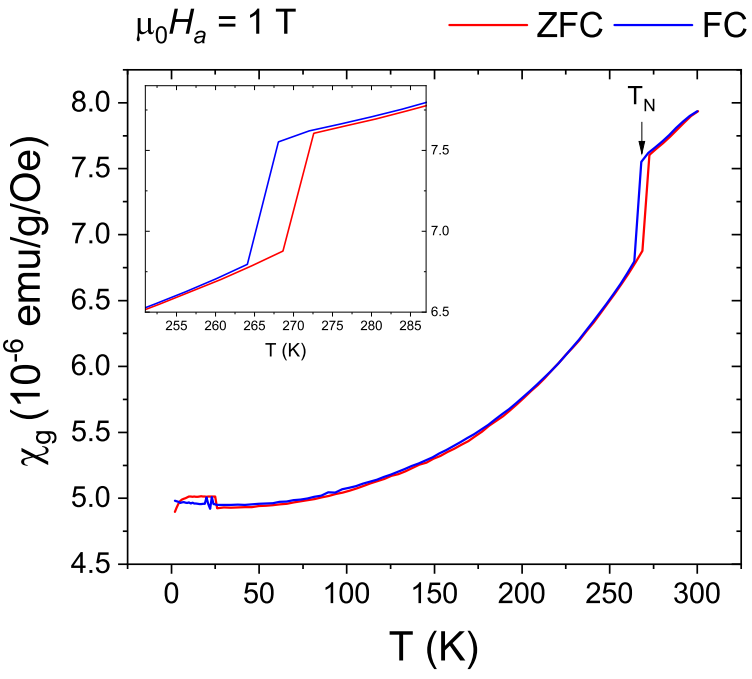

Figure 3.14.: Zero-field-cooled (ZFC) and field-cooled (FC) static mass magnetic susceptibility of CrAs single crystal, with magnetic field parallel to the a-axis. The black arrow indicates the Néel temperature (T_N), corresponding to the transition from the paramagnetic phase to the double helical antiferromagnetic phase. The low temperature anomaly is due to sample off-centering. In the inset, the region 250-290 K, highlighting and the hysteresis of the first-order phase transition.

Magnetic mass susceptibility measurements of $CrAs_{1-x}P_x$ single crystals were performed with the help of Dr. Kristin Willa and Dr. Mehdi Frachet. The samples were glued to a polyether ether ketone substrate and mounted into a Quantum Design Physical Properties Measurement System (PPMS). The measurements were carried out using a standard vibrating sample magnetometer (VSM) with a static (DC) magnetic field of 1 T applied along the crystallographic *a*-axis. In VSM, a vertically oscillating sample within a set of pickup coils enables the detection of its magnetization via the voltage induced in the coils, following the principle of electromagnetic induction [67].

Fig. 3.14 shows a typical static VSM mass magnetic suscepitbility measurement of CrAs single crystal. At $T_N \approx 270$ K, CrAs undergoes a a first-order phase transition from a paramagnetic state to a double helical antiferromagnetic state. This transition is characterized by a sharp drop in the magnetic susceptibility, a behavior consistently observed in single crystals [7, 53]. A feature not observed in the polycrystalline samples studied prior to the first synthesis of single crystals [36, 39, 11].
Wu et al. linked the sharp drop to the strong coupling between the magnetic and structural degrees of freedom. In particular, they associated the magnetic anisotropy observed at T_N - whether χ increases or decreases, depending whether the applied magnetic field is perpendicular or parallel to the needle axis - with changes in the spin exchange constant along the unit cell axis, due to the abrupt expansion or contraction of the lattice parameters at T_N[53]. Notably, the conclusions from Wu et al. should be considered carefully, as their axis notation appears to be inconsistent with literature. This inconsistency is particularly significant because, due to the twinning present in the crystal structure (as discussed in Sec. 3.3.3), distinguishing between *b* and *c* crystallographic axis is not possible for the purpose of the magnetometry experiment [16] .

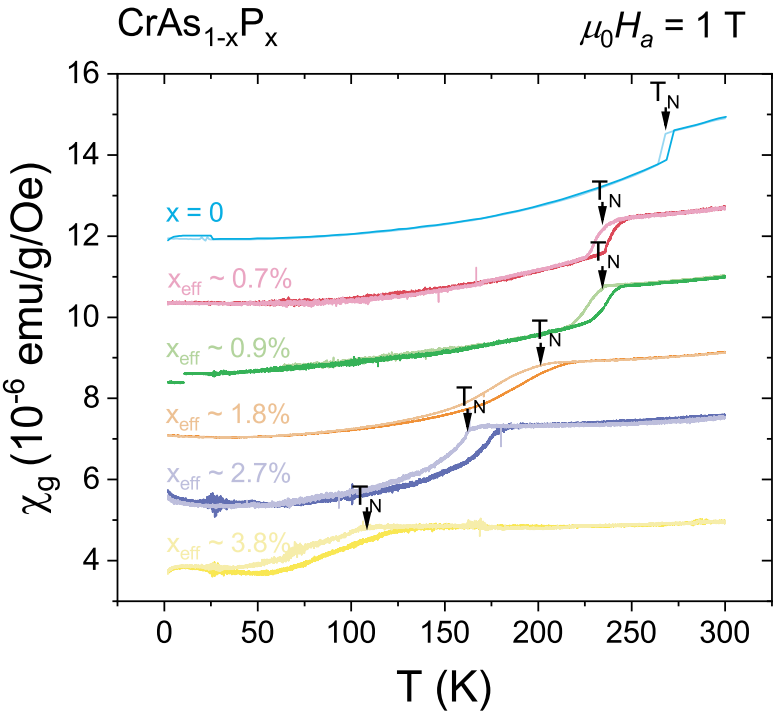

Figure 3.15.: Comparison of static magnetic mass susceptibility of $CrAs_{1-x}P_x$ single crystals for different nominal phosphorus concentration. Measurements were performed under a static applied magnetic field of 1 T, aligned along the crystallographic *a*-axis in both zero-field-cooled (ZFC) and field-cooled (FC) regimes. Data curves with $x_{\text{eff}} \approx 0\%, 0.7\%, 0.9\%, 1.9\%, 2.7\%$ are reproduced from [54]. The black arrows show the onset of the first-order magnetic transition. Curves have been shifted for comparison.

Fig. 3.15 displays the static magnetic susceptibility on the whole $CrAs_{1-x}P_x$ series[10]. T_N was determined as the onset of the decrease in magnetic susceptibility, using the same methodology employed by Matsuda et al. to facilitate direct comparison with their data on CrAs under pressure [11] [7]. The extracted T_N values are listed in Tab. 3.9. The observed decrease in T_N with increasing nominal phosphorus doping is consistent with the findings of Matsuda et al., suggesting that phosphorus substitution exerts a chemical pressure, suppressing the magnetic phase similarly to the application of physical pressure on the parent compound. The data also show an enhancement in hysteresis with higher doping levels, therefore confirming the persistence of a first-order nature of the phase transition. Similar to observations in the parent compound under pressure, the $\chi_g(T)$ curves transition from exhibiting a sudden jump at T_N to a continuous cusp-like behavior that broadens with increasing doping. Matsuda et al. have proposed that this evolution reflects a quasi-second-order magnetic transition approaching $T = 0$ at a critical pressure (P_c) or critical doping level (x_c), indicating the presence of quantum criticality in the system [7].

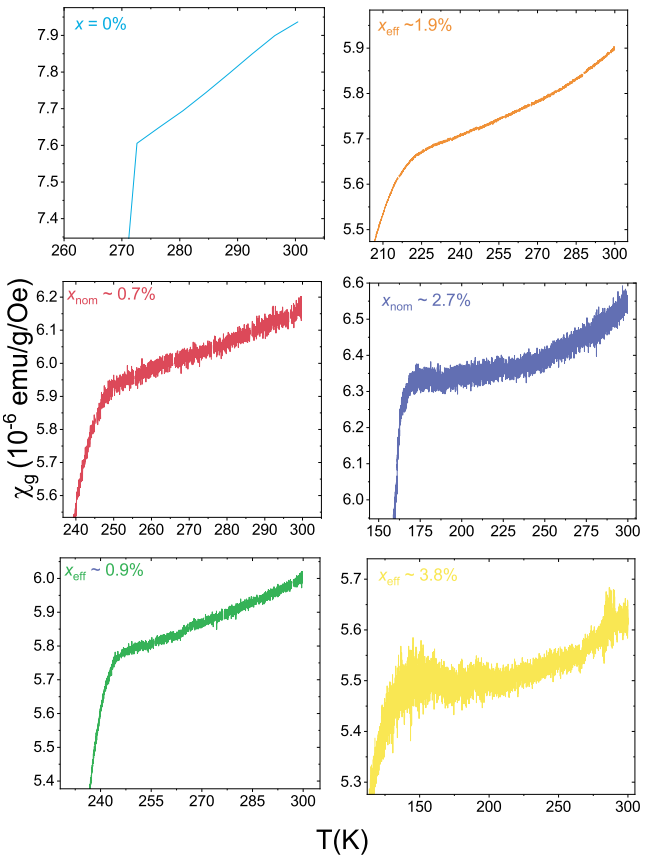

Figure 3.16.: Temperature dependence of the ZFC static magnetic susceptibility of $CrAs_{1-x}P_x$ single crystals for different phosphorus concentration, measured above their respective T_N. Increased noise at higher phosphorus content is due to the lower mass of the single crystals, as discussed in Sec. 3.1.3.

[10] The $x_{eff} \approx 1.8\%$ batch is not shown, as the available material was unsuitable for a reliable susceptibility measurement (see Sec. A)

[11] Selte et al. measured the magnetic susceptibility of polycrystalline $CrAs_{1-x}P_x$ but did not observe any anomalies to extract T_N from [36]. Similarly, Kanaya et al. measured polycrystalline $CrAs_{1-x}P_x$ while identifying T_N using PXRD data [39]. Unfortunately, Matsuda et al. did not report magnetization data for their phosphorus-doped samples [7].

$\mathbf{x}_{eff}$(%)	FC T_N(K)	ZFC T_N(K)
0	268 ± 1	273 ± 1
0.7 ± 0.1	240 ± 5	246 ± 5
0.9 ± 0.1	235 ± 5	242 ± 5
1.9 ± 0.2	207 ± 5	215 ± 5
2.7 ± 0.2	165 ± 5	180 ± 5
3.8 ± 0.3	107 ± 5	135 ± 5

Table 3.9.: Field-cooled (FC) and zero-field-cooled (ZFC) Néel temperatures (T_N) as a function of effective doping concentration of $CrAs_{1-x}P_x$single crystals, derived by mass susceptibility measurements discussed in Sec. 3.3.1.

Fig. 3.16 shows the temperature dependence of the ZFC magnetic susceptibility of $CrAs_{1-x}P_x$ single crystals for different phosphorus concentrations. The increase of magnetic susceptibility at higher temperatures suggests deviations from the typical Pauli and Curie-Weiss behavior. A linear temperature dependence in the paramagnetic state is a common feature observed in various unconventional supercondutors - notably, AFe_2As2 (A = Ca, Sr, Ba), and $LaFeAsO_{1-x}F_x$ iron pnictides [68, 69, 70, 71]. This behavior is attributed to the presence of antiferromagnetic spin fluctuations, which are considered responsible for the paring mechanism in these system [72, 73]. In CrAs single crystal, the magnetic suscepitibility's temperature dependence varies by a factor of 1.6, between 2 K and 300 K. For $CrAs_{1-x}P_x$ single crystals, with doping concentrations up to $x_{eff} \approx 3.8\%$, this temperature dependence remains constant across the different x_{eff}, with a factor of 1.3, between 2 K and 300 K. Additionally, at lower temperatures, the magnetic susceptibility does not exhibit any evidence of a Curie contribution attributed to paramagnetic impurity spins. Remarkably, we measure a downturn of the magnetic susceptibility of sample with $x_{eff} \approx 3.8\%$ between 2 K and 25 K.

3.3.2. Comparison of magnetic response under chemical and physical pressure

To systematically compare the effects of applied pressure and chemical pressure on CrAs, it is important to establish a common scale between these two parameters. Matsuda et al. investigated both doped single crystals and the parent compound single crystals, under pressure, showing that the $CrAs_{1-x}P_x$ samples with $x = 0.05$ display no magnetic transition, as equivalent to the CrAs sample under 1.0 GPa [7]. Based on this correlation, it is possible to construct a linear scale between doping and applied pressure. This scaling allows the direct comparison of the magnetic susceptibilities of the doped samples with that of CrAs under pressure.

To further examine the relationship between chemical pressure and physical pressure, we compare the molar susceptibility (χ_{mol}) data from our $CrAs_{1-x}P_x$samples with the results reported by Matsuda et al. for the parent compound, as shown in Fig. 3.17. Notably, the observed T_N to the AFM phase in our doped samples align closely with those reported for CrAs, under pressure, particularly at lower doping levels - for instance, the 0.9% sample, which correspond to an equivalent pressure of approximately 0.18 GPa, based on the linear pressure-doping conversion scale from Matsuda et al.
However, the correspondence becomes less accurate at higher doping levels. For 2.7% and 3.8% $CrAs_{1-x}P_x$ samples, the equivalent pressures derived are approximately 0.54 GPa and 0.76 GPa, respectively, while the transition temperatures match the one from curves of lower pressure.

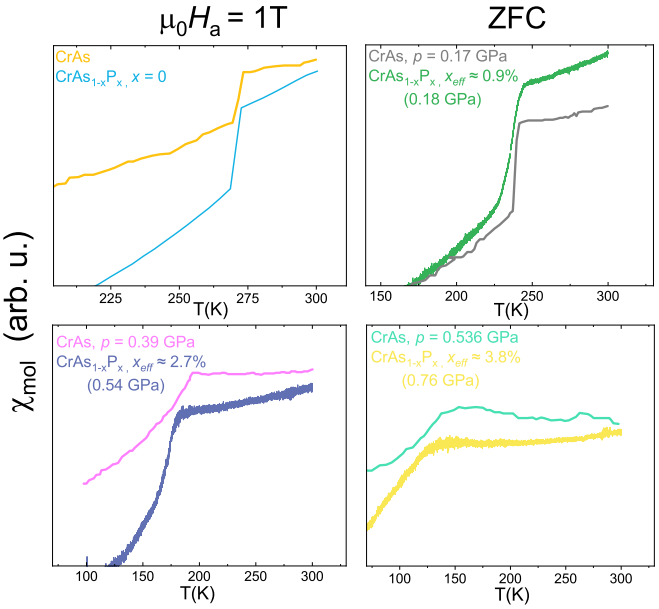

Figure 3.17.: Comparison between χ_{mol} of CrAs single crystals under pressure from [7] and that of $CrAs_{1-x}P_x$single crystals. In parenthesis, the equivalent pressure assigned to the doped samples, obtained from the linear pressure-doping conversion scale discussed in the text. Curves are vertically shifted for clarity.

This suggests the limit of the arbitrary choice made for the linear scale we employed, potentially also revealing the limits of the analogy between the effect of physical pressure and chemical pressure. Nevertheless, for the purpose of this study, we will continue to use the linear scale[12].

Fig. 3.18 shows the comparison between T_N of $CrAs_{1-x}P_x$ single crystals. Data from Matsuda et al. were extracted from the resistivity data, with T_N identified at the onset of the resistivity jump, consistent with the criterion used for extracting T_N from magnetometry data. Within the pressure-doping scale constructed directly from Matsuda's data, the $CrAs_{1-x}P_x$single crystals of this study align well with the T_N of pure CrAs under applied pressure. Notably, a discrepancy is observed between the transition temperatures determined by Matsuda et al. using resistivity and neutron diffraction measurements. In phosphorus doped samples, the resistivity exhibits a jump, instead of the observed decrease in the parent compound [7].
This resistivity jump has been attributed to the formation of cracks on single crystal samples, due the abrupt changes in the unit cell dimensions, at T_N, which are enhanced by the chemical pressure from phosphorus doping. The broadness of the resistivity jump may be interpreted as the observed broadening of the transition in the pure compound, under applied pressure[13]. However, neutron diffraction data for the 3.5% phosphorus-doped sample reveal a sharp structural transition at a significantly lower temperature than those indicated by resistivity measurement for the 3% and 4% samples, even when considering the end point of the resistivity jump as T_N. Therefore, we advice caution when interpreting the results for $CrAs_{1-x}P_x$single crystals from Matsuda et al., as additional evidence from magnetization, neutron diffraction or doping estimation is lacking.

[12]Notably, Matsuda et al. established the equivalence between 1.0 GPa to 5% of phosphorus doping also by extracting the T_N via resistivity measurements. Above 0.7 GPa, the χ_{mol} is dominated by the Curie-Weiss behavior - due to the presence of strong spin fluctuations - making it impossible to extract the transition temperature to the AFM phase [7].

[13]Notably, the jump of Matsuda's 4.5% sample is lower than the one of lower dopings, in contrast with the idea that a greater pressure will lead to bigger unit cell expansion [7].

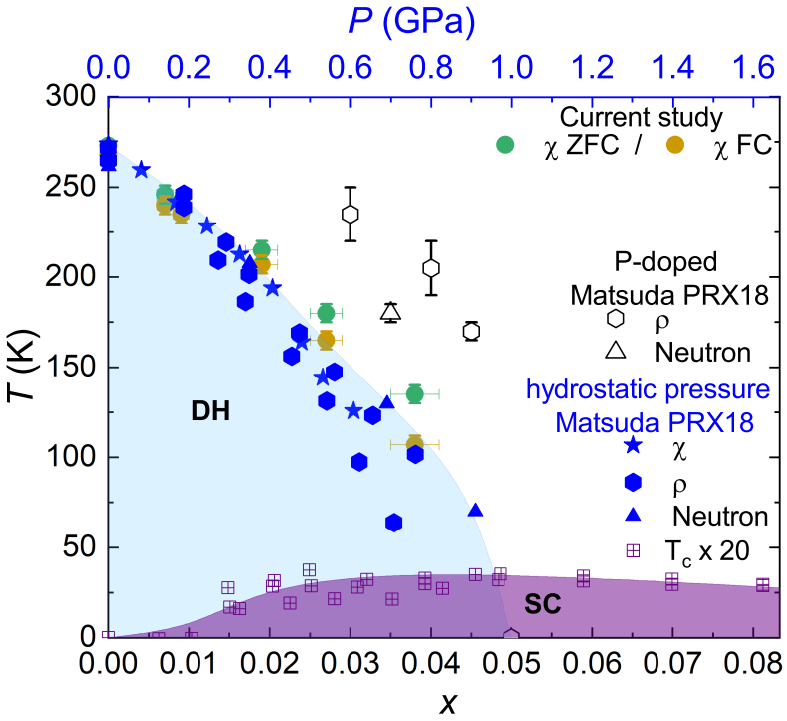

Figure 3.18.: Comparison of pressure-temperature phase diagram of CrAs single crystal under pressure from [7] with the P-doping-temperature phase diagram of $CrAs_{1-x}P_x$single crystals from [7] and this study. DH stands for double helical order and SC stands for superconductivity. The colored regions are provided as visual guides.

3.3.3. Effects of Phosphorus doping on crystal structure

The Rietveld refinement performed on the $CrAs_{1-x}P_x$crushed single crystals confirmed that all samples retain the orthorhombic MnP-type structure, with space group P_{nma}. The presence of a few unindexed reflections in the doped compound series, already mentioned in Sec. 3.2.1, does not pose a significant challenge for the phase identification, as only 5 out of 168 detected reflections remain unindexed, while the majority align with the well known *Pnma* structure of CrAs. These unindexed reflections do not exhibit any systematic shift in 2Θ with phosphorus content (see Fig.3.21 (b)), indicating that they are not related to the primary $CrAs_{1-x}P_x$phase . Instead, their doping-independent character suggests that they most likely originate from secondary phases produced by side reactions during the crystal growth process, such as flux penetration as discussed in Sec. 3.2.3. To determine the origin of these unindexed reflections, a single crystal X-ray diffraction experiment would be recommended. Nevertheless, given that the overwhelming majority of reflections are correctly indexed, the crystal structure can be reliably assigned to the *Pnma* space group for the entire doping series.

Fig. 3.19 shows a depiction of the refined $CrAs_{1-x}P_x$crystal structure. As discussed in Sec. 2.1, CrAs adopts the MnP-type structure, in which each Cr atom is coordinated by six As/P atoms in a distorted octahedral environment [$Cr(As/P)_6$], while each As/P atom is coordinated by six Cr atoms in a distorted trigonal prism. These coordination polyhedra form the local building blocks of the lattice and stack in a characteristic pattern along the three crystallographic axes. On average, there are two [$Cr(As/P)_6$] octahedra per unit cell along the *a* and *c* directions and only one along *b*.

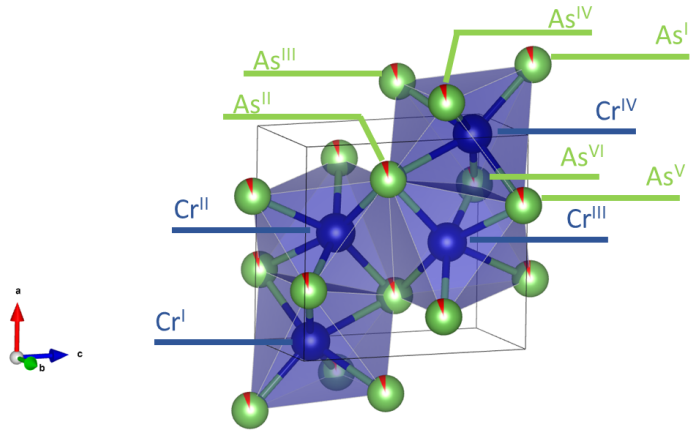

Figure 3.19.: The crystal structure of $CrAs_{1-x}P_x$drawn with VESTA software [74]. The Cr and As atoms are drawn in dark blue and light green, respectively. Phosphorus substitution at the arsenic site is represented as red markers. The labeling denotes the four chromium atoms within the unit cell and the six arsenic atoms forming the [$CrAs_6$] octahedra, which are shaded in light blue.

As discussed in Sec. 2.1.3, Yu et al. connected this to the anisotropic axial compressibility of CrAs under pressure, noting that the lower polyhedral density along b coincides with the reduced electronic charge density and its weaker gradient along the same direction, as highlighted in their band structure analysis [17]. Together, these structural and electronic factors make the b axis intrinsically more sensitive to both physical pressure and isovalent phosphorus substitution.

Fig. 3.20 shows the evolution of the lattice parameters a,b,c and of the unit-cell volume, normalized to their values in the undoped compound ($x_{eff} = 0$), as a function of effective phosphorus concentration. Over the examined doping range, both the b lattice parameter and the unit-cell volume decrease by approximately the same relative amount, reaching values close to -1.2% at the highest effective phosphorus concentration. This confirms that the reduction of the unit-cell volume is dominated by the contraction of the b axis. In contrast, the a and c lattice parameters display only small variations, remaining within a narrow range around their undoped values and showing no systematic monotonic trend. Their scatter is therefore consistent with an almost constant behavior when compared to the pronounced evolution of b and V, in close analogy with the observed structural response in pure CrAs under applied pressure [17, 18, 20].

A clearer illustration of the effect of phosphorus substitution is presented in Fig. 3.21, which displays the PXRD patterns of crushed $CrAs_{1-x}P_x$single crystals. In particular, Fig. 3.21(b) highlights the (200), (102), (111), and (201) reflections, where the (111) peak shifts to higher 2Θ by approximately 0.10° in the highest doped sample relative to the parent compound. Similarly, Fig 3.21(c) shows the (301), (212), (013), (020), and (203) reflections, with the (020) peak exhibiting a shift of about 0.30° towards higher angles. The larger shifts occur for reflections with a nonzero k index, confirming that the b lattice parameter is indeed the structural parameter most sensitive to the application of either physical pressure or chemical pressure. The systematic shift of peaks towards higher 2Θ confirms the progressive contraction of the unit cell as phosphorus content increases.

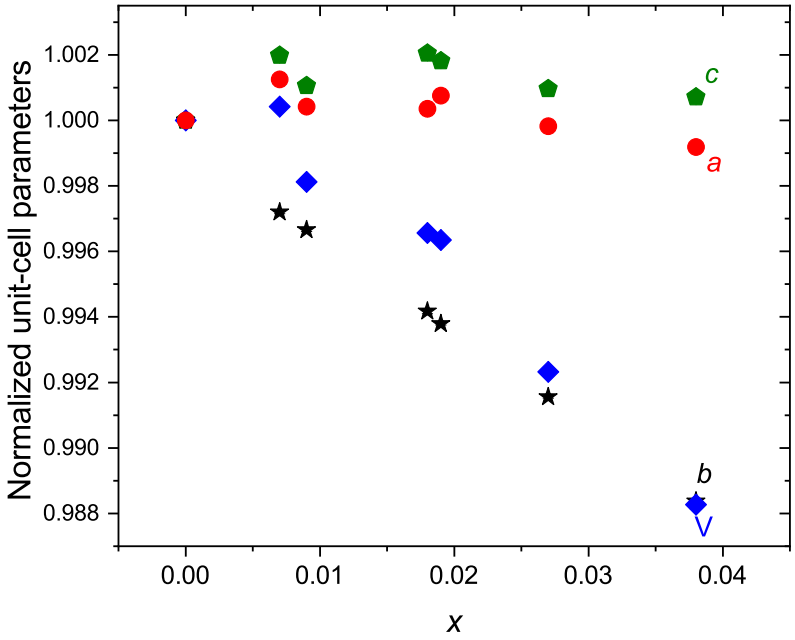

Figure 3.20.: Normalized unit-cell parameters and unit-cell volume of crushed $CrAs_{1-x}P_x$ single crystals, referenced to their values in the undoped compound ($x_{eff} = 0$) as a function of effective phosphorus concentration x_{eff}. Error bars are smaller than the symbol size.

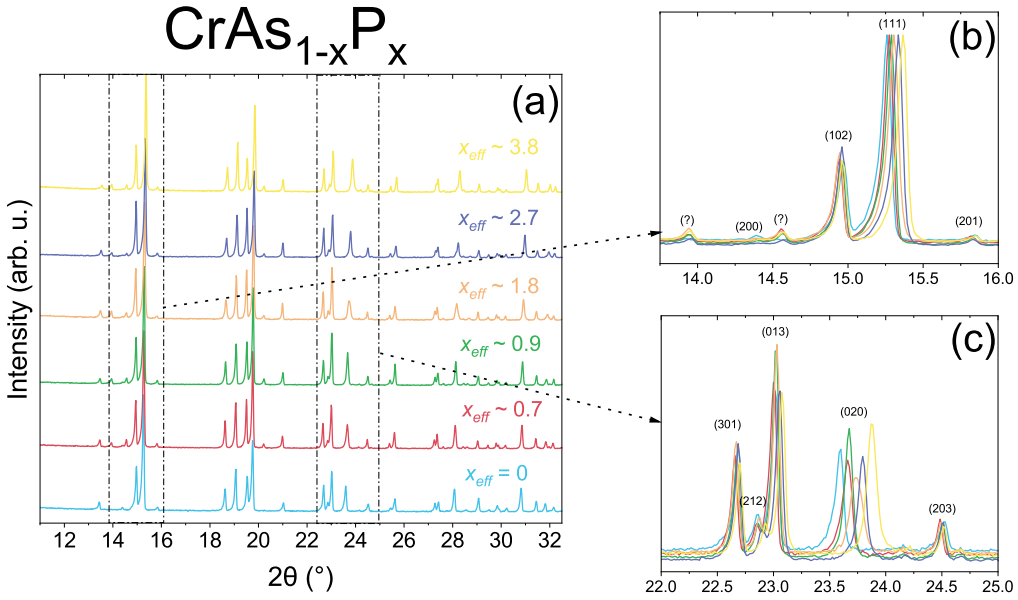

Figure 3.21.: (a) Selected PXRD data of $CrAs_{1-x}P_x$ crushed single crystals for different phosphorus doping levels, at ambient condition. Black boxes and arrows highlight regions of interest. Curves have been shifted vertically for clarity (b-c) Magnified regions of the regions highlighted in (a), displaying unshifted pxrd data with corresponding Miller indices in parentheses.

3.3.4. Comparison of structural response under chemical and physical pressure

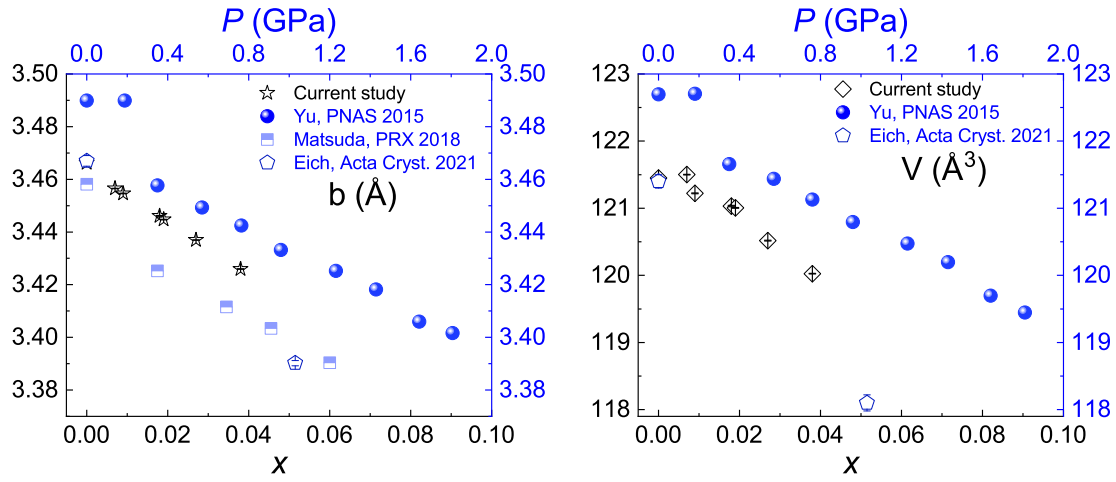

Figure 3.22.: Comparison of b lattice parameter and unit cell volume V of CrAs under pressure from [17, 18, 7] and $CrAs_{1-x}P_x$ at room temperature. Open and filled symbols correspond to data obtained on single crystal and polycrystalline samples, respectively.

Fig. 3.22 compares the doping evolution of the b lattice parameter and unit cell volume in our $CrAs_{1-x}P_x$ samples with pressure dependent behavior of pure CrAs reported in the literature. The comparison is performed using the same linear conversion scale between phosphorus concentration and applied pressure defined in Sec. 3.3.2. Within this framework, the overall trend of the doped crystal datasets aligns closely with the pressure evolution reported in the recent high pressure studies [18, 7]. Deviations from these modern datasets must also be interpreted in light of the intrinsic limitations of this conversion scheme, as already shown in Fig. 3.17.

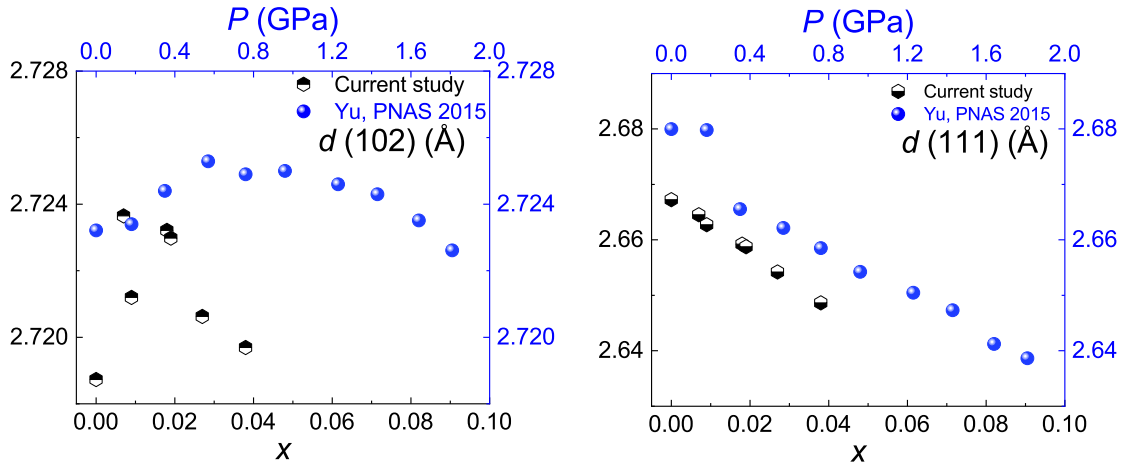

Figure 3.23.: Comparison of the (102) and (111) interplanar spacing of CrAs under pressure from [17] and $CrAs_{1-x}P_x$ at room temperature. Half-open and filled symbols correspond to data obtained on single crystal and polycrystalline samples, respectively.

A notable deviation arises when comparing the $CrAs_{1-x}P_x$ b axis data with the pressure dependent b axis behavior reported by Yu et al. [17]. The pressure-induced isostructural transition they proposed between 0.2–0.3 GPa is not reproduced in our doped samples at the corresponding concentration level defined by the pressure–doping scale.

The b lattice parameter of $CrAs_{1-x}P_x$ exhibits an approximately linear evolution when expressed as a function of the effective phosphorus concentration x_{eff} (Sec. 3.2.2). It should be emphasized that x_{eff} is determined through a calibration based on the monotonic dependence of the b lattice parameter on phosphorus content. As a result, this representation is not sensitive to abrupt non-linear features, such as the sharp b-axis collapse reported under pressure by Yu et al. When examining the unit cell volume in Fig. 3.22, our doped samples again follow more closely the evolution reported in the modern high pressure datasets and clearly deviate from the trend of Yu et al. The same conclusions emerge from the comparison of interplanar spacings in Fig. 3.23. The doping evolution of the (102) and (111) reflections shows a smooth behavior - aside from some scatter in the (102) data - in clear contrast to the pressure dependent data of Yu et al., where the (111) spacing exhibits an abrupt discontinuity and the (102) spacing follows a qualitatively different trend.

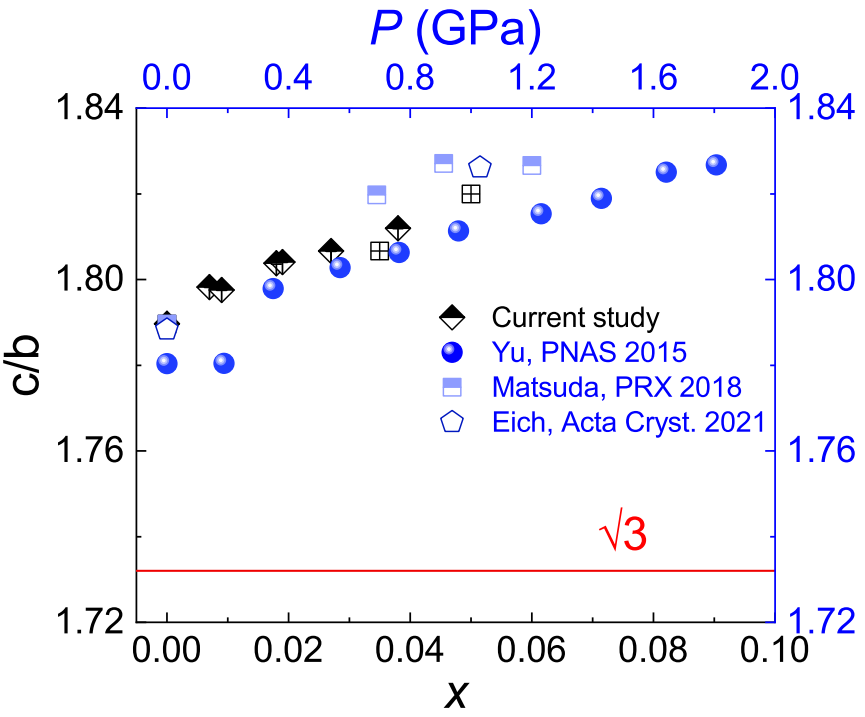

Figure 3.24.: Comparison of c/b ratio of CrAs under pressure from [7, 18, 17] and $CrAs_{1-x}P_x$at ambient condition. Open symbols and filled symbols are for single crystals and polycrystalline samples, respectively.

Fig. 3.24 compares the axial ratio c/b of $CrAs_{1-x}P_x$single crystals at ambient conditions with that of of pure CrAs under pressure. As phosphorus content increases, the c/b ratio increases similarly to the evolution observed under pressure. This suggests that doping similarly distorts the lattice from the parent hexagonal structure. Whether the doped samples undergo a crossing of the $c/b = \sqrt{3}$ value - at the relative transition point for the doped samples - can't be assessed here, as no temperature dependent X-ray diffraction measurement was conducted on the samples. This aspect remains to be investigated in future studies. Nonetheless, the observed changes in twin domain volume fraction on the facets of $CrAs_{1-x}P_x$ single crystals, as previously discussed and shown in Fig. 3.4 (c) and (d), suggest that same structural mechanism is occurring.

In the orthorhombic space group *Pnma*, Cr and As/P atoms occupy the Wyckoff position 4*c* with coordinates $(x_{Cr}, \frac{1}{4}, z_{Cr})$ and $(x_{As/P}, \frac{1}{4}, z_{As/P})$, respectively. Fig 3.25 compares the refined atomic position of Cr atoms and As/P atoms in $CrAs_{1-x}P_x$single crystals with those of CrAs under pressure from [16].

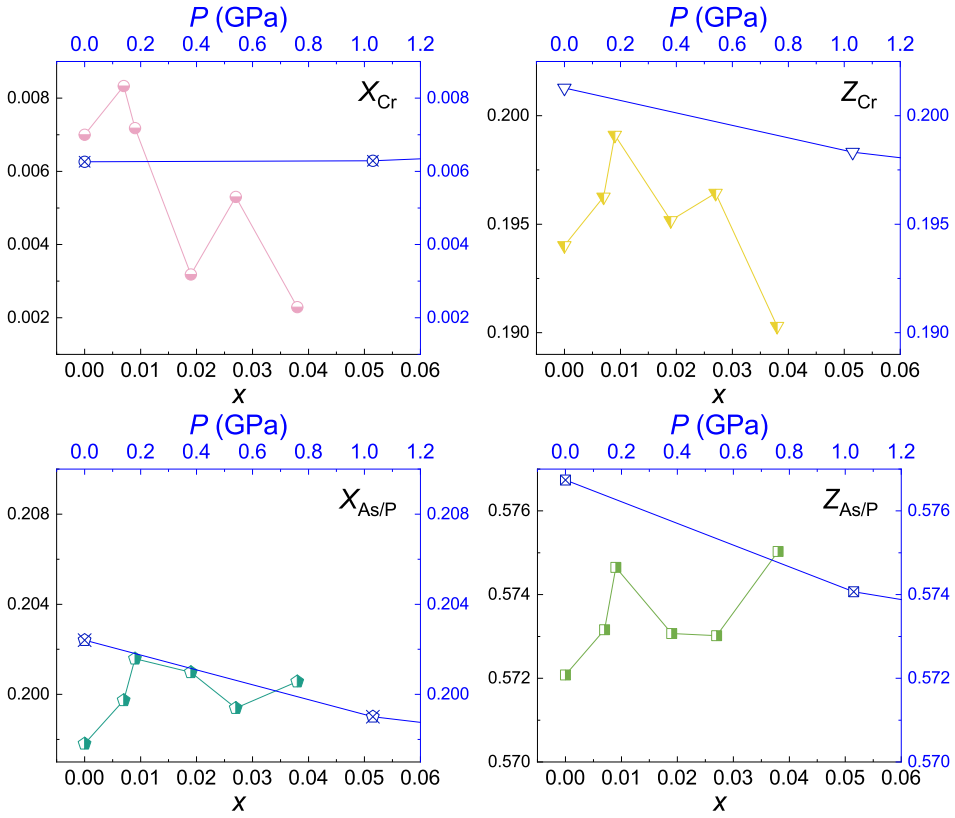

Figure 3.25.: Comparison of atomic position of Cr atoms and As/P atoms of CrAs under pressure from [16] and $CrAs_{1-x}P_x$ at room temperature. Connecting lines are visual guides.

The non-monotonic behavior and increased variability observed in the doped data, as well as the discrepancies relative to the pressure dependent results of the pure compound, reflect our limitation in the profile refinement of the PXRD data. Single crystals x-ray diffraction measurements would yield more accurate results for the atomic position and interatomic distances. Nevertheless, a clear trend in the evolution of atomic positions as a function of doping is observed. X_{Cr} decreases by approximately 67% and Z_{Cr} decreases by about 2%, from the pure compound to x_{eff} = 3.8% P doping. Conversely, $X_{As/P}$ increases by 1.4% and $Z_{As/P}$ increases by 0.5%.

Fig. 3.26 displays the evolution of Cr-Cr and Cr-As/P interatomic distances in $CrAs_{1-x}P_x$ single crystals as a function of doping, compared to pure CrAs under pressure from [16]. The labeling scheme for Cr and As/P atoms follows from Fig. 3.19[14]. Upon increasing the P-doping up to x_{eff} = 3.8%, the following trends are observed in the Cr-Cr interatomic distances: CrI–CrIII increases by 0.6%, CrI–CrII increases by 0.3%, and CrII–CrIII decreases by 1.6%, relative to the parent compound. For the Cr-As/P interatomic distances (from now on referred as Cr-As), the following doping-induced trends are observed: Cr–AsI decreases by 1.4%, Cr–AsII increases by 2.1%, Cr–AsIII/IV decreases by 0.6%, and Cr–AsV/VI decreases by 0.8%.

[14]With the following symmetry code: CrI (x, y, z), CrII $(x + \frac{1}{2}, y, -z + \frac{1}{2})$, CrIII $(-x + \frac{1}{2}, -y, z + \frac{1}{2})$, CrIV $(1, 1, 1) - (x, y, z)$ wich are equivalent to the position with same labeling in [16, 14].

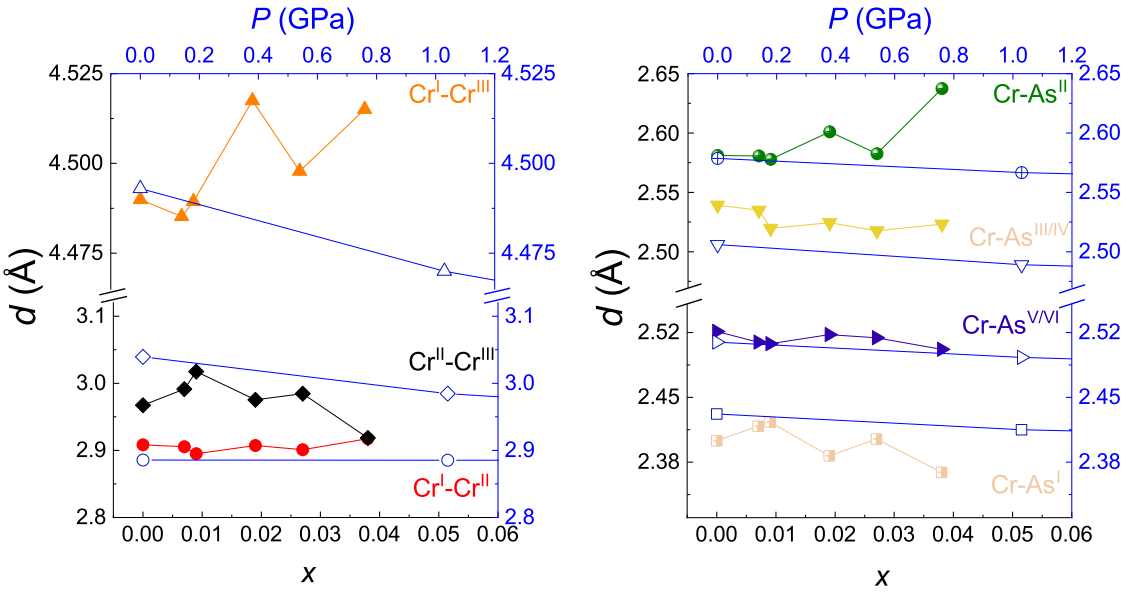

Figure 3.26.: Comparison of Cr-Cr and Cr-As/P interatomic distances of CrAs under pressure from [16] and $CrAs_{1-x}P_x$at room temperature. Connecting lines are visual guides.

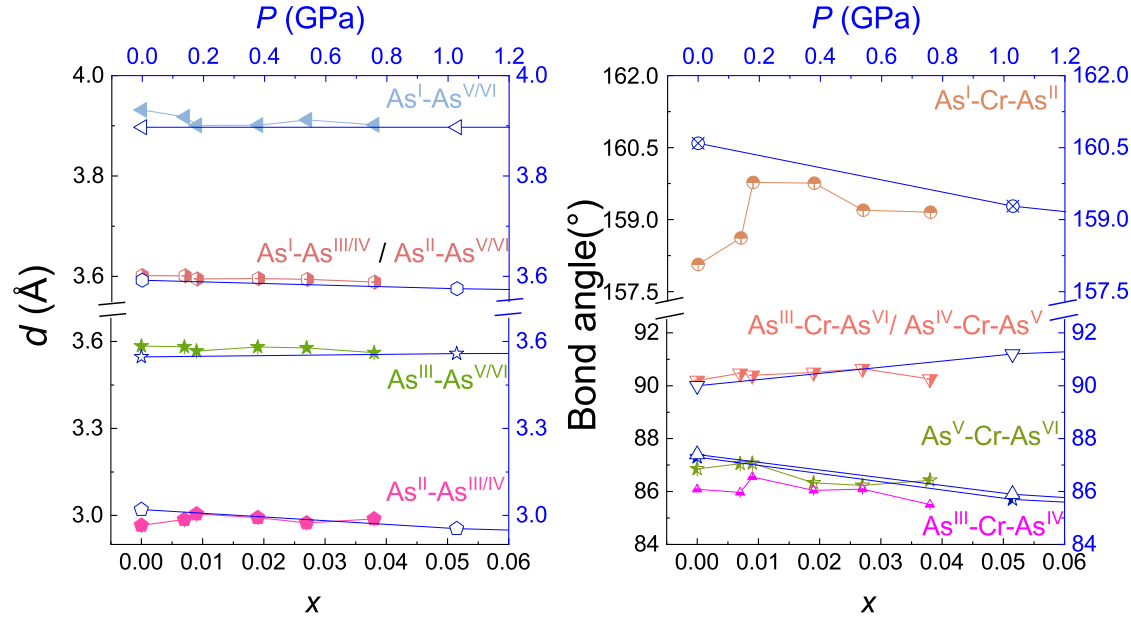

Figure 3.27.: Comparison of As/P-As/P interatomic distances and octhaedra internal angles of CrAs under pressure from [16] and $CrAs_{1-x}P_x$at room temperature. Connecting lines are visual guides.

Fig 3.27 shows the evolution of of As/P–As/P interatomic distances and the internal angles of the $[CrAs_6]$ octahedra in $CrAs_{1-x}P_x$single crystals as a function of phosphorus doping, compared to CrAs under pressure. The labeling scheme for Cr and As/P atoms follows from Fig. 3.19 [15]. With increasing phosphorus doping up to x_{eff} = 3.8%, the AsII–AsIII/IV distance increases by 0.8%, while

[15]The As/P atoms occupy the same Wyckoff position as the Cr atoms. Therefore, the symmetry code are the same, differing only in the specific fractional coordinates.

Direction	Label	Distance (Å)	Orbital/Band	Role
a-axis	CrI-CrII	2.886 → 2.885 2.908 → 2.917	d_{z^2}/a_1	Strongly AFM. Weak pressure-dependence
b-axis	CrI-CrI	3.490 → 3.390 3.466 → 3.426	$d_{x^2-y^2}/a_3$	Weakly AFM. Strong pressure-dependence
bc-plane	CrII-CrIII	3.039 → 2.985 2.967 → 2.918	d_{xy}/a_2	Strongly AFM. Weak pressure-dependence
NNN	CrI-CrIII	4.493 → 4.47 4.490 → 4.515		Unkn. int. [75, 15]. Strong pressure-dependence

Table 3.10.: Summary of selected Cr-Cr distances as a function of pressure and doping from Fig. 3.26. Values in blue are on CrAs under pressure 0 GPa → 1.03 GPa from [18]. Associated orbitals, bands and magnetic interaction are indicated, based on [24, 27], respectively.

the AsIII/IV–AsV/VI decreases by 0.6%, the AsI–AsIII/IV decreases by 0.4% and AsI–AsV/VI decrease by 0.4%, compared to the undoped compound. Regarding the internal angles of the [$CrAs_6$] octahedra, the following doping-induced trends are observed: the ∠ AsI–Cr–AsII angle increases by 0.7%, the ∠ AsIII–Cr–AsVI / AsIV–Cr–AsV increases by 0.1% , the ∠ AsVI–Cr–AsV decreases by 0.5% and the ∠ AsIII–Cr–AsIV decrease by 0.7%, relative to the undoped compound.

The refined Cr-Cr interatomic distances summarized in Tab. 3.10 show that phosphorus substitution reproduces most of the trends observed under pressure. This is consistent with the predictions from the band structure model, discussed in Sec. 2.1.3, in which a reduction of the interatomic distances is expected under both chemical or physical pressure. This Cr–Cr separation is not directly involved in the electronic states governing the low-energy electronic structure within the band model described in Sec. 2.1.3, which primarily emphasizes Cr–Cr interactions associated with orbitals oriented along the *a* axis and the *bc* plane.

As a result, the CrI–CrIII distance is not explicitly accounted for in that framework. Nevertheless, from a purely structural perspective, an overall contraction of the unit cell is expected under increasing chemical or physical pressure, suggesting that the CrI–CrIII distance should also decrease.
A further discrepancy is observed when comparing the evolution of the Cr–AsI and Cr–AsII distances in the $CrAs_{1-x}P_x$series as a function of phosphorus concentration with their pressure dependence in pure CrAs. While the Cr–AsI distance decreases with doping, in agreement with the trend observed under pressure, the Cr–AsII distance exhibits an unexpected increase. As discussed in Sec. 2.1.3, these Cr–As separations are primarily associated with Cr $3d_{xz}$ and $3d_{yz}$ orbitals, which hybridize strongly with As *p* states. Within this picture, a reduction of both Cr–As distances would be anticipated upon lattice compression, making the observed increase of the Cr–AsII distance under phosphorus substitution particularly unexpected.

The refined As/P-As/P interatomic distances and the internal angles within the [$CrAs_6$] octahedra, shown in Fig. 3.27, exhibit only a weak weak dependence on both phosphorus doping and applied pressure. This behavior is consistent with their secondary role in the electronic structure (Sec. 2.1.3), as these distances do not directly involve the Cr centered a_i bands that dominate the states near the Fermi level. However, the octahedral angles within the [$CrAs_6$] octahedra are directly influenced by the bond lengths between Cr and As atoms.

As pressure is applied, these lengths change, leading to distortion in the octhaedral geometry[16]. The distortion within the plane containing AsIII, AsIV, AsV and AsVI atoms is weakly pressure-dependent as the bond lengths between these atoms are not sensitive to chemical or physical pressure. Notably, there is a visible discrepancy in the ∠ AsI-Cr-AsII when comparing the $CrAs_{1-x}P_x$series to the pure CrAs under pressure. The expected decrease of Cr-AsI and Cr-AsII interatomic distances should lead to a decrease of ∠ AsI-Cr-AsII. However, a significant discrepancy is observed not only in the trend but also in the comparison between the absolute values for $x_{eff} = 0$ and pure CrAs at ambient pressure from [18].

Further investigation is required to clarify the anomalies observed in the CrI–CrIII and Cr–AsI/AsII bond lengths, as well as in the ∠ AsI-Cr-AsII. These discrepancies should be interpreted with caution, since they likely reflect the limitation of peak profile refinement in our PXRD data and, more broadly, by the intrinsic difficulties of extracting accurate local structural parameters from powder diffraction alone. Single crystal X-ray diffraction techniques could provide detailed insights into these structural irregularities.

3.4. Conclusions

In this chapter, we presented a comprehensive overview of the synthesis and characterization of $CrAs_{1-x}P_x$ single crystals. A two-step synthesis protocol involving the preparation of polycrystalline precursor followed by Sn-flux crystal growth led to the successful growth of high quality single crystals, especially for the $x_{nom} = 25\%$. However, the crystal size and domain homogeneity were found to be highly sensitive to doping levels and growth parameters, likely due to altered solubility conditions and supersaturation dynamics in the flux medium. Despite adopting a temperature profile similar to that reported by Kotegawa et al. (see Tab. 3.7) and nominally higher structural transition temperature to the hexagonal phase T_t (see Tab. 3.6) in an effort to stabilize monodomain crystals, the growth process repeatedly yielded multidomain CrAs and $CrAs_{1-x}P_x$ single crystals. These results highlight the intrinsic difficulty of producing monodomain $CrAs_{1-x}P_x$ single crystals, particularly at higher doping levels, and indicate that further optimization of the growth conditions may be required.

Powder X-ray diffraction measurements confirmed that all investigated samples crystallize in the orthorhombic MnP-type structure. However, the presence of a small number of unindexed reflections in the doped compounds suggests possible secondary phases or local structural distortions not captured by the current crystallographic model. Single-crystal X-ray diffraction measurements would allow for a more accurate refinement of atomic positions, bond lengths, and bond angles, and would enable a more direct and quantitative comparison with the pressure dependent structural data reported for pure CrAs. The effective phosphorus concentration x_{eff} was determined from the well established correlation between the b lattice parameter and phosphorus content, in good agreement with EDX measurements performed on crystal cross-sections. A central outcome of the compositional analysis is the identification of a pronounced phosphorus concentration gradient between the crystal surface and the bulk. This inhomogeneity reflects both the multi-step synthesis protocol and the intrinsic difficulty of achieving uniform phosphorus incorporation during crystal growth. As a result, bulk-sensitive techniques such as PXRD and magnetometry (see Sec. 3.3.1) predominantly probe the average bulk composition, characterized by the effective concentration x_{eff}, while surface-sensitive methods are governed by the near-surface stoichiometry x_{sur}, determined by EDX measurements on the as-grown crystal facets. The distinction between these two concentration scales is summarized in Tab.3.11.

[16]For a more detailed study on the evolution of the octahedral distortion in CrAs, as a function of pressure, see [16].

x_{nom}	0%	3%	5%	10%	13%	20%	25%
x_{eff}	0%	0.7% ± 0.1	0.9% ± 0.1	2.7% ± 0.2	1.9% ± 0.2	1.8% ± 0.2	3.8% ± 0.3
x_{sur}	0%	0.4%	0.6%	4.5%	3.2%	n.m.	0.6%

Table 3.11.: Nominal composition x_{nom}, effective concentrations x_{eff} obtained from $b(x)$ correlation and surface concentrations x_{sur} determined by EDX. "n.m." indicates that the surface concentration was not measured

Magnetization measurements revealed a systematic suppression of the Néel temperature T_N with increasing x_{eff} (see Tab. 3.9) consistent with the interpretation of phosphorus substitution acting as chemical pressure, analogous to physical pressure in pure CrAs. The persistence of thermal hysteresis confirms the first-order character of the magnetic transition, while its progressive broadening with increasing x_{eff} mirrors the behavior observed in CrAs single crystal under applied pressure. This resemblance supports the view that the transition acquires a quasi-second-order character near the critical doping level, potentially pointing towards the emergence of quantum criticality in $CrAs_{1-x}P_x$ single crystals. No superconductivity was detected down to 2 K in any measured sample, up to $x_{eff} \approx 3.8\%$.

Having established the structural, compositional, and magnetic properties of $CrAs_{1-x}P_x$ single crystals, and in particular the coexistence of bulk and surface doping regimes summarized in Tab. 3.11, we now turn to the investigation of lattice dynamics by Raman spectroscopy. Due to its intrinsic surface sensitivity, Raman scattering predominantly probes the near-surface stoichiometry, making the distinction between the effective concentration x_{eff} and the surface concentration x_{sur} essential for the interpretation of the Raman results presented in the following chapter.

4. Lattice dynamics and structural responses of CrAs and Phosphorus-doped CrAs

CrAs exhibits a strong interplay between its magnetic and structural degrees of freedom, evidenced by pronounced magnetoelastic effects and the formation of coexisting structural and magnetic domains. These features are further modified by physical pressure and phosphorus substitution, which tune the balance between competing phases and influence the evolution of lattice dynamics and structural coexistence. Understanding these changes across temperature, pressure and composition is essential for interpreting the complex phase behavior of CrAs and $CrAs_{1-x}P_x$.
In this chapter, we investigate these phenomena by combining Raman scattering to probe lattice dynamics with transmission electron microscopy (TEM), which provides insight into structural heterogeneity and nanoscale domain structure. Together, these complementary techniques allow us to track the onset, locality, and evolution of phonons and structural phase coexistence across the CrAs–P phase diagram.

4.1. Raman scattering: principles and methodology

Raman spectroscopy probes the inelastic scattering between light and low energy excitations, providing a direct access to the information on the excitation energies, symmetries and linewidths [76, 77]. In crystalline solids, lattice vibrations (phonons) represent one of the main contributions to the Raman response. Because phonons are highly sensitive to the changes in crystal structure and symmetry, Raman scattering is a powerful tool for studying the evolution of lattice dynamics under external tuning parameters. Moreover, the local character of Raman measurements allows the detection of spatially separated domains and heterogeneous structural responses [78, 79], making Raman spectroscopy a particularly well suited for investigating the magnetostructural transitions and phase coexistence in the CrAs-based system.
In this section, the basic principles of Raman spectroscopy are introduced, together with the experimental configuration and characteristics of the setups employed in this work. In addition, a summary of the existing results from the literature on Raman measurements of CrAs is presented as a framework for the experimental investigations discussed in the upcoming sections.

4.1.1. Principles of Raman scattering

A schematic representation of the Raman process and the principle of inelastic light scattering is shown in Fig. 4.1. An incident photon with wavevector $\vec{k}_I$ and frequency ω_I interacts with the electronic polarization of the system, temporarily exciting it to an intermediate virtual state. The system then transitions to a final state, accompanied by the emission of a scattered photon. If the scattered photon with wavevector $\vec{k}_S$ has a frequency $\omega_S < \omega_I$, the energy difference corresponds to the creation of an excitation within the material, also known as Stokes process.

If the scattered photon has a frequency $\omega_S > \omega_I$ the energy difference corresponds to the annihilation of an excitation in the material, also known as Anti-Stokes process. [76, 77].

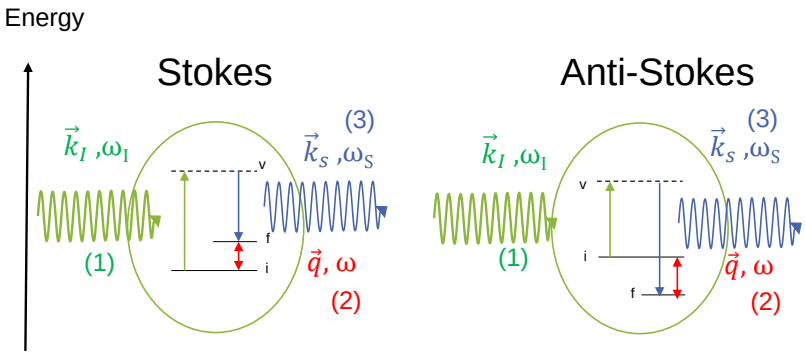

Figure 4.1.: Schematic illustration of the Raman scattering process. The incident photon (1), with $(\vec{k}_I, \omega_I)$ excites the system to a virtual intermediate state leading to emission of a scattered photon (3), with $(\vec{k}_S, \omega_S)$. On the left, the stokes process in which an excitation (2) is created with with $(\vec{k}_S - \vec{k}_I = \boldsymbol{q}, \omega_I - \omega_S = \omega)$. On the right, the anti-stokes process in which an excitation is annihilated with $(\vec{k}_S - \vec{k}_I = \boldsymbol{q}, \omega_S - \omega_I = \omega)$

In Raman scattering, the inelastic process can involve the creation or annihilation of a lattice vibrational quantum (phonon). These modes are the result of the modulation of the induced polarization of the material, due to the oscillating electric field of the incident light. The induced polarization is proportional to the electric field via the electronic susceptibility $\chi\left(\vec{\boldsymbol{k}}_I, \omega_I, \boldsymbol{u}\right)$, where $\boldsymbol{u}$ represents the atomic displacement associated with the vibrational mode. The first-order term in a Taylor expansion of the susceptibility, with respect to $\boldsymbol{u}$, defines the Raman tensor. The Raman scattering intensity is proportional to the square of the matrix element:

$$I_{\text{Raman}} \propto |\boldsymbol{e}_i \cdot \mathcal{R} \cdot \boldsymbol{e}_s|^2 \tag{4.1}$$

where $\mathcal{R} = \frac{\partial \chi}{\partial \boldsymbol{u}}\boldsymbol{u}$ is the Raman tensor and $\boldsymbol{e}_i$, $\boldsymbol{e}_s$ are the polarization vectors of the incident and scattered light, respectively. A mode is Raman-active if at least one component of the Raman tensor is nonzero.

Eq. 4.1 also defines the selection rules, which determine the measurable intensity of Raman-active modes, depending on the polarization configuration. These selection rules can also be derived for specific point group symmetries using group theory [76, 77]. Because the Raman tensor is directly influenced by the symmetry and atomic arrangement of the crystal, any variation in the structure - such as phase transitions, lattice strain, or disorder - can change the selection rules and the resulting Raman signal. This makes Raman spectroscopy particularly useful to probe the structural dynamics related to these changes[1].

[1]For a detailed discussion of Raman scattering physics see [76, 77, 80]

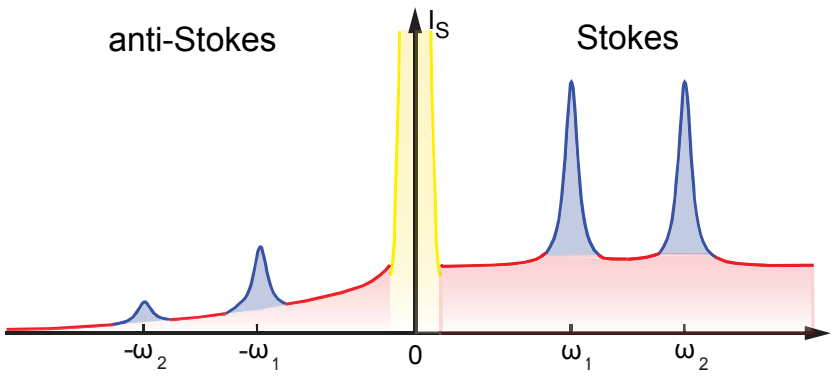

Figure 4.2.: Schematic spectrum of the scattered light. The intense elastic appears at the center (yellow) and the Raman response in the Stokes and anti-Stokes channels contains contributions from phonons (blue) and electrons (red). Figure adapted from [81].

Fig. 4.2 shows the schematic appearance of a typical Raman spectrum. In Raman spectroscopy, the scattered intensity is typically plotted as a function of the Raman shift $\omega = \omega_I - \omega_S$, defined previously in Fig. 4.1. Raman active phonons appear as discrete features corresponding to vibrational energies accessed through the Stokes process. Other than the inelastic scattering of light by lattice vibrations, scattering by other excitations in solids, such as magnons, plasmons and excitons, can occur through the same Raman mechanism [76, 82]. In addition, Raman spectroscopy can probe an electronic continuum associated with particle-hole excitations, which may manifest as a broad background (red) in the Raman response, as indicated in Fig. 4.2.

The focus of this thesis is primarily on the phononic contribution to the Raman spectra, which provides the relevant information for the results discussed in the following chapters. The number, position, and relative intensities of the phonon peaks are dictated by the crystal symmetry and by the selection rules imposed by the Raman tensors introduced above. The anti-Stokes side contains analogous features but is significantly weaker due to the detailed-balance relation linking Stokes and anti-Stokes scattering $I_{AS} = I_S e^{\frac{-\hbar\omega}{k_B T}}$ [76].

4.1.2. Raman measurement geometry and instrumentation

The Raman measurement geometry and the associated experimental setups used in this work are presented in this section, covering the optical setups and instrumentation employed for both ambient-pressure and high-pressure measurements. Ambient-pressure, temperature dependent measurements on $CrAs_{1-x}P_x$ were performed at the Institute for Quantum Materials and Technologies (IQMT), Karlsruhe Institute of Technology (KIT). Pressure and temperature dependent Raman scattering measurements on CrAs were instead carried out at Institut Néel, Grenoble. The instrumentation used for high-pressure measurement - including the diamond anvil cell (DAC) setup - will be described in a dedicated subsection.

4.1.2.1. Ambient-pressure Raman setup

Raman scattering experiments at ambient pressure were performed in the backscattering geometry using a Jobin-Yvon LabRAM HR Evolution spectrometer. A 10 mW He-Ne laser with 633 nm wavelength

was used as a light source. The spectrometer setup was mounted on a vibration-isolated optical table to minimize mechanical noise[2].

Figure 4.3.: Picture of the Jobin-Yvon LabRam HR Evolution spectrometer used in this study. Figure from [52].

The Raman setup operates in a micro-Raman configuration with confocal geometry, which provides lateral and axial spatial resolution by restricting the detected signal to a well defined focal volume. This is achieved through the use of a high-numerical-aperture (NA) objective and a spatial filter - typically a pinhole or entrance slit - placed at the spectrometer entrance at a plane conjugate to the laser focus in the sample.

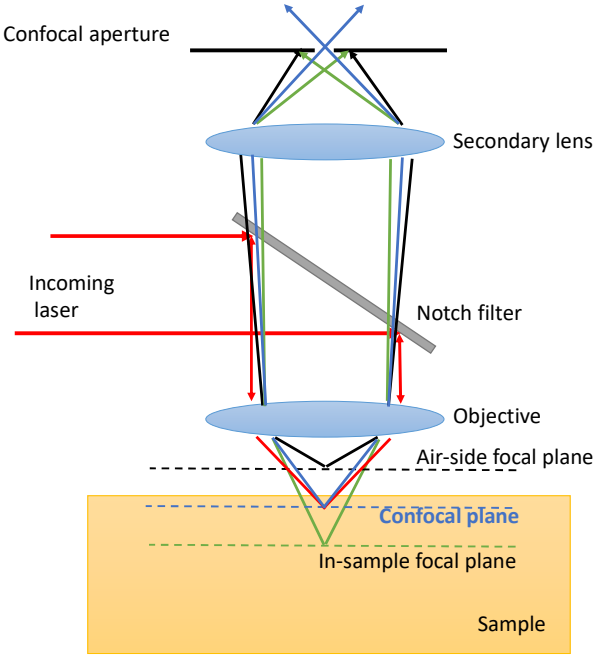

Figure 4.4.: Schematic representation of the confocal Raman microscope. The incoming laser beam is guided to the sample through the objective, with the help of a notch filter. Only light originating from the confocal plane is transmitted through the confocal aperture, while other contributions are suppressed. Figure adapted from [83].

[2]This particular setup configuration was previously described and reported in Yao's thesis [52].

Objective	Filter	Laser power(mW)
LMPlanFLN x50 ($5\mu m$ spot size)	3.2%	0.2
	5%	0.5
	10%	0.7
	25%	2.5
SLMPlan x100(ULWD) ($2\mu m$ spot size)	3.2%	0.1
	5%	0.3

Table 4.1.: Laser power measured after the LMPlanFLN x50 objective and the SLMPlan x100(ULWD) objective .

Fig. 4.4 shows a schematic representation of the confocal setup. The incoming laser beam (red ray) is guided toward the sample through the microscope objective, with the help of notch filter used to suppress the elastic line in the backscattering geometry, which defines the confocal plane (blue ray). In practice, the position of this plane corresponds to the z axis reference ($z = 0$) used during the measurement, determined by adjusting the microscope until the sample surface appears in best focus on the camera. Only photons originating from this focal region form a sharp image at the pinhole and are efficiently transmitted into the spectrometer. In contrast, light emitted from out of focus regions - such as the in-sample focal plane (green) or the air-side focal plane (black) - is strongly suppressed as it does not image correctly onto the pinhole. This spatial filtering removes background contributions from outside the focal volume and enables depth-sensitive analysis with micrometer scale, when not limited by the optical penetration depth of the examined sample [84].

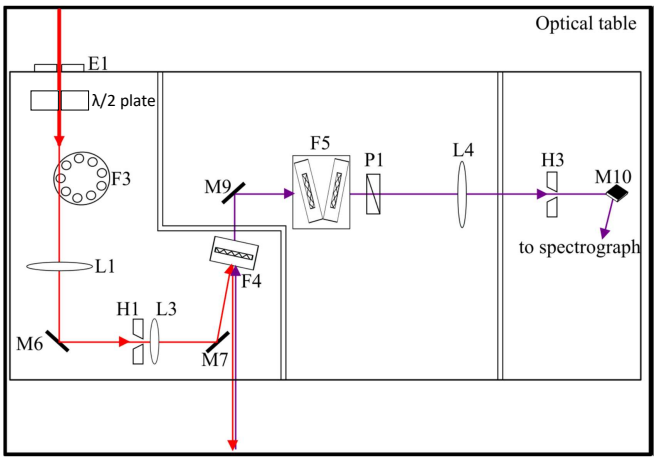

Figure 4.5.: Schematic representation of the Raman scattering setup employed at KIT. Figure adapted from [52].

Fig. 4.5 shows a schematic representation of the internal optical path of the spectrometer. The laser beam first passes through a $\lambda/2$ wave plate to select the incident polarization and then through an intensity filter (F3) to adjust the power. It is then focused by a lens (L1) onto a pinhole (H1) to spatially filter the beam profile to reduce optical aberrations and then recollimated by a second lens (L3). After recollimation by the lens (L3), the beam is redirected by a mirror (M7) toward the notch filter (F4), which at this stage acts as a reflective element, directing the beam toward the microscope objective and onto the sample.

Different microscope objectives were used depending on the type of measurement. The x50 objective, giving a laser spot size of approximately 5 μm, was used for all Raman measurements on single crystals (see Sec. 2.3 and 4.4). The x100 long-working-distance objective was used for Raman measurements on the lamellae (see Sec. 4.5.1) and provides a laser spot size of approximately 2 μm. The laser powers delivered to the sample for different filters and objectives are listed in Tab. 4.1. Since the measurements are performed in a backscattering configuration, the Raman signal is collected through the same microscope objective used for the incident light (blue arrows in Fig. 4.5). The scattered signal is then transmitted back through the notch filter (F4), which at this stage suppresses the elastically scattered laser line as well as plasma lines originating from spontaneous emission within the laser source. Further suppression of residual laser light is achieved using a set of Bragg filters (F5). Before entering the spectrometer, the beam passes through an analyzer (P1), which selects the polarization of the scattered light and is guided through the optical components L4, H3 and M10. The spectrometer is equipped with two diffraction gratings, with groove densities of 600 gr/mm and 1800 gr/mm. All measurements presented in this work were performed using the 600 gr/mm grating in order to maximize the detected signal intensity. The instrumental spectral resolution corresponding to this grating was determined from the emission lines of a neon (Ne) calibration lamp, yielding a resolution of 1.69 cm^{-1}. The dispersed Raman signal was finally detected using a Symphony CCD detector (Horiba), cooled with liquid nitrogen.

For the Raman temperature dependent measurements, a horizontal helium flow cryostat (Konti-Cryostat-Mikro, Cryovac) was employed and mounted beneath the microscope objective. The samples were mounted in the cryostat by gluing them onto the copper cold finger with Apiezon N grease for optimal thermal contact. The sample chamber was continuously evacuated to high vacuum ($< 5 \times 10^{-6}$ hPa) for better thermal insulation and to prevent condensation. Temperature was controlled via TIC500 temperature controller (Cryovac) with the lowest reachable temperature $\approx$ 4 K with a continuous helium flow.

4.1.2.2. Crystal orientation and measurement geometry

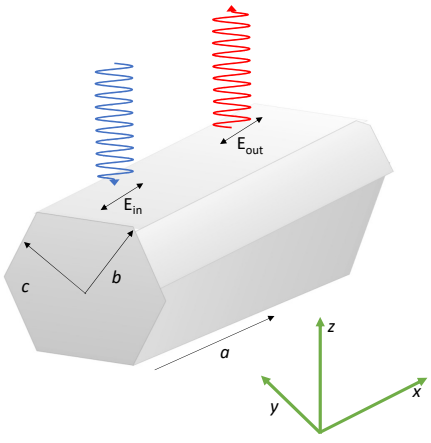

Figure 4.6.: Raman experiment scheme of the polarization geometry relative to the crystal facet. E_{in} and E_{out} stands for the polarization direction of incoming and outgoing (scattered) light, respectively. Image adapted from [8].

The needle-like morphology of $CrAs_{1-x}P_x$single crystals constrains the choice for the experimental configuration for Raman measurements. As mentioned in Sec. 3.1.3, the crystals grow as elongated needles with their long axis parallel to the crystallographic *a* axis.

As a consequence, they do not provide large, well defined flat surfaces perpendicular to *a*, which would be ideal for implementing a standard backscattering geometry.
The situation is further complicated by the presence of orthorhombic twin domains along the *a* axis - responsible for the pseudohexagonal habitus (see Sec. 3.1.3) - making the identification of a single crystallographic direction within the *bc* plane effectively impossible, as on the spatial scale of the Raman spot, the laser would probe multiple twin variants simultaneously. Attempts to overcome these limitations by cutting and polishing the crystals were unsuccessful, as polishing induced partial amorphization of the surface. This resulted in broadened and weakened phonon features, similar to what has been reported for polished CrAs [52].
For these reasons, all Raman measurements were carried out on natural as-grown facets. The crystal was mounted such that the incident laser beam arrives perpendicular to a natural as-grown facet, with the crystallographic *a* axis lying in the plane of this surface. In this configuration, both the incident and the scattered light propagate along a direction perpendicular to *a*, while the polarization of the incoming and outgoing beam is aligned parallel to the *a* axis (needle direction in Fig. 4.6). This defines a Raman measurement geometry described by the Porto notation $-z(aa)z$.

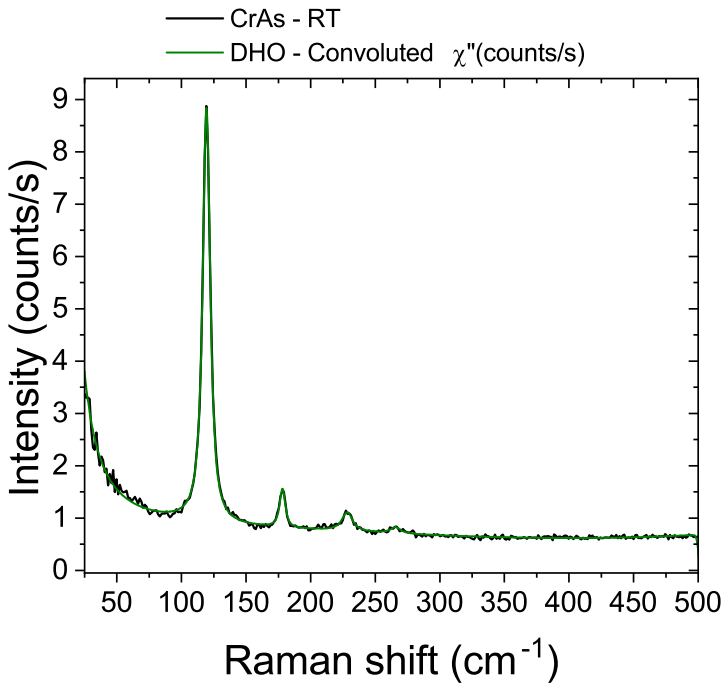

Figure 4.7.: Raman spectrum of a CrAs single crystal measured at ambient conditions in the parallel scattering configuration $-z(aa)z$. The solid green line represents a fit using a damped harmonic oscillator (DHO) model convoluted with the instrumental resolution function. Details of the fitting procedure are provided in the main text.

Fig. 4.7 shows a typical Raman spectrum measured on a CrAs single crystal at ambient conditions in the parallel polarization configuration, denoted in Porto notation as $-z(aa)z$[3]. In this geometry, the Raman selection rules determined by the Raman tensors of the *Pnma* space group (see App.C) allow only the A_g symmetry modes to be observed. All four expected A_g phonon modes are clearly observed and their relative intensities are consistent with the one reported in [8]. The strong increase in intensity below 70 cm^{-1} correspond to the elastic tail region and is due to the strong surface reflectivity due to the metallic character of CrAs.

[3]Unless otherwise specified, all spectra will be measured in this polarization configuration.

To remove any potential instrumental or environmental artifacts from the Raman spectra, the data were subjected to the following processing protocol. First, the dark counts signal - defined as the baseline noise level of the CCD detector - was subtracted. Then, the contribution from air scattering was removed. Because the space between the microscope objective and the cryostat window is not under vacuum, inelastic scattering from air can contribute to the measured signal[4].
The spectra fitting procedure was based on a model including a Lorentzian function centered at 0 cm^{-1} to account for the elastic tail region, a polynomial function to describe the background and Bose-corrected damped harmonic oscillator (DHO) functions for the phonon modes [52]. In order to extract the intrinsic phonon linewidths, the instrumental resolution of the spectrometer was explicitly included by convoluting the fitting model with a pseudo-Voigt profile. The parameters of this profile were determined from fitting the the neon (Ne) emission lines of a calibration lamp, as mentioned previously. The resulting fit is illustrated by the green line in Fig. 4.7. For plotting purposes only, the spectra were processed with a background subtraction, followed by Bose-correction and normalization. Unless otherwise specified, all plotted data were treated with this procedure.

4.1.2.3. High-pressure Raman setup

The configuration used for high-pressure Raman experiments follows the descriptions provided in the PhD thesis of Grasset [85] and the Master thesis of Baron [86].

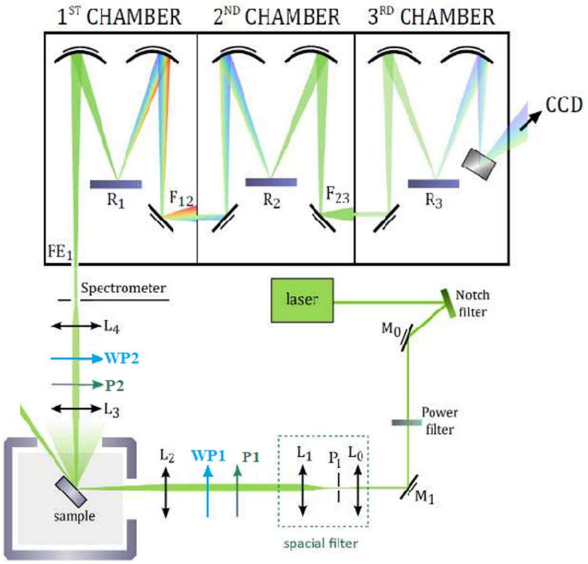

Figure 4.8.: Schematic of the Raman scattering setup employed at Néel institute. Figure from [86].

Fig 4.8 shows a schematic representation of the internal optical path. The laser beam passes first through a band-pass filter and then through a spatial filter consisting of two lenses (L0, L1) and a pinhole (P_I) to ensure both spatial and frequency purity. The filtered beam is then polarized using a polarizer (P1) and its intensity is tuned by using a waveplate (WP1). A focusing lens (L2) then directs the beam onto the sample, creating a laser spot with a size of approximately 20 μm.

[4]To remove airline signal, a reference spectrum was acquired by defocusing completely the microscope objective, capturing only the air scattered signal. This reference was then subtracted from the sample spectrum.

Unlike the standard backscattering geometry, the setup allows adjustment for the incident beam angle, as shown in Fig. 4.9. The 37.5° tilting ensures that the elastic signal, specularly reflected, is not collected by the collection optics, therefore reducing background noise and improving the signal to noise ratio. The scattered light is then collected by the objective (L3). Depending on the measurement conditions, additional filters can be inserted to further suppress the elastic scattering. The beam is then guided through a final focusing lens (L4), which directs it into the entrance slit of the spectrometer (FE1). A second polarizer (P2) together with a second waveplate (WP2) is positioned before the spectrometer slit to control selection rules and optimize signal intensity.

As shown in Fig. 4.8 the spectrometer consists of three stages used to analyze the collected signal. While the signal can be analyzed directly after the first diffraction grating (R1), this broad-range acquisition comes at the cost of energy cutoff around approximately 80 cm^{-1}, due to the required physical filters to suppress the elastic line. To access low-energy features, the full triple-stage configuration is employed. In this configuration, light diffracted by the R1 passes through the slit (F12) into a second stage, where the second grating (R2) is mounted in the -1 diffraction order. This stage recombines the dispersed light and sends it to the third stage (F23) to the third grating (R3), which functions similarly to R1, before sending it to the nitrogen cooled Pylon400 CCD detector. This configuration enables efficient elastic suppression with the low-energy cutoff of approximately 3 cm^{-1}.

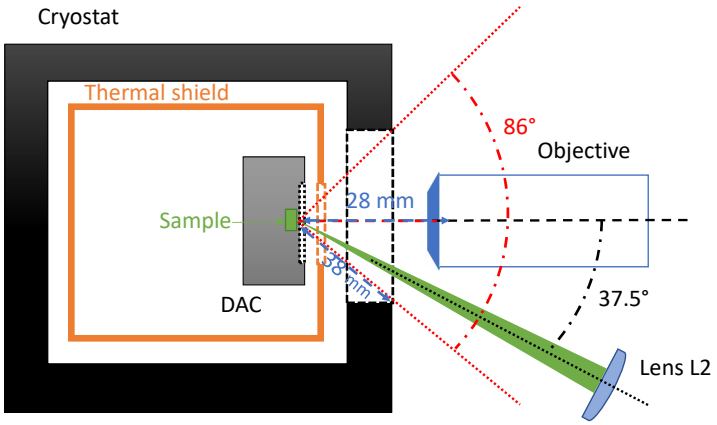

Figure 4.9.: Schematic representation of the incoming optical path geometry at the cryostat, with the sample mounted inside the diamond anvil cell (DAC). Figure adapted from [85].

4.1.2.4. Diamond Anvil Cell (DAC)

Fig. 4.10 shows a schematic representation of the diamond anvil cell (DAC) employed for the pressure experiment. High pressures are obtained by mounting two opposing, cut diamond anvils on a piston-cylinder system which allows relative motion between them. The sample is placed between the anvils inside a small hole drilled into a metallic gasket. A pressure transmitting medium fills the gasket cavity surrounding the sample to ensure hydrostatic conditions. For the present study, a membrane-driven diamond anvil cell (MDAC) was used. The cell body is made of Marval 18 steel, while the diamond seats are composed of tungsten carbide. The main advantage of the MDAC setup is its ability to adjust pressure at low temperatures. The flexible membranes, filled with pressurized with helium gas (^{4}He), exert a controlled force on one of the diamonds, while the other remains fixed. The membrane is connected to an external high-pressure helium reservoir through a capillary line, allowing pressure to be tuned at low temperatures.

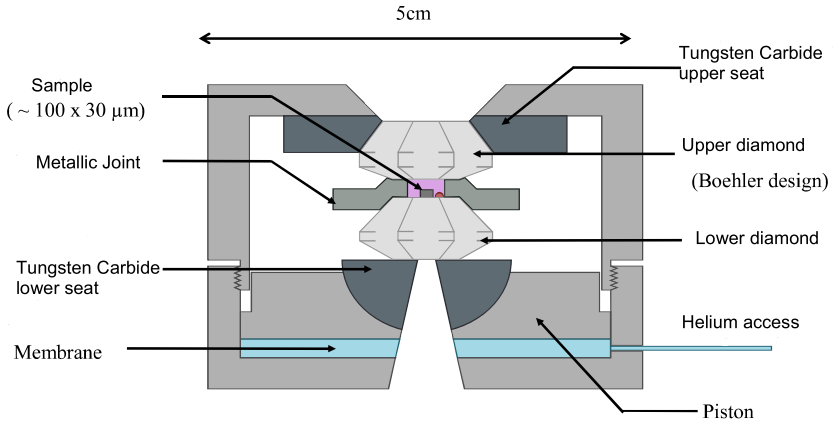

Figure 4.10.: Schematic representation of the structure of the diamond anvil cell. Figure adapted from [85].

Another key feature of the MDAC is its compatibility with Raman spectroscopy measurements. Since diamonds are transparent in the visible range, a laser beam can be focused directly onto the sample through one of the anvils, which simultaneously acts as an optical window.
Type IIa synthetic diamonds - shaped according to the Boehler geometry - are commonly used due to their intrinsic low Raman signal and minimal fluorescence, ensuring minimal optical background and a larger solid collection angle. Further details on pressure cell alignment, sample preparation and mounting can be found in [85].

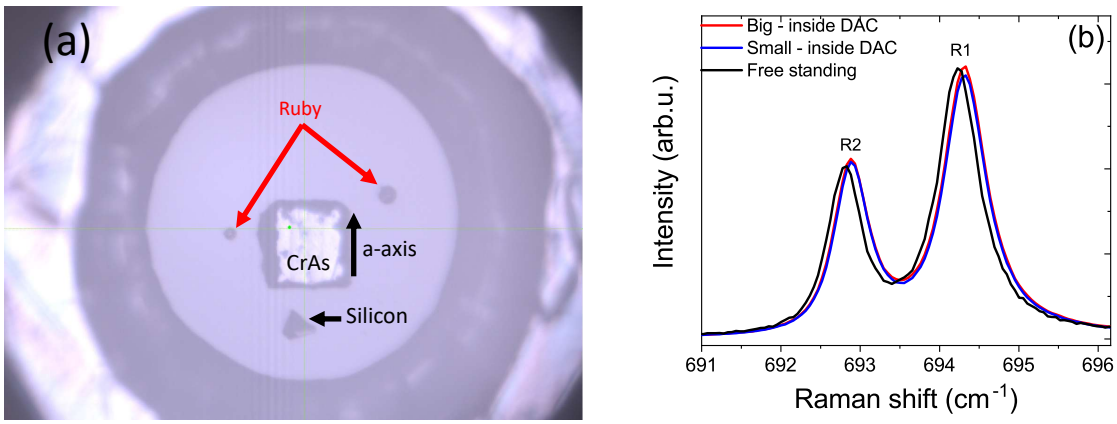

Figure 4.11.: (a) Image of the MDAC gasket cavity containing a CrAs single crystal, together with two ruby samples and silicon sample. (b) Comparison of Raman spectra on ruby samples inside and outside the MDAC.

Fig 4.11 (a) shows the inside of the MDAC gasket cavity, containing the CrAs single crystal together with two ruby samples for pressure calibration and a silicon sample for focus optimization. Reliable in situ pressure determination is obtained via ruby fluorescence measurement. The Cr^{3+} impurities in ruby give rise to two sharp fluorescence lines, R1 and R2, as shown in Fig.4.11 (b). The R1 line is commonly used for pressure calibration due to its well characterized linear shift as a function of pressure, up to 20 GPa [87]. In this work, the R1 fluorescence was recorded from both ruby samples in order to detect any possible deviation from hydrostatic conditions.

To extract the pressure value, the R1 peak frequency - together with measured temperature, inside the MDAC - was then inserted into a open source calibration applet[5], based on the calibration method from Shen et al. [87]. The R1 peak hardening shown in Fig. 4.11 (b) of both ruby samples, in the MDAC, compared to the free standing ruby sample, corresponds to a pressure of approximately 0.3 GPa inside the cell.

To achieve cryogenic temperatures, a PT407-RM pulse tube cryostat (CryoMech) was used. This cryostat is based on a closed cycle circulation of ^{4}He gas, which is compressed and expanded within a cold head. In order to minimize vibrations, the cold head is mechanically decoupled from the sample region, while thermal contact in ensured with copper braids. Before cooling, the cryostat chamber is evacuated to a pressure around 10^{-6} mbar.

As described in Sec. 4.1.2.2, high-pressure Raman spectra were processed using a protocol for minimizing instrumental and environmental artifacts as airline subtraction. Background removal was performed before both data fitting and plotting. The spectra fitting procedure was based on a model which includes Bose-corrected damped harmonic oscillator (DHO) functions for describing the phonons. Due to the use of a 2400 gr/mm grating, the spectral range required to capture all A_g phonos could not be acquired in a single scan. Instead, the data were collected in two overlapping spectral windows: one from 7 to 200 cm^{-1} and another from 170 to 340 cm^{-1}. For plotting, each window was subjected to background subtraction and Bose correction. The two windows were then stitched together by removing the overlapping region and joining the remaining parts. After merging, the resulting spectrum was normalized. Unless otherwise specified, all plotted data were treated with this procedure.

4.1.3. Previous Raman studies of CrAs

In this section, we summarize the key Raman results on CrAs, as these provide the baseline for interpreting the measurement discussed in the following sections. The Raman-active optical modes of CrAs were initially investigated by Sen et al., with a more detailed treatment provided in the PhD thesis of Yao [8, 52]. CrAs crystallizes in the orthorhombic space group P_{nma}, which corresponds to the centrosymmetric point group D_{2h}. Within this structure, both Cr and As atoms occupy the 4c Wyckoff positions, leading to a unit cell with four Cr and four As atoms. This configuration results in a total of 24 zone-center vibrational modes, of which the following 12 are Raman active[6] [52]:

$$\Gamma_{\text{Raman}} = 4A_g + 2B_{1g} + 4B_{2g} + 2B_{3g} \tag{4.2}$$

Due to the weak intensity and negligible temperature dependence of the B_{1g} and B_{2g} modes, along with the experimental challenges in detecting the B_{3g} modes (see Sec. 4.4), earlier investigations focused primarily on the A_g phonon modes.
Fig. 4.12 shows a typical Raman spectrum of CrAs measured in the parallel polarization configuration, where both the incident and scattered light are polarized along the a-axis. The spectrum reveals all four expected A_g phonon mode, clearly observable both above and below the magnetostructural transition temperature T_N. The temperature dependence of all the A_g phonons is well described by the anharmonic decay model in both the paramagnetic and magnetic phase.
However, the rate of frequency change is significantly higher in the paramagnetic state, suggesting a more pronounced anharmonicity in the non-magnetic phase [52, 88].

[5] Available at the following link: http://kantor.50webs.com/ruby.htm

[6] The phonon eigenvectors, based on DFT analysis are shown in App. C. For further details on Raman tensors, polarization selection rules and DFT mode calculations see [52].

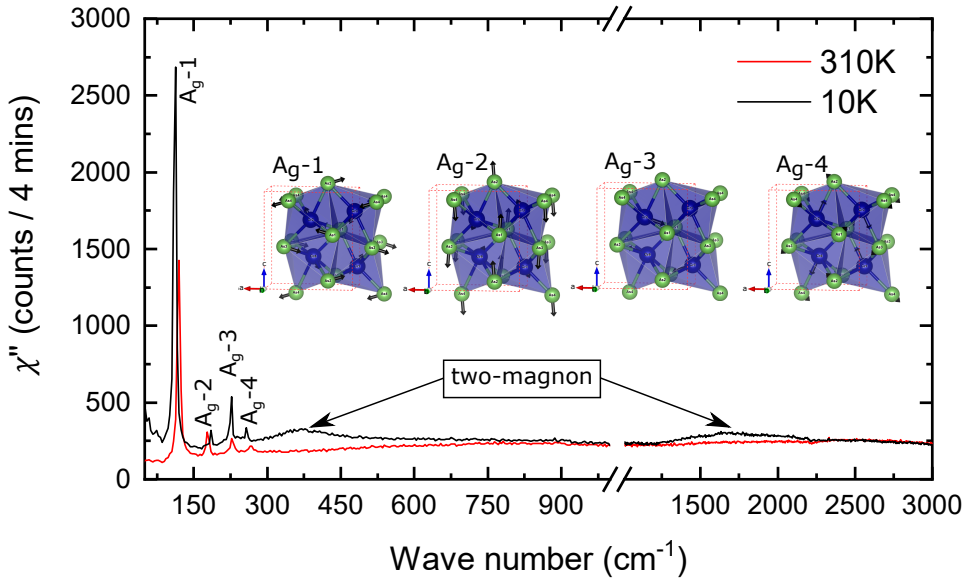

Figure 4.12.: Raman spectra of CrAs showing the A_g symmetry modes measured at two temperatures, above and below the magnetostructural transition temperature T_N. Below T_N, phonon renormalization is observed and higher-energy features corresponding to two-magnon excitations emerge. The inset displays the eigenvectors associated with the four A_g phonon modes. Image adapted from [8].

4.1.3.1. Large phonon renormalization at T_N

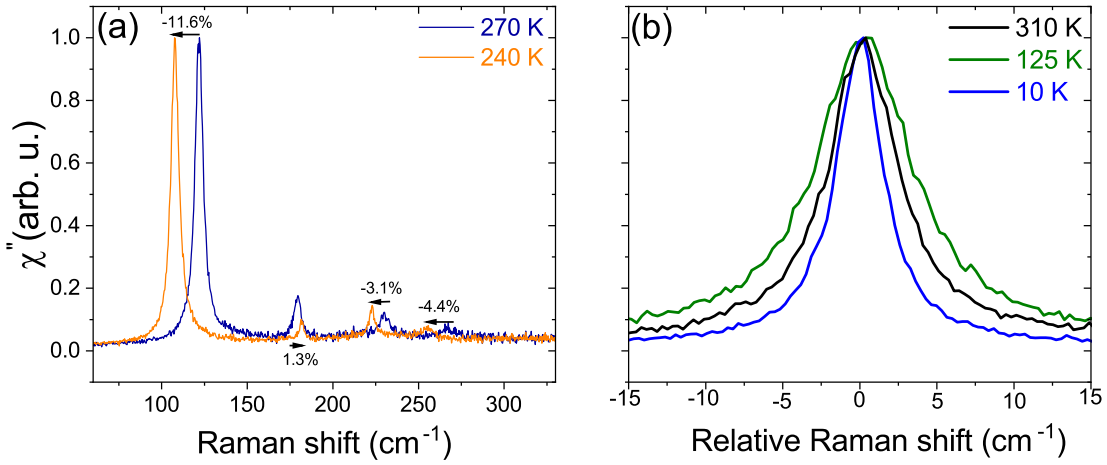

Figure 4.13.: (a) Raman spectra of CrAs measured in the parallel polarization configuration above and below T_N. Black arrows denote the direction of frequency shifts at T_N with relative changes labeled. (b) Overlay of the A_g-1 phonon mode at 310 K, 125 K and 10 K. Curves had been horizontally shifted, for clarity, to enhance the broadening effect reached around 125 K. Data from [8].

Fig 4.13 (a) shows the abrupt phonon renormalization occurring at T_N, reflecting the first-order character of the phase transition. Phonon A_g-1,A_g-3 and A_g-4 exhibit significant softening while the A_g-2 hardens. Phonon frequencies are highly sensitive to volume changes and as CrAs crosses T_N, the unit cell volume expands by approximately 2% [7, 18].

To estimate qualitatively the contribution the contribution of volume variations to the observed changes in Raman shifts, the mode-specific Grüneisen parameter can be defined [52, 89]

$$\gamma_{\text{mode}} = -\frac{\Delta w/w}{\Delta V/V} \tag{4.3}$$

where $\Delta w/w$ represents the relative change in phonon frequency and $\Delta V/V$ represents the relative change in unit cell volume. Applying Eq. 4.3 to the observed behavior of the A_g modes yields the following Grüneisen parameters: $\gamma_{A_g-1} = 5.3$, $\gamma_{A_g-2} = 0.6$, $\gamma_{A_g-3} = 1.4$ and $\gamma_{A_g-4} = 2$. Notably, the anomalous value of γ_{A_g-1} stands out, as it significantly exceeds the typical range - usualy a few units - commonly observed for Grüneisen parameters in semiconducting and metallic system [52, 90, 91].

First-principles calculations corroborate the presence of a strong spin-phonon coupling. When magnetic ordering is forced on Cr atoms, the expected values of structural parameters - particularly those associated to magnetic exchange paths (see Fig. D.1) - show improved agreement with experimental values obtained from single crystal xray diffraction [8, 52]. Sen et al. concluded, based on the analysis of phonon eigendisplacement, that the A_g-1 and A_g-2 phonon modes predominantly modulate the J_{c2} exchange path, which is assumed to be the dominant one [7]. This interpretation helped explain why their calculated phonon frequencies better matched experimental observation when magnetic ordering was included [8, 52].

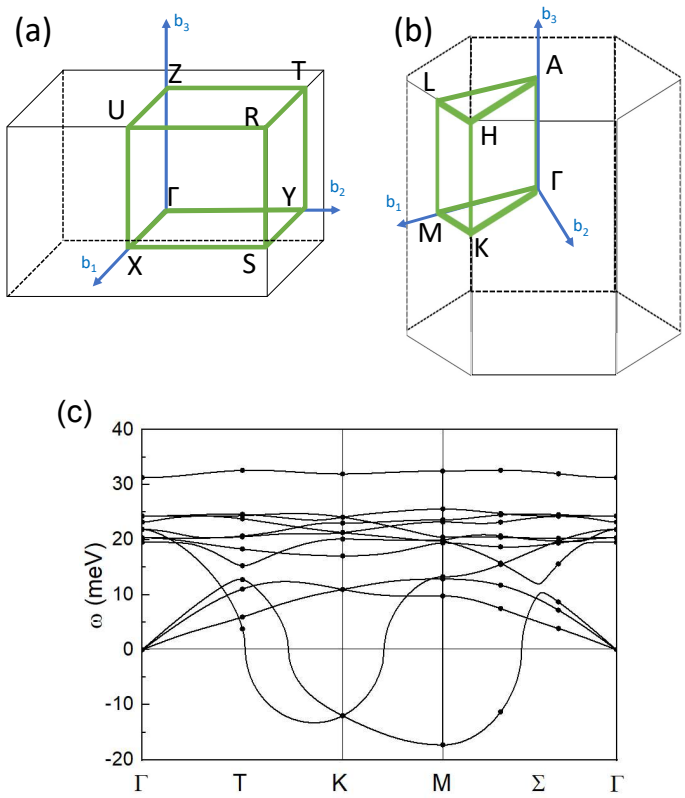

Figure 4.14.: Schematic depiction of Brillouin zones of CrAs and their corresponding high-symmetry points for the (a) orthorhombic P_{nma} and (b) hexagonal $P6_3/mmc$ crystal structures. (c) First-principles calculations of the phonon dispersion relations for the hexagonal phase of CrAs, reproduced from [52].

[7] Based on neutron scattering measurement performed on polycrystalline samples from [7].

Notably, the relative change $(\Delta\omega_{95K-310K})/(\omega_{310K})$ reported by Sen et al. is almost quantitatively reproduced without forcing magnetic ordering on the Cr atoms. In particular, the nonmagnetic calculations tend to overestimate the relative shifts of the A_g-1 and A_g-3, while underestimating those of A_g-2 and A_g-4 [8] The agreement between experimental results with the nonmagnetic calculations suggests that the phonon softening has no magnetic origin [8].

Further insights into the softening of the A_g-1 phonon mode were obtained by Yao through a similar approach to that of Lazewski et al. for MnAs [92], based on phonon dispersion calculations of CrAs in its high-temperature hexagonal phase, shown in Fig. 4.14 (c). In this analysis, the A_g-1 phonon mode observed in the orthorhombic phase appears to originate from the phonon branch associated with the dynamical instability at the M point of the Brillouin zone (BZ) in the high-temperature hexagonal structure. The location of this M point within the hexagonal BZ is shown in Fig. 4.14 (b), alongside the BZ corresponding to the orthorhombic phase in Fig. 4.14 (a) [9]. As the system crosses T_N, the c/b ratio approaches $\sqrt{3}$, bringing CrAs into the pseudohexagonal C_{mcm} setting, as discussed in Sec. 3.3.3. Although this setting retains the same point group as the orthorhombic P_{nma} space group - implying that the same A_g modes remain Raman-active in parallel polarization - Grzechnik et al. have shown that the atomic positions are distorted and closer to the one of the high-temperature hexagonal structure [58]. Therefore, CrAs structure at T_N lies closer to the configuration in which the M point is unstable, resulting in the softening of A_g-1, as the system approaches a geometry where the parent branch of this phonon is lower in energy, leading to a decrease in frequency.

The influence of magnetism is not limited to phonon frequency but also in the behavior of phonon linewidths. At T_N, the phonon renomalization is accompanied by a 50% linewidth reduction for the A_g-2, A_g-3 and A_g-4 modes. The A_g-1 mode displays a different behavior: its linewidth does not change abruptly at T_N and instead continues to broaden until $T \approx 125$K, before narrowing again at lower temperatures, as shown in Fig. 4.13 [52]. The observed decrease in the linewidth of A_g-2, A_g-3 and A_g-4 modes resembles the behavior observed in other magnetic systems such as $BaFe_2As_2$, where a drop in phonon linewidth is attributed to the onset of a spin-density-wave phase [52, 93]. As discussed in Sec. 3.3.1, CrAs shares with iron-based superconductors the increase in magnetic susceptibility, in the paramagnetic state, which is linked to the presence of spin fluctuations. The suppression of these fluctuations below T_N would reduce the scattering channel, leading to a lengthening of phonon lifetime. However, this interpretation does not account for the behavior of the A_g-1 mode, especially considering its sensitivity to magnetism, suggesting that a more complex mechanism might cause the broadening.

4.1.3.2. Magnetic Raman scattering

The two broad excitations observed at approximately 350 cm^{-1} and 1700 cm^{-1} in the parallel polarization configuration were interpreted by Sen et al. as originating from the two-magnon scattering process. Fig. 4.15 shows the emergence of the feature at 350 cm^{-1} and how the temperature-dependent integrated area, in the 150-750 cm^{-1} range, is correlated with the onset of the magnetic phase. Sen et al. interpret the two-magnon scattering process using the Fleury-Loudon exchange mechanism[10]. In this framework, the incident electric field $\mathbf{E}_i$ perturbs the exchange interaction between two neighboring

[8] This trend is preserved in the AFM calculations - even though the A_g-1 is no longer overestimated- while it gets reversed in the FM calculations [52].

[9] This instability has been proposed to drive the transition to the orthorhombic phase upon cooling to T_t. Any possible role of a phonon instability at the K point of the BZ has not discussed [52].

[10] For a detailed discussion on Fleury-Loudon mechanism for magnetic Raman scattering, see [52].

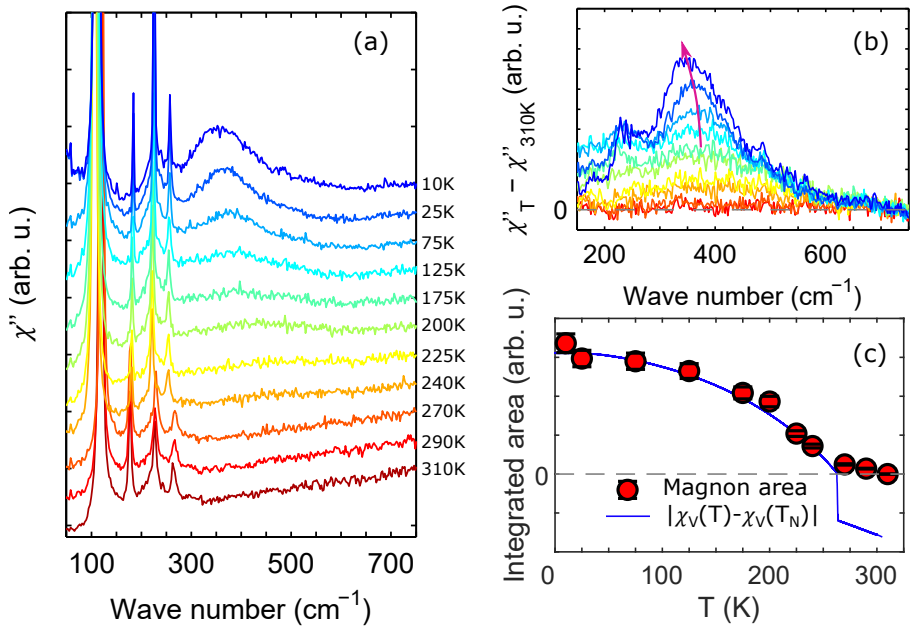

Figure 4.15.: a) Temperature-dependent Raman response of CrAs, measured in parallel polarization configuration. b) Difference spectra obtained by subtracting the 310 K Raman susceptibility from those at lower temperatures, in the spectral range of 150-750 cm^{-1}. c) Integrated area between 150-750 cm^{-1} as a function of temperature, plotted against the shifted magnetic susceptibility $|\chi_v(T) - \chi_v(T_N)|$. Figure from [8].

antiferromagnetically aligned spins. This perturbation brings the system to a virtual intermediate state, modifying the local exchange energy. The system then relaxes to a final state in which both spins are flipped - as required by total spin conservation - leading to the formation of a magnon pair with equal and opposite momenta. As a result, a scattered photon $\mathbf{E}_s$ is emitted with reduced energy, reflecting the cost of the simultaneous spin flip.

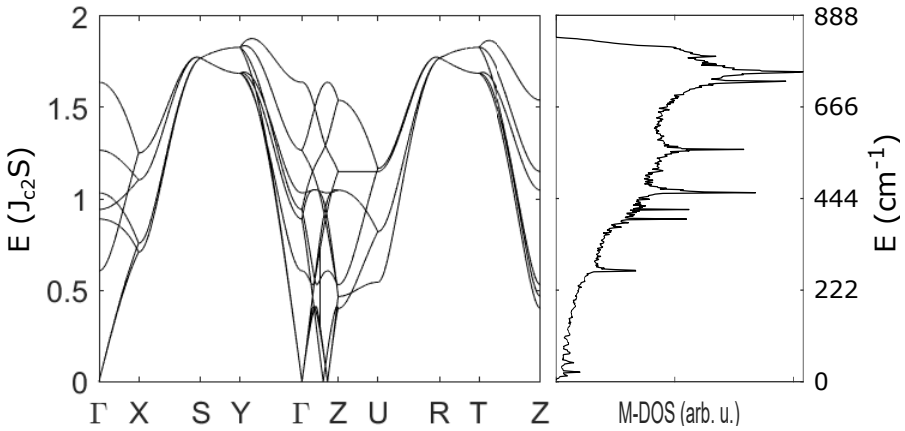

Figure 4.16.: On the left, calculated magnon dispersion in CrAs along the high-symmetry directions of the Brillouin zone, shown in units of J_{c2}. On the right, the corresponding magnon density of states, in units of cm^{-1}. in Figure from [8].

Sen et al. analyze the two two-magnon excitations observed at 350 cm^{-1} and 1700 cm^{-1} by calculating the magnetic density of states (M-DOS) and associated magnon dispersion, as shown in Fig. 4.16. The model was based on a predetermined set of exchange constant ratios (see Sec. 4.1.3.1): $J_{c2}/J_a = 7.1$, $J_{c1}/J_a = -0.5$ and $J_a/J_b = 1.3$ [8].

The resulting M-DOS shows a dominant feature at an energy estimated to be approximately 754 cm^{-1}. Since, this corresponds to the energy of a single magnon, the two-magnon feature is expected near twice the energy, around 1508 cm^{-1}, which is relatively close to the observed feature at 1700 cm^{-1}. However, this model fails to account for the feature at 350 cm^{-1}, suggesting the need of an alternative or extended theoretical interpretation.

4.2. Raman signature of phase coexistence in CrAs

In this section, Raman measurements on CrAs single crystals near T_N = 268 K, as determined from magnetic characterization (see Sec. 3.3.1), are presented with the aim of demonstrating the ability of Raman spectroscopy to detect phase coexistence. Raman spectroscopy offers a direct way of probing the formation of structural or other phase domains [78, 79]. In the case of CrAs and its isostructural phase transition - where domains have same space group but different lattice parameters - the presence of domains could manifest in the Raman signal as doublets or asymmetric peak broadening. The spectroscopic signatures of phase coexistence identified here establish the basis for the analysis presented in the following sections of this thesis, where Raman spectroscopy is employed to investigate phase coexistence in phosphorus-doped CrAs at ambient conditions and in pure CrAs under applied pressure.

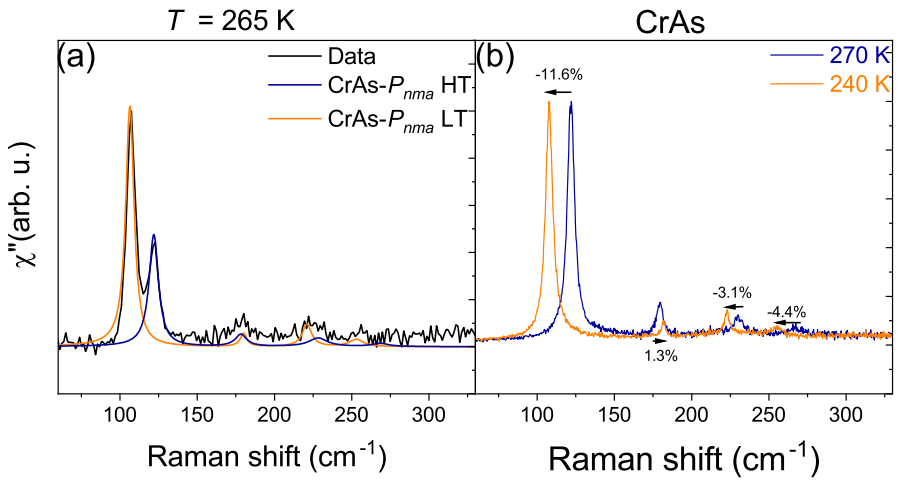

Figure 4.17.: (a)Raman spectrum of CrAs at ambient pressure, measured at 265 K, showing signatures of phase coexistence. The blue and orang curves represent the expected Raman response in CrAs in the non magnetic high-temperature phase and the magnetic low-temperature phase, respectively. The intensities of the reference curves have been arbitrarly scaled to match the experimental data, for visual comparison (b) For reference, the Raman spectra of CrAs in the parallel polarization configuration, measured above and below T_N (see Fig. 4.15), highlight the characteristic phonon profiles of each phase used in panel (a) for comparison.

Temperature dependent Raman scattering measurements were carried out on CrAs single crystals, using the experimental setup described in Sec. 4.1.2.1. The previous Raman study by Sen et al. did not investigate the Raman response of CrAs around T_N [8]. In order to probe the lattice dynamics across the first-order transition, and potentially detecting signatures of phase coexistence, the region around T_N was specifically targeted. To minimize the risk of abrupt cracking or uncontrolled crossing of the transition, the sample was cooled with a controlled rate of $1 - 2$ K/min.

Fig 4.17 shows the Raman spectrum of pure CrAs, at ambient pressure, measured at 265 K. The number of observed phonon modes is higher than expected for a single phase CrAs, in this polarization configuration. By superimposing the Raman responses corresponding to the high-temperature (HT) and low-temperature phase (LT), it is evident that the additional features appear at frequencies characteristic of the LT phase, therefore providing clear evidence of phase coexistence in pure CrAs at the well-established transition temperature (see Sec. 2.3). It is also worth noting that the LT phase component of the A_g-1 mode appears more intense than the HT one, indicating that the probed volume at 265 K is already predominantly in the LT phase. The doublets associated with the A_g-1 phonon mode are the most clearly visible and easily resolved, due to the anomalous softening which affects this mode upon crossing T_N (see Sec. 4.1.3.1.). The A_g-2 mode does not show any clear evidence of splitting; however, this absence may be due to the limited spectral resolution of the 600 gr/mm grating. The A_g-3 mode does show signs of splitting and although the components are not fully resolved, the feature is still detectable. It is less clear whether the A_g-4 mode is actually displaying any splitting due to its relative low intensity and broad linewidth which makes it difficult to distinguish from background noise.

4.2.1. Focus dependence of phase coexistence in CrAs

To evaluate how the observed signatures evolve with the focal conditions of the micro-Raman setup, the Raman coexistence response is examined as a function of the objective position.

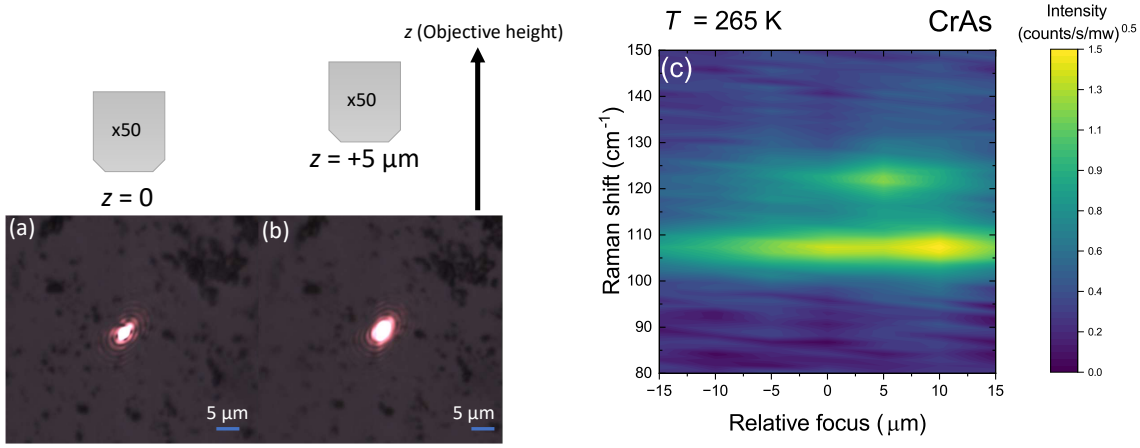

Figure 4.18.: Schematic representation of the focus dependent Raman experiment performed on the surface of a CrAs single crystal using the x50 microscope objective. (a) Optimally focused laser spot at $z = 0$ μm. (b) Slightly defocused laser spot at $z = +5$ μm. (c) Intensity map of Raman spectra in the 80-150 cm^{-}1 range, displaying the focus dependence of the relative intensity of the doublets associated with the A_g-1 phonon mode.

Fig 4.18 (a-b) shows a schematic representation of the focus dependent measurement. The experiment consisted in repeatedly measuring the same spot on the sample at a fixed temperature of 265 K, while systematically changing the relative position of the microscope objective with respect to the sample surface, after each measurement. The vertical displacement of the objective, defined as the z parameter in Sec. 4.1.2.1, was used to control the focal conditions. The position $z = 0$ correspond to the laser spot being optimally focused on the sample surface, as shown in Fig. 4.18 (a). Positive z values indicate that the objective is moved away from the surface (upwards), while negative z values correspond to the objective being brought closer to sample surface.

Fig 4.18 (c) displays the intensity map of Raman spectra in CrAs, focusing on the A_g-1 doublets region, measured at 265 K as a function of the vertical (z) position of the objective relative to the sample surface. As the objective is moved below the optimal focus ($z < 0$) the overall Raman intensity decreases due to beam defocusing but the HT phase contribution vanishes first, as it is the weakest component of the spectrum. When the objective is raised above the surface ($z > 0$), the signal from HT phase increases, with a maximum around 5μm, before decreasing again at larger offsets.

The metallic nature of CrAs implies that, at visible wavelengths, the optical penetration depth is limited to tens or a few hundred of nanometers. While the penetration depth of CrAs has not been reported in the literature, this estimate is reasonable in view of its strong optical absorption typical of metallic systems. As a consequence, the Raman signal predominantly reflects the structural configuration within a near-surface region of the sample. This does not imply that the phase coexistence is only limited to the near-surface region, since these features have been detected with bulk-sensitive methods such as neutron diffraction by Matsuda et al. and NMR by Kotegawa et al. (see Sec. 2.3) [7, 28, 30]. Although the penetration depth constrains the depth from which Raman scattering originates, changing the objective position does shift the confocal plane relative to the sample surface. As a result, the effective sampling volume - while still restricted to a near-surface region - can move slightly closer to or deeper below the surface over lengths scales comparable to the penetration depth, even if the mechanical displacement of the objectives is in the micrometer range. This indicates that the Raman response from the HT phase - in the coexistence region, at 265 K, where the LT-phase signal is overall stronger - in enhanced when the sampling region is closer to the surface.

While laser-induced heating could, in principle, contribute to the formation and stabilization of the HT phase near T_N, this effect is expected to be strongest around the optimal focus ($z \approx 0$), where the surface power density on the spot is highest. The HT phase signal increase at 5μ - with laser defocused and the surface power density is therefore reduced - suggests that the enhancement of the HT phase is unlikely to be only a consequence of local heating. Instead, it supports the interpretation that the HT phase is more prominent in regions closer to the surface and that the change in focal position modifies which part of this near-surface region contributes most strongly to the measured signal. Nonetheless, this does not exclude the possibility that laser-induced heating indeed plays a role in modifying the phase balance. To further investigate the influence of laser-induced heating, Raman spectra were acquired as a function of incident laser power.

4.2.2. Power dependence of phase coexistence in CrAs

Fig. 4.19 (a) shows the Raman spectra of CrAs measured at 266 K under varying incident laser powers. The measurement sequence was designed to mimic a cooling thermal cycle: starting with highest laser power, followed by a five minute waiting period for local thermalization and then measuring the same spot with progressively lower laser power. At the highest laser power used (2.5 mW), the Raman spectrum displays only the HT phase, with no evidence of coexistence. As the power is reduced (0.7 mW), signatures of coexistence begin to appear - on the A_g-1 and A_g-3 - as shown in Fig. 4.17. In the intermediate power range (0.5 mW), changes in the relative intensity of the mode doublets suggest a shift in the volume fraction from the HT phase to the LT phase. This effect is clearly visible in the A_g-1 mode as it has the highest relative intensity, between the allowed phonon modes of CrAs. At the lowest laser power used (0.2 mW), the Raman spectrum shows only features of the LT phase, as the local temperature increase is not sufficient to stabilize any fraction of HT phase.

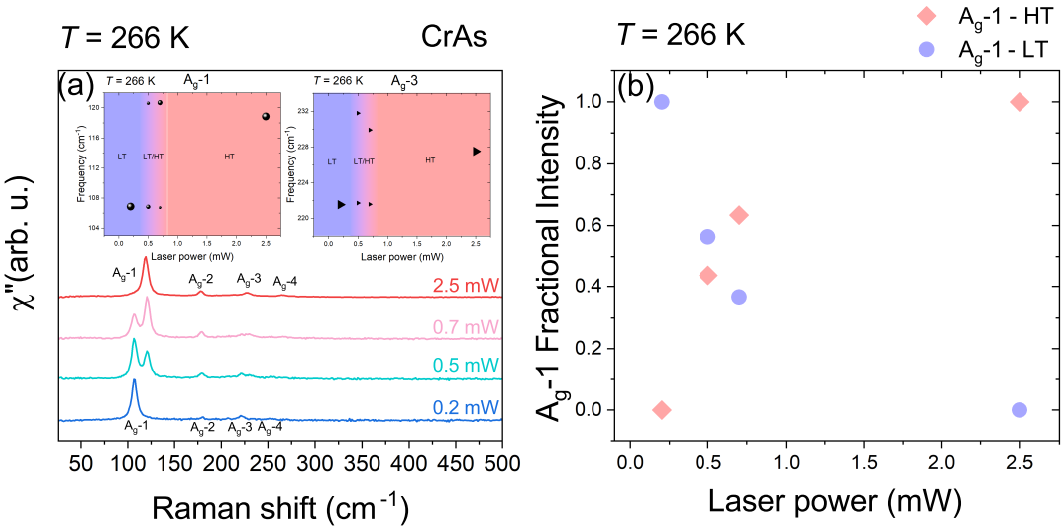

Figure 4.19.: Raman spectra of CrAs measured at 266 K as a function of incident laser power. In the inset, the fitted peak positions of the mode doublets corresponding to the A_g-1 and A_g-3 phonon modes. (b) Fractional intensity of the A_g-1 mode, defined in the main text, as a function of the incident laser power at 266 K.

This progression shows how laser-induced heating can indeed influence the local domain distribution at the sample surface[11]. A visual guide to this effect is shown in Fig. 4.19 through two complementary representations. In the inset of Fig. 4.19 (a), the size of each data point reflects the fractional contribution of the corresponding peak, defined as $I_i/(I_1 + I_2)$, where I_1 and I_2 are the integrated intensities of the two components forming the doublet. In addition, Fig 4.19 (b) display the same fractional intensity plotted explicitly as a function of the incident laser power. Together, these representations offer a way to directly see how one phase grows at the expense of the other, capturing the evolving phase balance.It is worth noting that Fig. 4.17, which shows evidence of coexistence at 265 K, was obtained on a similar CrAs sample using a higher laser power of 0.7 mW.

Fig. 4.20 shows the temperature dependence of the Raman spectra of CrAs, measured at different incident laser powers. The 0.2 mW and 2.5 mW datasets were acquired within the same thermal cycle, while the 0.7 mW dataset was collected during a previous cycle.
The insets in Fig.4.20 show the evolution of the A_g-1 phonon frequency as a function of temperature, for different laser powers. At the onset of the phase coexistence, the relative frequency shift $(\omega_{LT} - \omega_{HT})/\omega_{HT}$ decreases systematically with the increasing laser power. Notably, the temperature at which the onset of coexistence becomes detectable is close to the bulk T_N, suggesting that the effect is due to the local temperature gradient between the surface and the bulk. As laser power increases, the HT phase stabilized at the surface is at a higher temperature, while the underlying bulk remains at in the LT phase.

Because the A_g-1 phonon in the HT softens with increasing temperature, as reported by Sen et al. [8], the frequency separation between the two components of the doublet decreases at the onset of the coexistence. The A_g-1 phonon frequency at 0.7 mW in the LT phase differs from that at 0.2 mW and 2.5 mW, which where measured in the same thermal cycle. This suggests the presence of small offsets between thermal cycles, as no offset temperature correction were applied.

[11] Penetration depth is not affected by laser power.

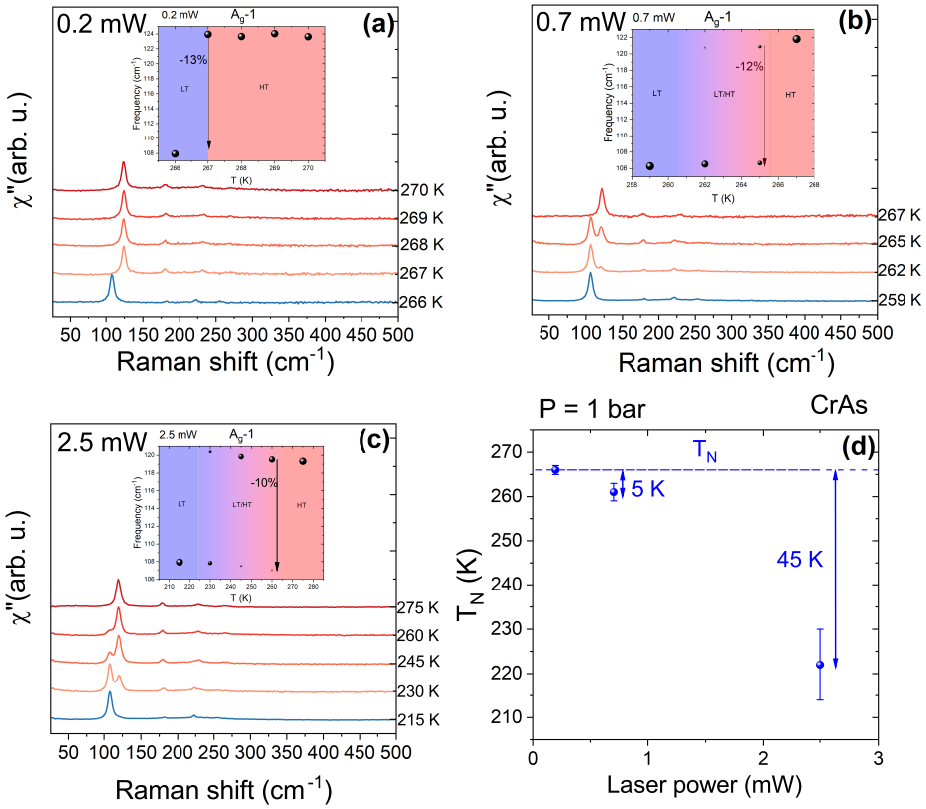

Figure 4.20.: (a-c) Temperature dependent Raman spectra of CrAs measured with incident laser power of 0.2 mW, 0.7 mW and 2.5 mW, respectively. Insets show the fitted A_g-1 peak positions as a function of temperature, highlighting the onset of phase coexistence. Black arrows indicate the relative frequency shift $(\omega_{LT} - \omega_{HT})/\omega_{HT}$ at the onset of the coexistence. (d) Apparent transition temperature as a function of incident laser power, defined as the average between the temperature at which the HT phase component is no longer detectable and the preceding temperature step.

However, this difference in thermal history does not affect the relative temperature trends observed within each cycle. This consistency is also reflected in Fig. 4.20 (d), which shows the apparent transition temperature, as a function of laser power. At the lowest power (0.2 mW), the transition at 266 K detected by Raman coincides, within experimental error, with the bulk T_N obtained from thermodynamic measurements in Sec. 3.3.1, demonstrating that laser induced heating is negligible. This makes the use of the lowest laser power essential for accurately probing the transition temperature via Raman spectroscopy. As the lower power increases, the temperature required to fully stabilize the LT phase at the probed spot shift down by about 5 K at 0.7 mW and by about 45 K at 2.5 mW, compared to the bulk T_N determined from thermodynamic measurements.

Fig. 4.21 shows Raman spectra measured at 266 K, with 0.2 mW laser power, on two distinct spots of a CrAs single crystal, measured within the same thermal cycle. Despite the use of minimal laser power, both spectra exhibit weak but clear signatures of phase coexistence on the A_g-1 phonon mode. The difference in the relative intensities of the LT and HT components, between the two spots, suggests a varying local volume fraction of the HT phase. This evidence points toward a spatial variation in phase domain structure close to the surface, where the balance between HT and LT phase appears sensitive to local conditions, like strain or domain wall configurations.

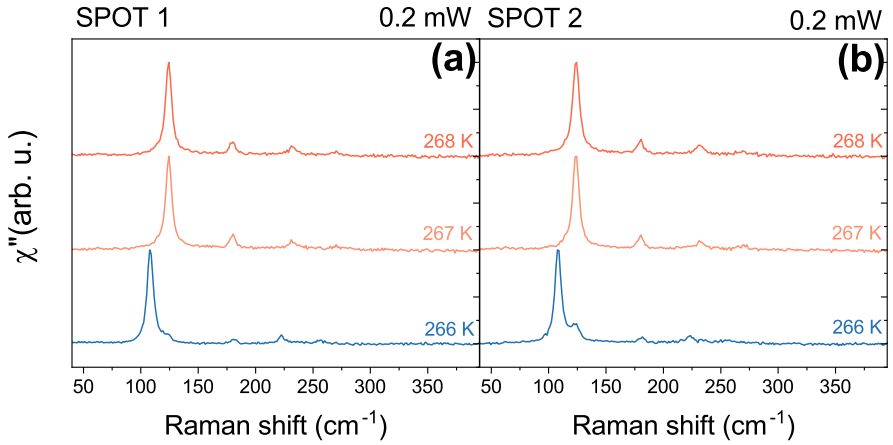

Figure 4.21.: Raman spectra of another CrAs single crystal measured at two distinct surface locations, using 0.2 mW laser power, during the same thermal cycle: (a) spot 1 (b) spot 2. Both spots show signatures of phase coexistence, despite the use of minimal laser power.

Notably, this behavior is not the result of laser induced damage or illumination effects: spots that do not display coexistence at minimal power continue not to show signatures even after repeated thermal cycling or exposure to higher laser powers, up to 2.5 mW, as the spot shown in Fig. 4.19. This spatial sensitivity may be consistent with the domain rearrangement occurring at T_N, as discussed in Sec. 3.1.3 and shown in Fig. 3.4, where CrAs crystals exhibit heterogeneous domain configurations across the transition. These local variations may promote the stabilization of the HT phase, in specific regions, because of the strain accumulated at the interfaces between differently oriented part of the sample. Therefore, selecting the proper measurement spot, as well the proper laser power, becomes critical parameters for reliably detecting phase coexistence and characterizing the structural dynamics of CrAs.

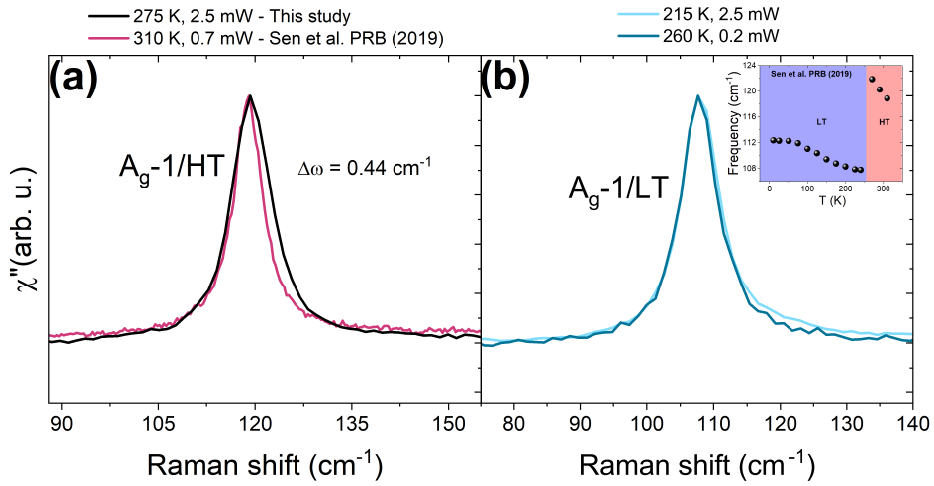

Figure 4.22.: (a) Comparison of Raman spectra focused on A_g-1 phonon in the full HT phase: data from this study (275 K, 2.5 mW incident laser power) and from Sen et al. (310 K, 0.7 mW) [8]. The frequency difference between the two spectra, Δw, is obtained from the fitted A_g-1 peak positions and labeled alongside the spectra (b) Comparison of Raman spectra focused on the A_g-1 phonon in the full LT phase: data from this study (260 K, 0.2 mW) and from a separate thermal cycle (215 K, 2.5 mW). The inset shows the A_g-1 phonon frequency of CrAs from [8].

Different Raman thermometry considerations can be applied in order to quantify the amount of local heating induced on the surface, which is also important for applying a proper Bose correction to the Raman spectra at higher laser powers[12]. In particular, a well-established dependence of phonon frequency on temperature or laser power can provide a reliable way to estimate the local temperature at the probed spot [94]. The experimental configuration used in this study did not allow for direct measurements of either absorbed or reflected laser power. Instead, the temperature dependence of the A_g-1 phonon frequency - chosen for its high relative intensity - was used to estimate the local temperature at the spot, based on the reference data from Sen et al. [8].

Fig. 4.22 (a) compares the A_g-1 phonon in the full HT phase, measured at different combinations of temperature and laser power. The small mismatch in phonon frequency observed at 275 K with 2.5 mW, compared to the frequency value reported by Sen et al. at 310 K with 0.7 mW, implies that the local temperature at the probed spot is slightly lower than 310 K. This follows from the fact that the A_g-1 mode softens monotonically with increasing temperature in the HT phase (see inset of Fig. 4.22 (b)) [8]. By extrapolating their temperature dependence, the frequency we observe at 275 K with 2.5 mW correspond approximately to that expected at 305 K with 0.7 mW laser power. Therefore, in the HT phase, a laser power of 2.5 mW induces a local temperature increase of approximately 25-30 K[13]. The broader linewidth observed with 2.5 mW is a consequence of the different gratings used in the two experiments: 1800 gr/mm in Sen et al., and 600 gr/mm in this study. Nevertheless, since the instrumental resolution affects only the linewidth and does not shift the peak position, the phonon frequency remains directly comparable between the two measurements. Fig. 4.22 (b) shows a comparison of the A_g-1 phonon in the full LT phase from two different thermal cycles: one measured at 215 K, with 2.5 mW, and the other at 260 K, with 0.2 mW. The matching frequencies suggest a similar local temperature rise of 40-45 K because of the 2.5 mW. A comparable ΔT is also observed in the LT phase down to 200 K, as shown in Appendix Fig. C.2, further supporting this estimation.

These estimates of local ΔT can be used to gain insight into the heat dissipation properties of CrAs. Raman thermometry offers a reliable approach for estimating the thermal conductivity of a sample, by combining measurements of phonon frequency shifts together with laser absorption coefficient, reflectivity, into proper thermal transport modeling [95]. While a quantitative extraction of thermal conductivity from our data is not feasible due to the lack of these parameters and simulation tools, the observed power-dependent heating effects, together with the phonon modes temperature dependence, offer useful qualitative insights.
In particular, the larger temperature increase observed in the LT phase compared to the HT phase suggest that the thermal conductivity of CrAs is reduced below T_N, since lower κ leads to less efficient heat dissipation and stronger local heating. This result is consistent with the thermal conductivity measurements by Hu et al. on polycrystalline CrAs [51], which shows a pronounced drop around 265 K[14]. A more detailed qualitative evaluation and modeling of thermal conductivity is carried out in Sec. 4.4, based on the power dependence of phonon frequencies in $CrAs_{1-x}P_x$ single crystals, for different temperatures.

[12]Unless otherwise specified, the temperature chosen for the Bose correction at higher laser power is based on the temperature dependence of the A_g-1 frequency from [8].

[13]As discussed earlier, 0.7 mW laser power also induces a heating effect, increasing the spot temperature of $\approx$ 5 K, compared to the lowest power (0.2 mW), in the HT phase, as shown in Fig. 4.20 (d). This suggests that 275 K with 2.5 mW corresponds approximately to 300 K with 0.2 mW

[14]Notably, the drop in thermal conductivity occurs at a higher temperature than the structural transition they report (235-240) K which differs from typical literature values.

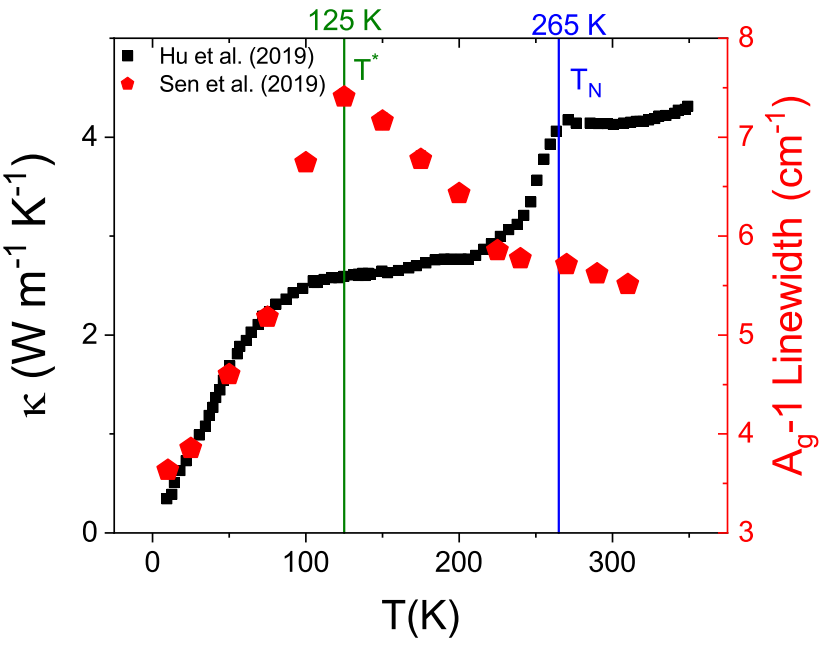

Figure 4.23.: Comparison between the temperature dependent thermal conductivity of polycrystalline CrAs, digitized from Hu et al. [51], and the A_g-1 phonon mode linewdith of CrAs single crystal, from Sen et al. [8] The blue line represents the Néel temperature (T_N = 265 K), while the green line represents the temperature at which the A_g-1 linewidth reaches its maximum broadening.

Fig. 4.23 shows a comparison between the temperature dependence of thermal conductivity in polycrystalline CrAs, as reported by Hu et al. [51], and the linewidth evolution of the A_g-1 phonon mode in single crystal CrAs, measured by Sen et al. [8]. As discussed in Sec. 4.1.3.1, the narrowing of the A_g-2,A_g-3 and A_g-4 modes below T_N can be attributed by the suppression of AFM spin fluctuations, leading to increased phonon lifetimes. However this interpretation does not account for the anomalous broadening of A_g-1 mode below T_N. While strain-driven scattering from structural phase coexistence could contribute near the transition[15], it can not explain the maximum linewidth observed around 125 K, where coexistence is no longer detectable.

Notably, this temperature range aligns with two distinct phenomena previously unlinked. First, the emergence of a well defined magnon peak in the Raman spectrum, which becomes sharply resolved between 175 K and 125 K (see Fig. 4.15), supporting the notion of the strong magnetoleastic coupling in the system. Second, the inflection point in the thermal conductivity curve of CrAs, shown in Fig. 4.23, which may reflect the onset of a real microscopic damping mechanism.
Recent work by Riffe et al. [96] showed that, in complex rare earth oxides, broadening and redshifting of zone-center optical phonons correlate with a reduction in thermal conductivity, due to the presence of local bonding distortions. In CrAs a qualitatively similar trend is observed, though the microscopic origin is probably different. The broadening of the A_g-1 phonon between T_N and 125 K may reflect enhanced damping of optical phonons due to spin-phonon interaction, possibly linked to the emergence of magnons. This also corresponds to the soft linear suppression of thermal conductivity, in the same temperature range, suggesting a correlation between optical phonon damping and heat transport.

[15]This effect is not observed in the A_g-3 mode - despite it also shows signatures of phase coexistence - suggesting that it's indeed related to the coupling to the dominant exchange interactions mentioned in Sec. 4.1.3.1 and D.

However, below 125 K this correlation breaks down: the A_g-1 linewidth narrows sharply, while the magnon intensity increases and the thermal conductivity continues to decrease, even faster than before. This behavior suggests a shift in the dominant scattering mechanism, possibly with an enhanced phonon-magnon interactions or changes in the phonon dispersion. While the analogy with the work of Riffe et al. [96] must be drawn with caution - as their study focuses on static disorder and room temperature behavior - their findings support the principle that the damping of zone-center optical phonons, when coupled to other degrees of freedom, can significantly impact thermal transport. This perspective could be relevant to CrAs, where thermal conductivity is known to be phonon dominated [51] and spin-lattice coupling is strong [8]. Future studies such inelastic x-ray scattering (IXS) on CrAs single crystals could help clarify whether any hybridization occurs between the acoustic phonons and either optical phonons or magnons.

The results above demonstrate that Raman spectroscopy provides a sensitive probe of phase coexistence in high quality CrAs single crystals, revealing both the expected formation of HT and LT domains near T_N at ambient pressure and the way their relative contributions depend on depth and local heating. Having establish the suitability of Raman scattering for detecting mixed phase behavior, the evolution of the lattice dynamics across the coexistence region under applied physical and chemical pressure can now be examined.

4.3. Raman under pressure

To characterize the pressure evolution of the lattice dynamics in CrAs, high-pressure Raman scattering measurements were performed on CrAs single crystals. These experiments were carried out at Institut Néel, in collaboration with Dr. Marie-Aude Méasson, Dr. Owen Moulding and Dr. Mehdi Frachet. Details of the Raman setup configuration and pressure cell can be found in Sec. 4.1.2.3 and 4.1.2.4. Part of the dataset presented in this work - specifically the measurements at 0.35, 0.5 an 0.7 GPa - was previously acquired by Yao using the same setup and crystals from the same growth batch, enabling direct comparison with the measurements reported here.

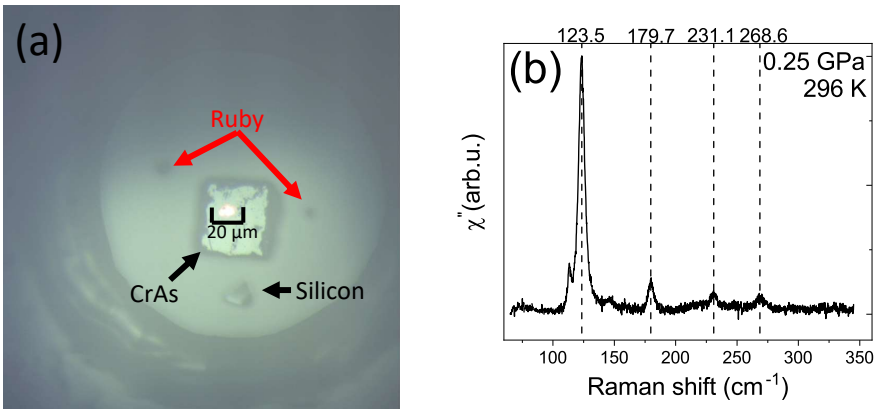

Figure 4.24.: (a) Image of the MDAC gasket cavity containing a CrAs single crystal, together with two ruby samples and silicon sample. The obtained laser spot size is approximately 20 μm, as mentioned in Sec. 4.1.2.3. (b) Raman spectrum at 0.25 GPa of a CrAs single crystal at 296 K. The dashed lines indicate the A_g phonon modes, with their corresponding frequencies labeled above.

Fig. 4.24 (b) shows the Raman spectrum of a CrAs single crystal at 0.25 GPa, measured at room temperature. The A_g phonon modes, highlighted by the dashed lines, show a frequency hardening which is consistent with the application of pressure, in agreement with the volume-frequency relationship outlined in Eq. 4.3. In addition to the A_g modes, a sharp feature is observed around 115 cm^{-1}[16]. The appearance of this additional mode might suggest the phase coexistence scenario. However, this interpretation is excluded thermodinamically: in CrAs, the magnetic transition temperatures lowers under pressure and any phase coexistence is therefore expected to occur at lower temperatures, not at room temperature. Furthermore, pressure inhomogeneities can be ruled out at this stage. As shown in Fig. C.3 (in Appendix C.1) the ruby fluorescence data confirm that the pressure remained homogeneous at room temperature, with shifts and broadening appearing only upon cooling. The presence of this additional feature at 115 cm^{-1} can be attributed to the specific scattering geometry used in this measurement, as described in Sec. 4.1.2.3. The non-normal laser incidence in the used setup modifies the selection rules compared to the ideal backscattering conditions, allowing forbidden phonons to be observed. In particular, based on frequency range and pressure-induced hardening, the mode is consistent with a B_{2g} phonon mode, as reported in [52].

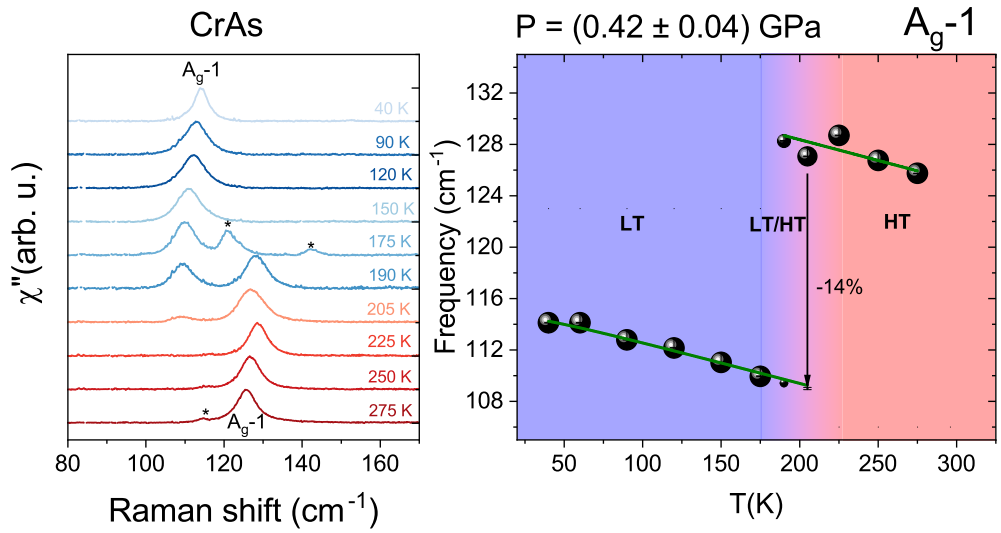

Figure 4.25.: Left: Selected region of CrAs single crystal Raman spectra under pressure, showing the evolution of the A_g-1 phonon mode. Temperature and corresponding pressure values are shown alongside the curves. The asterisk marks additional features unrelated to the A_g-1 mode, as discussed in the main text. Right: temperature dependence of the A_g-1 phonon frequency, at approximately 0.42 GPa. Black arrows indicate the relative frequency shift $(\omega_{LT} - \omega_{HT})/\omega_{HT}$ at the onset of the coexistence. The size of each data point reflects the fractional contribution, as defined in Sec. 4.2.2. The green lines represent fits using the Klemens model, introduced later in the main text [88, 97].

Raman measurement on CrAs single crystal under pressure, as a function of temperature, proved to be particularly challenging. Pressure loss (see Fig. C.3) and sample displacement - likely caused by the enhanced volume expansion, as a function of pressure, as previously discussed in Sec. 2.1.1[17] - (see Fig. C.4) introduced additional uncertainties. These complications affected the ability to measure the full temperature range and led to increased noise in some spectra.

[16]The weaker and broader feature around 145 cm^{-1} appears only in this measurement and is not reproducible, suggesting it is not relevant physically.

[17]The greater the volume expansion, the more mechanical stress accumulates in the sample. Empirically, during temperature-dependent measurements on both CrAs under pressure and $CrAs_{1-x}P_x$at ambient pressure, this stress was released unpredictably at temperatures below their respective T_N, often resulting in sudden detachment or ejection of the sample from the Apiezon glue on the sample holder.

Laser power(mW)	Spot size(μm)	Surface power density (mW/μm^2)
0.2	5	0.01
0.7	5	0.04
2.5	5	0.13
11.2	20	0.04

Table 4.2.: Summary of laser parameters used in the Raman experiments on CrAs and $CrAs_{1-x}P_x$ single crystals at ambient pressure, in Sec. 4.2.2 and 4.4, and on CrAs under applied pressure.

Despite accumulating three consecutives frames of 20 minutes each - for a total acquisition time of one hour per temperature point - the signal-to-noise ratio remained insufficient to resolve the weaker A_g-3 and A_g-4 phonon modes. Their intrinsically low intensity, combined with the high background level of the high pressure Raman measurements led these modes to remain effectively hidden in the noise, preventing a reliable fitting. For these reasons, the discussion on CrAs under pressure will focus on the A_g-1 phonon mode, which remains well-resolved throughout the dataset and provides a reliable probe of both T_N and the phase coexistence. Data on the A_g-2 phonon mode are included in Appendix C.1

Fig. 4.25 shows the Raman spectra of CrAs single crystal under approximately 0.42 GPa, illustrating the evolution of the A_g-1 phonon frequency as a function of temperature. As the sample was cooled, the pressure cell began to lose hydrostaticity - see Fig. C.3 -, resulting in the observation of a pressure gradient within the cell. The pressure values shown in the plot correspond to the average between the two rubies measurements. Fluctuations in the overall pressure were observed during cooling across all pressure measurements. This behavior is likely due to the complex equilibrium dynamics of the membrane-drive diamond anvill cell (MDAC) during changes in temperature.

Upon the application of pressure, the observed T_N - defined as the average between the temperature at which the high-temperature phase A_g-1 is no longer detectable and the preceding temperature step, reported in Tab. 4.3 - is lowering, in agreement with the trend reported on CrAs under pressure. In addition to this shift, the relative frequency change $(\omega_{LT} - \omega_{HT})/\omega_{HT}$ at the onset of coexistence increase with pressure. Moreover, the onset of phase coexistence is also shifted to lower temperatures and the temperature range over which the coexistence occurs is broadened to approximately 30 K, compared to the low power ambient pressure measurements on pure CrAs shown in Fig. 4.20. This is consistent with the broadening of the transition observed by Matsuda et al. and shown in Fig. 2.14, where, for $P \approx 0.35$ GPa, CrAs exhibit a coexistence range of comparable width [7].

The Grüneisen parameter of the A_g-1 phonon was calculated, following the same method of Sen et al. [8]. This was done by calculating the ratio between the relative frequency and volume change across the transition, using temperature steps fully within the LT or HT phases, therefore excluding the coexistence region. The resulting value of $\gamma_{Ag-1} \approx 5.4$ at 0.42 GPa is slightly higher than the $\gamma_{Ag-1} \approx 5.3$ reported for CrAs at ambient pressure by Sen et al.[8]. This behavior is consistent with the effect of pressure in enhancing both the volume expansion at T_N and the relative softening of the A_g-1 phonon across the transition. Specifically, pressure causes a stronger hardening of the HT phase mode, compared to the LT phase mode - see Tab. 4.4 and Fig. 4.31 - resulting in a larger relative frequency change, between the phases. To assess whether the broadening of coexistence and lowering of T_N could be attributed to the induced laser heating, a comparison of the surface power densities used in the Raman measurements of this study is listed in Tab. 4.2. In particular, the surface power density in the high-power 20 μm spot size regime used for the pressure measurements is comparable to that of the intermediate power regime, with a 5 μm spot size used in the ambient pressure experiment, with both corresponding to a surface power density of approximately 0.04 mW/μm^2 .

This suggests that the changes observed under pressure in the evolution of the A_g-1 as a function of temperature can be attributed mainly to the application of pressure on CrAs and that we can neglect the role of induced laser heating. Fig 4.26 and 4.27 show the temperature evolution of Ag-1 phonon at approximately 0.77 GPa and 1.15 GPa, respectively. As previously mentioned, experimental constraints prevented measurements over the full temperature range. For the measurement at 0.77 GPa, data were collected down to 100 K, with no sign of transtion observed in this temperature range. For the 1.15 GPa dataset, measurements extended to 15 K, with no transition observed. This behavior is consistent with the reported critical pressure (P_c) value reported by Matsuda et al. [7] for the suppression of the magnetic phase.

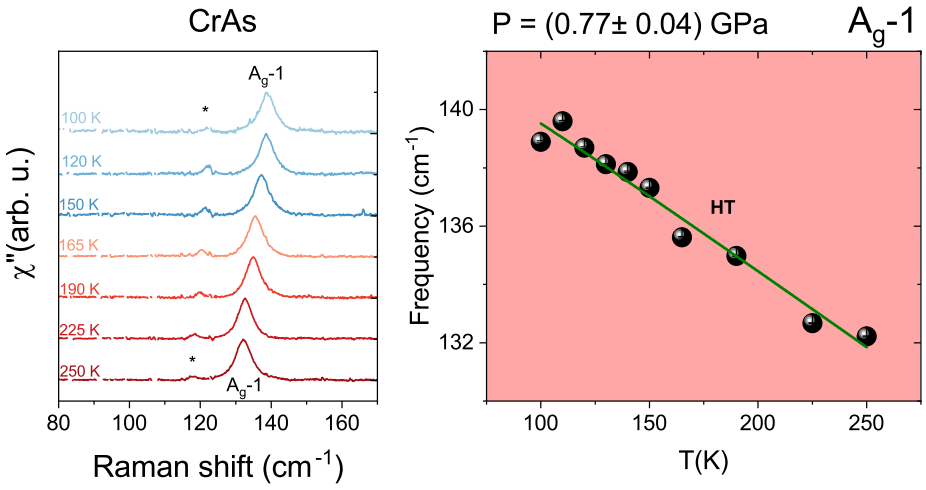

Figure 4.26.: Left: Selected region of CrAs single crystal Raman spectra under pressure, showing the evolution of the A_g-1 phonon mode. Temperature and corresponding pressure values are shown alongside the curves. The asterisk marks additional features unrelated to the A_g-1 mode, as discussed in the main text. Right: temperature dependence of the A_g-1 phonon frequency, at approximately 0.77 GPa. The green lines represent fits using the Klemens model, introduced later in the main text [88, 97].

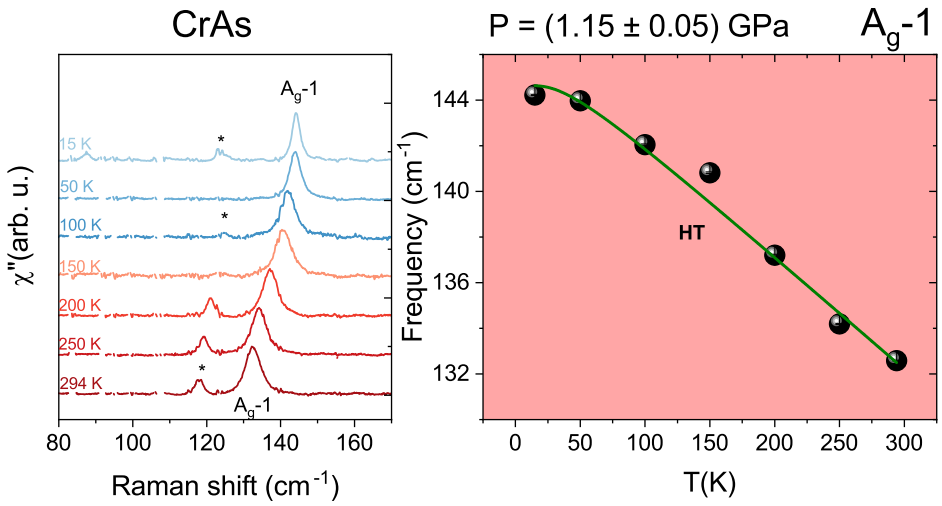

Figure 4.27.: Left: Selected region of CrAs single crystal Raman spectra under pressure, showing the evolution of the A_g-1 phonon mode. Temperature and corresponding pressure values are shown alongside the curves. The asterisk marks additional features unrelated to the A_g-1 mode, as discussed in the main text. Right: temperature dependence of the A_g-1 phonon frequency, at approximately 1.15 GPa. The green lines represent fits using the Klemens model, introduced later in the main text [88, 97].

Pressure(GPa)	T_N(K)
0.42	182 ± 7
0.77	< 100
1.15	< 15

Table 4.3.: Summary of transition temperatures (T_N) of CrAs under pressure, calculated as the average between the temperature at which the HT phase A_g-1 is no longer detectable and the preceding temperature step. For the measurement 0.77 GPa and 1.1 GPa, no sign of the transition was detected above 100 K and 15 K, respectively.

Phase	Pressure (GPa)	ω_0 (cm$^-$1)	A (cm$^-$1)
LT	0	113.52	1.00
LT	0.42	115.97	1.35
HT	0	142.47	3.87
HT	0.42	135.08	1.60
HT	0.77	145.30	2.77
HT	1.15	147.27	2.63

Table 4.4.: Summary of the Klemens model fitting parameters for the A_g-1 phonon in CrAs, extracted for both the low-temperature (LT) and high-temperature (HT) phases at different pressures. Data at 0 GPa are from [8].

Following the approach described by Sen et al. [8], the temperature dependence of the A_g-1 phonon frequency was fitted using the Klemens anharmonic decay model [88, 97]:

$$\omega(T) = \omega_0 - A\left(1 + \frac{2}{e^{\hbar\omega_0/2k_BT} - 1}\right) \tag{4.4}$$

where ω_0 and A correspond to the phonon frequency at 0 K and the anharmonic constant, respectively. The model describes accurately the observed behavior across all pressure measurements - see Fig. 4.26 and 4.27 - without any additional term for thermal expansion of the lattice. This suggests that the dominant contribution to the phonon hardening upon cooling arises from the anharmonic effects. This is consistent with the reported weak temperature dependence of the lattice parameter of CrAs at ambient and under pressure [7, 18, 20]. The extracted ω_0 and A fit parameters are listed in Tab. 4.4. The parameters for the A_g-1 phonon in the low-temperature (LT) phase show a clear increase of both ω_0 and A with pressure, suggesting an enhancement of anharmonic effects upon compression. However, between 0 and 0.42 GPa both ω_0 and A decrease for A_g-1 and A_g-2 (see Sec. C.1) in the high-temperature (HT) phase, indicating a possible reduction in the anharmonicity in this pressure range. At higher pressure (0.77 and 1.1 GPa), ω_0 continues to increase while A remains below the ambient pressure value. Whether this non-monotonic behavior of A in the HT phase reflects an intrinsic feature of CrAs remains unclear. Nevertheless, the overall trend points to a more complex anharmonic response in the HT phase compared to the LT phase, under pressure.

The temperature dependence of the extracted A_g-1 phonon linewidth (FWHM) - here including also the instrumental broadening contribution - was fitted using Klemens anharmonic delay model [8, 88, 97]:

$$\Gamma(T) = \Gamma_0 + C\left(1 + \frac{2}{e^{\hbar\omega_0/2k_BT} - 1}\right) \tag{4.5}$$

where Γ_0 represents the residual linewidth at 0 K and C is an anharmonic costant.

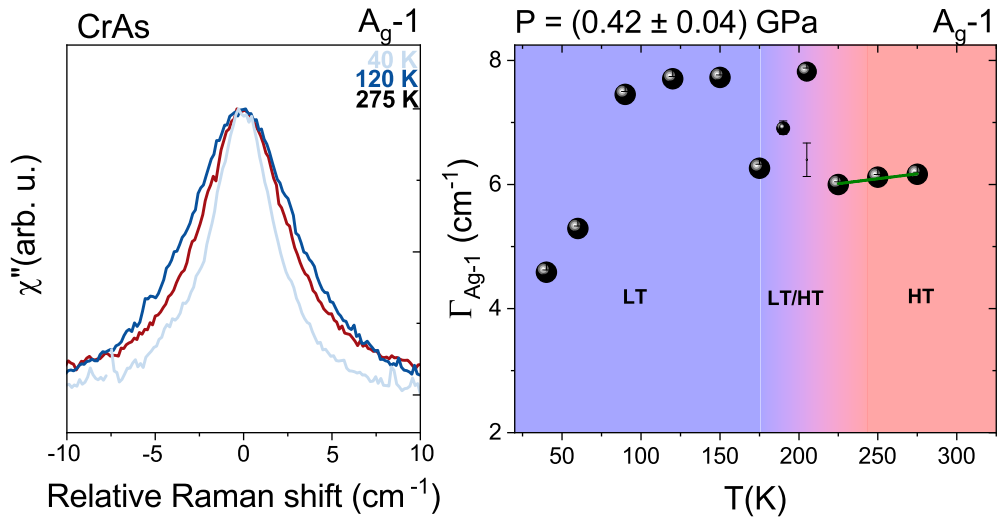

Figure 4.28.: Left: Overlay of A_g-1 phonon spectra of CrAs under pressure, horizontally shifted for clarity. Different temperature and pressures are labeled on top. Right: Extracted FWHM of the A_g-1 phonon as a function of temperature at approximately 0.42 GPa. The green line represents fit using Klemens model [88, 97].

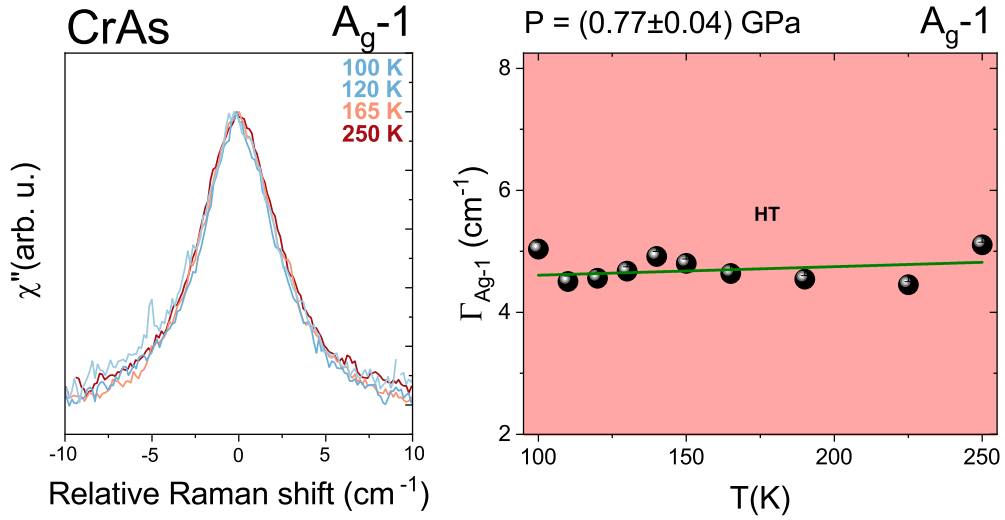

Figure 4.29.: Left: Overlay of A_g-1 phonon spectra of CrAs under pressure, horizontally shifted for clarity. Different temperature and pressures are labeled on top. Right: Extracted FWHM of the A_g-1 phonon as a function of temperature at approximately 0.77 GPa. The green line represents fit using Klemens model [88, 97]. A marked deviation from the model is observed.

Notably, across all pressure measurements, the FWHM - of both A_g-1 and A_g-2 phonons (see Fig C.9) - shows non neglible deviations from the expect trend for both HT and LT phase. Due to this limitation, the fits were only applied over restricted temperature ranges and the extracted parameters are not listed in the main text. For reference, the fit parameters are reported in Appendix C.1. Fig. 4.28 shows the extracted linewidth (FWHM) of the A_g-1 phonon in CrAs under approximately 0.42 GPa, as a function of temperature. The overall trend shows similarities to the reported one for CrAs at ambient pressure [8].

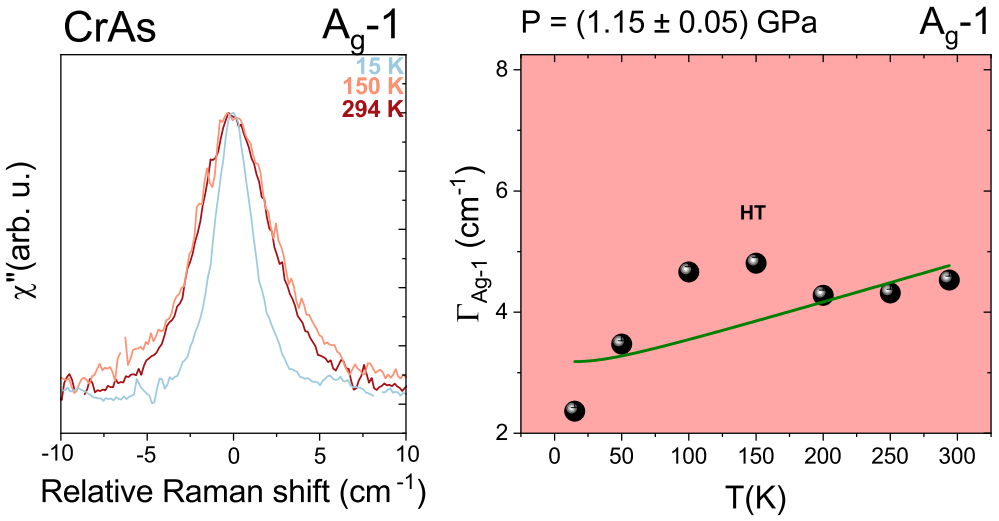

Figure 4.30.: Left: Overlay of A_g-1 phonon spectra of CrAs under pressure, horizontally shifted for clarity. Different temperature and pressures are labeled on top. Right: Extracted FWHM of the A_g-1 phonon as a function of temperature at approximately 1.15 GPa. The green line represents fit using Klemens model [88, 97]. A marked deviation from the model is observed.

However, some notable differences are observed. In the HT phase, the FWHM increases with cooling at ambient pressure, while it decreases in the pressure data (see also Fig. 4.31 for a direct comparison). Within the coexistence region, the FWHM of the HT A_g-1 phonon increases and reached values comparable to those of the LT A_g-1 mode, around 150 K. In this temperature range, the FWHM of the LT A_g-1 mode also displays a non-monotonic behavior. Once entering the full LT phase, the A_g-1 phonon reaches a maximum FWHM around 150 K. This value is comparable to the maximum reported in the ambient pressure data, occurring around 125 K (see Fig. 4.31). Unlike the ambient pressure data, where the FWHM begins to decrease immediately after the maximum, the data at approximately 0.42 GPa show a plateau between 150 K and 100 K, followed by a decrease which matches the trend observed at ambient pressure.

Fig. 4.29 and 4.30 show the temperature evolution of the A_g-1 phonon at approximately 0.77 GPa and 1.15 GPa, respectively. The extracted FWHM values for both pressures appear consistently lower than those observed at ambient pressure or 0.42 GPa. Data at 0.77 GPa, exhibit a substantial scattering in the measured temperature range, preventing the identification of a trend in the FWHM. As shown in Fig. 4.29, the Klemens model fails to describe the behavior and the overlay of A_g-1 phonon spectra between 250 K to 100 K does not reveal any consistent variation between the FWHM. Data at 1.15 GPa (Fig. 4.30) follow a clearer temperature dependence, similar to the one observed for 0.42 GPa. The FWHM decreases between room temperature and 200 K, reaches a maximum around 150 K (lower in absolute value to the 0.42 GPa data) and then shows a narrowing below 100 K. This trend is clearly observable also in the overlaid spectra. As for the data at 0.77 GPa, the temperature dependence deviates from the Klemens model.

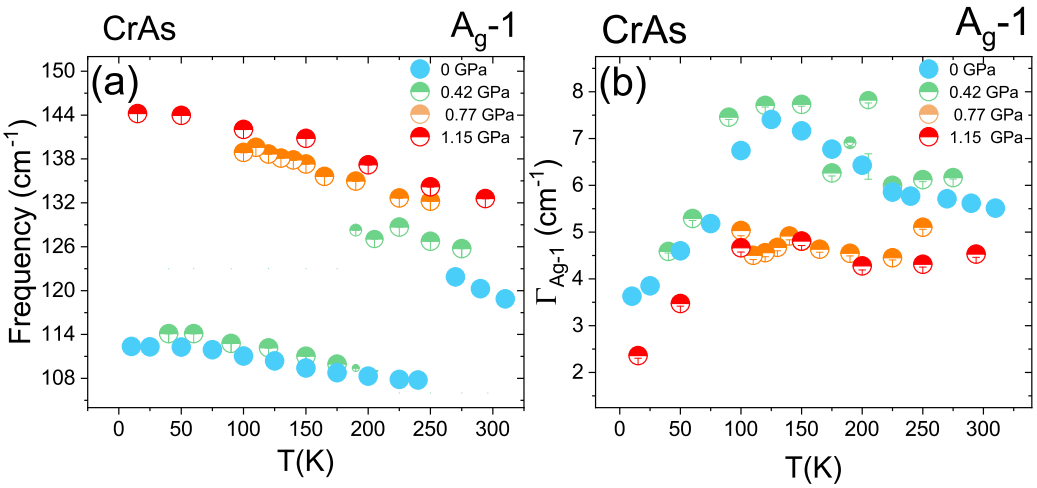

Figure 4.31.: Temperature dependence comparison of the A_g-1 phonon mode in CrAs, at different pressures: (a) phonon frequency (b) FWHM. Data at 0 GPa are taken from [8].

Fig.4.31 summarizes the evolution of both the frequency and the extracted FWHM of the A_g-1 phonon in CrAs as a function of temperature, measured at different applied pressures. In Fig.4.31 (a), the comparison of phonon frequencies shows the lowering of T_N with increasing pressure, until no transition is observed down to 15 K, at approximately 1.15 GPa, consistently with the reaching of P_c observed in literature. Moreover, at fixed temperature, the expected phonon hardening due to lattice compression is observed. In contrast, Fig.4.31 (b) shows more pronounced variations in the FWHM across different pressure. Nevertheless, the temperature evolution of the FWHM remains qualitatively similar between the pressure datasets: except for the 0.77 GPa data - where limited temperature range prevents the identification of a trend - each pressure exhibits a relative maximum of the FWHM.
The plateau region around this maximum appears to broaden in temperature range as the pressure increases, followed then by a narrowing at low temperatures. As noted in Sec. 4.1.3.1, the broadening of the A_g-1 mode at ambient pressure was linked to the appearance of an additional scattering channel associated with the magnetic order, consistent with the spin-phonon coupling and magnon excitations. The pressure dependence of the FWHM provides additional support for this interpretation. In particular, the anomalous broadening observed at low or ambient pressure disappears from 0.77 GPa - where the dataset matches the 1.15 GPa dataset over the common temperature range - indicating that the FWHM evolution originates from spin-phonon coupling rather than from intrinsic phonon effects.

Fig. 4.32 presents a complementary view to Fig. 4.31 to better isolate the pressure dependence of the phonon frequency and FWHM at selected fixed temperatures. In Fig 4.32 (a), clear phase transitions are observed around 250 K at approximately 0.2 GPa and around 150 K and 100 K at approximately 0.5 GPa and 0.6 GPa, respectively. These results are largely consistent with the phase diagram shown in Fig. 3.18. Based on these observations, along with the one listed in Tab. 4.3, an updated version of the phase diagram is presented in Fig. 4.33. Fig. 4.32 (b) shows that, at a given temperature, increasing pressure leads to a clear narrowing of the A_g-1 phonon mode[18] Once pressure reaches approximately 0.7 GPa, the Ag-1 FWHM converges to nearly the same values - at that particular pressure - from room temperature down to 100 K (as shown in Fig. 4.32 (b)).

[18] A similar behavior is observed also for A_g-2, as shown in Fig. C.10 , excluding room temperature, where it is broadening.

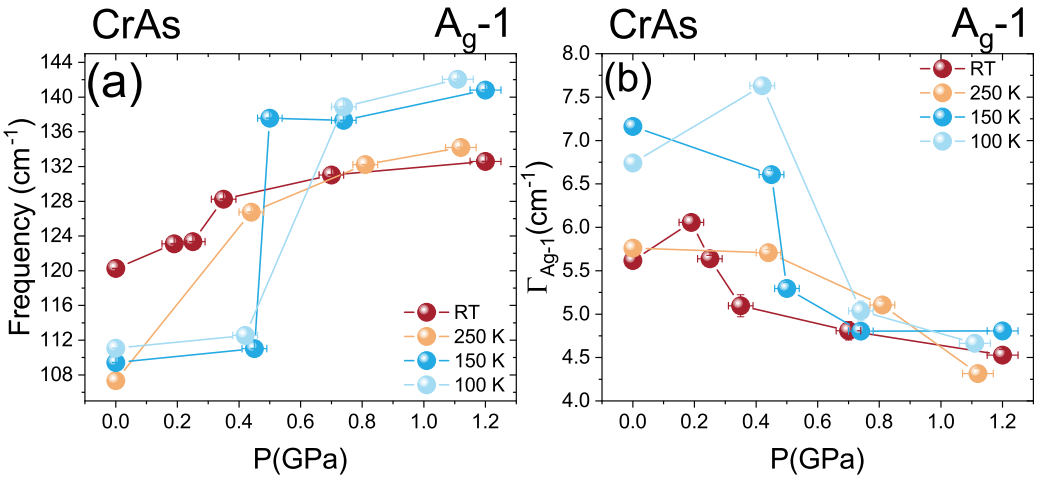

Figure 4.32.: Pressure dependence of the A_g-1 phonon mode parameters in CrAs at selected temperatures: (a) phonon frequency (b) FWHM. Data at 0 GPa are taken from [8]

This suggests that, as the system approaches the critical pressure, antiferromagnetic fluctuations are also suppressed, removing a phonon decay channel, resulting in narrower phonon modes. This interpretation is consistent with our earlier observation of the disappearance of the anomalous broadening around 0.77 GPa (Fig. 4.31) and further supported by the known sensitivity of the A_g-1 mode to magnetism [8, 52].

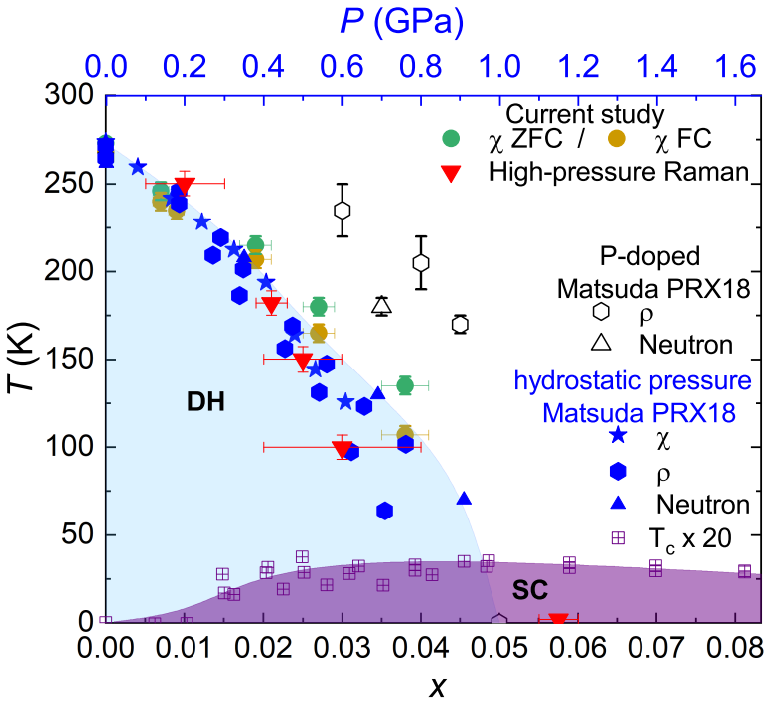

Figure 4.33.: Comparison of pressure-temperature phase diagram of CrAs single crystal under pressure from [7] with the P-doping-temperature phase diagram of $CrAs_{1-x}P_x$single crystals from [7] and from this study, along with high-pressure Raman data on CrAs, in red. DH stands for double helical order and SC stands for superconductivity. The colored regions are provided as visual guides.

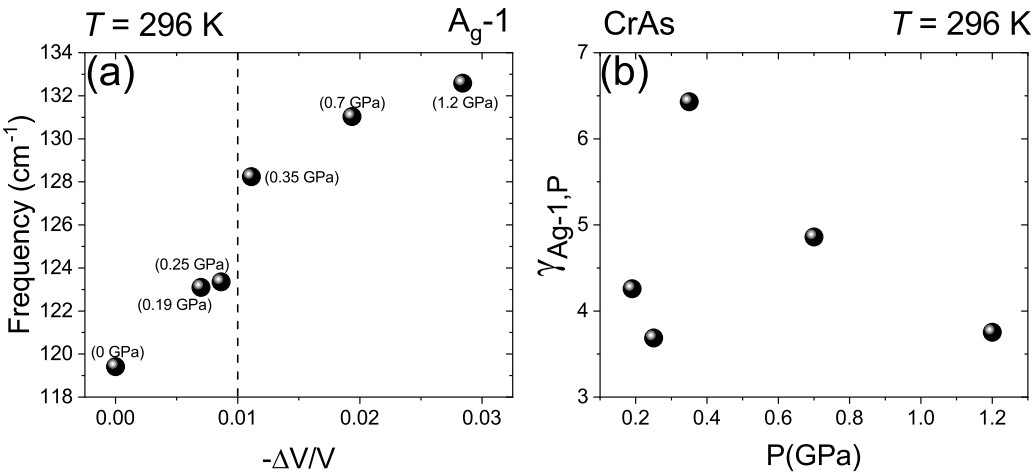

Figure 4.34.: (a) Volume dependence of the A_g-1 phonon frequency at room temperature. Dashed line represent the critical volume (b) Pressure dependence of the Grüneisen parameter for the A_g-1 phonon at room temperature, calculated using the lattice parameter data from [18].

To further evaluate the influence of pressure on the A_g-1 phonon frequency, Fig. 4.34 shows its evolution as a function of the relative volume change $\frac{-\Delta V}{V}$ of CrAs. In Fig. 4.34 (a), the phonon frequency is plotted against the volume compression values corresponding to the different pressures at room temperature, extrapolated from the equation of state from Eich et al. [16, 18]. A clear discontinuity is observed around $\frac{-\Delta V}{V} \approx 0.01$, corresponding to 0.30 GPa. This is also reflected in the pressure dependent Grüneisen parameter $\gamma_{iP} = \frac{-V}{w_i}(\frac{dw_i}{dV})_T$[19], shown in Fig. 4.34, with a pronounced enhancement at the same pressure. In the absence of a structural transition, phonon frequencies should vary smoothly as a function of volume, as expressed by Grüneisen parameter [98, 99]. The observed abrupt hardening of the phonon frequency, therefore suggest a simultaneous collapse in the lattice volume [100, 101]. This behavior is consistent with the pressure-induced isostructural transition proposed by Yu et al. [17], in the 0.18 -0.35 GPa range, where an electronic rearrangement under compression enhances the volume compressibility and drives a sudden volume collapse (see Sec. 2.1.3). Moreover, the magnitude of the inferred volume drop - although extracted from a smooth equation of state [18] - is consistent with the 1% collapse reported by Yu et al. [17]. This interpretation is further reinforced by the similar discontinuity in the A_g-2 phonon mode frequency as a function of relative volume change, shown in Fig. C.11.

A possible quantum critical point has been suggested in a similar pressure range based on transport measurements by Kotegawa et al. [30]. However, as discussed in Sec. 2.2, the reported pressure-temperature phase diagram of CrAs varies substantially between studies and our crystals have not been characterized under pressure by resistivity or magnetization. Therefore, the presence or location of any candidate quantum critical point in our samples can't be established. For this reason, the strong enhancement of the mode-specific Grüneisen parameter near 0.3 GPa is interpreted as evidence of a pressure-induced volume instability consistent with the isostructural transition of Yu et al., rather than as a direct manifestation of quantum criticality. Future measurements, such as single crystal X-ray diffraction under pressure to directly resolve the lattice-volume discontinuity and transport experiments would provide complementary validation and help clarify whether quantum critical behavior emerges in this regime.

[19] Calculated with the same volume values of Fig. 4.34 (a)

The presence of an isostructural transition around 0.3 GPa also provides a natural framework to reinterpret the non-monotonic pressure dependence of the Klemens model parameters reported for the high temperature phase. In particular, the reduction of both ω_o and A extracted at 0.42 GPa (see Tab. 4.4) indicates that these parameters do not simply track a continuous pressure evolution within a single lattice configuration. A volume-collapse-type isostructural transition - together with changes in the underlying microscopic environment - could alter the reference phonon frequency and the available anharmonic decay channels, which may lead to an apparent reduction of ω_o and A just above the transition. In particular, the non-monotonic pressure dependence of A, suggests that additional contributions beyond conventional lattice anharmonicity may play a role and requires further investigation.

Altogether, the pressure dependent Raman measurements presented in this section reveal how hydrostatic pressure reshapes the lattice dynamics of CrAs, strengthening the evidence for pronounced magnetoelastic coupling, providing spectroscopic support for the pressure-induced isostructural transition proposed by Yu et al., and showing the expected pressure-induced widening of the temperature range over which phase coexistence is observed, as reported in previous studies. This provides a reference for evaluating how the same phonon modes respond to chemical pressure introduced by phosphorus substitution.

4.4. Raman on Phosphorus-doped samples

To gain further insights on how chemical pressure affects the lattice dynamics of CrAs, Raman scattering experiments were carried out on $CrAs_{1-x}P_x$ single crystals. Building on the spectroscopic signatures of phase coexistence identified in pure CrAs at ambient and applied pressure, this section investigates how chemical substitution influences the lattice response and the possible persistence or modification of phase coexistence. The experiments used the same configuration and setup described in Sec 4.1.2.1 and 4.1.2.2. The protocol used to process and analyze the data follows the same procedure outlined in Sec. 4.1.2.2. Before discussing the Raman response of the doped samples, it is important to recall that the elemental analysis presented in Sec. 3.2.3 revealed a systematic difference between the phosphorus concentration at the as-grown crystal surface and in the bulk (see Tab. 3.11). Since Raman spectroscopy probes primarly the near-surface region determined by the optical penetration depth, the relevant concentration for the present measurements is the surface value x_{sur}. For clarity, all Raman data in this section are therefore organized and discussed as a function of x_{sur}[20].

Fig 4.35 (a) shows the Raman spectra of the $CrAs_{1-x}P_x$ single crystals measured at room temperature with an incident laser power of 0.7 mW. All four expected A_g phonon modes are clearly observed, confirming that phosphorus substitution preserves the orthorhombic *Pnma* structure and is therefore isostructural. A progressive hardening of the modes is visible with increasing phosphorus content, with the strongest effect observed for the A_g-1 phonon. As discussed in Sec. 2.1.2 and 3.3.3, phosphorus substitution acts as a form of chemical pressure, leading to a reduction of the unit cell volume. According to the mode-specific Grüneisen relation (see Eq. 4.3), a decrease in volume is expected to result in an increase in phonon frequency. A quantitative evaluation of this expected hardening within the volume driven Grüneisen picture is presented below. Fig. 4.35 (b) shows the A_g-1 phonon frequency and linewidth as a function of the surface concentration x_{sur}. The overall evolution is qualitatively consistent with the expected hardening but the data exhibit a noticeable degree of scattering compared to the pressure dependent behavior observed for pure CrAs (see Fig. 4.32).

[20]The corresponding x_{eff} are indicated in parentheses when needed.

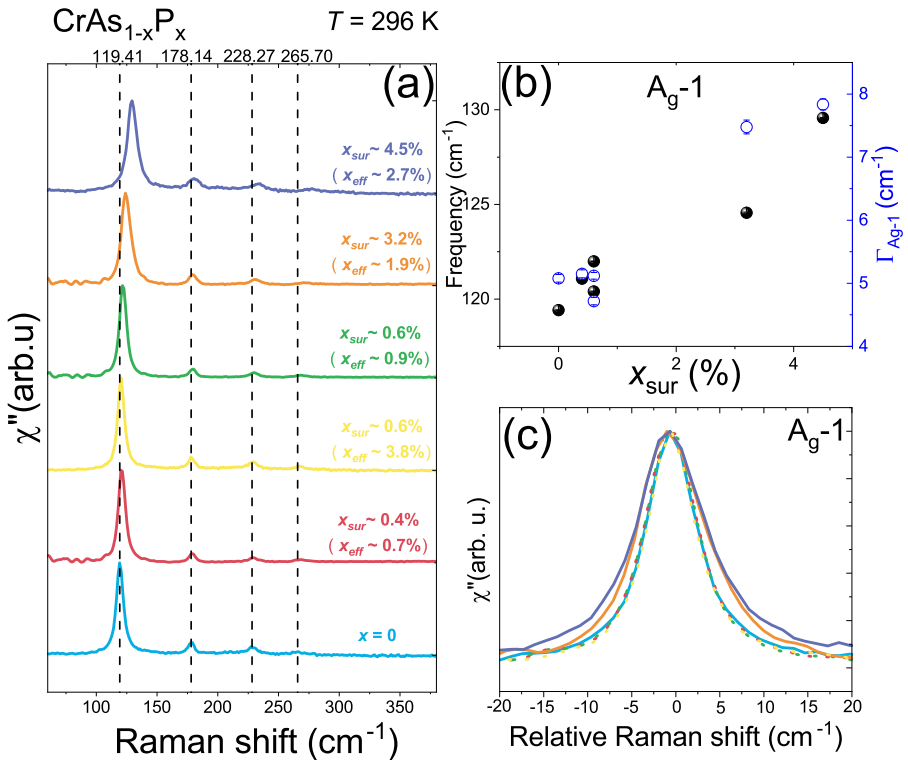

Figure 4.35.: (a) Raman spectra of $CrAs_{1-x}P_x$ single crystals at room temperature, measured in the -z(aa)z configuration with an incident laser power of 0.7 mW. The spectra are ordered and plotted as a function of the phosphorus concentration x_{sur} (defined in Sec. 3.2.3), which is indicated next to each curve. The corresponding effective bulk concentration x_{eff} (also defined in Sec. 3.2.3) is shown in parentheses for reference. The color scheme follows Fig. 3.15. Curves are shifted vertically for clarity, and the dotted line marks the A_g phonon frequencies of the parent compound CrAs. (b) A_g-1 phonon frequency and linewidth as a function of x_{sur}. (c) Overlay of A_g-1 phonon spectra for different x_{sur}, horizontally shifted for clarity. Dotted lines indicate A_g-1 phonons with a linewidth matching that of the parent compound.

A clear example occurs at $x_{sur} \approx 0.6\%$, where two samples show distinct phonon frequencies. This dispersion likely reflects the different areas probed by EDX and Raman spectroscopy. For EDX, a relatively large region (on the order of 10^{-1} mm^2) was chosen to provide a more reliable estimate of the average surface concentration, while the Raman laser spot probes only an area around 20 μm^2. As a result, the actual local phosphorus content at the Raman spot might differ from the nominal x_{sur} measured by EDX[21].

Contrary to the pressure-induced behavior of pure CrAs, the phonon linewidths of $CrAs_{1-x}P_x$ single crystals broaden with increasing doping (A_g-2, A_g-3 and A_g-4 frequency and linewidth are shown in App. C.2). In pure CrAs, the narrowing observed under pressure - particularly near P_c - was interpreted as the weakening of a phonon decay channel associated with the suppression of antiferromagnetic fluctuations and the antiferromagnetic phase itself (see Sec. 4.3). This mechanism can not account for the behavior of the doped crystals: even in batches where the Raman probed spot shows a x_{sur} concentration high enough to suppress the transition (see Fig. 4.37 and 4.38) no pressure-like narrowing is observed. A possible interpretation is that the linewidth broadening originates from doping induced disorder, an effect that is known to be caused by the phosphorus substitution [7].

[21] This consideration applies to all data points, even though most appear to follow the trend.

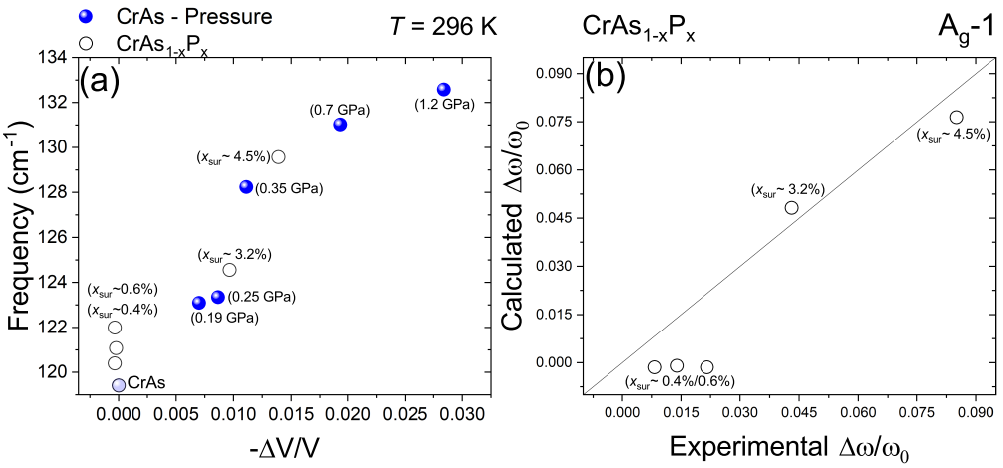

Figure 4.36.: (a) A_g-1 phonon frequency as a function of the relative volume change for CrAs under hydrostatic pressure (see Sec. 4.3) and for $CrAs_{1-x}P_x$ single crystals. (b) Relative A_g-1 phonon frequency change, $\Delta\omega/\omega_0$, calculated using the volume-driven Grüneisen formalism, plotted against the experimentally measured relative A_g-1 phonon frequency change at room temperature. The solid lines have unit slope and indicate perfect agreement between calculated and experimental frequency shifts.

Another contributing factor may be related to spatial inhomogeneity in the phosphorus content within the probed Raman spot, both across the surface and with depth[22]. A further possible interpretation is that doping might enhance the electron-phonon coupling, producing broader and asymmetric phonon lineshapes, similar to those reported in Co-doped $BaFe_2As_2$. [102] Fig. 4.35 (c) shows the overlay of the A_g-1 phonon modes from the $CrAs_{1-x}P_x$ crystals, highlighting the linewidth variation as a function of x_{sur}. The dotted lines indicate A_g-1 phonons whose linewidths match that of the parent compound. In contrast, the A_g-1 spectra for samples with $x_{sur} \approx 3.2\%$ and $x_{sur} \approx 4.5\%$ exhibit a clear asymmetry. However, attempts to model these spectra using a Fano lineshape were unsuccessful, indicating that enhanced electron-phonon coupling is unlikely to be the origin of the observed broadening.
Although the relative contributions of disorder and spatial inhomogeneity can't be unambiguously disentangled, the absence of the pressure-like narrowing, together with the inability to reproduce the lineshapes with a Fano model, suggests that the linewidth evolution of $CrAs_{1-x}P_x$ single crystals is governed by disorder introduced through phosphorus substitution, possibly accompanied by residual compositional variations within the Raman probed volume.

Having established the qualitative evolution of the phonon frequencies and linewidths with phosphorus substitution, the observed phonon hardening is quantitatively assessed to determine whether it can be accounted for by a volume driven Grüneisen description. For consistency with the pressure-dependent analysis of pure CrAs, the quantitative comparison is restricted here to the A_g-1 phonon mode[23]. Fig. 4.36 (a) compares the frequency of the A_g-1 phonon mode as a function of the relative volume change, $-\Delta V/V$, for pure CrAs under hydrostatic pressure (see Sec. 4.3) and for $CrAs_{1-x}P_x$ single crystals. For the $CrAs_{1-x}P_x$ single crystals, the relative volume change as a function of the surface concentration x_{sur} was extrapolated from Fig. 3.20. Two distinct regimes can be identified. At low x_{sur}, the measured phonon frequencies do not follow the pressure induced trend observed for pure CrAs, exhibiting a non negligible hardening despite an essentially negligible relative volume change.

[22] As mentioned in Sec. 4.2.1, the penetration depth of CrAs extends over several tens to a few hundred nanometers. Given the similar metallic character of $CrAs_{1-x}P_x$single crystals and that phosphorus doping acts primarily as chemical pressure, the penetration depth is assumed to be unchanged.

[23] The corresponding comparison for the A_g-2 mode is shown in Appendix C.2.

This behavior may indicate a hardening mechanism that is not purely volume-driven and is instead associated with phosphorus substitution. Alternatively, it may again reflect a discrepancy between the local phosphorus concentration probed by Raman spectroscopy and the nominal surface concentration x_{sur} determined by EDX. In contrast, samples with higher x_{sur} fall directly onto the pressure dependent trend of pure CrAs. While the possible mismatch between the Raman-probed composition and the nominal x_{sur} also applies to these samples, their alignment with the pressure trend suggests that the same transition observed in pure CrAs around 0.2-0.3 GPa is likewise realized in the $CrAs_{1-x}P_x$ single crystals.

To calculate the expected phonon hardening within the volume-driven Grüneisen framework, Eq. 4.3 was employed using the pressure dependent Grüneisen parameter at room temperature extracted from Fig. 4.34. For each data point, the Grüneisen parameter was selected according to its position along the pressure trend in Fig. 4.36 (a), giving $\gamma_{A_g\text{-}1,P} = 4$ for low x_{sur}, and $\gamma_{A_g\text{-}1,P} = 5$ and $\gamma_{A_g\text{-}1,P} = 5.5$ for $x_{sur} = 3.2\%$ and $x_{sur} = 4.5\%$, respectively. The resulting calculated relative phonon frequency changes, $\Delta\omega/\omega_0$, are shown in Fig. 4.36 (b). For the low x_{sur} samples, significant deviations between the calculated and experimentally measured values are observed, consistent with either non volume-driven contributions to the phonon hardening or an uncertainty in the local phosphorus concentration probed by Raman spectroscopy. In contrast, the high x_{sur} samples display very good agreement between calculated and experimental $\Delta\omega/\omega_0$, reinforcing the conclusion that these compositions follow the same volume-driven behavior observed under hydrostatic pressure in pure CrAs[24] .

Overall, these results establish the characteristic room temperature Raman response of the phosphorus doped samples and set the basis for examining how their lattice dynamics evolve upon cooling.

4.4.1. Temperature-dependent Raman scattering in Phosphorus-doped samples

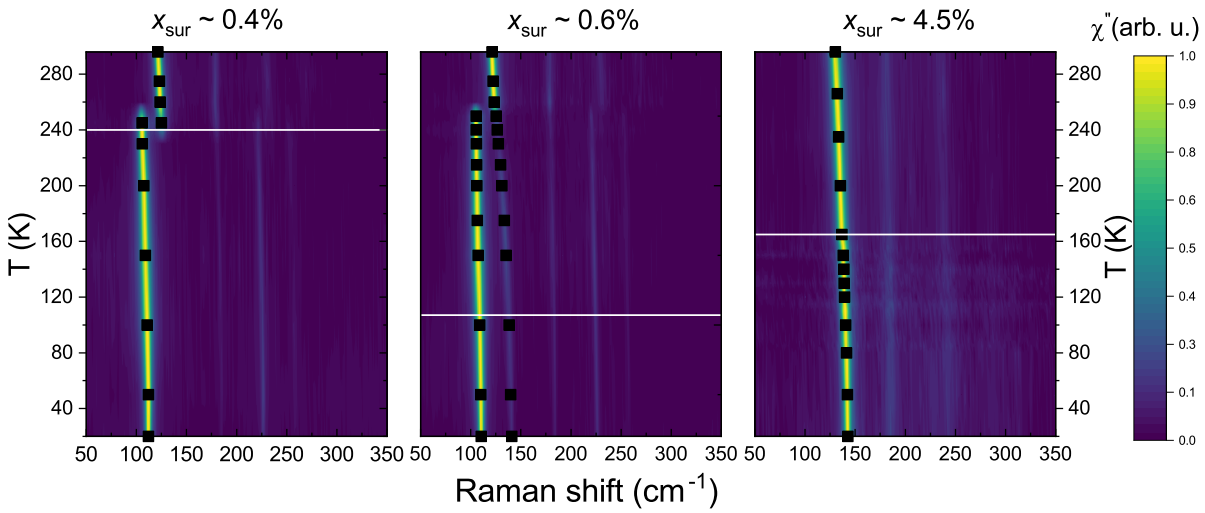

Figure 4.37.: Raman intensity maps of $CrAs_{1-x}P_x$ single crystals spectra (measured with 0.2 mW incident laser power) as a function of temperature, with surface x_{sur} compositions written above. The white lines indicate the T_N of the respective batch, as listed in Sec. 3.3.1. Overlaid scatter symbols represent the fitted A_g-1 phonon frequencies as a function of temperature.

[24] A similar analysis applied to the A_g-2 mode does not yield a comparable agreement with the pressure-dependent behavior, even at higher x_{sur} (see Appendix C.2), indicating that this mode is not predominantly governed by volume-driven effects under phosphorus substitution.

This section focuses on three representative $CrAs_{1-x}P_x$ single crystals batches, selected on the basis of their surface phosphorus concentration x_{sur}, corresponding to low, intermediate and high doping levels. The batches discussed have surface concentrations of $x_{sur} \approx 0.4\%$, $x_{sur} \approx 0.6\%$ and $x_{sur} \approx 4.5\%$, respectively. Fig. 4.37 shows the Raman intensity maps of these $CrAs_{1-x}P_x$ single crystals measured as a function of temperature using an incident laser power of 0.2 mW. This power was chosen to minimize laser induced heating, as discussed in Sec. 4.2.2. The data shown here correspond to cooling measurements. For the intermediate doping level, two batches with $x_{sur} \approx 0.6\%$ were available. In the following, the data correspond to the batch with an effective bulk concentration $x_{eff} \approx 3.8\%$, which is referred to simply as $x_{sur} \approx 0.6\%$.

The Raman response of the $x_{sur} \approx 0.4\%$ and $x_{sur} \approx 4.5\%$ batches is discussed first, followed by a separate discussion of the $x_{sur} \approx 0.6\%$ batch. The $x_{sur} \approx 0.4\%$ batch exhibits a reduced T_N compared to pure CrAs. In addition, with 0.2 mW laser power, the coexistence region - for both the A_g-1 and A_g-3 phonon modes - is detected at lower and broader temperature intervals (245-260 K). Both observations are consistent with the analogy between chemical and physical pressure. In particular, the T_N determined from the Raman data as the average between the first temperature displaying the full LT phase and the previous temperature, as discussed in Sec. 4.2.2, is (238 ± 8) K. This value is consistent with the $T_N \approx 245$ K value obtained by magnetometry (see Sec. 3.3.1), shown as a white line in Fig. 4.37. The agreement between the transition temperatures suggests that, for this low doped batch, any surface-to-bulk doping gradient is negligible on the scale probed by Raman spectroscopy.
The $x_{sur} \approx 4.5\%$ batch shows no transition detectable by Raman down to 20 K. In contrast, magnetometry measurements on the same batch (see Sec. 3.3.1) indicate a transition at $T_N \approx 165$ K, shown as a white line in Fig. 4.37. The absence of any corresponding Raman signatures indicates that, within the Raman probed region, the phosphorus content is sufficiently high to fully suppress the structural and magnetic transition. This behavior further supports the analogy between chemical and physical pressure, indicating that - at least in terms of phonon frequency shifts - this batch effectively reproduces the high-pressure regime on pure CrAs, allowing pressure-like effects to be explored without the application of physical pressure. Notably, as shown in Fig. 4.36, the A_g-1 phonon frequency of the $x_{sur} \approx 4.5\%$ sample lies between the values observed for pure CrAs under applied pressures of approximately 0.35 and 0.7 GPa. However, this correspondence does not extend to the transition temperature: while pure CrAs exhibits a pressure-induced transition near 150 K in this pressure range (see Fig. 4.32), no transition is observed by Raman spectroscopy for the $x_{sur} \approx 4.5\%$ batch down to base temperature. This comparison highlights that, although phosphorus substitution can reproduce pressure like effects on phonon frequencies, the relative volume change alone is insufficient to fully capture the evolution of the magnetic and structural transition. Therefore, this suggest the need for caution when inferring thermodynamic properties solely from volume and phonon based considerations.

The $x_{sur} \approx 0.6\%$ batch displays an anomalous behavior. Below $T_N = (255 \pm 5)$ K, signatures of a possible coexistence between HT and LT phases appear and remain detectable down to 20 K, in contrast to what is observed in other batches or CrAs under pressure. Here, T_N is defined as the average between the first temperature at which coexistence is detected and the preceding temperature step, since the HT contribution does not vanish upon cooling. The unexpected persistence of this coexistence over such an extended temperature range raises questions regarding the nature of the additional phonon. Although polarization-resolved measurements were not performed, several considerations support the classification of the additional peak as the HT A_g-1 mode. First, the hardening values reached by this additional mode are comparable to those of $CrAs_{1-x}P_x$ at higher doping levels or of CrAs under applied P_c (see Fig. 4.39), therefore ruling out poor thermal contact artifacts, even though the detailed temperature dependence differs. Second, this behavior is reproducible across different thermal cycles (see Fig. C.21), measured spots and samples (see Sec. 4.5.1 and Fig. C.15).

x_{sur}(%)	$T_N^{\downarrow}$(K)	$T_N^{\uparrow}$(K)
0	266 ± 2	271 ± 2
0.4	238 ± 8	255 ± 2
0.6	255 ± 5	260 ± 5
4.5	< 20 K	

Table 4.5.: Summary of the Raman transition temperatures upon cooling ($T_N^{\downarrow}$) and warming ($T_N^{\uparrow}$) for $CrAs_{1-x}P_x$ single crystals as a function of the surface phosphorus concentration x_{sur}. Transition temperatures are calculated as the average between the temperature at which the HT phase A_g-1 mode is no longer detected and the preceding temperature step. For the $x_{sur} \approx 0.6\%$ sample, where phase coexistence persists upon cooling, T_N is instead defined as the average between the temperature step at which coexistence first appears and the preceding temperature step. For $x_{sur} = 4.5\%$ sample no sign of transition was detected above 20 K.

While these arguments do not directly establish the microscopic origin of the mode, they provide strong evidence that the observed coexistence involves the HT and LT A_g-1 phonons and that this extended temperature range is an intrinsic feature of this $CrAs_{1-x}P_x$ crystal batch. Within this interpretation, the fact that the extracted T_N for this batch is higher than that of the $x_{sur} \approx 0.4\%$ batch can be naturally explained by a local variation of the phosphorus content at the Raman probed spot, which is likely slightly lower than the nominal surface concentration. This scenario is consistent with the spatial inhomogeneity discussed above.

4.4.1.1. Temperature-dependent Ag-1 phonon evolution in doped CrAs

Transition temperatures upon cooling ($T_N^{\downarrow}$) and warming ($T_N^{\uparrow}$) extracted from Raman measurement performed with an incident laser power of 0.2 mW on pure CrAs (not shown here) and on $CrAs_{1-x}P_x$ single crystals, are summarized in Tab. 4.5. The overall trend of suppression of T_N with increasing phosphorus content is also reflected in the Raman data. For pure CrAs, the transition temperatures extracted from Raman are indistinguishable, within uncertainty, from those obtained by magnetometry, as discussed in Sec. 4.2.2.
For the $x_{sur} \approx 0.4\%$ batch, a clear thermal hysteresis of approximately 17 K is observed between cooling and warming, consistent with the persistence of the first-order nature of the transition (see Fig.C.19). For the $x_{sur} \approx 4.5\%$ batch, no transition is detected above 20 K and thus no hysteresis can be identified within the accessible temperature range. For the $x_{sur} \approx 0.6\%$ batch, the temperature steps used during the measurement do not allow a definitive assessment of the order of the transition (see Fig. C.20), as the transition temperatures obtained on cooling and warming are indistinguishable within the experimental uncertainty. Although the evidence presented above supports the identification of the additional phonon as the HT A_g-1 mode, a more precise determination of the transition characteristics would be essential to assess whether it corresponds to the same transition observed in CrAs or should instead be regarded as a distinct one. As discussed previously, the fact that the $x_{sur} \approx 0.6\%$ sample exhibits a higher T_N than the less doped $x_{sur} \approx 0.4\%$ batch is likely due to a locally lower phosphorus content within the Raman probed volume compared to the average surface concentration determined by EDX.

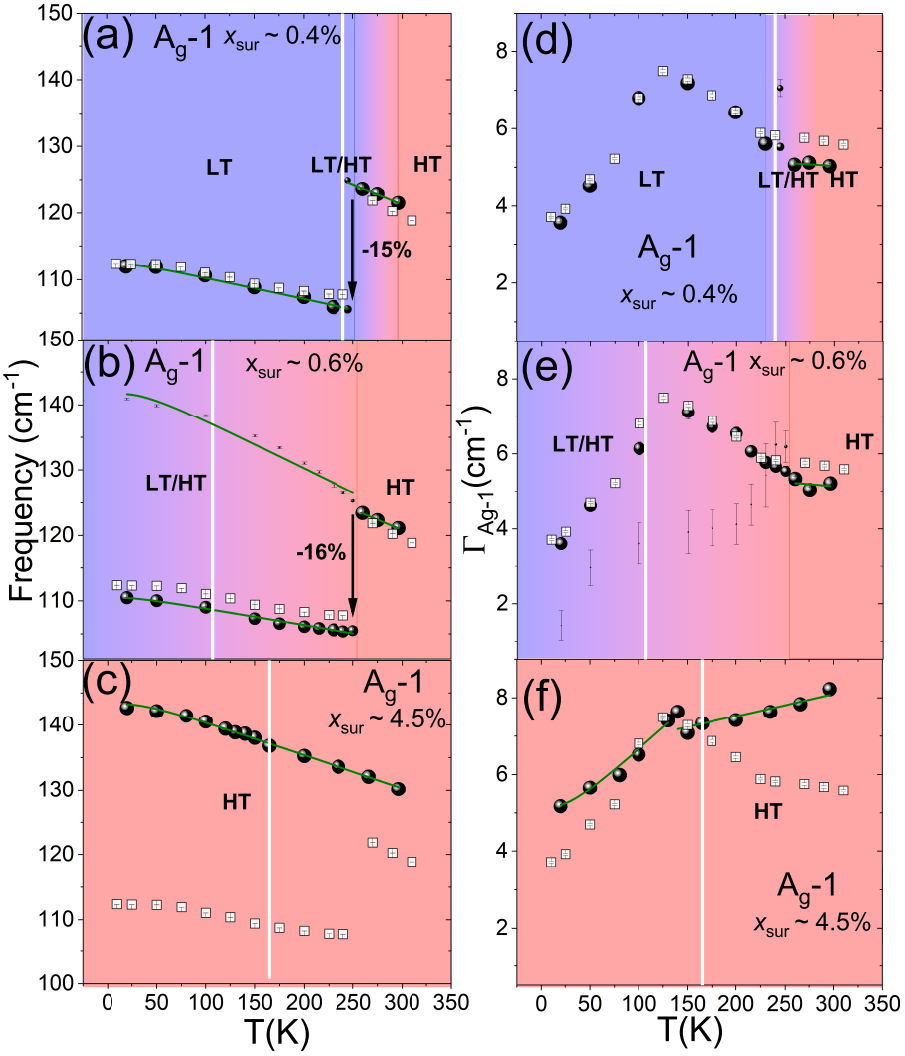

Figure 4.38.: Temperature dependence of the A_g-1 phonon mode parameters in $CrAs_{1-x}P_x$ for $x_{sur} \approx 0.4\%, 0.6\%, 4.5\%$, respectively, measured with 0.2 mW laser power: (a-c) Phonon frequency (d-f) Phonon linewidth. The white lines indicate the T_N of the respective batch, as listed in Sec. 3.3.1. Black arrows indicate the relative frequency shift $(\omega_{LT} - \omega_{HT})/\omega_{HT}$ at the onset of the coexistence. A marked deviation of the linewidth from the Klemens model is observed (green lines). Open squares correspond to A_g-1 data of pure CrAs measured at 0.7 mW, from Ref. [8].

For a clearer comparison between the different A_g-1 behaviors, Fig. 4.38 shows the temperature dependence of the A_g-1 phonon frequency and linewidth for the examined $CrAs_{1-x}P_x$ batches[25] together with reference data for pure CrAs reproduced from [8]. Although the latter were measured using a higher incident laser power (0.7 mW), which may induce additional local heating and therefore affect the absolute phonon frequencies, they still provide a meaningful qualitative comparison for the present discussion, as the focus is on the overall temperature evolution of the phonon parameters.
The temperature dependence is analyzed using the same Klemens framework for anharmonic phonon decay introduced in Sec. 4.3 For the $x_{sur} \approx 0.4\%$ batch, the temperature dependence of the phonon frequency resembles that observed in pure CrAs.

[25]The temperature dependence of the A_g-2, A_g-3, A_g-4 phonon modes for the different $CrAs_{1-x}P_x$ batches is shown in Appendix. C.2.

Interestingly, the relative frequency shift $(\omega_{LT} - \omega_{HT})/\omega_{HT}$ at the onset of phase coexistence is larger than the -14% observed in the 0.42 GPa measurement, despite the higher T_N[26]. However, the linewidth evolution follows a trend similar to that of pure CrAs at ambient pressure - particularly in the plateau region - rather than the behavior observed at 0.42 GPa (see Fig. 4.39).
In the $x_{sur} \approx 4.5\%$ batch, the frequency evolution differs from that of pure CrAs at ambient pressure and instead is comparable to that of pure CrAs near P_c. However, the temperature evolution of the linewidth is distinct from that observed both in pure CrAs and in CrAs under applied pressure near P_c. In particular, the characteristic plateau region is absent and the data instead reveal two distinct temperature regions separated around 145 K. Notably, this temperature coincides not only with the bulk transition temperature T_N (indicated by white line in Fig.4.38), but also with the temperature at which the linewidth of pure CrAs at ambient pressure reaches its maximum. Nevertheless, the absence of any hysteresis in the warming data (see Fig. C.20) rules out a direct connection to the first-order bulk transition. The persistence of these two regimes across different thermal cycles suggests that this behavior is intrinsic to this $CrAs_{1-x}P_x$ batch, although its microscopic origin remains unclear.

The $x_{sur} \approx 0.6\%$ batch exhibits the most pronounced anomaly. Below $T_N = 255$K, the temperature dependence of the A_g-1 frequency changes abruptly. The phonon identified as the HT A_g-1 mode hardens - following a noticeably steeper trend - to values comparable to those observed under high physical pressure or at high phosphorus content. This behavior is also visible in Fig. 4.38, where the frequency evolution deviates strongly from the Klemens model that successfully describes the A_g-1 behavior at high pressure and high doping. Notably, the relative frequency shift at the onset of the coexistence is larger than that observed in all other samples studied so far, whether under physical or chemical pressure. This behavior contrasts with the trend observed under applied pressure, where a larger relative frequency shift is accompanied by a lower T_N. In the present case, despite the larger shift - consistent with a higher effective pressure inferred from the surface doping - the transition temperature is higher than in the $x_{sur} \approx 0.4\%$ batch. This discrepancy, when compared to pressure dependent data on pure CrAs, indicates that the expected relation between effective pressure, T_N and $\Delta\omega/\omega$ no longer holds once chemical substitution is involved. The underlying origin of this behavior remains unclear. The linewidth evolution also shows an abrupt change. The LT A_g-1 mode exhibits a behavior similar to that observed in low pressure or low doping measurements, with a peak and a plateau extending from approximately 200 K down to 100 K. In contrast, the phonon identified as the HT A_g-1 mode displays a distinct temperature dependence: it differs completely from that observed in the $x_{sur} \approx 4.5\%$ batch and after an initial steep decrease, follows a temperature dependence similar to that of pure CrAs near P_c from 200 K down to the lowest measured temperature (see Fig. 4.39).

4.4.1.2. Comparison of Raman response under chemical and physical pressure

Tab 4.6 compares the Klemens model parameters obtained for the A_g-1 phonon in CrAs under pressure and in $CrAs_{1-x}P_x$ single crystals with different surface concentrations x_{sur}[27]. The datasets compared here were acquired using different surface power densities, which influence the extracted phonon frequencies through local laser induced heating (see Sec. 4.2.2 and Sec. 4.4.2).

[26]The relative frequency shift $\Delta\omega$ is expected to scale with the volume expansion ΔV, following from the Grüneisen relation (Eq. 4.3). Since ΔV at T_N increases with pressure [7], a larger $\Delta\omega$, at the onset of the coexistence, should correspond to a higher effective pressure and therefore to a lower T_N.

[27]For reference, the fit parameters of the other phonon modes, including both frequency and linewidth, are reported in Appendix C.2.

Phase	Pressure (GPa) / x_{sur}(%)	ω_0 (cm^{-}1)	A (cm^{-}1)
LT	0 GPa	113.52	1.00
LT	0.42 GPa	115.97	1.35
LT	0.4%	113.66	1.31
LT	0.6%	111.48	1.03
HT	0 GPa	142.47	3.87
HT	0.42 GPa	135.08	1.60
HT	0.77 GPa	145.30	2.77
HT	1.15 GPa	147.27	2.63
HT	0.4%	139.83	3.08
HT ($T > T_N$)	0.6%	140.41	3.26
HT ($T < T_N$)	0.6%	145.63	3.94
HT	4.5%	146.08	2.73

Table 4.6.: Summary of the Klemens model fitting parameters for the A_g-1 phonon in CrAs under applied pressure and $CrAs_{1-x}P_x$ single crystals with different surface concentration x_{sur}. Values are reported for both the low-temperature (LT) and high-temperature (HT) phases. Raman measurements on pure CrAs (ambient pressure and under pressure) were performed using a surface power density of 0.04 mW/μm^2, while measurements on $CrAs_{1-x}P_x$ samples at ambient pressure were carried out with a lower surface power density of 0.01 mW/μm^2. Data at 0 GPa are from [8].

Although this affects the absolute temperature dependence of the phonon frequencies - and therefore the values extracted from the Klemens model - the comparison remains meaningful for assessing the analogy between chemical and physical pressure. In particular, as discussed in Sec. 4.3, the pressure dependence of the A_g-1 phonon Klemens parameters in pure CrAs has been interpreted as an additional signature of the isostructural transition around 0.3 GPa, associated with a renormalization of ω_0 and A. In the LT phase, increasing x_{sur} is accompanied with a decrease in both ω_0 and A, which would suggest a reduction of anharmonic effects with phosphorus substitution. However, for the $x_{sur} \approx 0.6\%$ sample the Raman probed volume is likely characterized by a lower effective phosphorus content than the nominal surface concentration extracted by EDX, as discussed above. Therefore, the comparatively weak change in the LT phase Klemens parameters is naturally accounted for and that apparent similarity to pure CrAs at ambient pressure does not necessarily reflect the nominal x_{sur}. Notably, for the $x_{sur} \approx 0.4\%$ sample the extracted value of A is comparable to that obtained at 0.42 GPa, suggesting that, in the LT phase, chemical pressure reproduces the effect of moderate hydrostatic pressure on the phonon anharmonicity.

In the HT phase, a correspondence with the pressure dependent behavior is observed at low doping. The $x_{sur} \approx 0.4\%$ sample exhibits reduced values of both ω_0 and A with respect to pure CrAs at ambient pressure, indicating a shift of the anharmonic phonon parameters in the same direction as that induced by applied pressure. This similarity suggests that light phosphorus substitution affects the lattice dynamics in a pressure like manner as discussed in Sec. 4.3. However, as shown by the comparison of the phonon frequency as a function of the relative volume change in Fig. 4.36, the pressure-induced transition would be expected to occur at substantially higher phosphorus concentrations. Therefore, variations in the Klemens parameters at low doping should not be interpreted as a reliable signature of a pressure-induced transition under chemical substitution. As the nominal surface phosphorus concentration increases, the interpretation becomes less straightforward. For the $x_{sur} \approx 0.6\%$ sample, both ω_0 and A increase in the HT phase, both below and above its T_N at approximately 255 K. However, the Raman probed volume in this sample is likely characterized by a lower effective phosphorus content than the nominal one extracted by EDX.

Therefore, the apparent non-monotonic behavior of the Klemens parameters can't be directly associated with a systematic evolution as a function of chemical pressure. Instead, the most prominent feature in this intermediate doping regime is the anomalous behavior of the HT phase A_g-1 phonon within the phase coexistence region. In particular, below T_N, the temperature dependence of the phonon frequency deviates from the Klemens model - as shown in Fig. 4.38 - and the extracted value of A captures the steeper evolution only phenomenologically. This behavior suggests that, in the coexistence regime, the temperature dependence of the phonon goes beyond a simple lattice anharmonicity picture, with additional contributions related to disorder and local compositional variations.
Finally, for the $x_{sur} \approx 4.5\%$ sample, the extracted HT phase Klemens parameters approach those obtained for pure CrAs at pressures close to the critical pressure P_c, with an increased ω_0 and a reduced anharmonic coefficient compared to the intermediate doping case. This behavior is consistent with the suppression of long range magnetic order and indicates that, in this limit, chemical substitution reproduces more closely the high pressure in terms of the A_g-1 phonon frequency evolution.

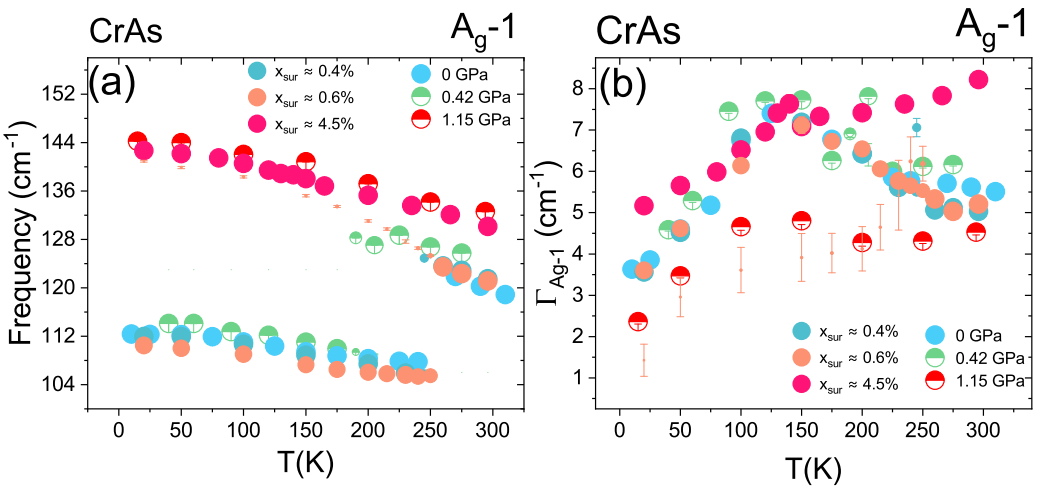

Figure 4.39.: Temperature dependence comparison of the A_g-1 phonon mode in CrAs, at different pressures and dopings: (a) phonon frequency (b) FWHM. Data were measured with 0.01 mW/μm^2 and 0.04 mW/μm^2 surface power densities for $CrAs_{1-x}P_x$ single crystals and CrAs under pressure, respectively. Data at 0 GPa for pure CrAs are taken from [8]. The size of each data point reflects the fractional contribution when coexistence is detected, as defined in Sec. 4.2.2

To summarize the discussion above, Fig. 4.39 provides an overview of the temperature evolution of both the frequency and the linewidth of the A_g-1 phonon in CrAs under pressure and in $CrAs_{1-x}P_x$ single crystals at ambient pressure. The pressure and doping datasets were acquired using 0.04 mW/μm^2 and 0.01 mW/μm^2 surface power densities, respectively. Nevertheless, as discussed in Sec. 4.2.2 and 4.4.2, the resulting differences in phonon frequency and transition temperature are limited to a few kelvin. Therefore, the comparison remains meaningful for identifying qualitative trends associated with chemical and physical pressure tuning.

Fig 4.39 (a) shows the temperature dependence of the A_g-1 phonon frequency. The overall similarity between the temperature evolution of the phonon frequencies in both the HT and LT phases supports the analogy between phosphorus substitution and applied pressure. This correspondence persists regardless of the effective phosphorus content in the Raman probed volume and of the detailed microscopic mechanisms governing the phonon temperature dependence, as discussed above, indicating that the analogy between the chemical substitution and applied pressure is most robust at the level of the phonon frequencies.

At the same time, the comparison highlights a clear exception in the $x_{sur} \approx 0.6\%$ batch, where an additional phonon appears below approximately 255 K and persists down to the lowest measured temperatures. This extended coexistence of HT and LT A_g-1 modes is not observed in other doped batches or in pure CrAs under pressure.

Fig. 4.39 (b) shows the temperature dependence of the A_g-1 phonon linewidth. In the low doping regime, particularly in the LT phase, the linewidth evolution closely resembles that of pure CrAs at ambient or low pressure. In contrast, for the higher phosphorus content the correspondence with pressure data becomes less direct. The $x_{sur} \approx 4.5\%$ batch displays a linewidth evolution that differs from that observed in pure CrAs near P_c, with the absence of the characteristic plateau region and the emergence of two temperature regimes separated around 145 K. The phonon linewidth in the highly doped sample is systematically broader than in the pressure dataset over the entire temperature range, including at low temperature where anharmonic phonon-phonon scattering is expected to be strongly suppressed [88]. This behavior points to the presence of an enhanced residual linewidth contribution, which persists down to low temperatures and can be attributed to static disorder introduced by phosphorus substitution. As a consequence, phonon linewidths - being sensitive to disorder - do not follow the same pressure like trends observed for the phonon frequencies, highlighting a limitation of the analogy between chemical and physical pressure when probed by Raman spectroscopy. Notably, within the extended coexistence regime of the $x_{sur} \approx 0.6\%$ batch, the temperature dependence of the linewidth associated with the additional phonon closely resembles that of the HT A_g-1 phonon in pure CrAs near the critical pressure P_c. The physical origin of this similarity remains unclear.

Overall, the results presented here show that chemical substitution reproduces the main pressure-like trends in the A_g-1 phonon frequency over a broad range of temperature and compositions, supporting the analogy between chemical and physical pressure at the level of lattice dynamics. At the same time, deviations in the linewidth behavior and the emergence of extended phase coexistence highlight the role of disorder and spatial inhomogeneity, which set intrinsic limits to this analogy when probed by Raman spectroscopy.

4.4.2. Thermal conductivity of Phosphorus-doped samples

The Raman measurements on pure CrAs and phosphorus-doped CrAs revealed a pronounced sensitivity to laser induced heating in the parent compound and an extended temperature range of phase coexistence in the doped samples, compared to pure CrAs under pressure. Since laser induced local heating strongly depends on heat dissipation at the sample surface, these observations raise the question of how phosphorus substitution affects thermal transport at the microscale and whether such changes can influence the apparent stability and extent of phase coexistence probed by Raman spectroscopy. In this section, we use power dependent Raman thermometry to qualitatively assess the effective surface thermal conductivity of $CrAs_{1-x}P_x$ single crystals and to evaluate its role in shaping the observed phase coexistence and the limits of chemical pressure analogy.

To directly probe heat dissipation at the sample surface, measurements with different incident laser powers were performed on the $CrAs_{1-x}P_x$ single crystals of the examined batches, in order to mimic a cooling experiment, as described in Sec. 4.2.2. Starting from the highest laser power (2.5 mW), spectra were recorded and, after thermalization, the measurements were repeated at intermediate (0.7 mW) and then at the lowest laser power (0.2 mW)[28]. As in Sec. 4.2.2, the analysis is restricted to the A_g-1 phonon mode, due to its strong intensity and well established temperature dependence [8].

[28]The dataset collected at 0.2 mW are those presented in Sec. 4.4.

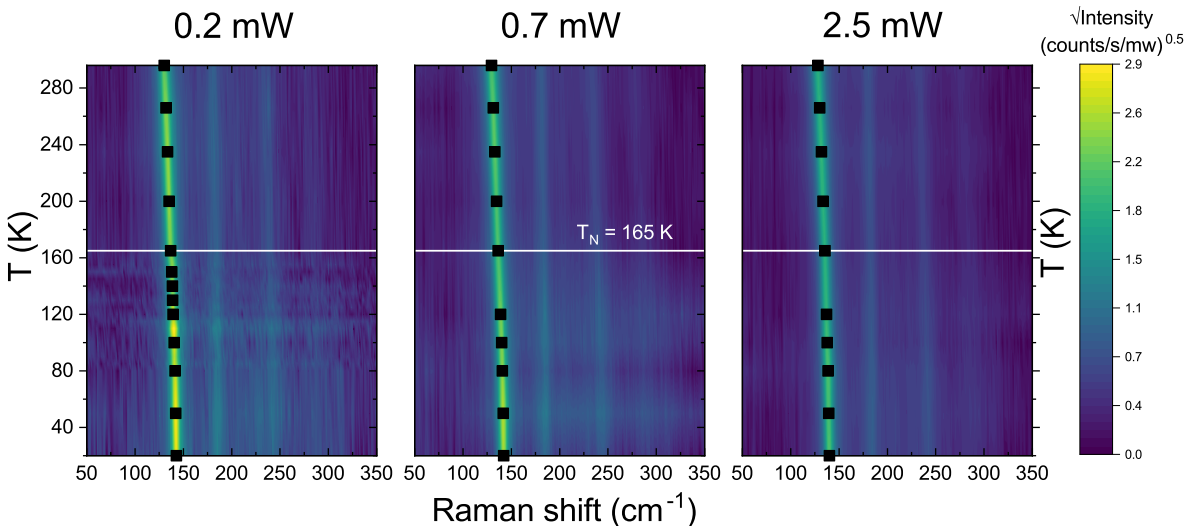

Figure 4.40.: Raman intensity maps of $CrAs_{1-x}P_x$ single crystals spectra ($x_{sur} \approx 4.5\%$) as a function of temperature. The incident laser power used for each measurement is written above. The white lines indicate the T_N of the batch, as listed in Sec. 3.3.1. Overlaid scatter symbols represent the fitted A_g-1 phonon frequencies as a function of temperature.

Fig. 4.40 shows Raman intensity maps of the $x_{sur} \approx 4.5\%$ sample measured under the three laser powers discussed above. At this critical surface phosphorus concentration, no magnetostructural transition is detected within the investigated temperature range (see Sec. 4.4.1), such that the Raman response remains entirely in the HT phase. As a result, the power dependent evolution of the Raman signal provides direct information on the laser induced heating and heat dissipation at the sample surface in the absence of phase coexistence, establishing a reference for the thermal response of the HT phase.

To quantify the effect of laser-induced heating on the A_g-1 phonon and to examine how the magnitude of this heating evolves with temperature, we follow the same Raman thermometry procedure introduced in Sec. 4.2.2. This approach consists in comparing spectra acquired at high incident laser power and low nominal temperature with reference spectra measured at the lowest laser power - where laser induced heating is negligible - and identifying the temperature at which the phonon frequencies coincide. The corresponding frequency shifts used for this analysis are summarized in Fig. 4.43 (a).
Fig 4.41 compares the Raman spectra focused on the A_g-1 phonon in the full HT phase of a $CrAs_{1-x}P_x$ single crystal with $x_{sur} \approx 4.5\%$, measured at different combinations of temperature and incident laser power during cooling in the same thermal cycle. In Fig 4.41 (a), the frequency measured at 20 K with 2.5 mW matches the one obtained at 110 K with 0.2 mW, where laser heating is negligible, implying a local temperature increase of approximately 90 K. Similarly, in Fig. 4.41 (b) the frequency mismatch between spectra measured at 100 K (2.5 mW) and 160 K (0.2 mW) corresponds to a local temperature at the spot of about 158 K, giving a local heating of approximately 60 K. For the higher-temperature cases shown in Fig 4.41 (c) and (d), the frequencies align as in panel (a), giving reduced heating values of approximately 35 K and 30 K, respectively. The overall decreasing of laser induced local heating with increasing temperature is consistent with the behavior observed in pure CrAs (see Sec. 4.2.2). Since heat dissipation at the sample surface is ultimately governed by thermal transport into the bulk, this trend indicates an increase in heat dissipation efficiency at higher temperatures, consistent with the temperature dependence of the bulk thermal conductivity reported by Hu et al. on pure CrAs [51].

When using Raman phonon frequencies as a local thermometer to obtain information on the thermal transport properties of the sample, the interpretation of power-dependent frequency shifts is not straightforward. An increase in incident laser power leads to a local temperature rise at the Raman spot, which in turn shifts the phonon frequency according to its intrinsic temperature dependence.

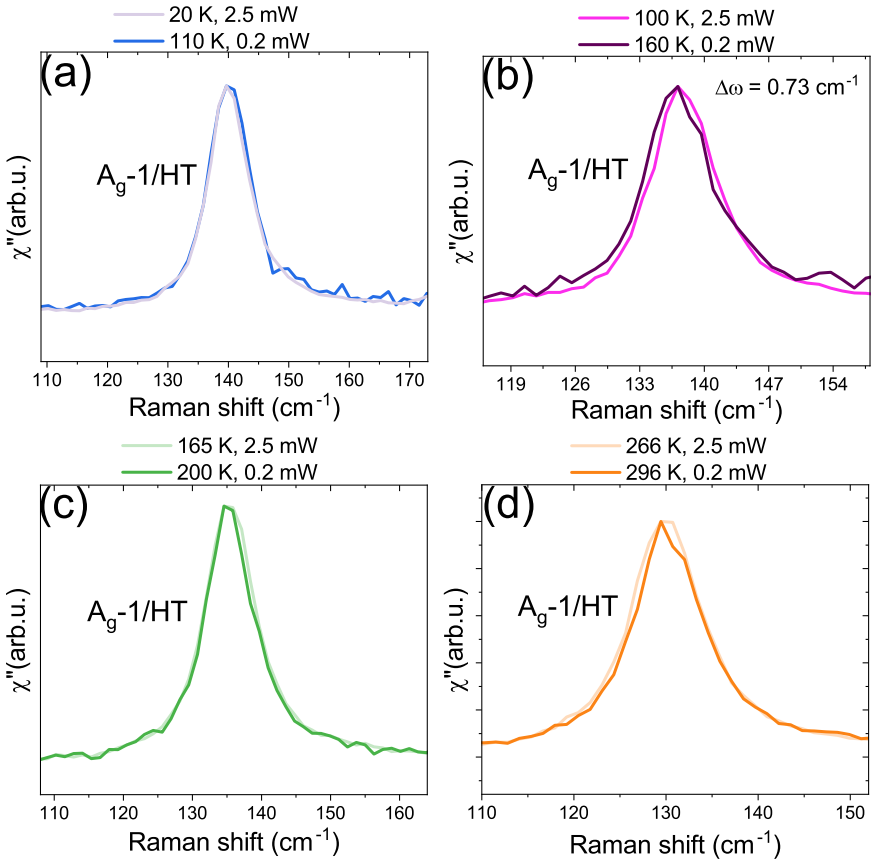

Figure 4.41.: Comparison of Raman spectra focused on the A_g-1 phonon in the full HT phase of a $CrAs_{1-x}P_x$ single crystal with $x_{sur} \approx 4.5\%$. (a) Spectra measured at 20 K (2.5 mW) and 110 K (0.2 mW). (b) Spectra measured at 100 K (2.5 mW) and 160 K (0.2 mW) from a different thermal cycle. The frequency difference between the two spectra $\Delta\omega$, is obtained from the fitted A_g-1 peak positions and labeled alongside the spectra. (c) Spectra measured at 165 K (2.5 mW) and 200 K (0.2 mW). (d) Spectra measured at 265 K (2.5 mW) and 296 (0.2 mW).

As a result, the frequency-power coefficient $d\omega/dP$ alone cannot provide direct information on heat dissipation, since it is influenced by the intrinsic phonon anharmonicity encoded in $\omega(T)$. Therefore, to disentangle these effects it is necessary to relate the power-induced frequency shifts to the independently determined temperature dependence of the phonon frequency. However, as noted in Sec. 4.2.2, even when this procedure is applied, the absence of a proper thermal modeling does not allow for a reliable quantitative determination of the thermal conductivity of these samples [94, 95]. Nevertheless, qualitative information on the temperature dependence of thermal transport can still be obtained from the Raman data. To compare the observed temperature dependence of laser induced heating in a systematic manner, an effective thermal conductivity K_{eff} is introduced following the approach proposed by Fangcheng et al. [95]:

$$K \approx K_{eff} = \frac{d\omega/dT}{d\omega/dP} \tag{4.6}$$

Here, $d\omega/dT$ is the frequency-temperature coefficient of the A_g-1 phonon, obtained from the temperature dependence of the Raman peak position on temperature, while $d\omega/dP$ is the frequency-power coefficient, extracted from the peak position as a function of incident laser power.

This formula provides only an approximation of the real thermal conductivity, since parameters like absorption coefficient, probed volume and local temperature distribution inside the material are not determined in our study. As pointed out by Fangcheng et al. [95], Eq. 4.6 is valid when Raman peak position shows a linear dependence both as a function of temperature and incident laser power. Although the temperature dependence of the A_g-1 phonon in this $CrAs_{1-x}P_x$ single crystal follows the Klemens decay model (see Sec. 4.4) it can be reasonably approximated by a linear trend within the investigated temperature range.

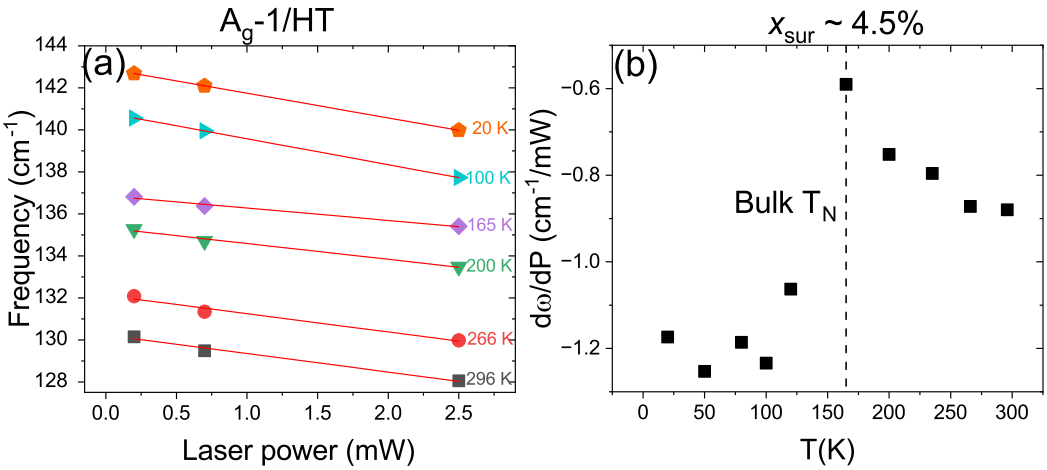

Figure 4.42.: (a) A_g-1 phonon mode frequency dependence on laser power of $CrAs_{1-x}P_x$ single crystal with $x_{sur} \approx 4.5\%$ for selected temperatures. Red lines indicate the best linear fit of the data (b) Temperature dependence of the power coefficient extracted from the linear fit in (a). Dotted line represents the bulk T_N of this $CrAs_{1-x}P_x$ batch, extracted from magnetometry measurements (see Sec. 3.3.1).

The validity of Eq. 4.6 is therefore examined by analyzing the power dependence of the A_g-1 phonon frequency at different temperatures. Fig 4.42 (a) shows the dependence of the A_g-1 phonon frequency on laser power for different temperatures. The frequency shift remains linear with laser power across all temperature range, although the slope, $d\omega/dP$, changes with temperature. Fig 4.42 (b) shows the extracted $d\omega/dP$ coefficients as a function of temperature. The slope increases gradually down to 165 K, at the bulk T_N of this batch - indicated by the dotted line - before decreasing sharply and then remaining approximately constant at lower temperatures.

Having established that the power induced frequency shifts remain linear over the investigated temperature range and having extracted the temperature dependence of $d\omega/dP$, these results can now be combined with the independently determined $d\omega/dT$ to evaluate the effective thermal conductivity defined in Eq. 4.6. Fig.4.43 shows the effective surface thermal conductivity K_{eff} of the $CrAs_{1-x}P_x$ single crystal with $x_{sur} \approx 4.5\%$, obtained from Eq. 4.6 at each measured temperature. Upon cooling from room temperature, K_{eff} increases gradually down to approximately 165 K, where a maximum is observed, before decreasing and remaining at a lower, nearly constant value at lower temperatures. The position of this maximum coincides with the bulk T_N of this batch, indicated by the dotted line. The increase of K_{eff} upon cooling down to 165 K is consistent with the temperature dependence of the power coefficient $d\omega/dP$ shown in Fig. 4.42 (b), indicating that the surface heat dissipation inferred from Raman thermometry remains sensitive to the bulk related changes. The apparent enhancement of K_{eff} near 165 K, compared to room temperature, may seem in contrast with the larger laser induced local heating inferred from Fig. 4.41(c) at 165 K relative to higher temperatures (Fig. 4.41(d)).

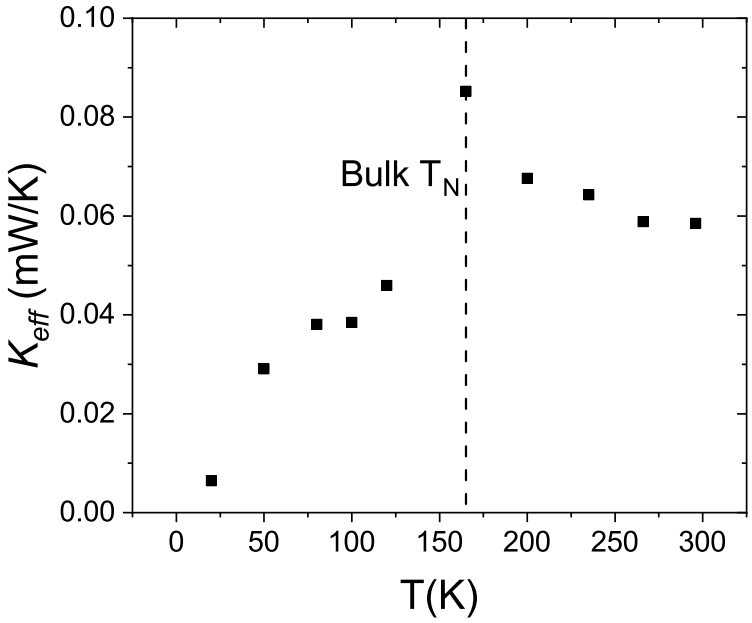

Figure 4.43.: Effective surface thermal conductivity K_{eff} of the $CrAs_{1-x}P_x$ single crystal with $x_{sur} \approx 4.5\%$. The dotted line represents the bulk T_N of this $CrAs_{1-x}P_x$ batch, extracted from magnetometry measurement (see Sec. 3.3.1).

However, as discussed above, this discrepancy reflects the fact that the phonon frequency depends both on the intrinsic temperature dependence and on laser induced heating. Since the temperature slope of the A_g-1 phonon frequency remains nearly constant between 165 K and room temperature, the behavior of K_{eff} is dominated by the power coefficient $d\omega/dP$.
Although the detailed temperature dependence of K_{eff} differs from that reported for pure CrAs - most notably in that K_{eff} increases upon cooling toward temperatures close to T_N, while Hu et al. report a decrease at the transition in the bulk thermal conductivity - the overall trend remains qualitatively comparable as thermal transport is substantially reduced at low temperatures [51]. In our case, this reduction amounts to approximately a factor of six between room temperature and base temperature, compared to a reduction by roughly a factor of four in the pure compound. In addition, K_{eff} exhibits a plateau between 75 and 100 K, which does not coincide with cusp-like anomaly in the A_g-1 phonon linewidth shown in Fig. 4.38. In Sec. 4.2.2, the linewidth anomaly was discussed in the context of bulk thermal transport, while measurements under applied pressure (Sec. 4.3) showed that this anomaly is suppressed, indicating that it is more closely related to the suppression of magnetic order than to thermal conductivity.

The analysis of the $x_{sur} \approx 4.5\%$ sample therefore establishes a reference case in which the Raman probed near surface region remains entirely in the high temperature phase over the full investigated temperature range and does not exhibit a magnetostructural transition or phase coexistence. Although the simplified thermal model employed here does not allow for a quantitative determination of the thermal conductivity, the temperature dependence of K_{eff} extracted from Raman thermometry captures systematic variations in the heat dissipation and provides insight into how laser induced local heating evolves with temperature. Notably, this reference behavior suggests that the effective thermal response inferred from Raman measurements may reflect a coupled system, in which heat deposited in the near surface region is exchanged with the underlying bulk.

As a consequence, K_{eff} can be regarded as an effective, surface sensitive quantity that may still be influenced by bulk related changes, even in the absence of a surface phase transition. In this sense, the $x_{sur} \approx 4.5\%$ sample represents a limiting case in which the thermal response of the Raman probed region can be characterized without the additional complexity introduced by surface phase transition or phase coexistence. The analysis can then be extended to the $x_{sur} \approx 0.6\%$ sample, in which surface phase coexistence persists down to the lowest measured temperatures, providing a markedly different thermal environment for the Raman-probed region.

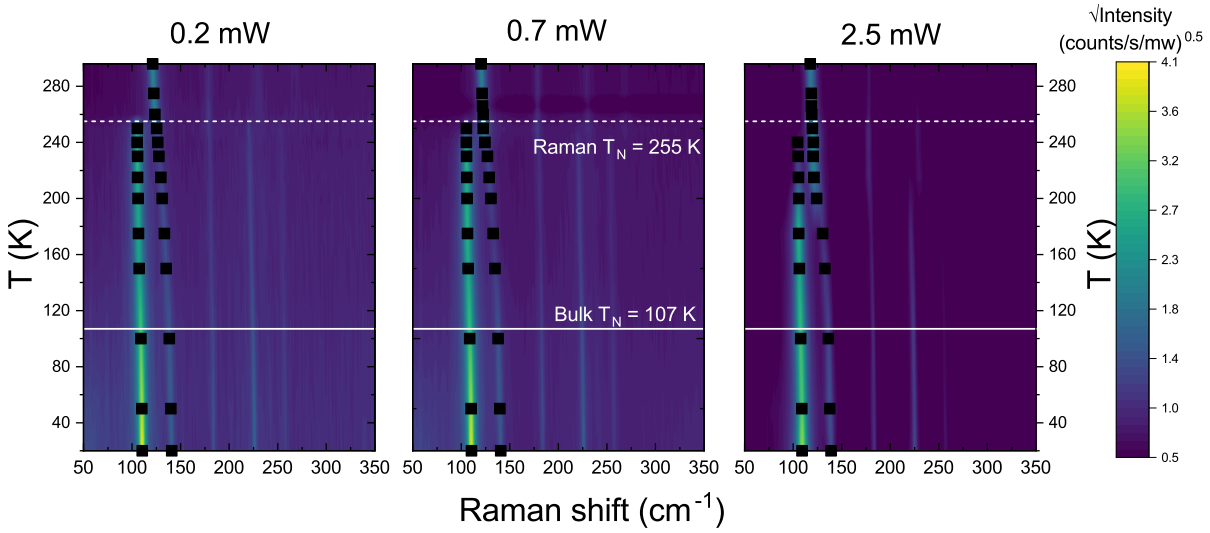

Figure 4.44.: Raman intensity maps of $CrAs_{1-x}P_x$ single crystals with $x_{sur} \approx 0.6\%$ as a function of temperature. The incident laser power used for each measurement is written above. The white dotted line marks the transition temperature probed by Raman spectroscopy, while the white solid line indicates the bulk transition temperature extracted from magnetometry measurements (Sec. 3.3.1). Overlaid scatter symbols represent the fitted A_g-1 phonon frequencies as a function of temperature.

Fig. 4.44 shows Raman intensity maps of the $x_{sur} \approx 0.6\%$ sample as a function of temperature for the three laser powers employed. At this surface concentration, a transition is observed at approximately 255 K, marking the onset of phase coexistence at the surface. Compared to pure CrAs (see Fig. 4.20), the influence of laser induced heating on the apparent transition temperature is significantly reduced. While at an incident power of 0.7 mW the transition remains close to 255 K, increasing the laser power to 2.5 mW shifts the transition to approximately 245 K, corresponding to a reduction of about 10 K. This shift is substantially smaller than the approximately 50 K reduction observed in pure CrAs under the same laser power, indicating that the onset of phase coexistence in the $x_{sur} \approx 0.6\%$ sample is less sensitive to laser induced local heating. To quantify the corresponding local temperature increase and assess how laser induced heating evolves within the coexistence regime, the same Raman thermometry procedure applied to the $x_{sur} \approx 4.5\%$ sample is now employed.

Fig 4.45 compares the A_g-1 phonon within the coexistence regime for different combinations of temperature and incident laser power, all acquired upon cooling within the same thermal cycle. The corresponding frequency shifts extracted from these measurements are summarized in Fig. 4.46 (a) and (c). In Fig 4.45 (a), the frequency measured at 20 K with 2.5 mW matches with that obtained at 100 K with 0.2 mW, suggesting a local temperature increase of about 80 K. In Fig 4.45 (b) and (c), between 100 K and 150 K, the frequency match is observed only for the LT A_g-1 phonon, while the additional mode, identified as the HT A_g-1 mode, does not show a comparable response and the mismatch grows with increasing temperature. Therefore, the induced heating and effective thermal conductivity are determined from the LT A_g-1 mode, which remains the most intense and reliable feature within the coexistence regime.

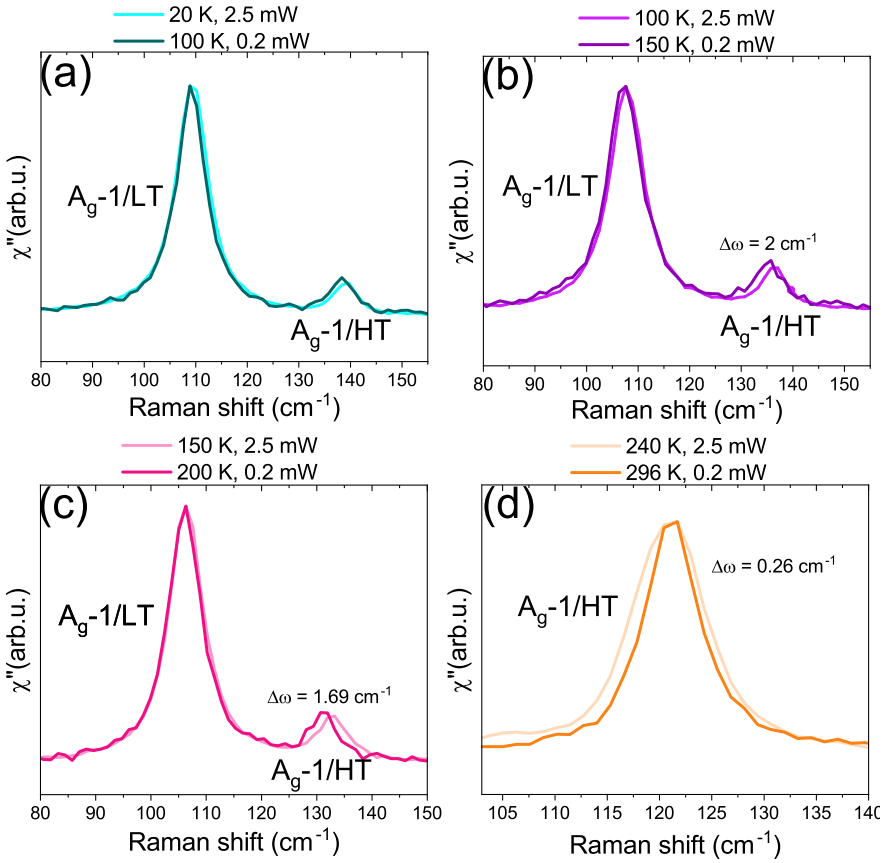

Figure 4.45.: Comparison of Raman spectra focused on the A_g-1 phonon in the coexistence phase and HT phase of a $CrAs_{1-x}P_x$ single crystal with $x_{sur} \approx 0.6\%$. (a) Spectra measured at 20 K (2.5 mW) and 100 K (0.2 mW). (b) Spectra measured at 100 K (2.5 mW) and 150 K (0.2 mW). (c) Spectra measured at 150 K (2.5 mW) and 200 K (0.2 mW). (d) Spectra measured at 240 K (2.5 mW) and 296 (0.2 mW). The frequency difference between the two spectra $\Delta\omega$, is obtained from the fitted A_g-1 peak positions and labeled alongside the spectra.

The comparison between 2.5 mW and 0.2 mW measurements of the LT mode gives an estimated local temperature increase of approximately 50 K, in both panel (b) and (c). A comparable heating is detected in Fig. 4.45 (d), where the HT A_g-1 measured at 240 K with 2.5 mW - with the bulk still in the coexistence phase - appears softer than the HT A_g-1 measured at 296 K with 0.2 mW. From the A_g-1 temperature dependence, this corresponds to a local spot temperature of approximately 300 K, i.e. a temperature increase of 60 K.

The evolution of laser induced heating with temperature differs from that of the $x_{sur} \approx 4.5\%$ sample. At base temperature, the induced heating is slightly reduced, while in the intermediate temperature range it remains nearly constant instead of decreasing progressively with increasing temperature. In contrast to the reference case where the probed region remains in the high temperature phase, the presence of coexisting phases therefore appears to modify the local heat dissipation, leading to a temperature range where the induced heating is nearly temperature independent. The corresponding power dependence of the A_g-1 phonon frequency is shown in Fig. 4.46. Unlike the critically doped sample, $x_{sur} \approx 4.5\%$, the HT A_g-1 mode does not maintain linearity with laser power across the entire temperature range. Above the Raman measured transition temperature T_N, a pronounced deviation from linearity appears between approximately 240 K and 200 K, while linear behavior is recovered at lower temperatures.

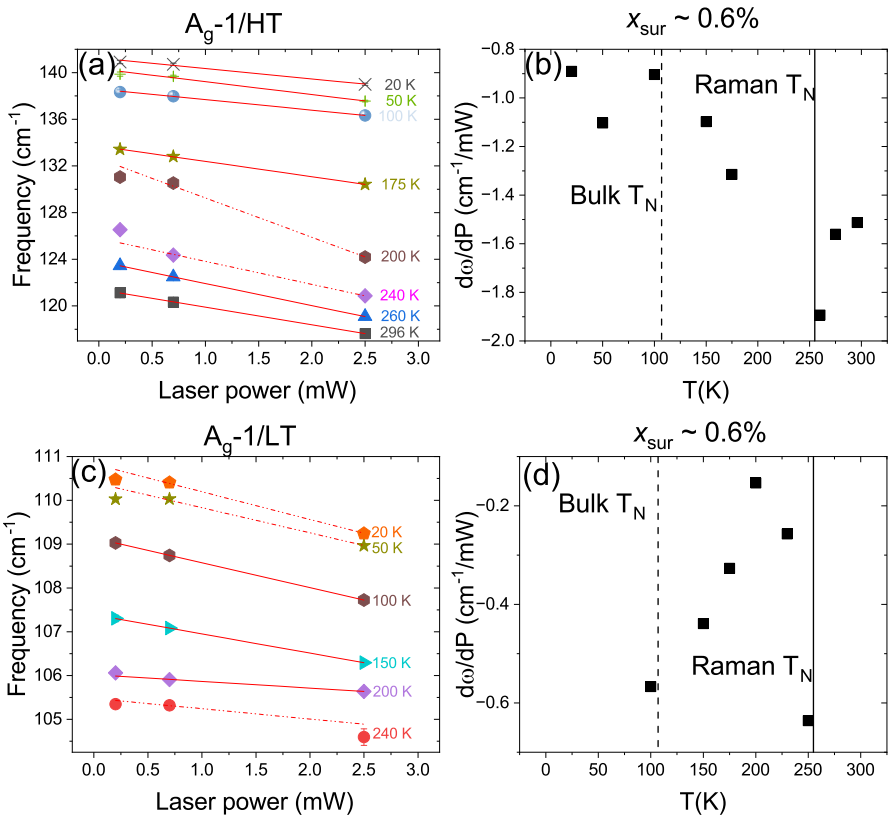

Figure 4.46.: (a) Frequency of the HT phase A_g-1 phonon mode as a function of laser power for the $CrAs_{1-x}P_x$ single crystal with $x_{sur} \approx 0.6\%$, shown for selected temperatures. Red lines represent linear fits: solid lines correspond to datasets consistent with linearity, while dotted lines correspond to deviations. (b) Temperature dependence of the power coefficient extracted from only the linear fits in (a). The dotted black line marks the bulk T_N of this batch, extracted from magnetometry measurements (see Sec. 3.3.1), while the solid black line marks the Raman measured T_N at which the coexistence sets in (c) Frequency of the LT phase A_g-1 phonon mode as a function of laser power for the same sample, with linear fits shown as in (a). (d) Temperature dependence of the corresponding power coefficient, with the bulk T_N and Raman measured T_N indicated as in (b).

The behavior of the LT A_g-1 mode, shown in Fig. 4.46(c), differs: linearity persists between approximately 200 K and 100 K before deviations appear at lower temperatures. Fig. 4.46 (b) and (d) display the extracted power coefficients $d\omega/dP$ as a function of temperature for the linear regimes of the high temperature and low temperature modes, respectively. For the HT phase A_g-1, the slope decreases upon approaching the Raman measured T_N, then increases again at lower temperatures, while for the LT phase A_g-1 phonon the slope rises to a maximum around 200 K before decreasing.

Since coexistence results in two distinct A_g-1 modes appearing simultaneously, only the dominant mode of each phase is considered for estimating effective thermal parameters and therefore K_{eff} is calculated from the thermal coefficient ($d\omega/dt$) and power coefficient ($d\omega/dP$) of the dominant mode. Fig 4.47 compares the effective surface thermal conductivity K_{eff} extracted for the $CrAs_{1-x}P_x$ single crystals with $x_{sur} \approx 0.6\%$ and $x_{sur} \approx 4.5\%$. For the $x_{sur} \approx 0.6\%$ sample, K_{eff} is evaluated only in the temperature intervals where linearity is preserved. Unlike the $x_{sur} \approx 4.5\%$ sample, where K_{eff} exhibits a maximum close to the bulk transition temperature, the $x_{sur} \approx 0.6\%$ sample displays a broad maximum around 200 K. This feature does not coincide with either the Raman-measured T_N or the bulk T_N, nor does it correspond to any pronounced anomaly in the temperature dependence of the phonon frequency or linewidth for this batch (see Fig. 4.38). Its origin therefore remains unclear.

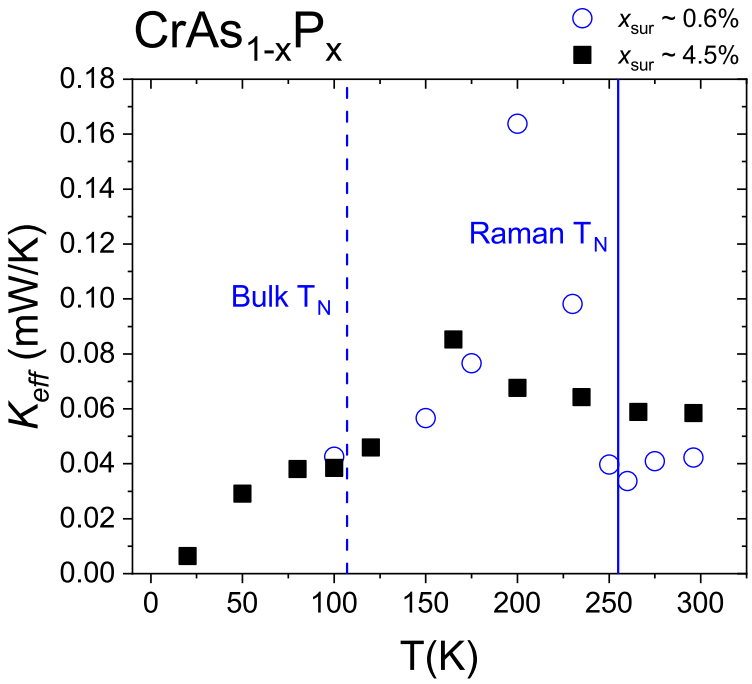

Figure 4.47.: Comparison of the effective surface thermal conductivity K_{eff} for the $CrAs_{1-x}P_x$ single crystals with $x_{sur} \approx 0.6\%$ and $x_{sur} \approx 4.5\%$. The dotted line indicates the bulk T_N of the $x_{sur} \approx 0.6\%$ sample, extracted from magnetometry measurements (see Sec. 3.3.1), while the solid black line marks the Raman determined T_N for the same composition.

This behavior contrasts with the trend reported for pure CrAs, where thermal conductivity decreases at low temperature and shows a pronounced anomaly at the magnetic transition [51]. At the same time, the extracted K_{eff} values for the two compositions become remarkably similar between approximately 100 K and 150 K, after differing by nearly 30% in the 300-250 K range. While this convergence does not directly imply identical bulk thermal transport properties, it suggests that the effective surface response inferred from Raman thermometry may become less sensitive to the underlying phase differences in this intermediate temperature regime. The deviation observed in the $x_{sur} \approx 0.6\%$ sample reflects both the presence of coexisting phases and the difficulty of interpreting K_{eff} as a direct proxy for bulk thermal transport in a thermodynamically heterogeneous probed region. While the temperature differences extracted from Fig. 4.41 and Fig. 4.45 provide a meaningful estimate of laser induced local heating, the analysis of K_{eff} should be regarded as qualitative. The simplified model assumes spatially uniform heating and a single thermodynamic phase within the probed volume, conditions that are not fully satisfied once surface phase coexistence sets in. A more complete determination of thermal transport across the phase diagram would require direct measurements of thermal conductivity for different doping levels, particularly to account for the known phosphorus gradient between surface and bulk in these crystals.

Taken together, the power dependent Raman measurements for the $x_{sur} \approx 4.5\%$ and $x_{sur} \approx 0.6\%$ samples highlight how laser induced local heating interacts with the presence or absence of surface phase coexistence. In the $x_{sur} \approx 4.5\%$ sample, where no transition occurs within the Raman probed region, K_{eff} evolves smoothly with temperature. In contrast, for the $x_{sur} \approx 0.6\%$ sample the onset of coexistence shifts by only about 10 K when increasing the laser power from 0.7 mW to 2.5 mW which is substantially less than the shift observed in pure CrAs under comparable conditions. This reduced sensitivity suggest that laser induced heating can not account for the stabilization of the HT phase or the apparent extension of the coexistence regime.

Although significant local heating is still present, its temperature dependence is modified once coexistence develops and the absence of a consistent frequency match for the additional HT A_g-1 mode further indicates that the thermal response of the probed region cannot be described by a single, uniform temperature. Consistently, deviations from linear power behavior and the altered temperature dependence of K_{eff} in the $x_{sur} \approx 0.6\%$ sample show that the effective heat dissipation probed by Raman spectroscopy becomes sensitive to thermodynamic heterogeneity at the surface. These observation suggest that spatial variations in thermal transport and surface bulk coupling may contribute to the extended coexistence regimes observed in doped CrAs, therefore placing practical limits on how closely the chemical substitution can reproduce the behavior induced by hydrostatic pressure.

4.4.3. Magnetic Raman in Phosphorus-doped samples

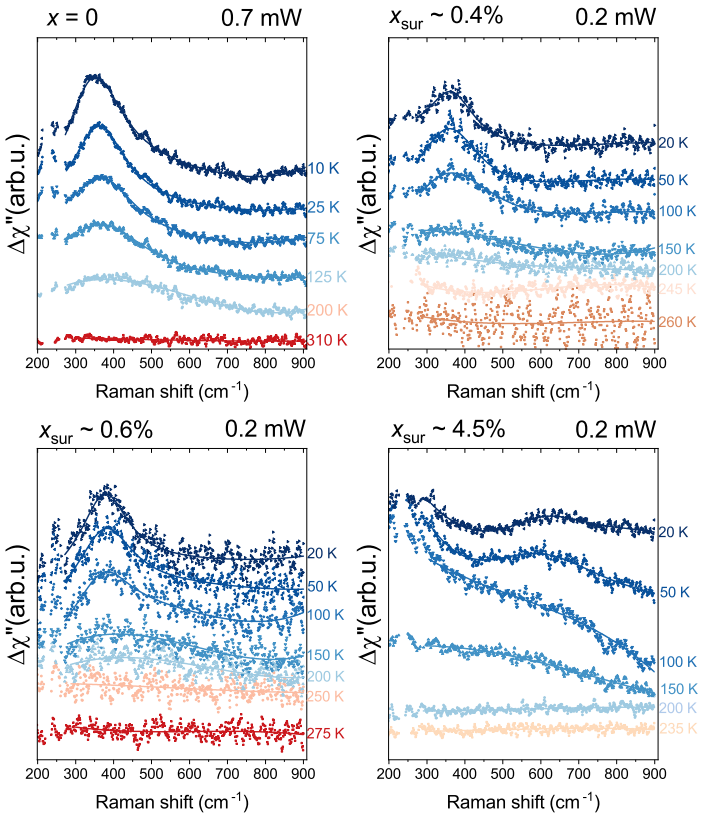

Figure 4.48.: Comparison of the temperature dependent section of differential Raman response $\Delta\chi^{"}(T) = \chi^{"}(T) - \chi^{"}(296K)$ for pure CrAs and the different $CrAs_{1-x}P_x$single crystal batches. The spectra were measured upon cooling with an incident laser power of 0.7 mW for pure CrAs and 0.2 mW for the doped samples. Prior to subtraction, the phonon contributions were removed from all spectra. The continuous lines represent the best fit. The corresponding phosphorus percentages are indicated above each panel and the temperatures are labeled next to each curve. Curves have been shifted for comparison. Data for pure CrAs are from [8].

Phosphorus-doped samples were investigated to evaluate the effect of chemical substitution on the low energy magnetic excitations. As established in the previous sections, phosphorus substitution acts in a similar way to the application of pressure, leading to a progressive weakening of the magnetic order. The doped CrAs single crystals were therefore studied to access this regime without the experimental constraints associated with the application of physical pressure in the high pressure Raman measurements used in this work.

The extraction of the low energy magnon from the Raman spectra of the $CrAs_{1-x}P_x$ single crystal batches follows the procedure outlined by Sen et al. [8] and Yao [52]. The phonon contributions were removed from all spectra. The resulting phonon-free spectrum at 296 K was used as a reference and subtracted from the spectra measured at lower temperatures - defining the following differential Raman response $\Delta\chi''(T) = \chi''(T) - \chi''(296K)$ - in order to isolate the emergence and growth of the low energy feature below T_N. The magnon peaks were fitted with Lorentzian functions to extract their characteristic frequencies and linewidths.

Fig. 4.48 shows the differential Raman response $\Delta\chi''$ as a function of temperature for pure CrAs and for the different $CrAs_{1-x}P_x$ single crystal batches. The data for the doped samples were measured upon cooling with an incident laser power of 0.2 mW, chosen to minimize laser induced heating effects, while the data for the pure CrAs were acquired with an intermediate laser power of 0.7 mW [8]. Despite this difference, the comparison remains meaningful as a qualitative reference for the characteristic energy scale and lineshape of the low energy magnetic feature and for its appearance below T_N. The sample from the $x_{sur} \approx 0.4\%$ batch shows no evident change in $\Delta\chi''$ above 200 K. Between 200 K and 150 K, the onset of the low energy feature becomes apparent, and it is clearly distinguishable from 100 K downward, continuing to grow in intensity down to base temperature. The energy of this feature is comparable to that observed in the spectra reported by Sen et al. [8]. This behavior is similar to that observed in the sample from $x_{sur} \approx 0.6\%$ batch, where the feature also emerges below 200 K, becomes fully apparent from 100 K downward and continues to grow in intensity upon further cooling. The emergence of the low energy feature around 200 K in these low doped samples is consistent with the behavior observed in pure CrAs.

The sample from the $x_{sur} \approx 4.5\%$ batch exhibits a first noticeable change in the background around 150 K, instead of 200 K as observed in the lower doped samples. A weaker and broader feature also appears between 100 K and base temperature. Notably, this feature occurs at an energy that is not comparable with those observed in the low doped samples or in the data reported by Sen et al. [8]. As mentioned in Sec. 4.4, the surface doping of this batch is high enough to not show any transition, therefore no trace of the magnetic order should be detectable. To verify whether this signal corresponds to a real effect rather than an artifact arising from temperature dependent background variations or imperfect background subtraction, the same feature can be studied as a function of temperature upon warming.

Fig. 4.49 shows the differential Raman response $\Delta\chi''$, as a function of temperature for the $x_{sur} \approx 0.6\%$ $CrAs_{1-x}P_x$ single crystal batch, measured both upon cooling and upon warming with an incident laser power of 0.2 mW, on the same sample and same spot. The low energy magnon persists upon warming up to approximately 160 K, a higher temperature compared to the cooling sequence, where only a noticeable change in the background is observed around 150 K. The temperature dependent differential Raman response $\Delta\chi''$ for the $x_{sur} \approx 4.5\%$ $CrAs_{1-x}P_x$ single crystal batch - shown in Fig. 4.50, also measured on the same sample and spot - displays a different behavior. Upon warming, the feature is no longer detectable at temperatures where it was visible during cooling. This suggest that the apparent signal observed upon cooling for the $x_{sur} \approx 4.5\%$ sample is an artifact arising from imperfect background subtraction in the construction of the differential Raman response.

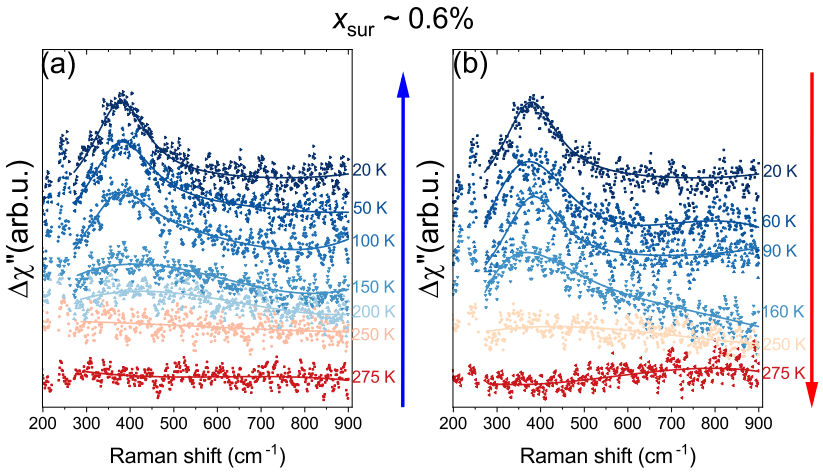

Figure 4.49.: Temperature dependent section of the differential Raman response $\Delta\chi^{"}(T) = \chi^{"}(T) - \chi^{"}(296K)$ for the $x_{sur} \approx 0.6\%$ $CrAs_{1-x}P_x$ single crystal batch, measured with an incident laser power of 0.2 mW: (a) upon cooling and (b) upon warming. The blue and red arrows indicate the direction of temperature change during the cooling and warming cycles, respectively. The continuous lines represent the best fits. The corresponding measurement are labeled next to each curve. Curves have been shifted for comparison.

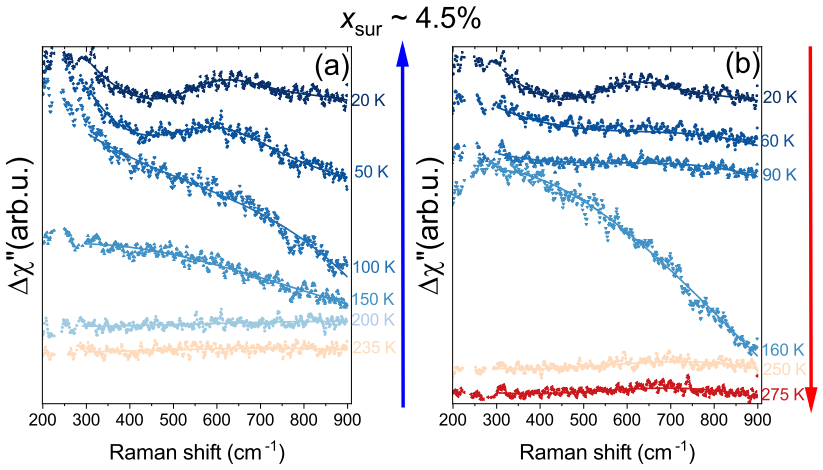

Figure 4.50.: Temperature dependent section of the differential Raman response $\Delta\chi^{"}(T) = \chi^{"}(T) - \chi^{"}(296K)$ for the $x_{sur} \approx 4.5\%$ $CrAs_{1-x}P_x$ single crystal batch, measured with an incident laser power of 0.2 mW: (a) upon cooling and (b) upon warming. The blue and red arrows indicate the direction of temperature change during the cooling and warming cycles, respectively. The continuous lines represent the best fits. The corresponding measurement are labeled next to each curve. Curves have been shifted for comparison.

Fig. 4.51 shows the comparison between the temperature dependence of the fitted parameters of the low energy magnon in pure CrAs and in the $x_{sur} \approx 0.6\%$ $CrAs_{1-x}P_x$single crystal batch, measured upon cooling and warming with an incident laser power of 0.7 mW[29]. The low energy magnon in the $x_{sur} \approx 0.6\%$ batch appears to harden compared to pure CrAs, as shown in Fig. 4.51 (a) and in the inset of Fig. 4.51(b). This observation seems to contrast with the expectation that either physical or chemical pressure suppresses magnetic order.

[29]The fitted parameter obtained from the dataset measured with 0.2 mW are shown in Fig. C.24. These data are presented separately because the lower excitation intensity results in a reduced signal-to-noise ratio and therefore to larger scatter in the fitted parameters, making direct comparison with the 0.7 mW data less meaningful.

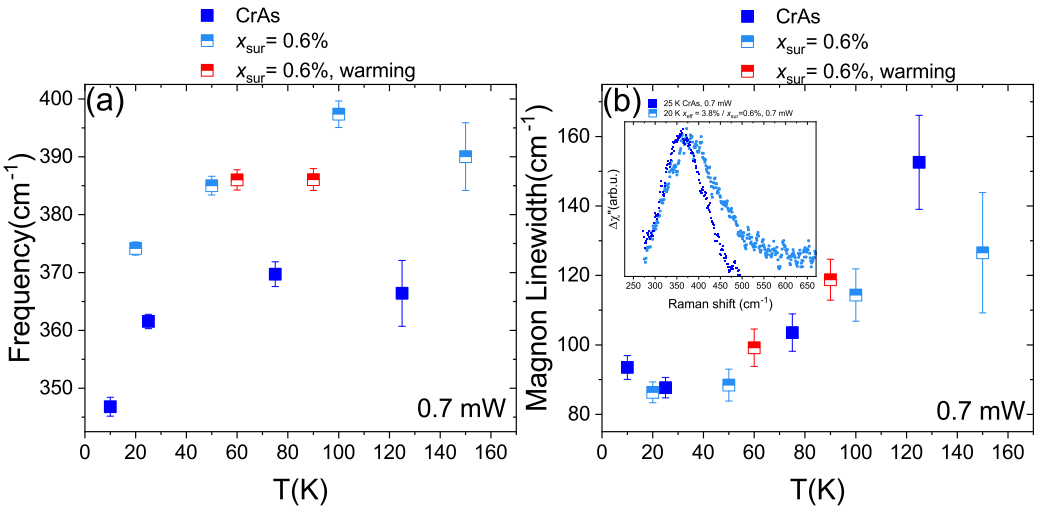

Figure 4.51.: Temperature dependence of the low energy magnon in pure CrAs and in the $x_{sur} \approx 0.6\%$ $CrAs_{1-x}P_x$ single crystal batch, measured upon cooling and warming with an incident laser power of 0.7 mW: (a) Frequency and (b) Linewidth. The inset compares the datasets at 20 K for the $CrAs_{1-x}P_x$ single crystal and at 25 K for pure CrAs. Data for pure CrAs are taken from [8].

Matsuda et al. reported the absence of any sharp magnetic excitation in the critically doped polycrystalline $CrAs_{1-x}P_x$ sample, consistent with the collapse of the long range magnetic order [7]. Therefore, with increasing phosphorus content, one would expect the low energy magnon to broaden, possibly together by a softening of the feature. However, the linewidth shown in Fig. 4.51 (b) remains essentially unchanged, suggesting that the damping of the magnetic excitation is not significantly affected, at least within this doping regime. This hardening behavior could be interpreted as an enhancement of the local exchange interactions, likely resulting from the reduced Cr-Cr distances induced by chemical pressure, which leads to a higher magnon energy.

To the best of our knowledge, such a pressure or doping induced increase in magnon frequency has not been previously reported for CrAs. This results highlight that, at low substitution levels, chemical pressure can modify the magnetic excitation spectrum in a nontrivial way, without inducing a significant increase in damping. Further insight into the nature of this excitation and its relation to the underlying exchange interactions would require complementary probes, such as Raman measurements under an external magnetic field for both the pure and phosphorus-doped samples, as well as other inelastic scattering techniques.

4.5. Domain formation and local lattice response in Phosphorus-doped CrAs

In this section, spatially resolved measurements are employed to investigate the spatial variation of phase coexistence at both the surface and in the bulk of CrAs-based system samples. Such an approach may provide insight into the underlying mechanism of structural competition between the magnetic and non-magnetic phases, as each is characterized by a distinct lattice response. Raman mapping is first used to probe the spatial variation of the Raman response across the surface of phosphorus-doped CrAs single crystals, with particular focus on the HT and LT A_g-1 phonon modes as local probes of the spatial distribution and proximity of the corresponding lattice responses. To complement these measurements and to access structural information at smaller length scales, transmission electron microscopy (TEM) is

employed on selected compositions to investigate local lattice responses and potential domain-related features. This complementary approach is further motivated by several studies in the literature where Raman spectroscopy and TEM have been employed together to identify structural phase coexistence in other materials [103, 104, 105, 106]. This dual technique framework therefore enables a nanoscale investigation of the evolving structural competition that characterizes the magnetostructural transition in the CrAs-based system.

4.5.1. Spatial variation of the Raman response

Spatially resolved Raman mapping measurements were performed on the $CrAs_{1-x}P_x$ single-crystal batches to examine the spatial variation of the Raman response as a function of temperature, with particular focus on the presence of the HT and LT A_g-1 phonon modes. A specific region of the crystal surface was selected over which a grid of 30 points was measured, covering an area of approximately $35 \times 45\ \mu m^2$. The measurements were performed upon cooling with an incident laser power of 0.2 mW, in order to minimize any laser induced heating that could otherwise broaden the temperature range of the phase coexistence.

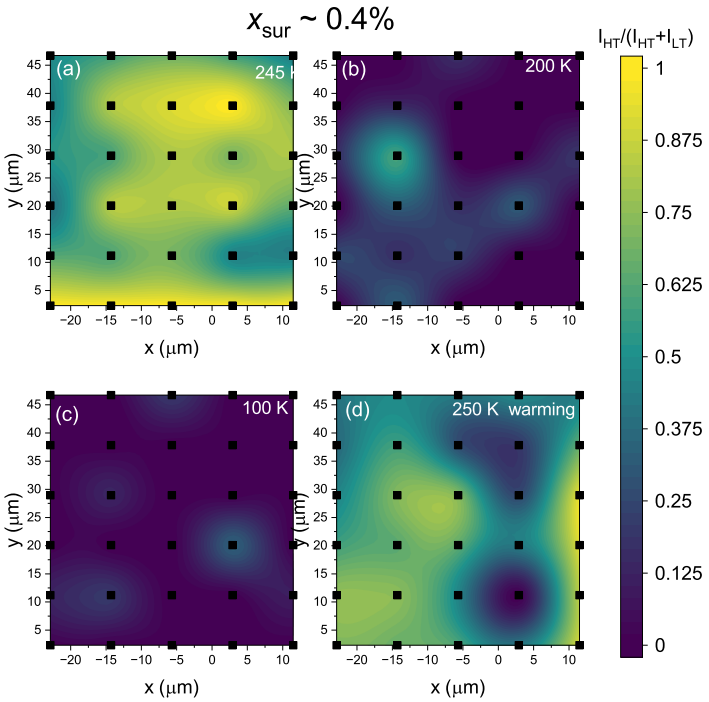

Figure 4.52.: Raman mapping of the $x_{sur} \approx 0.4\%$ $CrAs_{1-x}P_x$ single crystal upon cooling and then warming, measured with an incident laser power of 0.2 mW. The selected temperatures at which the measurements were taken are indicated in each panel. Panels (a-c) belong to the same cooling cycle, while panel (d) was measured during a warming cycle. Overlaid scatter symbols represent the measurement spots.

Fig. 4.52 shows the Raman mapping of the $x_{sur} \approx 0.4\%$ sample at different temperatures, measured upon cooling and then warming with an incident laser power of 0.2 mW. At 245 K, the Raman response on the surface begins to clearly show sign of phase coexistence - consistently with the results shown in Fig. 4.38 - with the HT A_g-1 being predominant.

Between 200 K and down to 100 K, some localized regions on the surface still exhibit the HT A_g-1 mode. This suggest a more complex phase dynamics at the as-grown surface, involving the formation of domains that can persist well below the bulk transition temperature. Upon warming to 250 K, the proportion of the HT phase increases again, without recovering fully, in agreement with the higher transition temperature upon warming due to hysteresis (see Tab. 4.5). Interestingly, the spatial distribution of the HT and LT domains also appears to change between cooling and warming cycles. This behavior may indicate a rearrangement of coexisting structural or magnetic regions at the surface, possibly influenced by local strain. A similar spatial reconfiguration of coexisting domains has been reported in other first-order magnetostructural systems, such as $Fe_{1+y}Te$[30] [107], where strain and competing magnetic interactions were shown to influence the domain morphology upon thermal cycling.

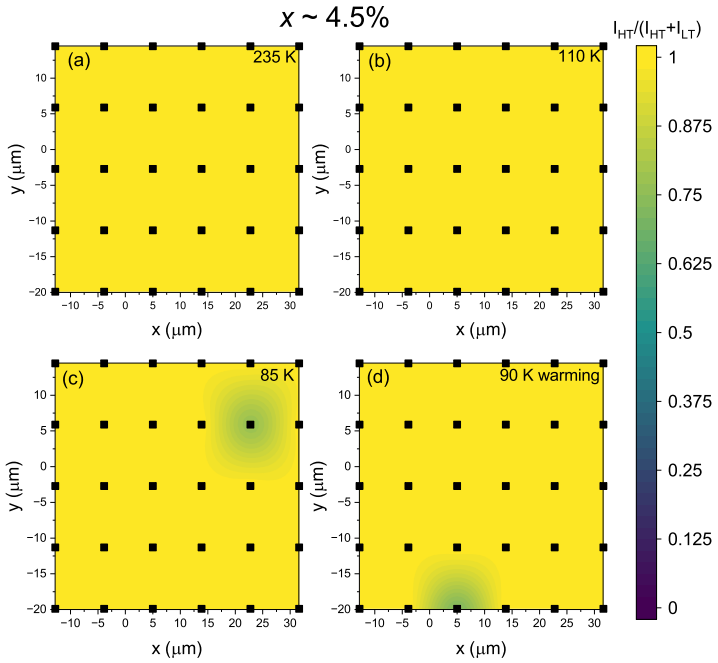

Figure 4.53.: Raman mapping of the $x_{sur} \approx 4.5\%$ $CrAs_{1-x}P_x$ single crystal upon cooling and then warming, measured with an incident laser power of 0.2 mW. The selected temperatures at which the measurements were taken are indicated in each panel. Panels (a-c) belong to the same cooling cycle, while panel (d) was measured during a warming cycle. Overlaid scatter symbols represent the measurement spots.

Fig. 4.53 shows the Raman mapping of the $x_{sur} \approx 4.5\%$ sample at different temperatures, measured upon cooling and warming with an incident laser power of 0.2 mW. The HT phase remains predominantly stable across all examined temperatures down to 85 K, consistent with the temperature dependence[31] shown in Fig. 4.38. However, at approximately 85 K, a few localized regions exhibiting the LT A_g-1 phonon mode can still be detected. A spatial reconfiguration of domains is observed both during cooling and between thermal cycles, in contrast to the $x_{sur} \approx 0.4\%$ sample, where reconfiguration occurred only between cycles.

[30] Where the sample with $y > 0.13$ display a magnetostructural transition from a high-temperature paramagnetic tetragonal to an incommensurate helimagnetic orthorhombic phase.

[31] The temperature dependent measurements presented in Sec. 4.4 extends to 20 K, while the mapping was limited to a minimum temperature of 85 K.

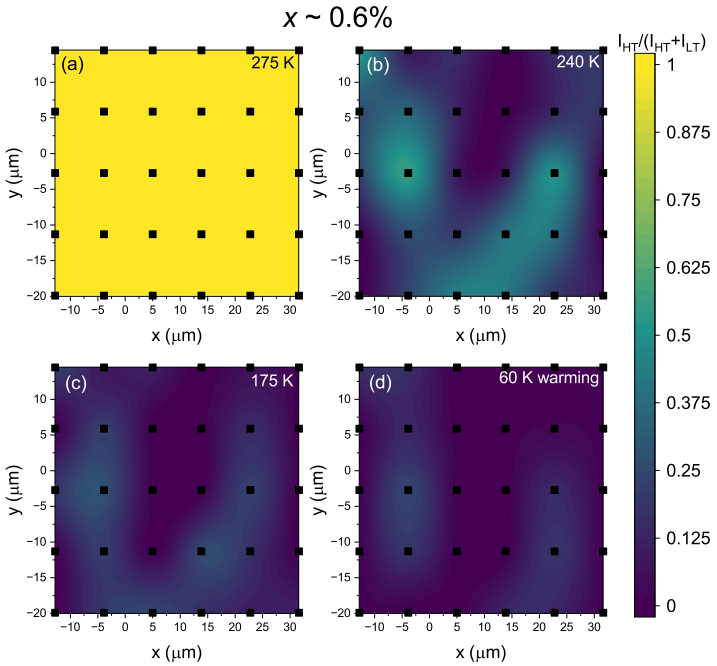

Figure 4.54.: Raman mapping of the $x_{sur} \approx 0.6\%$ $CrAs_{1-x}P_x$ single crystal upon cooling and then warming, measured with an incident laser power of 0.2 mW. The selected temperatures at which the measurements were taken are indicated in each panel. Panels (a-c) belong to the same cooling cycle, while panel (d) was measured during a warming cycle. Overlaid scatter symbols represent the measurement spots.

Fig. 4.54 shows the Raman mapping of the $x_{sur} \approx 0.6\%$ sample at different temperatures, measured upon cooling and warming with an incident laser power of 0.2 mW. Below the Raman measured T_N, the LT phase becomes predominant, while a few localized regions still display traces of the HT A_g-1 phonon mode down to 60 K, consistent with the temperature dependence[32] shown in Fig. 4.38. This provides further evidence that the additional phonon observed corresponds to the HT A_g-1 mode, as the Raman mapping shows that the surface is predominantly in the LT phase - where no extra phonon is present - while the additional feature originates only from a few localized regions in which the HT A_g-1 mode remains detectable. However, the origin of the persistent phase separation observed at the surface in this batch remains unclear. Upon cooling, some localized spots exhibiting the HT A_g-1 disappear, while other remain unchanged. Upon successive warming, no evident spatial reconfiguration of the domain is observed, as shown in Fig. C.25. This behavior explains why no significant change was detected in the Raman response, at the chosen spot in the temperature dependent measurements outlined in Sec. 4.4, as it was likely located within one of the domains that remain stable. The origin of this fixed domain configuration, which appears insensitive to thermal cycling, remains unclear.

The spatial resolution of the Raman mapping performed in this study is inherently limited by the laser spot size, which is approximately 5 μm, as discussed in Sec. 4.1.2.1. Therefore, the measured signal may be an average over multiple regions of potentially different phase character. In order to establish the intrinsic domain size and its evolution at the nanoscale, higher resolution techniques such as transmission electron microscopy (TEM) are required, as discussed in the following paragraph.

[32] As in the previous case, the temperature dependent measurements of Sec. 4.4 extended down to 20 K but the mapping was limited to 60 K.

4.5.2. Lamella preparation for TEM

Electron-transparent lamellae suitable for TEM measurements were prepared in collaboration with Dr. Di Wang and Lucas Brauch at the Institute for Nanotechnology (INT), Karlsruhe Institute of Technology (KIT). The TEM measurements and data analysis were also performed at the same institute.
Samples for transmission electron microscopy were prepared using a focused ion beam (FIB) process[33]. Two cross-sectional lamellae were fabricated: one from a pure CrAs single crystal and one from the $x_{sur} \approx 0.4\%$ $CrAs_{1-x}P_x$ single crystal batch[34].

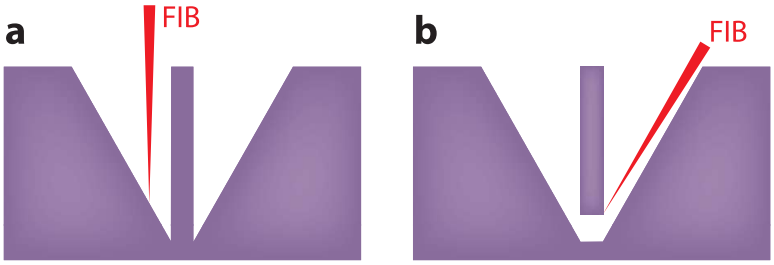

Figure 4.55.: Schematic of the focused ion beam (FIB) process used to prepare electron-transparent lamellae. (a) Trenches are milled to define a slab of the material with the target depth. (b) Undercutting beneath the slab frees it from the surrounding bulk crystal. Figure adapted from [109].

Fig. 4.55 shows a schematic overview of the focused ion beam (FIB) milling sequence employed for lamella preparation. The preparation involved successive ion-milling steps aimed at isolating a cross-sectional lamella from the bulk crystal and thinning selected regions to electron transparency.
First, Ga-ion milling at an accelerating voltage of 16 kV was used to remove material by trench milling and undercutting around the target region, isolating the lamella from the bulk crystal. This was followed by Ga-ion polishing at 5 kV in order to minimize surface damage and reduce the amorphous layer produced during the initial milling. Finally, the lamellae were subjected to Ar-ion nanomilling at 1 kV to obtain clean, electron-transparent regions suitable for TEM measurements.

The lamellae were extracted from cross sections of the single crystals such that the exposed surface corresponds to the *bc* crystallographic plane. This orientation is particularly suitable for detecting signatures of phase coexistence, as the *b* lattice parameter exhibits the strongest relative change at the magnetostructural transition. After preparation, each lamella was attached to a copper TEM support grid by means of platinum deposition, ensuring good thermal and mechanical stability and providing a fiducial reference.

The final geometry of the lamellae is shown in Fig. 4.56. Each lamella exhibits a wedge-like shape with lateral dimensions of approximately $15 \times 10\,\mu m^2$, and a thickness gradually varying from about 300 nm near the platinum attachment region to roughly 50 nm in the free-standing area.

[33] For an introduction to FIB techniques, see [108].

[34] As the lamella represents a cross-sectional cut of the bulk crystal, the corresponding effective phosphorus concentration is $x_{\text{eff}} \approx 0.7\%$. For clarity, the sample is nevertheless labeled according to its surface concentration.

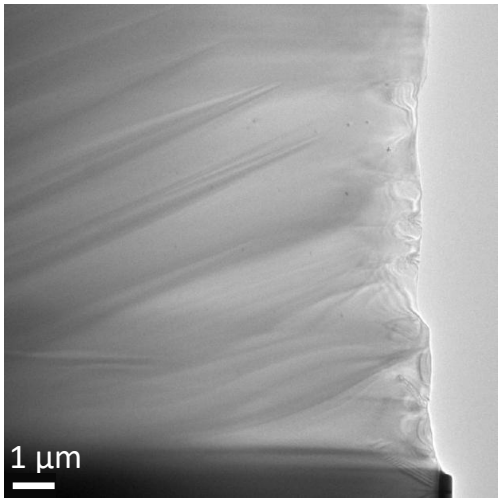

Figure 4.56.: Top-view SEM image of the CrAs lamella (surface normal to the *a*-axis, corresponding to the *bc* plane) prepared for TEM measurements, acquired at 88 K. The darker region at the bottom corresponds to the platinum deposition used to attach the lamella to the copper TEM support. The fine oblique lines visible across the surface are planar defects, likely related to the internal stress state of the material.

4.5.3. Local lattice response from TEM

Temperature dependent transmission electron diffraction was performed using a Thermo Fisher Scientific Themis 300 transmission electron microscope operated at 300 kV, equipped with a liquid nitrogen cryogenic holder and an Oxford Instruments temperature controller[35]. Diffraction patterns were acquired over regions of approximately 0.5 μm^2. During the cooling process, significant thermal drift prevented maintaining the electron beam on a fixed region of the lamella. As a result, diffraction patterns were collected from different regions of the lamella at different temperatures[36]

Fig. 4.57 shows the temperature dependence, upon cooling, of the *b* and *c* lattice parameters for the pure CrAs lamella and the $x_{sur} \approx 0.4\%$ doped lamella, normalized to their respective values at 296 K. Both datasets display a relatively high level of noise, most likely arising from thermal drift during cooling, as diffraction patterns were collected from different regions of the lamellae at different temperatures. Additional scatter may originate from local damage induced during ion milling or polishing, as well as from variations in sample thickness. Normalization to 296 K was applied to emphasize the relative changes of the lattice parameters and to facilitate the identification of the phase transition and possible phase coexistence. This approach is justified by the fact that the diffraction behavior of the CrAs system is already well documented in the literature [17, 18, 20, 7, 34, 38, 39].

As discussed in Sec. 2.3, the *c* axis is expected to exhibit larger scatter than the *b* axis. Nevertheless, the relative changes at the transition remain above the noise level for both lattice parameters. Notably, the *b* lattice parameter in the pure CrAs lamella expands by approximately 3%, which is lower than the 3.4% to 4% expansion typically reported in literature [7, 8]. In contrast, the *c* axis shows a contraction of approximately -0.8% in good agreement with previous findings.

[35]For an introduction to transmission electron microscopy and diffraction see [110].
[36]This limitation arises from the microscope configuration, which does not allow simultaneous imaging and diffraction.

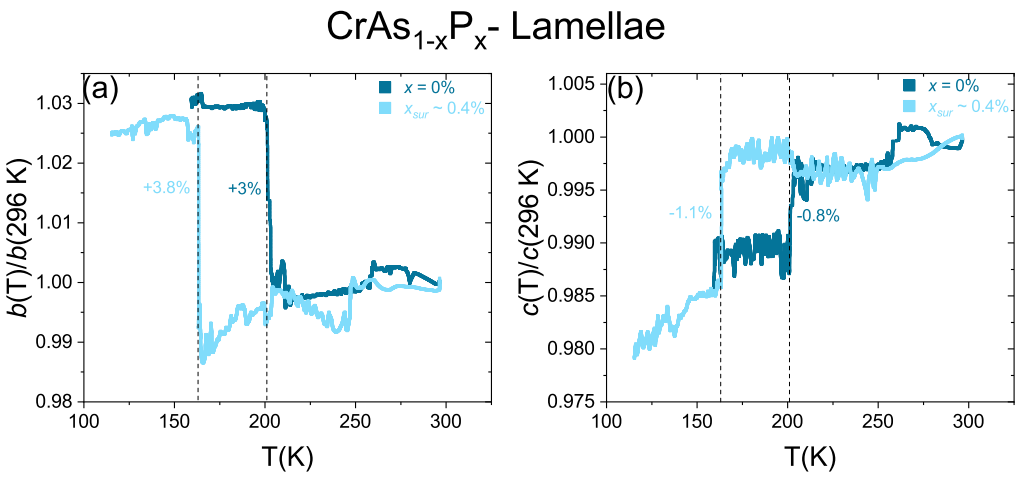

Figure 4.57.: Temperature dependence, upon cooling, of the (a) b lattice parameter and (b) c lattice parameters, normalized to their respective values at 296 K, for pure CrAs lamella and the $x_{sur} \approx 0.4\%$ doped lamella. The dotted lines indicate the transition temperatures and the relative changes at the transition are annotated next to each curve.

$x_{sur}(\%)$	$T_N^{\downarrow}$(K)	$T_N^{\uparrow}$(K)
0	200 ± 5	220 ± 5
0.4	160 ± 5	209 ± 5

Table 4.7.: Summary of the cooling ($T_N^{\downarrow}$) and warming ($T_N^{\uparrow}$) transition temperatures of $CrAs_{1-x}P_x$ lamellae as a function of surface phosphorus concentration x_{sur}, extracted from the temperature dependence of the b lattice parameter.

The transition temperatures extracted from the temperature dependence of the lattice parameters during cooling and warming[37] are summarized in Tab. 4.7. The values obtained from the lamellae are systematically lower than those reported in Sec. 3.3.1 for the corresponding bulk single crystal batches, suggesting the presence of additional experimental effects. One possible interpretation is related to unintended modification of the lamella crystal structure by Ga-ion implantation, a well known effect that can influence the phase diagram and physical properties of various materials [111, 112, 113]. However, comparison with the effects of Al doping in CrAs, as reported by Park et al. [35], suggests that this scenario is unlikely to have directly modified the transition temperature. Al doping is known to mimic a negative chemical pressure on the lattice due to its slightly larger covalent radius, resulting in an increase of T_N, as observed similarly for Mn or Sb doped CrAs [38, 75]. Within a purely chemical-pressure picture, the fact that gallium and aluminum both belong to Group 13 of the periodic table, with gallium lying further down the group, would therefore suggest a higher, rather than lower, T_N.

A second possible interpretation is related to electron beam induced heating during the TEM experiment. Electron beam heating is an unavoidable consequence of TEM experiments [114, 115]. In this context, the apparent temperature shift observed for the pure CrAs lamella is comparable to the induced 2.5 mW laser heating on the bulk single crystal, as shown in Fig. 4.20, where the transition temperature at the surface is approximately 220 K. This interpretation is consistent with the Raman measurements performed on the pure CrAs lamella, presented in the following subsection, where a comparable laser-induced heating effect is quantified.

[37] The b and c lattice parameters measured upon warming are shown in Fig. C.26. Warming data for CrAs are not included here.

These observations suggest that, although the effect of Ga-ion implantation cannot be completely excluded, it is likely secondary compared to beam-induced heating under the present experimental conditions.

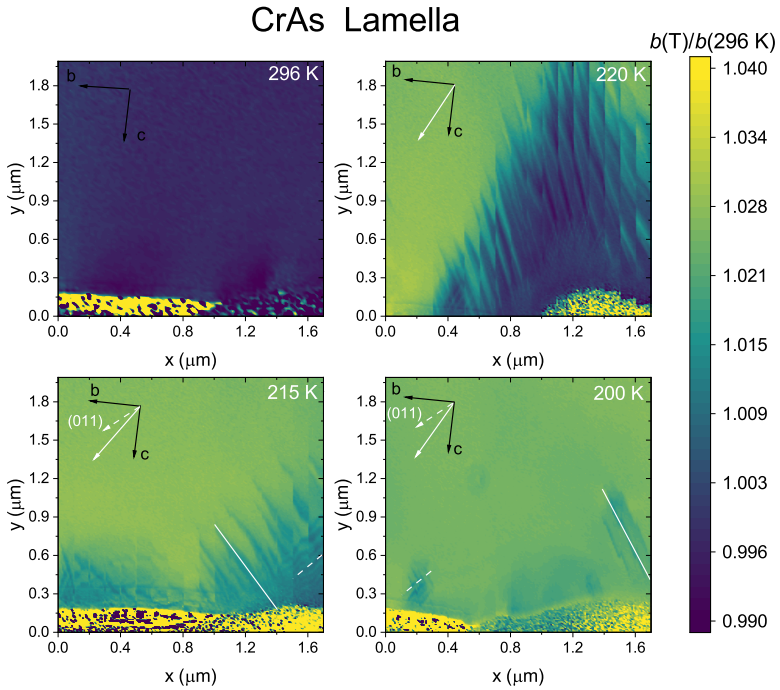

Figure 4.58.: TEM mapping of the pure CrAs lamella upon cooling. The temperatures at which the measurements were acquired, together with the corresponding lattice parameter directions, are indicated in each panel. Continuous white lines mark the orientation of the dominant stripe domain, while dotted lines indicate the weaker domain. The corresponding white arrows indicate the relative orientation of these domains with respect to the crystallographic axes.

No clear signature of phase coexistence could be resolved in the temperature-dependent selected-area diffraction measurements, which probe regions of approximately 0.5 μm^2. To investigate possible local structural variations on smaller length scales, a diffraction mapping mode was employed. For these measurements, the lamellae were cooled to selected temperatures with a thermalization time of approximately 30 minutes to minimize drift effects. The mapping covered an area of approximately 4 μm^2, with the electron beam focused to probe regions of about 1 nm^2 and a spatial increment of 10 nm between adjacent points.

Fig. 4.58 shows the mapping of the pure CrAs lamella[38], upon cooling, displayed as an intensity map of the ratio between the measured b lattice parameter at each temperature and the reference b lattice value at 296 K[39]. At room temperature, the mapped region shows a homogeneous b lattice parameter across the scanned area. The bottom portion showing a distinct contrast corresponds to the platinum attachment region, which serves as a reference marker to monitor possible thermal drift of the lamella. Upon cooling to 220 K, clear signatures of the phase coexistence appear.

[38]The lamella used for the mapping measurements (Fig.4.58) is not the same as that used for the temperature dependent diffraction series in Fig. 4.57. Both lamellae were prepared from the same pure CrAs batch and exhibit identical lattice parameters evolution and transition temperatures.

[39]For both the pure and doped lamellae, the reference value of b(296 K) used for normalization were taken from the corresponding data shown in Fig. 4.57

$T(K)$	**Phase**	θ_b (°)	**Width** (nm)
296	HT		
220	HT + LT	70 ± 3	
215	HT + LT	54 ± 3/45 ± 3	50 ± 10/50 ± 10
200	HT + LT	64 ± 3/45 ± 3	40 ± 10/30 ± 10

Table 4.8.: Summary of the average HT domain stripe orientation (θ_b) and widths determined from TEM mapping of the pure CrAs lamella at selected temperatures. Coexisting HT phase domain orientations at the same temperature are separated by slashes.

Although the mapped region differs slightly from the room temperature map due to minor drift during cooling, the datasets remain comparable. At 220 K, the HT phase, shown in blue, occupies approximately 1.6 μm^2, corresponding to nearly half of the mapped area.

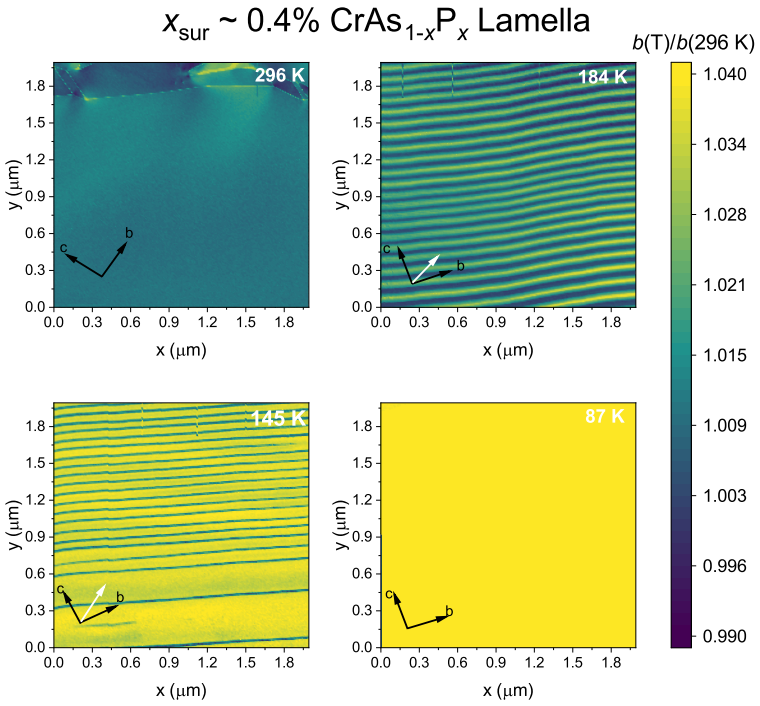

Figure 4.59.: TEM mapping of the $x_{sur} \approx 0.4\%$ $CrAs_{1-x}P_x$lamella upon cooling. The temperatures at which the measurements were acquired, as well as the corresponding lattice parameter directions, are indicated in each panel. The white arrows indicate the relative orientation of the domains with respect to the crystallographic axes.

The HT domains appear as sharp, line-like features oriented at an angle of approximately 70° with respect to the b axis, as determined from the diffraction pattern measured previously. Apparent discontinuities along these lines arise from scanning artifact during data acquisition; nevertheless, the overall orientation and spatial extent of the domains remain unaffected. The corresponding domain orientations and widths, shown in Fig. 4.58 are listed in Tab. 4.8, while the summary for all measured temperatures is presented in Tab. C.8.

Despite the substantial fraction of LT phase at 220 K, the diffraction signal shown in Fig. 4.57 remains dominated by the HT phase, indicating that the LT phase develops in spatially isolated regions. Therefore, during the temperature-dependent diffraction experiment, thermal drift likely caused the probed areas to correspond predominantly to the HT phase. Within the LT regions, the b lattice parameter expands by approximately 3%, consistent with the discontinuity observed at the transition in Fig. 4.57.

Upon further cooling at 215 K, the mapped region shows a reduced fraction of phase coexistence, with the LT phase spreading across a larger portion of the surface. At this temperature, two preferred orientations of the remaining HT domains become observable: one at approximately 54° with respect to the b axis and a second one at 45°, corresponding to the (011) direction. The latter occurs less frequently, indicating that most HT domains adopt the 54° alignment. This trend persists down to 200 K, close to $T_N^{\downarrow}$, where most of the surface has transitioned to the LT phase. At this stage, only weak traces of the HT phase remain, appearing either along the (011) direction or at angles of approximately 60° relative to the b axis. Overall, these observations indicate that phase coexistence occurs on a very local length scale, with line-like (or stripe) domains whose width decreases from approximately 60 nm at 220 K to 40-30 nm at lower temperatures. The observed non-monotonic reorientation of certain domains as a function of temperature suggests their alignment may be influenced by local strain fields or stress relaxation processes at the phase boundaries, arising from the lattice parameters mismatch between the HT and LT phase.

Fig. 4.59 shows the mapping of the $x_{sur} \approx 0.4\%$ $CrAs_{1-x}P_x$ lamella upon cooling, displayed as an intensity map of the ratio $b(T)/b(296\text{K})$. At 296 K, the mapped region exhibits a homogeneous b lattice parameter across the scanned area, similarly to the pure CrAs lamella. The upper portion of the image showing a distinct contrast corresponds to regions of the sample where adjacent $CrAs_{1-x}P_x$ domains are rotated in-plane by discrete angles of 120° with respect to each other (see Fig. C.27 for a clearer view). This behavior is in direct agreement with the twin domain structure discussed in Sec. 3.1.3 and illustrated in Fig. 3.3. This feature was initially used as a reference marker to monitor potential thermal drift of the lamella during cooling, although a residual drift could not be fully avoided. Upon cooling to 184 K, clear signatures of phase coexistence are observed, with line-like HT domains becoming visible. In contrast to the pure CrAs lamella, where the transition appears more spatially abrupt, the doped sample exhibits a more homogeneous and pervasive coexistence, characterized by a single dominant domain orientation alternating periodically with HT stripes.

A summary of the measured domains (both HT and LT phase) orientations and widths for selected temperatures is listed in Tab. 4.9 and in Tab. C.9 for the complete dataset. As in the pure sample, the observed non-monotonic reorientation of domains with temperature is consistent with the presence of local strain fields or stress relaxation effects at HT–LT phase boundaries[40]. However, in the doped lamella a single dominant orientation persists over the entire temperature range, while the spatial distribution of domain widths evolves during cooling. In particular, LT domains broaden preferentially in the lower part of the mapped region, reaching widths of several hundred nanometers, while the upper portion remains denser, with alternating HT and LT domains of narrower width. Between 175 and 160 K (see Tab C.9) - which is also the temperature range of the transition observed in Fig. 4.57 - the domains align to the (011) crystallographic direction. What evolves during cooling is the spatial distribution of the domain widths: the LT domains become noticeably broader in the lower part of the mapped region, while the upper portion remain denser, showing alternating HT and LT domains with narrower widths. This behavior develops gradually from around 155 K down to approximately 136 K (see Fig. C.29).

[40] As mentioned previously, different portions of the same lamella may be slightly rotated relative to one another. Therefore, due to thermal drift during cooling, the probed area may correspond to a region with a small in-plane rotation.

$T(K)$	**Phase**	θ_b (°)	**HT Width** (nm)	**LT Width** (nm)
296	HT			
184	HT + LT	11 ± 3	20 ± 10	70 ± 10
145	HT + LT	21 ± 3	30 ± 10	280 ± 10/60 ± 10
87	LT			

Table 4.9.: Summary of both HT and LT domain stripe orientation (θ_b) and widths determined from TEM mapping of the $x_{sur} \approx 0.4\%$ $CrAs_{1-x}P_x$lamella at selected temperatures. Coexisting LT domain widths at the same temperature are separated by slashes.

The nature of the coexistence seems to change with phosphorus doping. When comparing the pure and doped lamellae, clear differences appear in how long the HT phase persists below the transition temperature. In the pure CrAs lamella, faint traces of the HT domains are still visibile at 200 K - the T_N measured in TEM - but they disappear completely by 185 K, about 15 K below the TEM measured transition (see Fig. C.28). In the doped lamella, instead, well defined HT domains remain visible down to 145 K - approximately 20 K below the TEM measured transition - and persist until around 136 K (see Fig. C.29). Moreover, the temperature window over which the transition occurs also broadens with doping: in the pure lamella, the coexistence extends approximately from 220 K and 200 K, while in the doped one it goes from about 184 K to 114 K (not shown here). This difference can't only be ascribed to electron beam heating. Firstly, the induced heat should, in principle, have no influence on the shape or orientation of the domains. Secondly, although beam induced heating is indeed present, the fact that samples prepared under identical conditions and exposed to the same electron beam energy exhibit different ΔT values relative to their bulk T_N (listed in Sec.3.3.1) - about 65 K for the pure lamella and 80 K for the doped one - suggests that phosphorus doping affects the thermal conductivity of the sample, as discussed in Sec. 4.4.2, and therefore reinforces the idea that doping directly influences the nature of the coexistence. Still, given the complexity of the measurements and the limited number of samples and thermal cycles performed, some uncertainties remain. The observed coexistence range could depend on the specific temperature steps chosen or on the sample quality and it can't be excluded that a similar broadening might have been observed in the pure lamella had the measurements been extended to temperatures above 220 K.

Notably, the earlier onset of the LT phase combined with the prolonged persistence of the HT phase in the doped lamella remains insufficient for a clear detection in the TEM diffraction experiment discussed previously. The probed area in those measurements ($\approx 0.5\ \mu m^2$) was large enough for the average signal to be dominated first by the HT phase and then by the LT phase, once the transition was globally complete. Although the global transition in the doped sample is observed around 165 K, the width of the LT domains, as mentioned previously, begins to increase noticeably from about 155 K (see Tab. C.9 and Fig. C.29) and this evolution is not spatially uniform across the lamella. The domains expand mainly in the lower part of the mapped region, where they reach approximately 130 nm in width, while the upper portion remains denser, showing alternating HT and LT domains around 30 nm. Therefore, any estimate of a characteristic length scale at which LT domains contribute significantly to a larger-area diffraction signal should be regarded as approximate, but can be reasonably placed on the order of 10^2 nm, i.e. around 130 nm for the present dataset.

The mapping results confirm that phase coexistence extends down to the nanoscale within the bulk of the crystal, as probed through the cross-sectional lamella geometry. The shape and temperature range of this coexistence appear to be influenced by phosphorus doping, consistent with the broadening temperature range observed in the Raman results, both in the single spot spectra and in the mapping measurements. Given that the Raman laser spot size is approximately $5\mu m$, it effectively averages over hundreds of domains[41], of both of the HT and LT phase. However, it can't be stated with certainty that the thresholds width of 130 nm identified in TEM corresponds to the effective limit for domain detection in the Raman experiments.
This behavior likely arises from local strain fields and disorder introduced by phosphorus substitution, potentially stabilizing a spatially modulated phase coexistence [107, 116]. In particular, the persistence of nanoscale coexistence could be related to the mismatch between the doped and the undoped unit cells. This effect can't be ascribed to doping inhomogeneities within the sample, since both the HT and LT phases display an homogeneous b lattice parameter across the mapped region. As discussed in Sec. 3.2.1, the b parameter is the most sensitive to phosphorus content, indicating that the doping level is effectively uniform across the probed area [42]. In the doped sample, the orientation of the LT domains varies with temperature and occasionally aligns along specific crystallographic directions such as (011). Whether this preferred orientation is influenced by, or coupled to, the underlying magnetic order can't be reliably determined from the present data, as standard TEM diffraction is essentially insensitive to magnetic scattering[43]. Complementary experiments employing Lorentz TEM on additional batches would enable direct visualization of magnetic contrast and domain configurations [119].

While the present TEM measurements primarily probe structural distortions, the emergence of well defined and reproducible domain patterns indicates that the HT–LT transition proceeds through a spatially heterogeneous manner. This suggest that the observed domain structure may not be determined solely by local structural distortions or defect-related effects. In correlated systems, electronically driven instabilities are often coupled to the lattice and can give rise to periodic lattice modulations that appear as stripe-like in electron microscopy [120, 121, 122]. In this context, the structural contrast observed here does not uniquely identify the underlying driving mechanism, but may reflect the lattice response to a coupled electronic or magnetic instability. A more precise identification of the respective roles of structural strain and coupled electronic or magnetic degrees of freedom in stabilizing the observed nanoscale phase coexistence will therefore require additional experiments using probes sensitive to these degrees of freedom.

4.5.4. Raman spectroscopy on CrAs lamella

To clarify whether the magnetostructural transition in the lamellae is altered by sample preparation effects or induced electron beam heating, temperature dependent Raman measurements were performed. The CrAs lamella used for this experiment corresponds to the one shown in Fig. 4.57. The sample was mounted inside the cryostat described in Sec. 4.1.2.1, together with its copper TEM support grid. The grid was fixed to the sample holder using a small amount of Apiezon N grease to ensure optimal thermal contact. Due to the small size of the lamella (approximately 15 $\mu m \times 10\ \mu m$) a higher magnification microscope objective (x100) was employed.

[41] In Fig. 4.59, nearly 70 HT and LT domains can be counted within just 2 μm.

[42] Possible variations in the b lattice value could arise also from local bending (see Fig. C.27) or stacking faults (see Fig. 4.56). A more direct evaluation of the local doping homogeneity via EDX mapping could reinforce this conclusion. However, such measurements were not conducted in this study.

[43] The scattering intensity between electrons and magnetic moments is several orders of magnitude weaker than that of the electron-lattice interactions [117, 118].

The resulting laser powers, measured after the objective while using the same power filters as in Sec. 2.3 and 4.4, are listed in Tab. 4.10. Since the x100 objective focuses the laser onto a smaller spot (approximately 2 μm, compared to about 5 μm with the x50 objective), the effective surface power density is higher than in the previous measurements. This may lead to enhanced laser induced heating, further amplified by the reduced dimensions of the lamella and its limited ability to dissipate heat. This enhanced local laser heating therefore provides a way to verify whether the transition temperature measured via TEM, on the lamellae, differs from the bulk single crystal primarily due to induced heating effects.

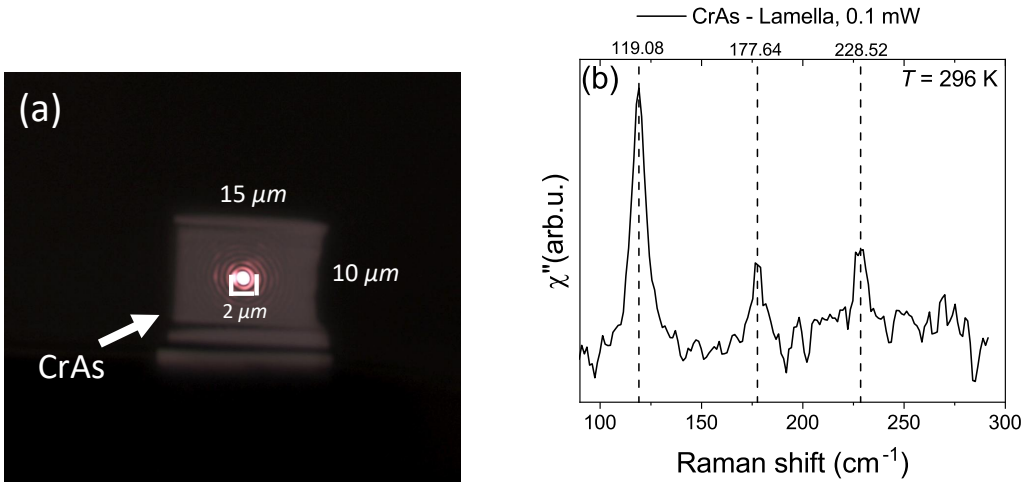

Figure 4.60.: (a) Top view image of the pure CrAs lamella in the cryostat. The resulting spot is approximately 2 μm. (b) Raman spectrum measured on the pure CrAs lamella at 296 K. The dashed lines indicate the A_g phonon modes, with their corresponding frequencies labeled above.

Fig. 4.60 (a) shows a top view image of the pure CrAs lamella measured in the Raman experiment. As discussed previously, the lamella surface corresponds to the *bc* plane of CrAs. In the employed Raman configuration, this corresponds to a backscattering geometry along the *a* axis, with an unknown in-plane polarization orientation. This uncertainty arises from the twinning of the sample, which prevents a reliable isolation of the crystallographic *b* or *c* directions (see Sec. 3.1.3 and 3.3.1). As a result, the parallel-polarization configuration used here - namely, using the same polarization for both the incident and scattered light - contains a mixture of both A_g and B_{3g} phonon modes[44]. For the purpose of determining the transition temperature and assessing laser induced heating and to ensure consistency with the previous measurements on bulk single crystals, the analysis is restricted to the A_g phonons. Fig. 4.60 (b) shows the Raman spectrum measured on the pure CrAs lamella at 296 K. Three out of four A_g phonons are detected. The phonon frequencies measured on the lamella differ from those measured in the CrAs single crystal (see Tab. C.10), suggesting a non negligible induced laser heating. Based on the temperature dependence of the A_g-1 mode measured on the pure CrAs single crystal at the lowest laser power (0.2 mW), the equivalent temperature increase at the laser spot is estimated to be approximately 10 K for a laser power of 0.1 mW and approximately 30 K for 0.3 mW, , where the laser powers are those measured after the ×100 objective and listed in Tab. 4.10.

[44]Based on the CrAs Raman tensor listed in App. C

Objective	Laser power(mW)	Spot size(μm)	Surface power density (mW/μm^2)
LMPlanFLN x50	0.2	5	0.01
	0.7	5	0.04
	2.5	5	0.13
SLMPlan x100(ULWD)	0.1	2	0.03
	0.3	2	0.09

Table 4.10.: Summary of laser parameters used in the Raman experiments on CrAs and $CrAs_{1-x}P_x$single crystals at ambient pressure, in Sec. 4.2.2 and 4.4, and on the pure CrAs lamella.

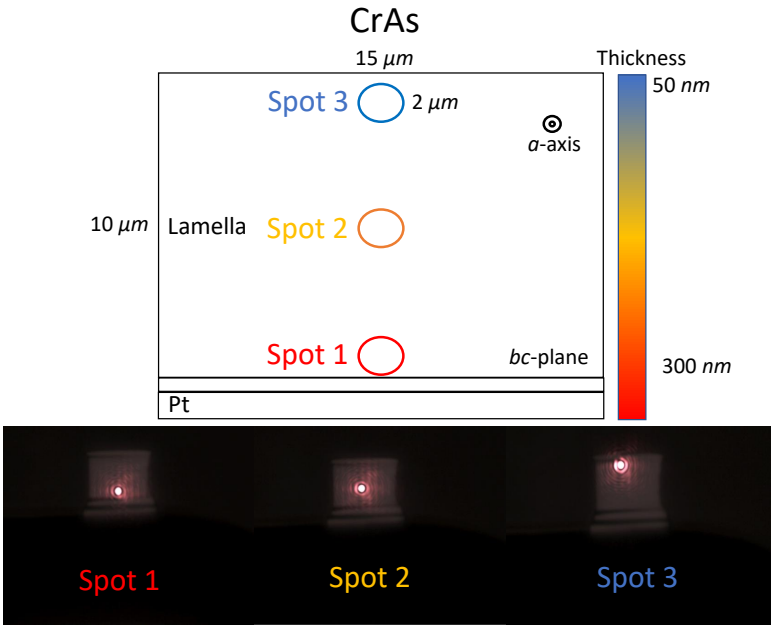

Figure 4.61.: Overview of the Raman measurement protocol on the pure CrAs lamella. Three measurement spots were selected along the thickness gradient of the lamella, and the corresponding microscope images of the laser spot at each position are shown in the bottom panel.

Fig. 4.61 summarizes the measurement protocol employed on the pure CrAs lamella. As discussed in Sec. 4.5.2, the lamella has a non uniform thickness, ranging from approximately 300 nm in the region where the platinum attachment fixes the lamella to the copper TEM grid, down to about 50 nm toward the outer edge. Three distinct spots were selected along this thickness gradient (see Fig.4.61) for a series of temperature dependent Raman measurements performed at different laser powers. The measurement protocol follows the power and the temperature dependent Raman experiments described in Sec. 2.3 and 4.4.2. To evaluate the effect of laser-induced heating and to probe T_N in a manner consistent with those sections, the analysis is restricted to the A_g-1 phonon.

Fig. 4.62 shows the Raman spectra of the A_g-1 phonon mode measured on the pure CrAs lamella at the three selected spots as a function of temperature, using a laser power of 0.1 mW. All measurements were collected upon cooling and within the same thermal cycle. The transition temperatures extracted from the Raman measurements are listed in Tab. 4.11. The difference between the transition temperatures obtained at a surface power density of 0.03 mW/μm^2 and those observed from the TEM experiment (see Tab. 4.7) confirms that the latter are affected primarily by induced electron beam heating.

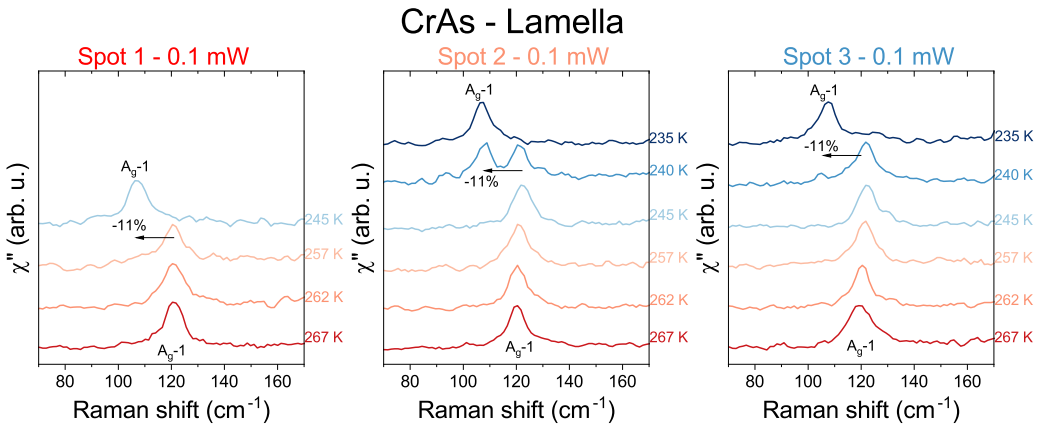

Figure 4.62.: Selected region of the Raman spectra of the pure CrAs lamella, showing the evolution of the A_g-1 phonon mode at the three different spots, measured upon cooling with 0.1 mW laser power. All spots were measured within the same thermal cycle. The corresponding temperatures are shown alongside the curves. Black arrows indicate the relative frequency shift $(\omega_{LT} - \omega_{HT})/\omega_{HT}$ at the onset of the transition or at the onset of the coexistence.

Laser power (mW)	$T_N^{\downarrow}$**-Spot 1(K)**	$T_N^{\downarrow}$**-Spot 2(K)**	$T_N^{\downarrow}$**-Spot 3(K)**
0.1	251 ± 6	237 ± 2	237 ± 2
0.3	n.e.	207 ± 7	207 ± 7
Laser power (mW)	$T_N^{\uparrow}$**-Spot 1(K)**	$T_N^{\uparrow}$**-Spot 2(K)**	$T_N^{\uparrow}$**-Spot 3(K)**
0.1	260 ± 5	242 ± 5	242 ± 5
0.3	242 ± 7	227 ± 7	220

Table 4.11.: Summary of the cooling ($T_N^{\downarrow}$) and warming ($T_N^{\uparrow}$) transition temperatures of the pure CrAs lamella, extracted from the temperature dependence of the A_g-1 phonon mode at the three selected spots, for different laser powers. "n.e." indicates that the transition temperature could not be extracted.

A systematic shift in the transition temperature is also observed between the three measured spots, with Spot 1 exhibiting a transition temperature approximately 15 K higher[45] than Spot 2 and 3. This behavior is consistent with thickness gradient of the lamella. Thinner regions dissipates heat less efficiently, requiring a lower cryostat temperature to compensate for the same absorbed laser power. This observation indicates that efficient dissipation of laser induced heating - in the present geometry - requires a sample thickness on the order of several hundred nanometers. Despite these differences in the transition temperatures, the relative frequency change $(\omega_{LT} - \omega_{HT})/\omega_{HT}$ at the onset of the transition or phase coexistence is essentially identical across all spots, with a value of approximately -11%. This value is lower than the -13% measured on the pure CrAs single crystal, consistent with the observed trend in the bulk crystal of a reduced relative softening of the A_g-1 mode with increasing induced heating at the laser spot (see Fig. 4.20).

Interestingly, signatures of phase coexistence are observed only at Spot 2. Laser induced heating can be ruled out as the cause of this behavior, since Spot 3, measured at the same power and within the same thermal cycle, does not display any coexistence. Considering the geometry of the lamella and the spot dimensions shown in Fig. 4.61, this suggests that the relevant domains are separated by distances of the order of the spot size (approximately 2 μm) along the direction of the lamella probed by the

[45] While still approximately 15 K lower than the bulk CrAs single crystal.

measurement. Moreover, the signatures of coexistence changes between different thermal cycles, both upon cooling and warming (see Fig. C.30). In some cycles, coexistence is observed only at Spot 2, while in others it becomes detectable at Spot 3 or disappears entirely (see Fig. 4.63). This behavior is consistent with a reconfiguration and rearrangement of domains, as discussed earlier in the Raman mapping (Sec. 4.5.1) and TEM measurements (Sec. 4.5.3).

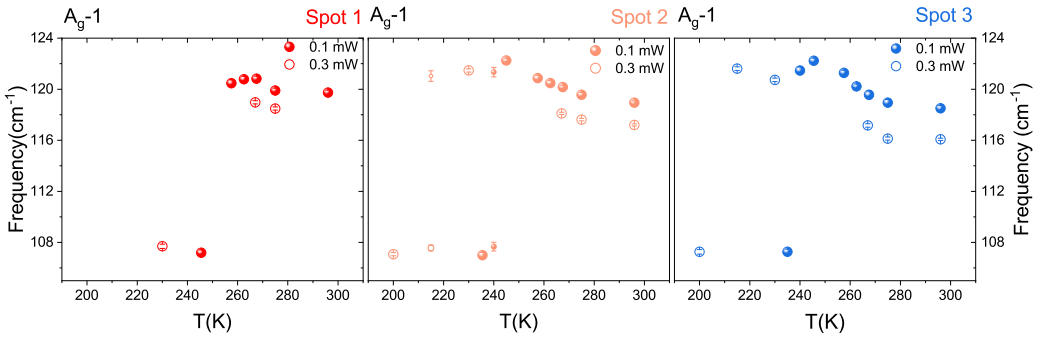

Figure 4.63.: Temperature evolution of the A_g-1 phonon frequency of the pure CrAs lamella measured upon cooling at the three selected spots. Filled and open symbols correspond to 0.1 mW and 0.3 mW laser power, respectively.

To further assess the impact of laser heating, additional measurements were performed at a laser power of 0.3 mW on the same three spots, in different thermal cycles. Fig 4.63 shows the temperature evolution of the A_g-1 phonon frequency of the pure CrAs lamella measured upon cooling at the three selected spots, for both the 0.1 mW and 0.3 mW laser power. The cooling and warming transition temperatures extracted from these measurements are are listed in Tab. 4.11 and summarized in Fig. 4.64. Increasing the laser power to 0.3 mW produces a systematic lowering of the transition temperature for all spots, with Spot 1 still exhibiting a higher T_N than Spot 2 and Spot 3. The transition temperatures reached at 0.3 mW are close to those obtained from the TEM diffraction experiment (see Tab. 4.11 and Fig. 4.64), indicating that the effective surface power density in the TEM experiment was comparable to that reached in the Raman measurement at approximately 0.09 mW/μm^2.

With respect to induced laser heating, the 0.3 mW measurements correspond to a temperature shift of approximately $\Delta T \approx 50$ K for Spot 2 and 3 relative to the bulk single crystal transition temperature. For Spot 1, the temperature steps in the cooling sequence were not sufficient to provide a reliable estimate of T_N at 0.3 mW. However, the warming data indicate a shift of about 30 K with respect to the bulk T_N.

In summary, the Raman measurements on the CrAs lamella show that the systematic lowering of the transition temperature observed in the TEM experiments (Sec. 4.5.3) is mainly due to induced heating effects. The transition temperature extracted from Raman spectroscopy decreases with increasing laser power and varies with the local lamella thickness. At the same time, the spatially localized and cycle dependent signatures of phase coexistence observed in Raman spectroscopy are consistent with a heterogeneous domain structure whose configuration can change between thermal cycles, in agreement with the TEM mapping results. While Raman spectroscopy is intrinsically limited by spatial averaging, it provides an independent confirmation of the local nature of the coexistence. Extending similar Raman measurements to phosphorus-doped lamellae would therefore represent a natural next step to further investigate the influence of doping on the coexistence regime.

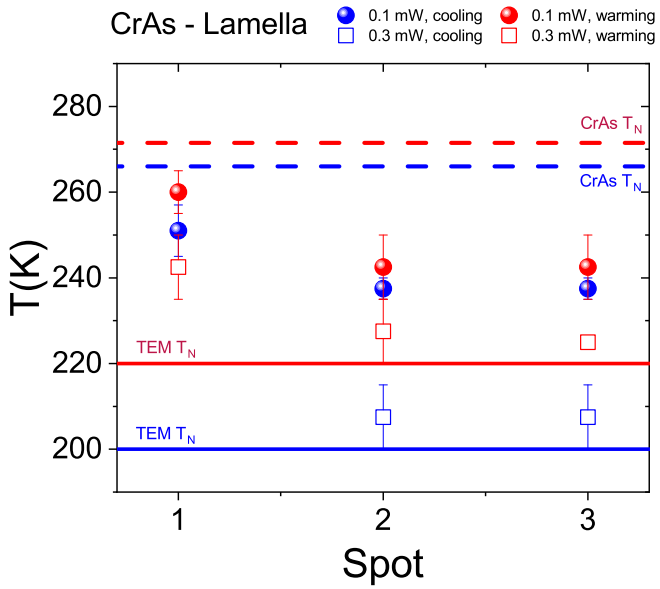

Figure 4.64.: Transition temperatures of the pure CrAs lamella measured at the three selected Raman spots upon cooling and warming. Filled and open symbols represent 0.1 mW and 0.3 mW laser power, respectively. Dashed solid lines indicate the (warming) $T_N^{\uparrow}$ and (cooling) $T_N^{\downarrow}$ measured on CrAs bulk single crystal, from Sec. 3.3.1. Continous solid lines show the $T_N^{\uparrow}$ and $T_N^{\downarrow}$ obtained from TEM diffraction, from Tab. 4.7.

4.6. Conclusions

In this chapter, Raman spectroscopy was established as a sensitive probe of the magnetostructural transition in CrAs and phosphorus-substituted CrAs, with a particular strength in detecting the coexistence between the high temperature (HT) and low temperature (LT) phases and tracking its evolution as a function of external parameters (e.g. applied pressure), as well as sample and measurement dependent conditions. The coexistence leaves a clear fingerprint in the Raman response through the appearance of two distinct components of the A_g-1 phonon mode, and its detectability was found to be strongly spot dependent, consistent with a heterogeneous domain structure close to the surface.
Both the transition temperature and the temperature range of HT-LT phase coexistence extracted from Raman measurements were found to be significantly affected by laser-induced heating and surface heat dissipation in the CrAs system. In both pure and phosphorus-substituted CrAs, increasing laser power shifts the stabilization of the LT phase to lower temperatures, while reduced sample dimensions further enhance this behavior. These results demonstrate that thermal transport plays a central role in the observation and interpretation of phase coexistence in CrAs-based systems.

Raman measurements under applied pressure on pure CrAs confirmed the suppression of the magnetic transition temperature with increasing pressure and provided further insight into the magnetoelastic coupling. In particular, the pronounced maximum in the linewidth of the A_g-1 phonon mode previously reported at ambient pressure in the LT phase [8] was found to be absent under pressure once the magnetic order is fully suppressed. This observation supports the interpretation that the linewidth anomaly originates from magnetoelastic effects [8]. In addition, anomalies observed in the pressure evolution of the phonon frequencies provide independent evidence for the isostructural pressure-induced phase transition proposed by Yu et al. [17], occurring between 0.2 and 0.3 GPa, here directly observed in single-crystal samples.

On phosphorus-doped CrAs, Raman measurements across different near-surface phosphorus concentrations x_{sur} confirmed that phosphorus substitution suppresses T_N in a manner qualitatively analogous to the application of external pressure. At a critical surface concentration of $x_{sur} \approx 4.5\%$, no magnetostructural transition was observed down to the lowest measured temperatures, similarly to pure CrAs at approximately 1 GPa. However, the analogy between chemical substitution and pressure breaks down when considering the temperature evolution of the phonon linewidths, which is most likely dominated by disorder effects introduced by phosphorus substitution rather than by magnetoelastic coupling alone.

Raman mapping measurements revealed that the spatial distribution of the HT and LT phases is strongly dependent on the local phosphorus concentration. In low-doped samples, phase coexistence was found to be highly inhomogeneous at the surface. For very low surface doping ($x_{sur} \approx 0.4\%$), the domain configuration reorganized upon thermal cycling. In contrast, for slightly higher but still low surface doping ($x_{sur} \approx 0.6\%$), phase coexistence persisted down to base temperature in localized regions, as evidenced by the continued presence of the HT A_g-1 phonon, while the overall domain configuration remained largely static. These observations support the assignment of the additional Raman peak to the HT A_g-1 mode and point to a complex and still poorly understood near-surface domain dynamics.

To probe phase coexistence at a more local length scale, TEM-ready lamellae were prepared from pure CrAs and from the $x_{sur} \approx 0.4\%$ doped batch. Temperature dependent electron diffraction revealed systematically lower transition temperatures compared to bulk measurements, an effect attributed to beam-induced heating and reduced heat dissipation in the lamella geometry. This interpretation was independently confirmed by Raman measurements on pure CrAs lamellae. These results emphasize the importance of thermal transport and sample geometry in the interpretation of the magnetostructural transition in CrAs. TEM measurements demonstrated that the HT-LT coexistence is intrinsically local and strongly dependent on the spatial resolution of the probe. While temperature dependent diffraction measurements averaging over large areas did not resolve coexistence, nanodiffraction mapping revealed phase separation on nanometric length scales. In phosphorus-doped lamellae, doping modifies the nature of the transition by inducing a stripe-like modulation, within which the LT phase progressively expands upon cooling. The microscopic origin of this behavior remains unclear and requires further investigation.

Taken together, the results presented in this chapter demonstrate the strength of combining spatially resolved Raman spectroscopy and transmission electron microscopy as a complementary approach to investigating phase coexistence in CrAs-based systems. To the best of our knowledge, this is the first study in which the temperature evolution of phase coexistence in these materials is tracked using both techniques across a broad range of experimental conditions. This combined methodology turns out to be able to provide a robust framework for future investigations of phase coexistence in correlated electron systems.

5. Summary

This thesis has investigated the structural, magnetic, and lattice dynamical properties of CrAs and phosphorus-substituted CrAs, with a particular focus on the magnetostructural transition and on phase coexistence between magnetic and non-magnetic states under different tuning parameters.

High-quality single crystals of phosphorus-doped CrAs were successfully grown, with bulk phosphorus concentrations reaching up to approximately 4%. The structural response of these materials to chemical substitution was examined using diffraction-based techniques, demonstrating that phosphorus substitution provides an effective way to tune the magnetostructural transition. The suppression of the Néel temperature with increasing phosphorus content, determined from magnetization measurements, is qualitatively analogous to the effect of external pressure, supporting the interpretation of phosphorus substitution as a form of chemical pressure. At the same time, deviations from this pressure–doping analogy were identified, indicating that disorder and local structural effects introduced by phosphorus have a significant impact on the physical response of the system.

Raman spectroscopy was shown to be a sensitive probe of phase coexistence and competition in CrAs-based systems. In both pure and phosphorus-doped CrAs, the coexistence between the high-temperature and low-temperature phases leaves a clear fingerprint in the Raman response, most clearly manifested by the appearance of two distinct components of the A_g-1 phonon mode. Spatially resolved Raman measurements further demonstrated that phase coexistence is a local, domain-based phenomenon, whose detectability depends on the probed volume and near-surface conditions, including local thermal transport properties, and can exhibit domain reconfiguration and the persistence of high-temperature domains in localized regions down to base temperature.
Raman measurements under applied pressure on pure CrAs confirmed the suppression of the Néel temperature with increasing pressure and showed that the previously reported linewidth anomaly of the A_g-1 phonon disappears around the critical pressure at which magnetic order is suppressed, reinforcing its magnetoelastic origin. In addition, anomalies observed in the pressure evolution of the phonon frequencies around 0.2–0.3 GPa provide independent evidence for a previously proposed isostructural pressure-induced phase transition in pure CrAs.

Transmission electron microscopy, enabling structural probing at nanometric length scales, revealed that phase coexistence in CrAs is intrinsically local. In phosphorus-doped lamellae, the transition is characterized by a stripe-like modulation that is not observed in the pure compound, within which the low temperature phase progressively expands upon cooling. The microscopic origin of this behavior remains unclear and points to a complex interplay between structural, magnetic, and electronic degrees of freedom induced by chemical substitution. This work also demonstrates the effectiveness of combining spatially resolved Raman spectroscopy with transmission electron microscopy as a complementary approach to investigating phase coexistence across length scales. To our knowledge, this is the first study to apply both techniques to track the temperature evolution of phase coexistence in CrAs-based systems, offering a useful framework for future studies of structurally inhomogeneous correlated materials.

Overall, the results of this thesis establish phase coexistence in CrAs as a spatially heterogeneous phenomenon governed by the interplay of magnetism, lattice dynamics, disorder and thermal transport. The local coexistence of magnetic and non-magnetic regions is particularly relevant because superconductivity in CrAs develops from the non-magnetic phase, making the evolution of this coexistence under external tuning parameters important for understanding the superconducting state. The additional complexity introduced by phosphorus substitution further indicates that chemical disorder and local structural modulations can qualitatively modify the nature of the transition, leaving open important questions for future investigations. Future studies combining complementary local probes and extending these measurements to the superconducting regime will be essential to determine how the observed phase coexistence and local structural modulations influence the development of superconductivity in CrAs-based systems.

Acknowledgments

This thesis is not only the result of scientific work, but also of the support, patience and encouragement of many people. The IQMT has proven to be an excellent scientific environment, from which I have greatly benefited through stimulating discussions and collaborations with many outstanding researchers.

First and foremost, I would like to express my sincere gratitude to Prof. Matthieu Le Tacon for his constant guidance throughout this work. I am especially grateful for his support during the more challenging phases of this project, which helped me navigate difficult moments along the way.

I would also like to sincerely thank PD Dr. Frank Weber for reviewing my work.

I would like to thank Dr. Amir-Abbas Haghighirad, Dr. Mehdi Frachet, Dr. Michaela Sofia Souliou, and Dr. Michael Merz for their direct support and many valuable discussions — and for reassuring me, more than once, that I had not been intoxicated, irradiated or irreversibly blinded in the process. I am especially grateful to Mehdi for his day-to-day guidance during my first year of doctoral studies. His constant availability, patience and willingness to help were invaluable during this initial and formative stage of my PhD.

This work was also shaped by numerous collaborations outside of IQMT. I would first like to thank Dr. Marie-Aude Measson and Dr. Owen Moulding for their help and guidance during the high-pressure experiments. I am grateful to Dr. Stefano Agrestini and Dr. Mirian Garcia for their assistance and support during our RIXS beam times, including the first experiment, which was carried out remotely due to COVID-19 restrictions. I would also like to thank Dr. Di Wang and Lucas Brauch for their help with the TEM experiments. In particular, I am deeply grateful to Lucas for his patience and dedication, especially during the many experiments that extended late into the evening.

Beyond direct scientific collaborations, I would like to thank all my colleagues for their constant support and for making everyday life at the institute both enjoyable and meaningful. In particular, I would like to mention the following people.

I would like to thank Tom Lacmann for always having answers to my many questions about navigating life in Germany, from administrative matters to language-related challenges. I am grateful to Philippa McGuinness for our many conversations on British culture, language and - most importantly - for the delicious Scottish shortbread. I would like to thank Fabian Henßler, Antoine Baron and Mai Ye for their invaluable help in refining the aesthetics of my figures and for the many breaks disguised as discussions on Raman spectroscopy. I am particularly grateful to Fabian for his help with German translations and for diligently replenishing our ice cream supply, to Antoine for the many music recommendations and to Mai for his financial lessons.

My thanks also go to Igor Vinograd, Mark Graf von Westarp and Arthur von Ungern-Sternberg Schwark for the many, many coffee breaks and for their emotional support during challenging experimental periods. I am also grateful to Dr. Shi Huanhuan, Dr. Arun Jaiswal and Shruti Roy for being wonderful office mates and for teaching me how to say "life is difficult" in their respective languages.

I would also like to thank Julia Wecker, Maximilian Röhrich, Chafic Fawaz and Luis Filsinger, who joined the group during the final phase of my PhD, for their patience in listening to my many unfiltered lunchtime reflections, particularly during the writing period.

Before moving on, I would also like to thank all other members of the IQMT for contributing to a stimulating and supportive scientific atmosphere. My sincere thanks also go to the members of the mechanical workshop for their diligent and highly valuable technical assistance. I am equally grateful to the administrative staff for their invaluable help and support with the many organizational and bureaucratic aspects of academic life.

While a stimulating and enjoyable working environment is essential, finding balance and support outside the institute is just as important.

I would like to sincerely thank my flatmates — Prashanta, Saloni, Vaishnavi, Jakob, Kai, and Helena — for being wonderful companions throughout this journey. I am especially grateful for their patience with my occasional absent-mindedness and the many distractions that inevitably accompanied the writing phase of this thesis.

Al di fuori della vita in istituto, desidero ringraziare anche quelle persone che, pur da lontano, non hanno mai fatto mancare la loro vicinanza e il loro sostegno.

In particolare, vorrei ringraziare Marco, Giacomo, Riccardo, Sebastiano e Martino per le infinite polemiche e per aver saputo alleggerire, anche a distanza, il peso di questo percorso nei momenti più impegnativi.

Così anche Angelo, Andrea, Fabio, Francesco e Mattia, con cui, tra chiamate e partite a giochi da tavolo, ho trovato momenti di leggerezza e sostegno più importanti di quanto si possa immaginare. Un ringraziamento va anche a tutti gli altri amici che, in modi diversi, mi sono stati vicini durante questi anni.

Desidero ringraziare la mia famiglia. Sia i miei fratelli che i miei cugini, in molti modi diversi — con un messaggio, una telefonata o anche un aiuto inaspettato davanti a qualche imprevisto con LaTeX— non hanno mai fatto mancare il loro sostegno. La loro vicinanza è stata fondamentale durante tutto questo percorso. Un ringraziamento speciale va ai miei genitori. Mamma e Papà, senza di voi nulla di tutto questo sarebbe stato possibile.

Enfin, à Mathilda, pour avoir porté mon cœur tout au long de ces années et pour m'avoir fait sentir chez moi, même loin de chez moi. Merci.

A. Appendix: Crystal Growth

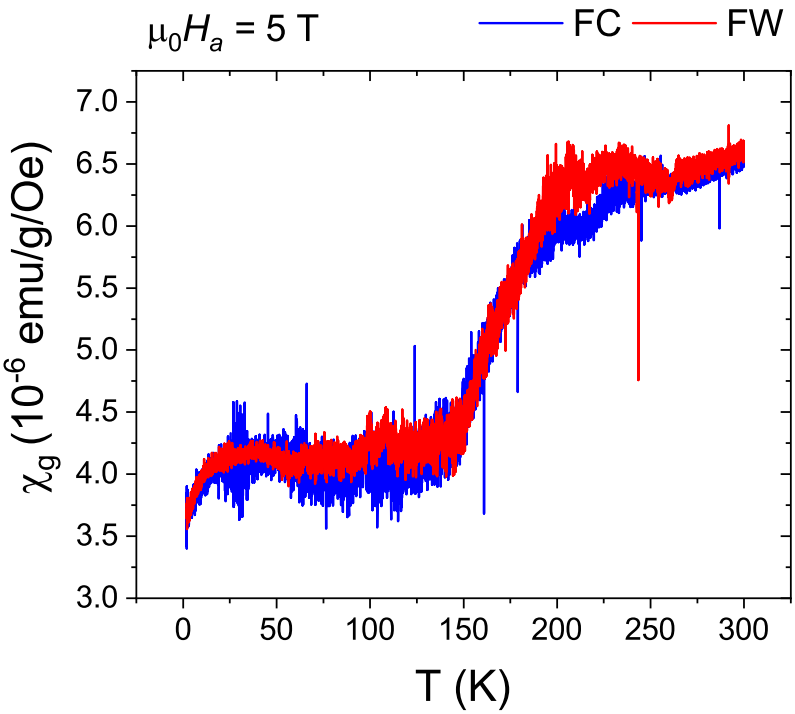

Figure A.1.: Field-cooled (FC) and field-warmed (FW) static mass magnetic susceptibility of $CrAs_{1-x}P_x$ single crystal, with x_{eff} = 1.8%. Measurements were conducted under a 5 T magnetic field applied parallel to the *a*-axis.

Fig. A.1 shows the static mass magnetic suscepitbility VSM measurement of $CrAs_{1-x}P_x$ single crystal with x_{eff} = 1.8%. The used measurement protocol differs from the one described in Sec. 3.3.1 due to the characteristics of this particular crystal batch. Given the very small sample mass (0.32 mg) and the intrinsically low magnetic moment of $CrAs_{1-x}P_x$- paramagnetic at ambient condition and antiferromagnetic at low temperatures - the sample was centered at room temperature under a 5 T field. The measurement was then performed while cooling and warming in the same applied field. The poor signal-to-noise ratio is due to the extremely low sample mass. Nevertheless, a magnetic transition is still apparent around 200 K, consistent with the expected T_N for x_{eff} = 1.8% based on the phase diagram shown in Fig. 3.18. No significant hysteresis is observed. However, due to the limited data quality, we can't conclude that the sample is near a critical doping x_c where the magnetic transition becomes second-order [7]. Furthermore the *b*-lattice parameter extracted from PXRD is larger than that of $CrAs_{1-x}P_x$ single crystals with an higher x_{eff}, which exhibit lower T_N and a clear first-order transition. The suppressed hysteresis could be attributed to the high measurement field or to residual field effects because of the different measurement protocol.

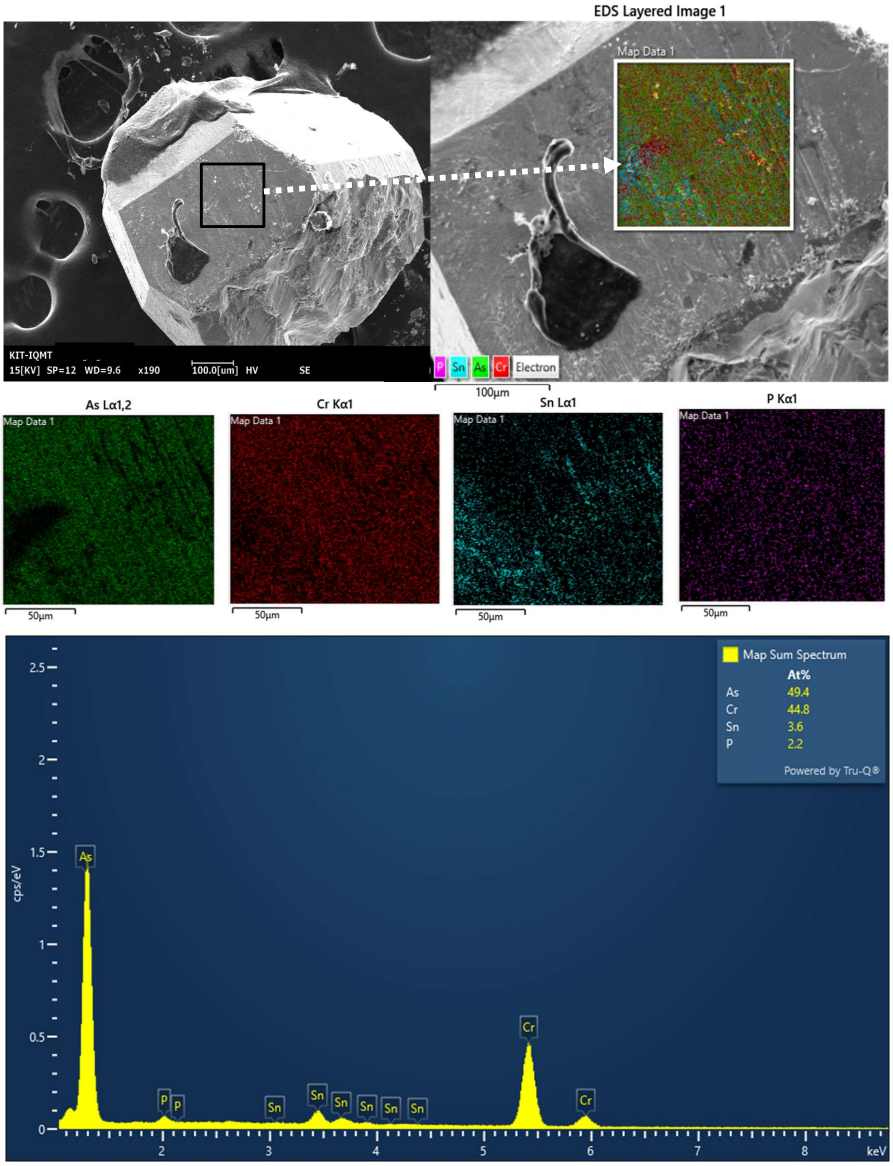

Figure A.2.: Top: Electron microscope image of a $CrAs_{1-x}P_x$ single crystal facet oriented along the *a*-axis. The highlighted region marks the area analyzed for elemental composition via EDX, shown with corresponding relative elemental maps. Bottom: EDX spectrum of the $CrAs_{1-x}P_x$ single crystal facet. In the inset, the atomic percentage of the detected elements are shown.

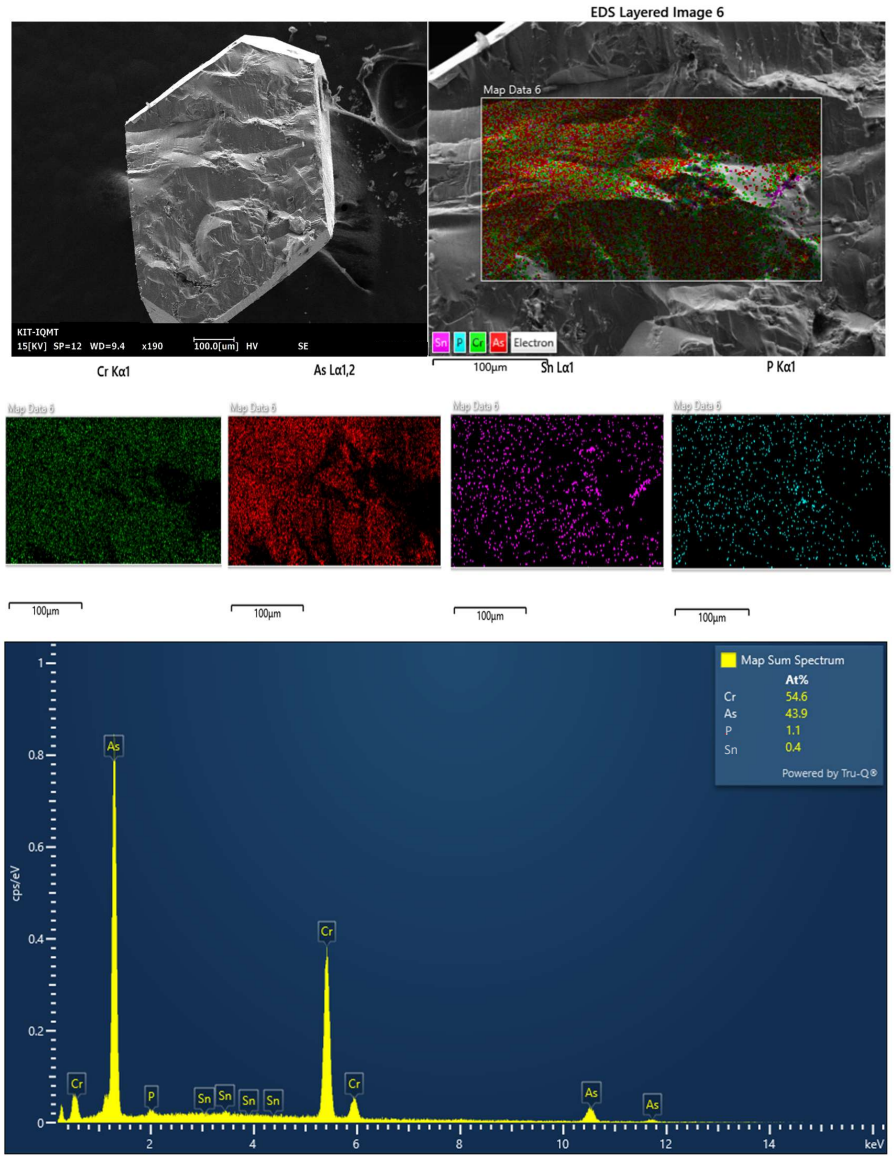

Figure A.3.: Top: Cross-sectional electron microscope image of $CrAs_{1-x}P_x$ single crystal, with the *a*-axis oriented out of plane. The highlighted region indicates the area analyzed for elemental composition using EDX, accompanied by relative elemental maps. Bottom: EDX spectrum of the cross-sectional of $CrAs_{1-x}P_x$ single crystal facet. In the inset, the atomic percentage of the detected elements are shown.

A.1. Byproducts of Crystal Growth

The technique of flux growth requires choosing a flux that does not react with the educts or form stable phases with the target compound [56]. However, this can't always be guaranteed and undesired reaction can occur and form growth byproducts.
During flux growth experiments, an unintentional formation of two binary compounds was observed, Cr_3Sn_2 and Sn_3As_2, shown in Fig. A.4 and A.5.

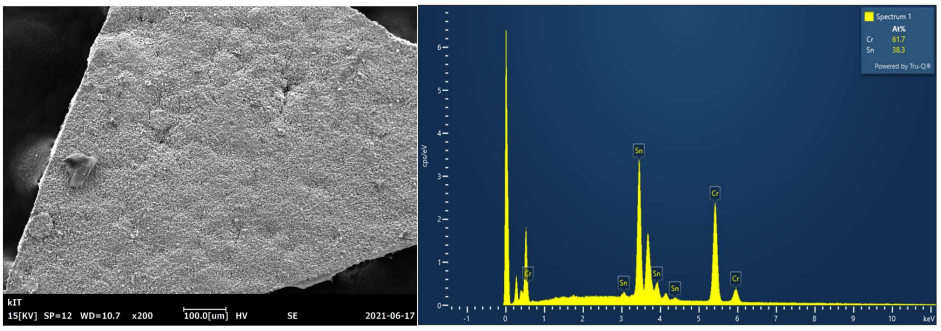

Figure A.4.: Electron microscope image of a Cr_3Sn_2 crystal. The highlighted region marks the area analyzed for elemental composition via EDX, shown with corresponding relative elemental maps.

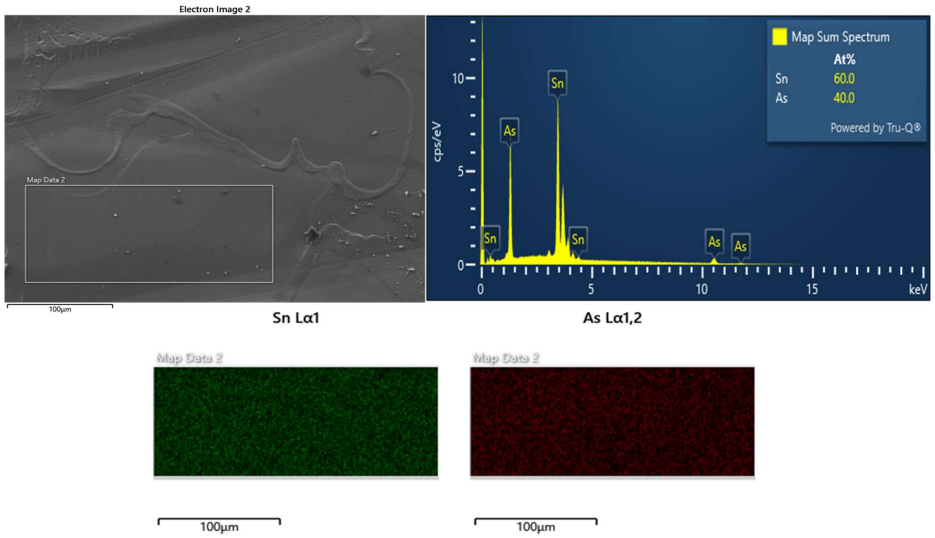

Figure A.5.: Electron microscope image of a portion of a Sn_3As_2 crystal. The highlighted region marks the area analyzed for elemental composition via EDX, shown with corresponding relative elemental maps.

These phases were identified via EDX, which confirmed stoichiometries consistent with a 3:2 ratio in both the Cr-Sn and Sn-As system. To our knowledge, this is the first direct experimental observation of Cr_3Sn_2 and Sn_3As_2 crystals, as no prior studies have reported the existence of these compounds in a clear crystalline form.

B. Appendix: Powder X-ray diffraction

Batch	AAH12	AAH75	AAH69	AAH70	AAH81	AAH89	AAH90
x_{nom}	0%	3%	5%	10%	13%	20%	25%
x_{ref}	0%	5.6%	4.4%	15.4%	3.2%	4.6%	4.1%
x_{eff}	0%	0.7%	0.9%	2.7%	1.9%	1.8%	3.8%
x_{sur}	0%	0.4%	0.6%	4.5%	3.2%	n.m.	0.6%
R_p	4.56%	5.08%	3.87%	3.70%	3.79%	6.80%	4.14%
w_p	6.78%	6.71%	5.89%	5.38%	5.93%	9.58%	6.48%
G.o.F.	0.08	0.09	0.08	0.07	0.08	0.07	0.08
a(Å)	5.64820(15)	5.65528(15)	5.65059(10)	5.64719(10)	5.65248(15)	5.65021(50)	5.64360(15)
b(Å)	3.46624(10)	3.45651(10)	3.45464(10)	3.43696(5)	3.44472(10)	3.446052(25)	3.42595(10)
c(Å)	6.20338(15)	6.21564(15)	6.20991(10)	6.20934(10)	6.21459(15)	6.21604(45)	6.20776(15)
V(Å^3)	121.450(5)	121.501(5)	121.222 (5)	120.518(5)	121.006(5)	121.032(10)	120.025(5)
X_{Cr}	0.00700	0.00833	0.00718	0.00530	0.00318	0.00273	0.00229
Z_{Cr}	0.19402	0.19626	0.19911	0.19643	0.19517	0.19415	0.19030
$X_{As/P}$	0.19781	0.19974	0.20158	0.19939	0.20098	0.20884	0.20057
$Z_{As/P}$	0.57208	0.57316	0.57465	0.57302	0.57307	0.57383	0.57503

Table B.1.: Powder x-ray diffraction results from Rieveld refinement for $CrAs_{1-x}P_x$ crushed single crystals at ambient condition.

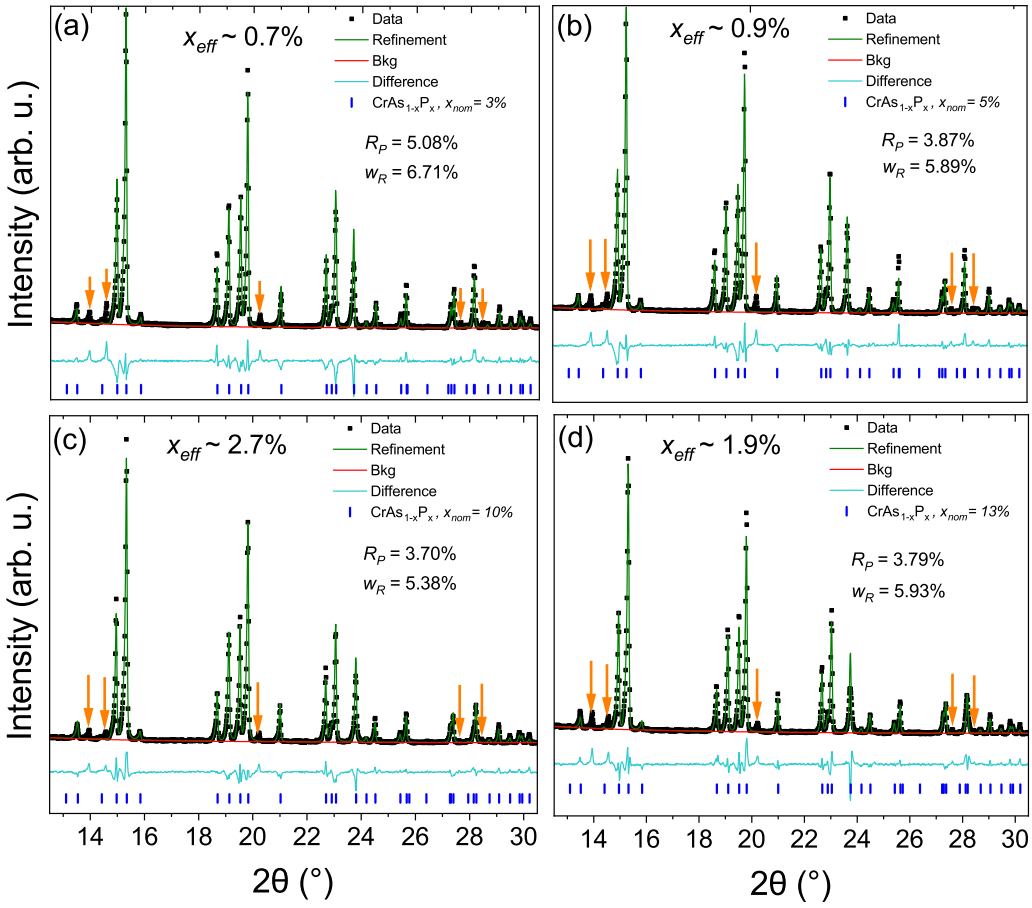

Figure B.1.: Selected region of PXRD refinement for crushed $CrAs_{1-x}P_x$ single crystals at ambient conditions, with effective doping levels of a) $x_{eff} \approx 0.7\%$ (b) $x_{eff} \approx 0.9\%$ (c) $x_{eff} \approx 2.7\%$ (d) $x_{eff} \approx 1.9\%$. Measured diffraction patterns (dots) are shown alongside the calculated profiles (solid lines). The difference curve (shown as gray lines) highlights the discrepancies between the observed and calculated intensities. Tick marks indicate the positions of expected Bragg reflections. Orange arrows indicate the unindexed reflections.

C. Appendix: Raman

Fig. C.1 shows the results of density functional theory (DFT) calculations on CrAs, performed with the mixed-basis pseudopotential to compute the zone-centered phonon modes, including the modes frequencies and eigendisplacements. For further details on the computational methods, see [52].

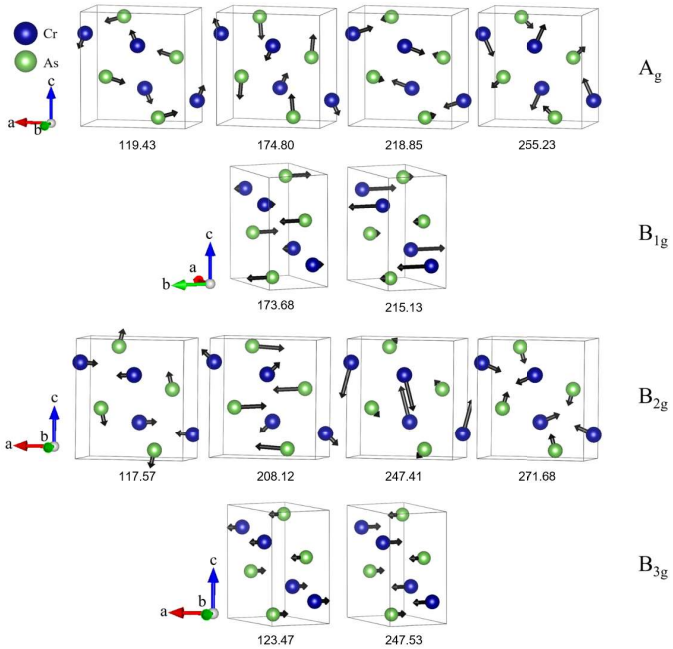

Figure C.1.: Schematic representation of Raman-active modes in CrAs, calculated using DFT. The phonon eigenvectors are indicated by black arrows with the corresponding frequencies shown below every illustration. The associated irreducibile representations are labeled on the right. Image from [52].

Tab. C.1 shows the Raman tensors corresponding to each irreducible representation of the Raman-active modes, as determined via nuclear site group analysis. For further details on the analysis of Raman modes in CrAs, see [52].

$\mathbf{A}_g$	$\mathbf{B}_{1g}$	$\mathbf{B}_{2g}$	$\mathbf{B}_{3g}$
$\begin{pmatrix} a & 0 & 0 \\ 0 & b & 0 \\ 0 & 0 & c \end{pmatrix}$	$\begin{pmatrix} 0 & d & 0 \\ d & 0 & 0 \\ 0 & 0 & 0 \end{pmatrix}$	$\begin{pmatrix} 0 & 0 & e \\ 0 & 0 & 0 \\ e & 0 & 0 \end{pmatrix}$	$\begin{pmatrix} 0 & 0 & 0 \\ 0 & 0 & f \\ 0 & f & 0 \end{pmatrix}$
xx, yy, zz	xy, yx	xz, zx	yz, zy

Table C.1.: Raman tensors and corresponding allowed polarization geometries for the Raman-active irreducible representations of the D_{2h} point group.

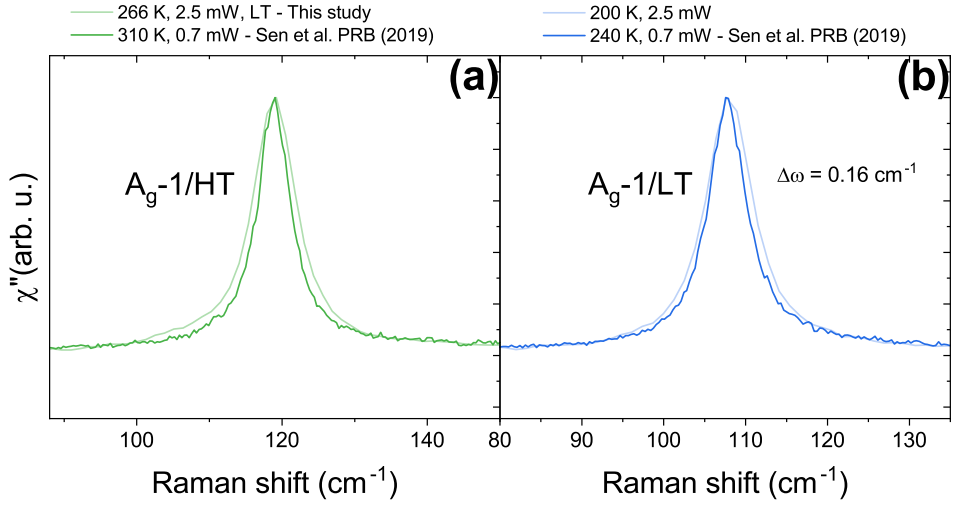

Figure C.2.: (a) Comparison of Raman spectra focused on A_g-1 phonon: data from this study (266 K, 2.5 mW incident laser power) in the bulk LT phase and from Sen et al. (310 K, 0.7 mW) [8]. The excess broadening in our data may arise from strain at the surface, due to coexistence of bulk LT and laser heated HT regions. (b) Comparison of Raman spectra focused on the A_g-1 phonon in the full LT phase: data from this study (200 K, 2.5 mW) and from Sen et al. (240 K, 0.7 mW). The frequency difference between the two spectra, Δw, is obtained from the fitted A_g-1 peak positions and labeled alongside the spectra

C.1. Pressure and Temperature Dependent Raman Experiments at Néel institute

Phase	Pressure (GPa)	ω_0 (cm$^-$1)	A (cm$^-$1)
LT	0	186.76	1.25
LT	0.42	187.72	1.28
HT	0	183.53	1.00
HT	0.42	182.77	0.61
HT	0.77	187.43	1.49
HT	1.1	189.22	1.58

Table C.2.: Summary of the Klemens model fitting parameters for the A_g-2 phonon in CrAs, extracted for both the low-temperature (LT) and high-temperature (HT) phases at different pressures. Data at 0 GPa are from [8].

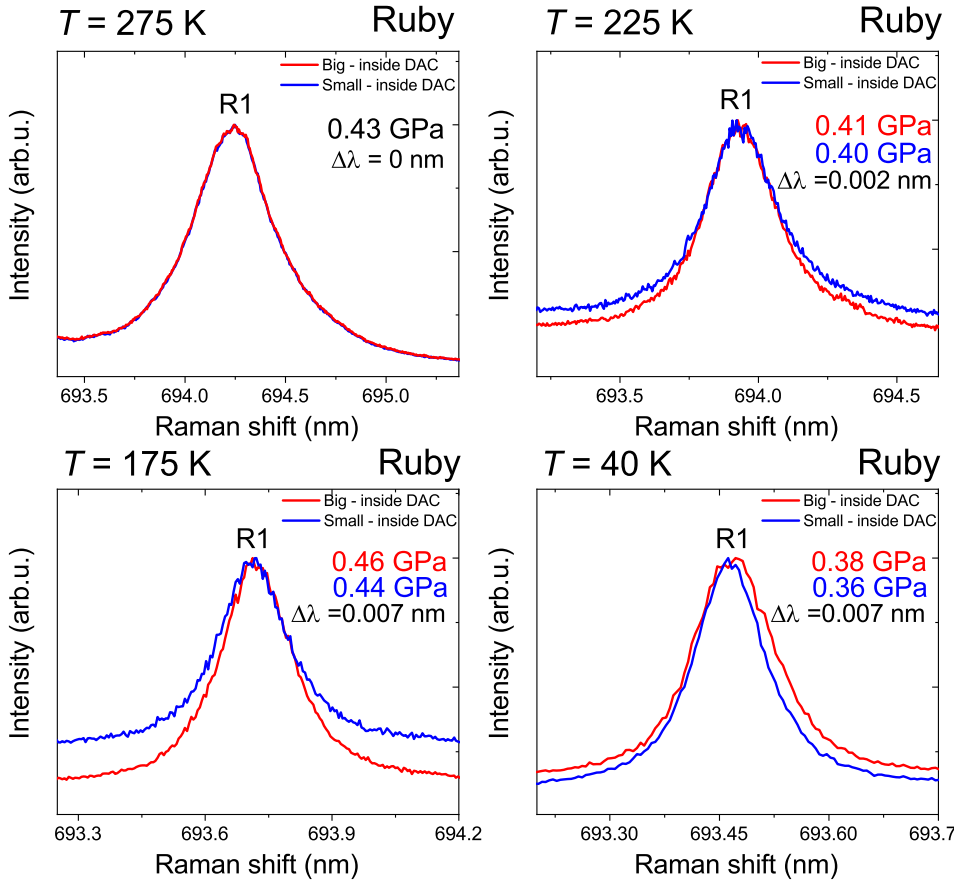

Figure C.3.: Raman scattering measurements of both rubies in the first MDAC cell, during the initial cooling cycle under ≈ 0.4 GPa, at different temperatures: 275 K, 225 K, 175 K, 40 K. Around 225 K, the smaller ruby consistently exhibits a redshift and broadening of its fluorescence. This suggests a devation from hydrostatic condition.

Phase	Pressure (GPa)	$\Gamma_{0_{Ag-1}}$(cm^{-1})	C_{Ag-1} (cm^{-1})	$\Gamma_{0_{Ag-2}}$(cm^{-1})	C_{Ag-2} (cm^{-1})
LT	0			0	0.62
LT	0.42			0	1.60
HT	0	7.10	−0.26	2.02	0.72
HT	0.42	5.28	0.16	5.59	0.25
HT	0.77	4.45	0.08	1.80	1.57
HT	1.1	2.84	0.34	2.69	0.85

Table C.3.: Summary of the Klemens model fitting parameters for the A_g-2 phonon in CrAs, extracted for both the low-temperature (LT) and high-temperature (HT) phases at different pressures. Data at 0 GPa are from [8].

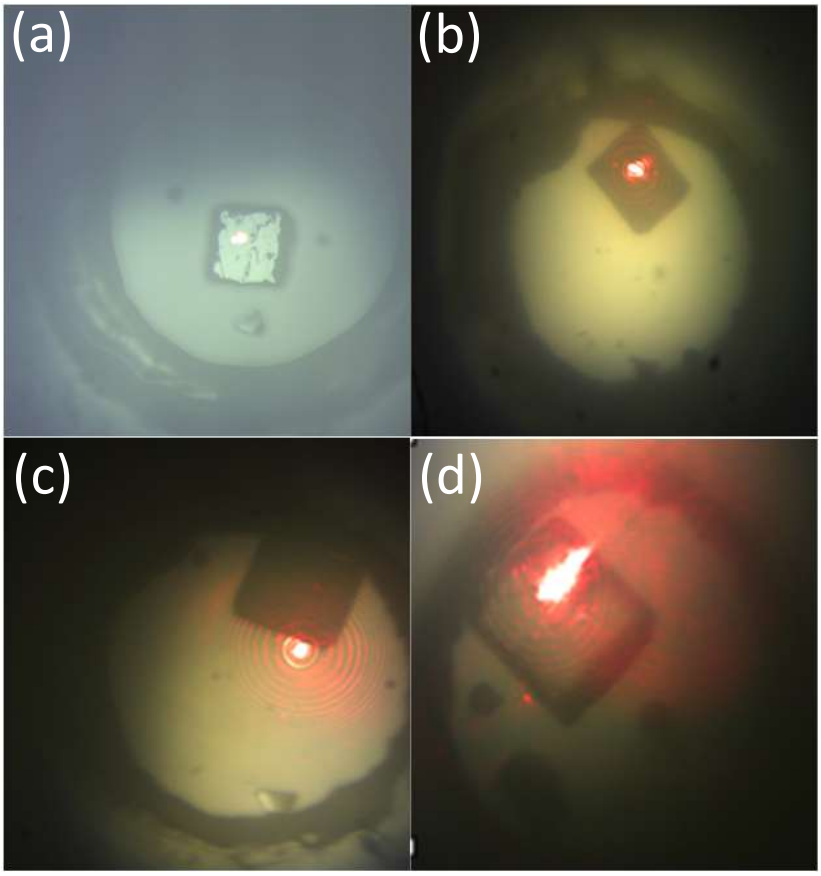

Figure C.4.: Images of the MDAC gasket cavities at different stages of the experiment, showing the sample displacement as a function of pressure and temperature. (a) At 296 K and 0.25 GPa. (b) At 175 K and ≈ 0.45 GPa, after the first observed shift of the sample, which occurred around 190 K. (c) At 300 K and ≈ 1.2 GPa, after the unsuccessful attempt to measure at 0.7 GPa. (d) At 300 K and ≈ 0.19 GPa, in newly mounted MDAC cell.

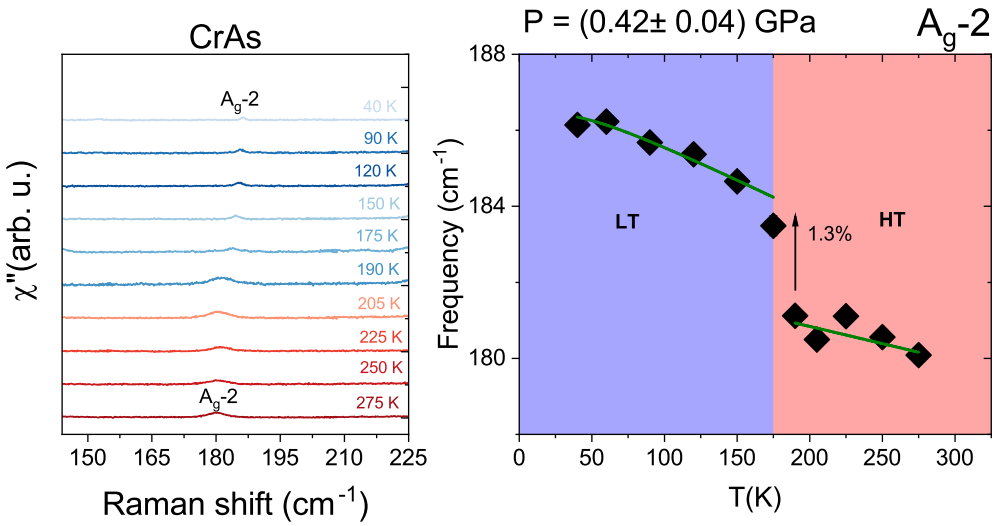

Figure C.5.: Left: Selected region of CrAs single crystal Raman spectra under pressure, showing the evolution of the A_g-2 phonon mode. Temperature and corresponding pressure values are shown alongside the curves. Right: temperature dependence of the A_g-2 phonon frequency, at approximately 0.42 GPa. Black arrows indicate the relative frequency shift $(\omega_{LT} - \omega_{HT})/\omega_{HT}$ at the onset of the transition. The green lines represent fits using the Klemens model [88].

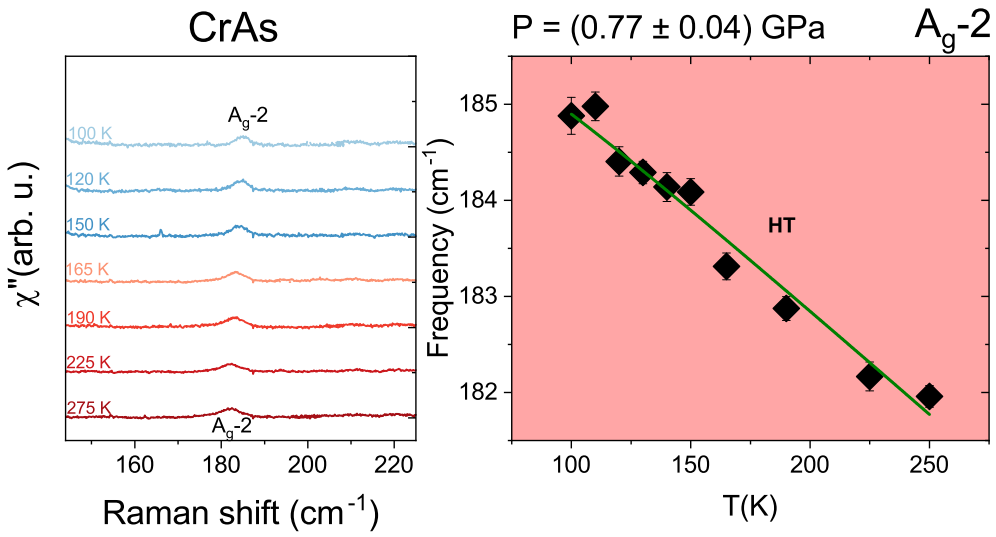

Figure C.6.: Left: Selected region of CrAs single crystal Raman spectra under pressure, showing the evolution of the A_g-2 phonon mode. Temperature and corresponding pressure values are shown alongside the curves. The asterisk marks additional features unrelated to the A_g-2 mode, as discussed in the main text. Right: temperature dependence of the A_g-2 phonon frequency, at approximately 0.77 GPa. The green lines represent fits using the Klemens model [88].

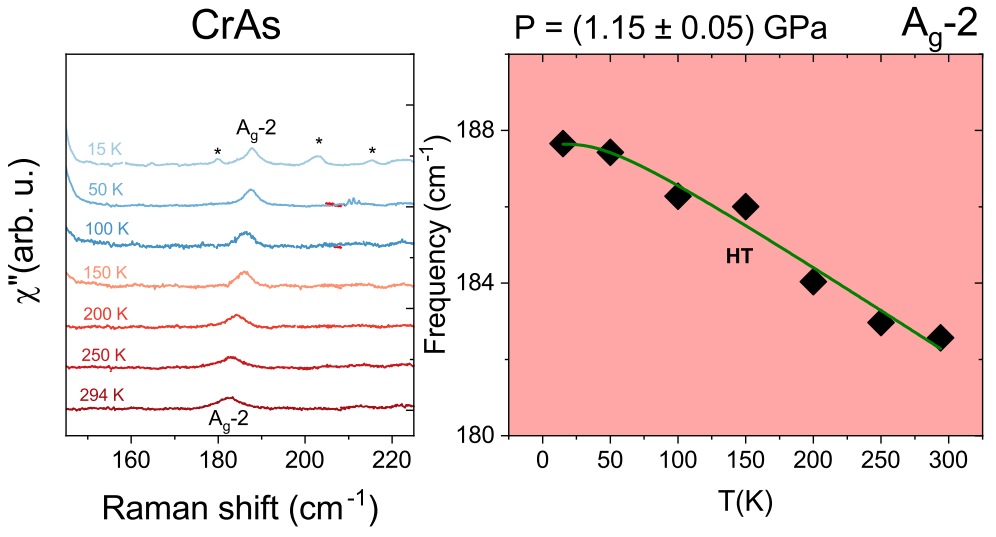

Figure C.7.: Left: Selected region of CrAs single crystal Raman spectra under pressure, showing the evolution of the A_g-2 phonon mode. Temperature and corresponding pressure values are shown alongside the curves. The asterisk marks additional features unrelated to the A_g-2 mode, as discussed in the main text. Right: temperature dependence of the A_g-2 phonon frequency, at approximately 1.15 GPa. The green lines represent fits using the Klemens model [88].

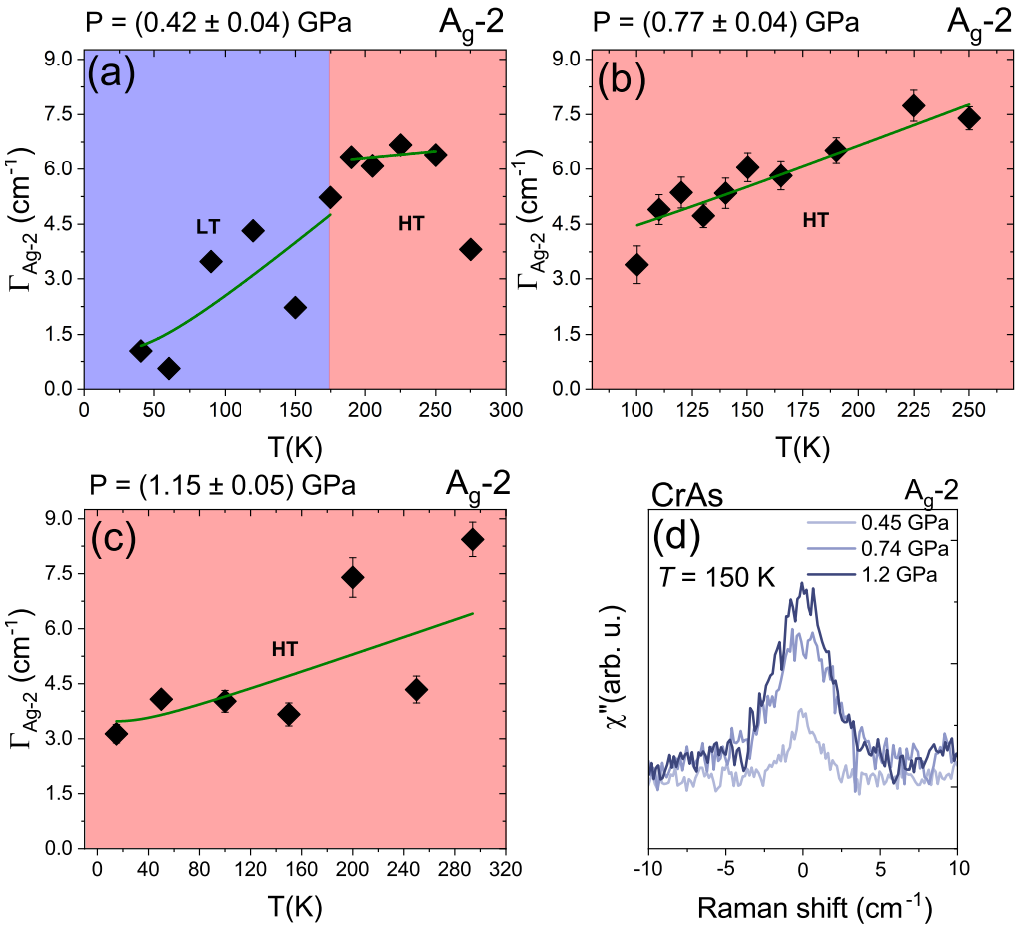

Figure C.8.: Temperature dependence of the measured FWHM of the A_g-2 phonon of CrAs under different applied pressure: (a) approximately 0.42 GPa, (b) approximately 0.77 GPa and (c) approximately 1.1 GPa. Green lines correspond to fits using the Klemens model [88]. (d) Comparison of the FWHM of the A_g-2 phonon at 150 K for different pressures. Spectra were horizontally shifted for visual clarity.

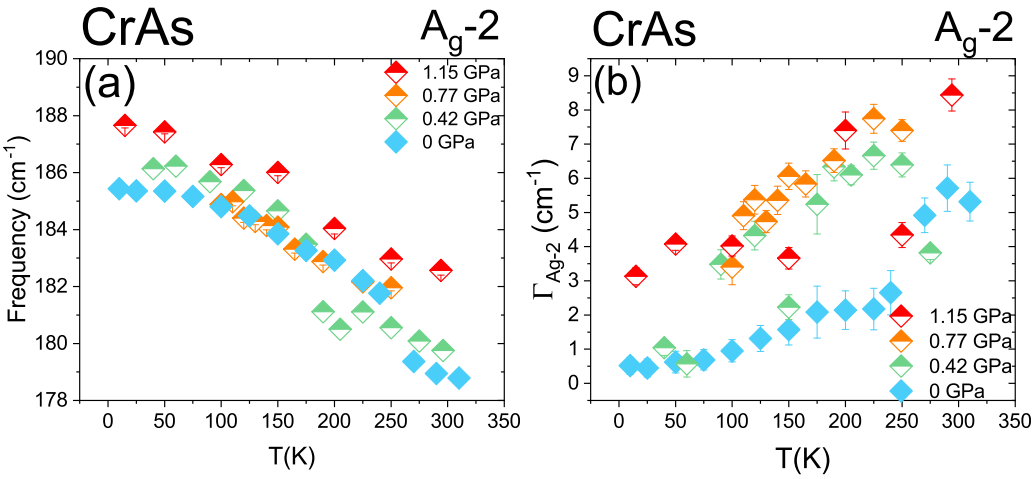

Figure C.9.: Temperature dependence comparison of the A_g-2 phonon mode in CrAs, at different pressures: (a) phonon frequency (b) FWHM. Data at 0 GPa are taken from [8].

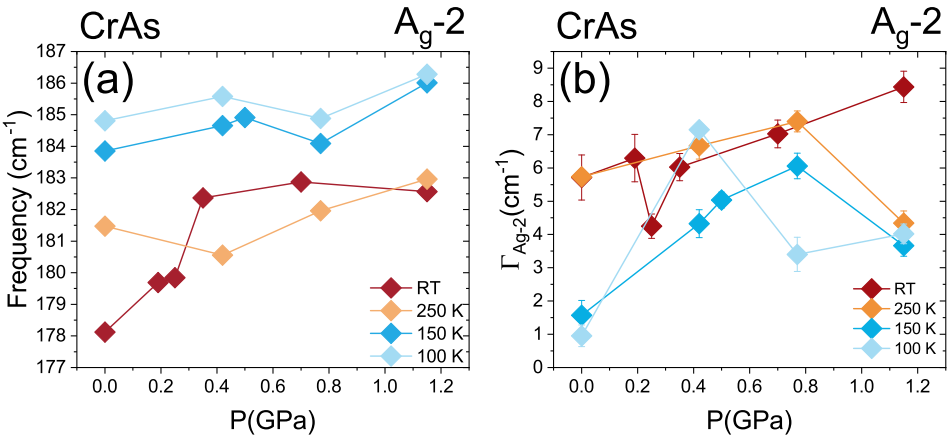

Figure C.10.: Pressure dependence of the A_g-2 phonon mode parameters in CrAs at selected temperatures: (a) phonon frequency (b) FWHM. Data at 0 GPa are taken from [8]

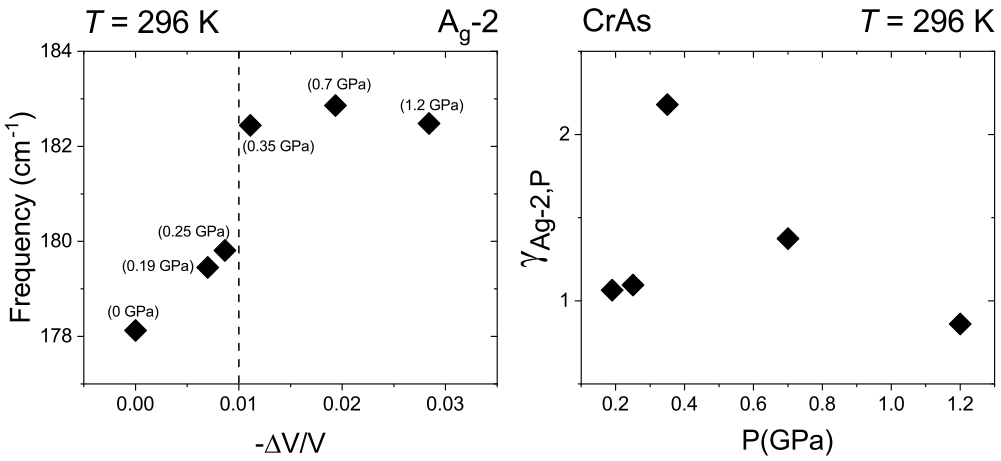

Figure C.11.: (a) Volume dependence of the A_g-2 phonon frequency at room temperature. Dashed line represent the critical volume (b) Pressure dependence of the Grüneisen parameter for the A_g-2 phonon at room temperature, calculated using the lattice parameter data from [18].

C.2. Raman on Phosphorus-doped samples

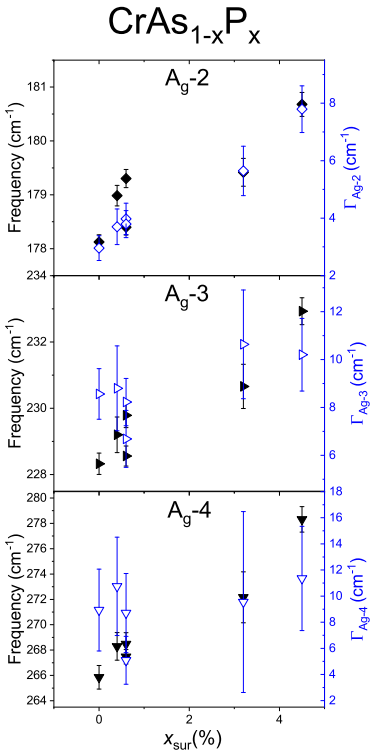

Figure C.12.: Room temperature $CrAs_{1-x}P_x$ single crystals phonon frequencies and linewidths of A_g-2, A_g-3 and A_g-4 as a function of the phosphorus concentration on the as grown surface, x_{sur}

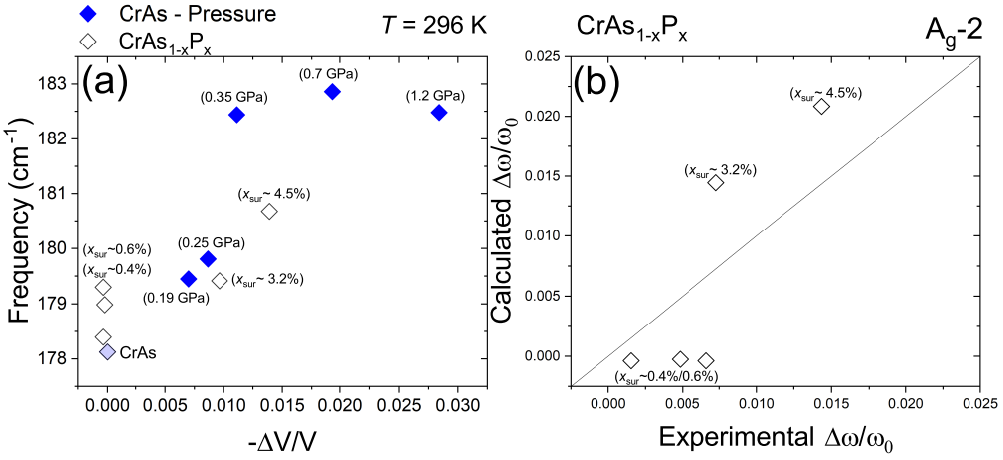

Figure C.13.: (a) A_g-2 phonon frequency as a function of the relative volume change for CrAs under hydrostatic pressure (see Sec. 4.3) and for $CrAs_{1-x}P_x$ single crystals. (b) Relative A_g-2 phonon frequency change, $\Delta\omega/\omega_0$, calculated using the volume-driven Grüneisen formalism, plotted against the experimentally measured relative A_g-2 phonon frequency change at room temperature. The solid lines have unit slope and indicate perfect agreement between calculated and experimental frequency shifts.

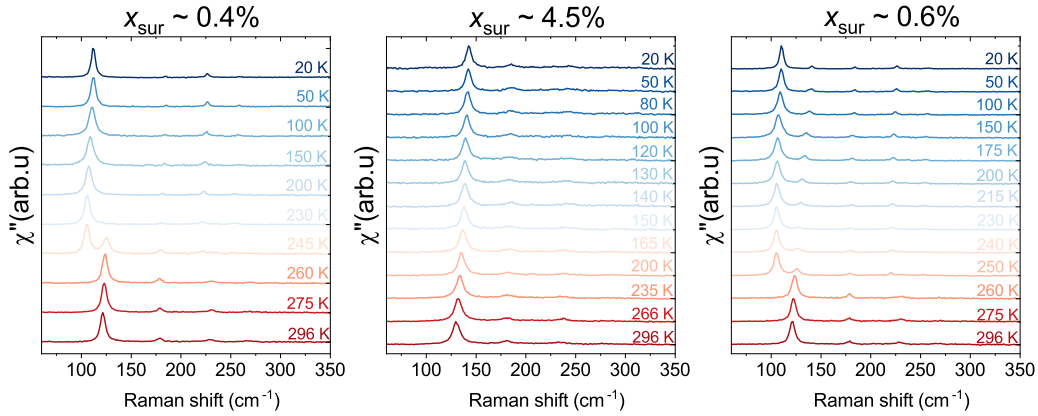

Figure C.14.: Temperature dependent Raman spectra of the different $CrAs_{1-x}P_x$single crystal batches. The corresponding temperatures are labeled next to the curves.

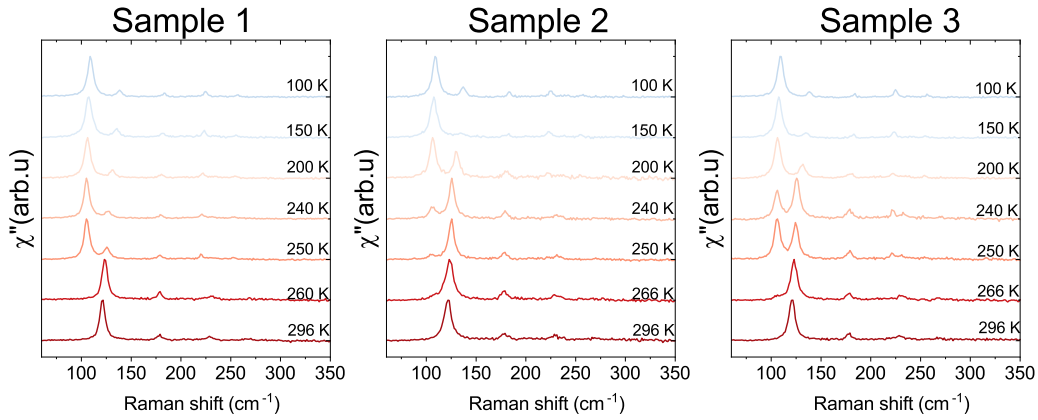

Figure C.15.: Temperature dependent Raman spectra of three different $CrAs_{1-x}P_x$single crystal from the $x_{sur} \approx 0.6\%$ batch, measured during the same thermal cycle with 0.2 mW incident laser power. The corresponding temperatures are labeled next to the curves.

Phase	**Pressure (GPa) / x_{sur}(%)**	Γ_0	C
LT	0 GPa		
LT	0.42 GPa		
LT	0.4%		
LT	0.6%		
HT	0 GPa	7.10	-0.26
HT	0.42 GPa	5.28	0.16
HT	0.77 GPa	4.45	0.08
HT	1.15 GPa	2.84	0.34
HT	0.4%	5.49	-0.07
HT	0.6%	5.80	-0.11
HT ($T > 145$K)	4.5%	6.19	0.33
HT ($T < 145$K)	4.5%	3.94	1.31

Table C.4.: Summary of the linewidth Klemens model fitting parameters for the A_g-1 phonon, obtained from CrAs under applied pressure and from $CrAs_{1-x}P_x$samples with different surface doping (x_{sur}). Values are reported for both the low-temperature (LT) and high-temperature (HT) phases at different pressures. Data at 0 GPa are from [8].

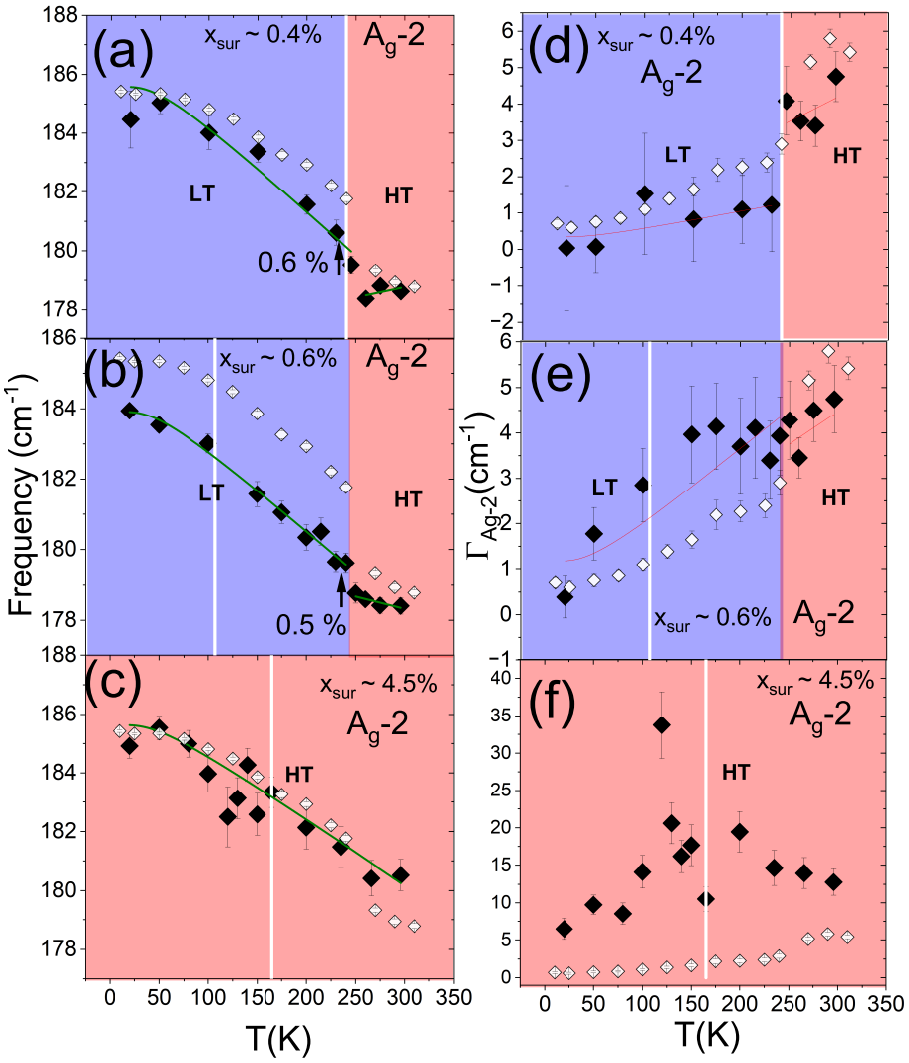

Figure C.16.: Temperature dependence of the A_g-2 phonon mode parameters in $CrAs_{1-x}P_x$for $x_{sur} \approx 0.4\%, 0.6\%, 4.5\%$, respectively, measured with 0.2 mW laser power: (a-c) Phonon frequency (d-f) Phonon linewidth. The white lines indicate the T_N of the respective batch, as listed in Sec. 3.3.1. Black arrows indicate the relative frequency shift $(\omega_{LT} - \omega_{HT})/\omega_{HT}$ at the transition. A marked deviation of the linewidth from the Klemens model is observed. Open symbols correspond to A_g-2 data of pure CrAs measured at 0.7 mW, from Ref. [8].

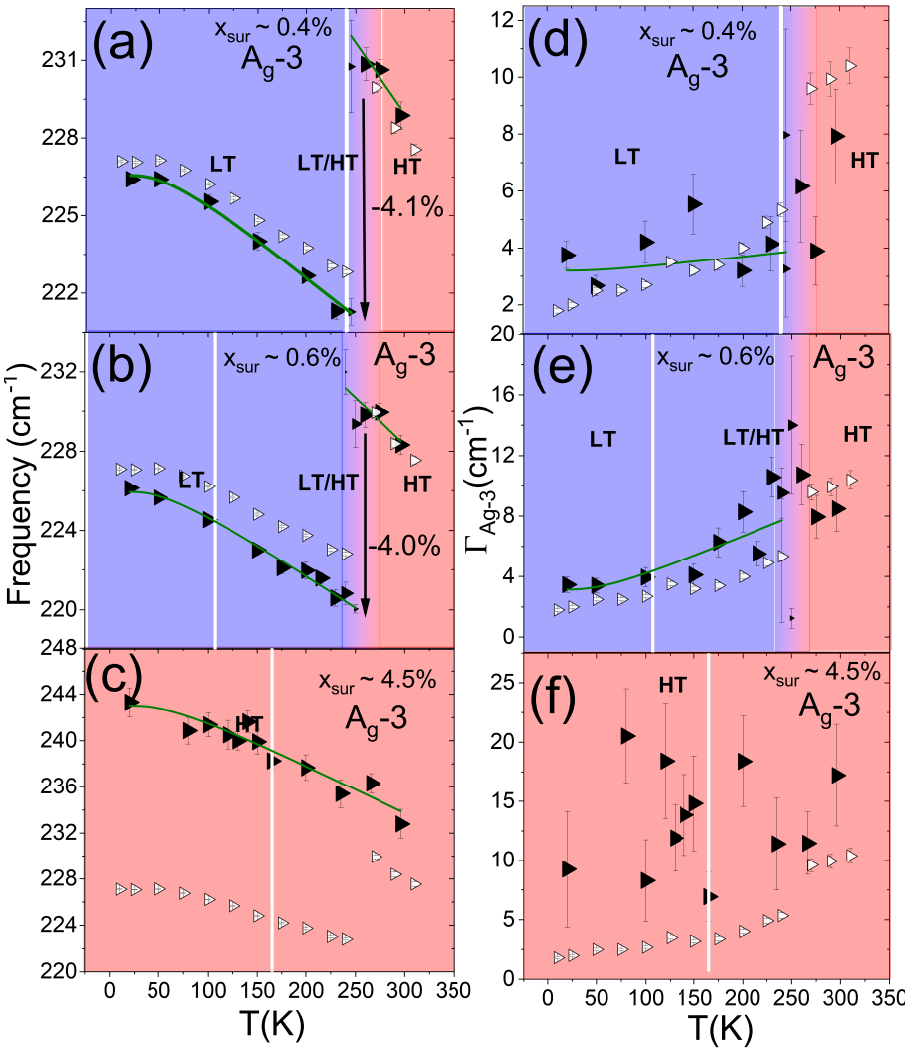

Figure C.17.: Temperature dependence of the A_g-3 phonon mode parameters in $CrAs_{1-x}P_x$ for $x_{sur} \approx 0.4\%, 0.6\%, 4.5\%$, respectively, measured with 0.2 mW laser power: (a-c) Phonon frequency (d-f) Phonon linewidth. The white lines indicate the T_N of the respective batch, as listed in Sec. 3.3.1. Black arrows indicate the relative frequency shift $(\omega_{LT} - \omega_{HT})/\omega_{HT}$ at the onset of the coexistence. A marked deviation of the linewidth from the Klemens model is observed. Open symbols correspond to A_g-3 data of pure CrAs measured at 0.7 mW, from Ref. [8].

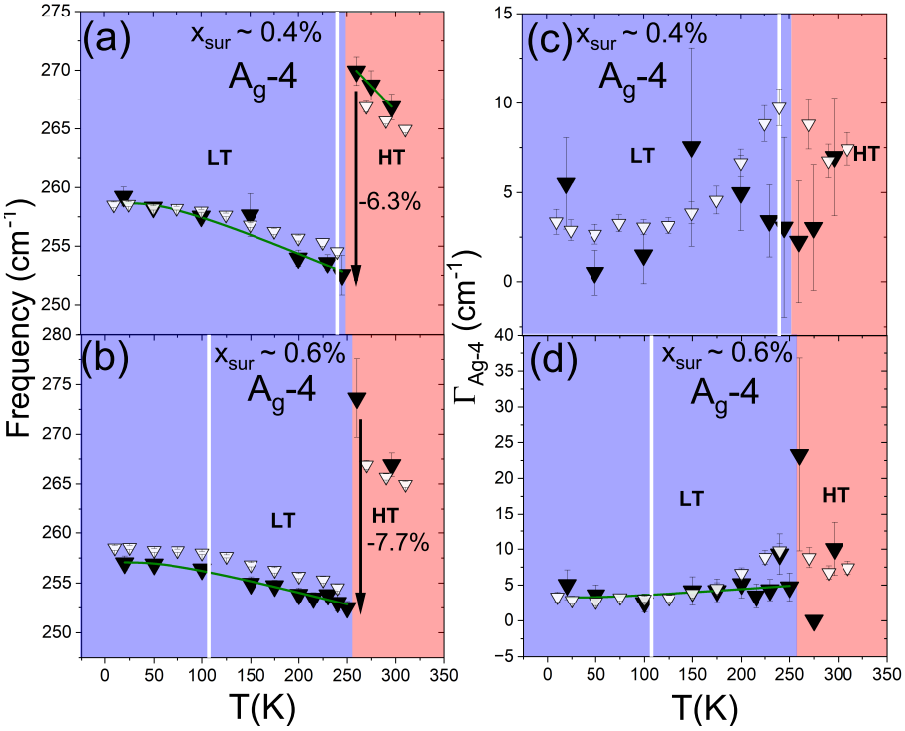

Figure C.18.: Temperature dependence of the A_g-3 phonon mode parameters in $CrAs_{1-x}P_x$, measured with 0.2 mW laser power. Data for the $x_{sur} \approx 4.5\%$ sample are not shown, as the A_g-4 mode could not be fitted with sufficient reliability. (a-b) show phonon frequency and panel (c-d) phonon linewidth for $x_{sur} \approx 0.4\%, 0.6\%$. The white lines indicate the T_N of the respective batch, as listed in Sec. 3.3.1. Black arrows indicate the relative frequency shift $(\omega_{LT} - \omega_{HT})/\omega_{HT}$ at the transition. A marked deviation of the linewidth from the Klemens model is observed. Open symbols correspond to A_g-4 data of pure CrAs measured at 0.7 mW, from Ref. [8].

Phase	**Pressure (GPa) / x_{sur}(%)**	ω_0 **(cm^{-}1)**	A **(cm^{-}1)**	Γ_0	C
LT	0 GPa	186.76	1.25	0	0.62
LT	0.42 GPa	187.72	1.28	0	1.60
LT	0.4%	187.64	2.06	0	0.34
LT	0.6%	185.53	1.61	0	1.18
HT	0 GPa	183.53	1.00	2.02	0.72
HT	0.42 GPa	182.77	0.61	5.59	0.25
HT	0.77 GPa	187.43	1.49	1.80	1.57
HT	1.15 GPa	189.22	1.58	2.69	0.85
HT	0.4%	176.60	−0.45	0	0.88
HT	0.6%	180.50	0.46	0	0.95
HT	4.5%	187.17	1.55		

Table C.5.: Summary of the Klemens model fitting parameters for the A_g-2 phonon, obtained from CrAs under applied pressure and from $CrAs_{1-x}P_x$ samples with different surface doping (x_{sur}). Values are reported for both the low-temperature (LT) and high-temperature (HT) phases at different pressures. Data at 0 GPa are from [8].

Phase	Pressure (GPa) / x_{sur}(%)	ω_0 (cm^{-}1)	A (cm^{-}1)	Γ_0	C
LT	0 GPa	229.36	2.21	0.72	0.88
LT	0.4%	229.12	2.56	2.88	0.32
LT	0.6%	228.66	2.72	0.88	2.26
HT	0 GPa	247.38	5.58	3.80	1.93
HT	0.4%	246.50	5.05		
HT	0.6%	243.51	4.31		
HT	4.5%	246.76	3.74		

Table C.6.: Summary of the Klemens model fitting parameters for the A_g-3 phonon, obtained from CrAs under applied pressure and from $CrAs_{1-x}P_x$ samples with different surface doping (x_{sur}). Values are reported for both the low-temperature (LT) and high-temperature (HT) phases at different pressures. Data at 0 GPa are from [8].

Phase	Pressure (GPa) / x_{sur}(%)	ω_0 (cm^{-}1)	A (cm^{-}1)	Γ_0	C
LT	0 GPa	260.68	2.03	1.71	1.51
LT	0.4%	262.04	3.37	2.88	0.32
LT	0.6%	259.40	2.33	2.41	2.26
HT	0 GPa	280.83	5.02		
HT	0.4%	294.38	9.43		
HT	0.6%	326.86	22.76		

Table C.7.: Summary of the Klemens model fitting parameters for the A_g-4 phonon, obtained from CrAs under applied pressure and from $CrAs_{1-x}P_x$ samples with different surface doping (x_{sur}). Values are reported for both the low-temperature (LT) and high-temperature (HT) phases at different pressures. Data at 0 GPa are from [8].

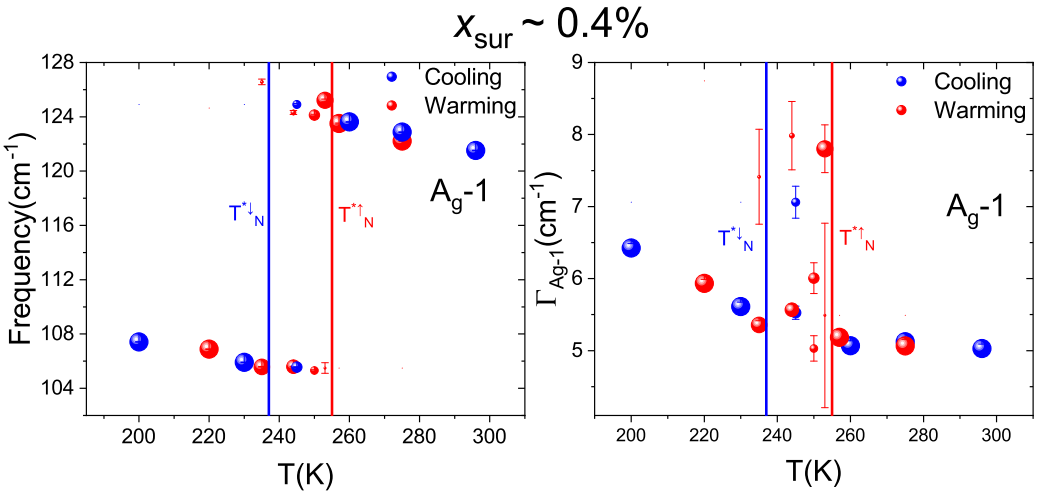

Figure C.19.: Selected region of the temperature dependence of the A_g-1 phonon mode in a $x_{sur} \approx 0.4\%$ $CrAs_{1-x}P_x$ single crystal, measured with 0.2 mW incident laser power during cooling (blue) and warming (red). The blue and red lines indicate the raman detected transition temperature (T_N^*) for cooling and warming cycles, respectively.

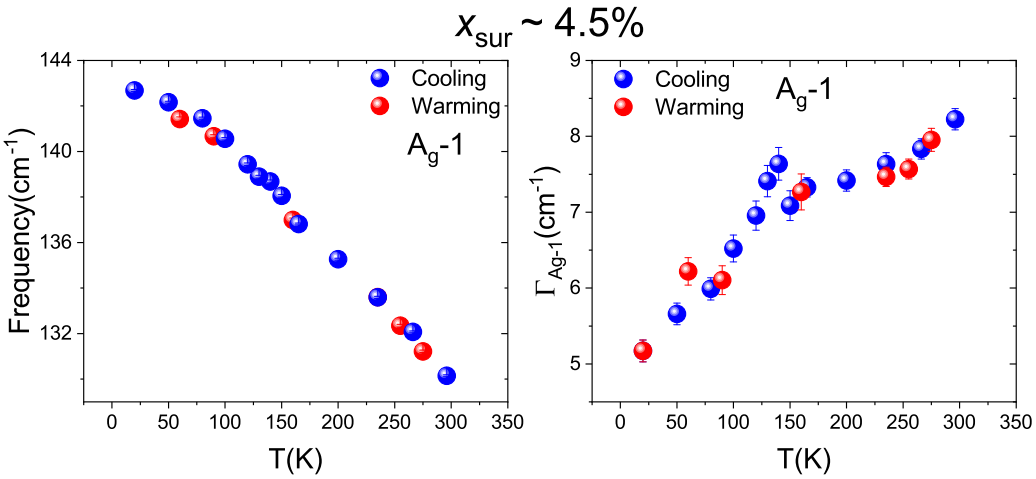

Figure C.20.: Temperature dependence of the A_g-1 phonon mode in a $x_{sur} \approx 4.5\%$ $CrAs_{1-x}P_x$single crystal, measured with 0.2 mW incident laser power during cooling (blue) and warming (red).

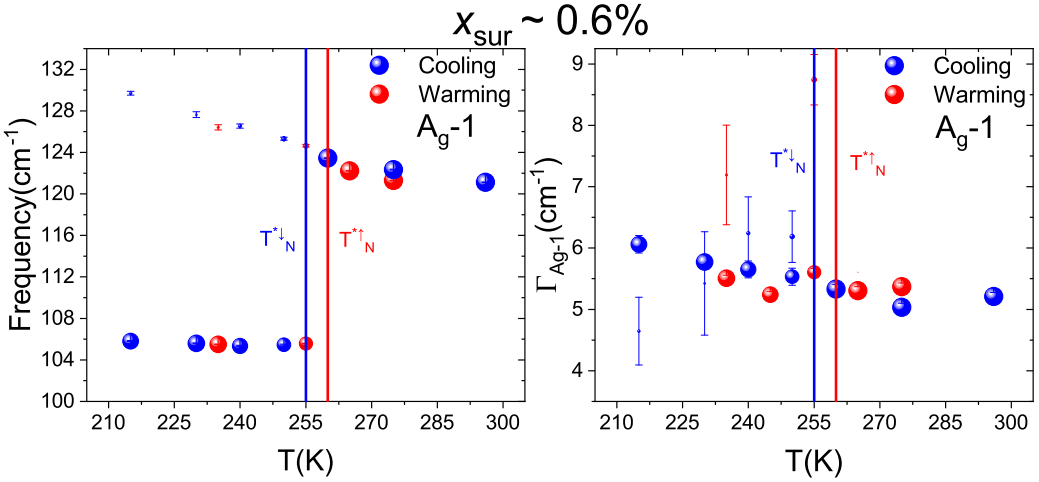

Figure C.21.: Selected region of the temperature dependence of the A_g-1 phonon mode in a $x_{sur} \approx 0.6\%$ $CrAs_{1-x}P_x$single crystal, measured with 0.2 mW incident laser power during cooling (blue) and warming (red). The blue and red lines indicate the raman detected transition temperature (T^*_N) for cooling and warming cycles, respectively.

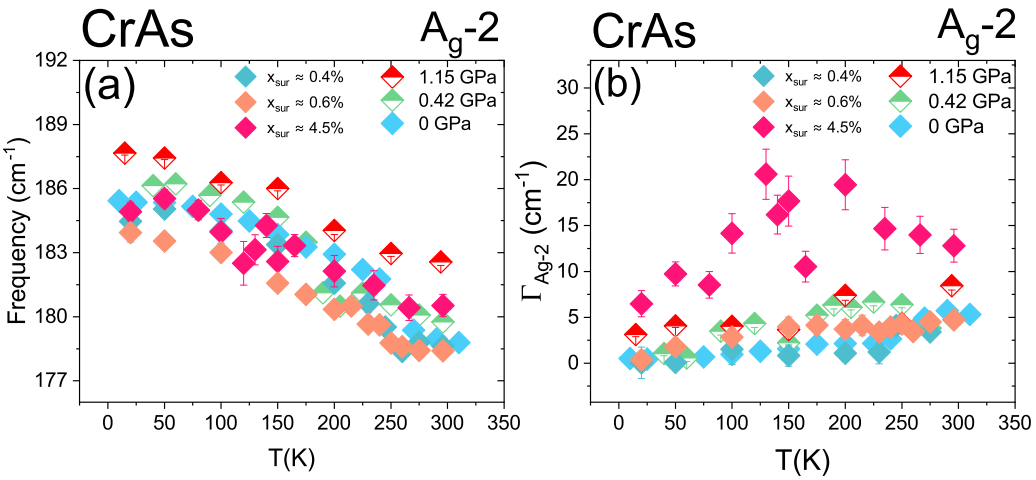

Figure C.22.: Temperature dependence comparison of the A_g-2 phonon mode in CrAs, at different pressures and dopings: (a) phonon frequency (b) FWHM. Data at 0 GPa for pure CrAs are taken from [8].

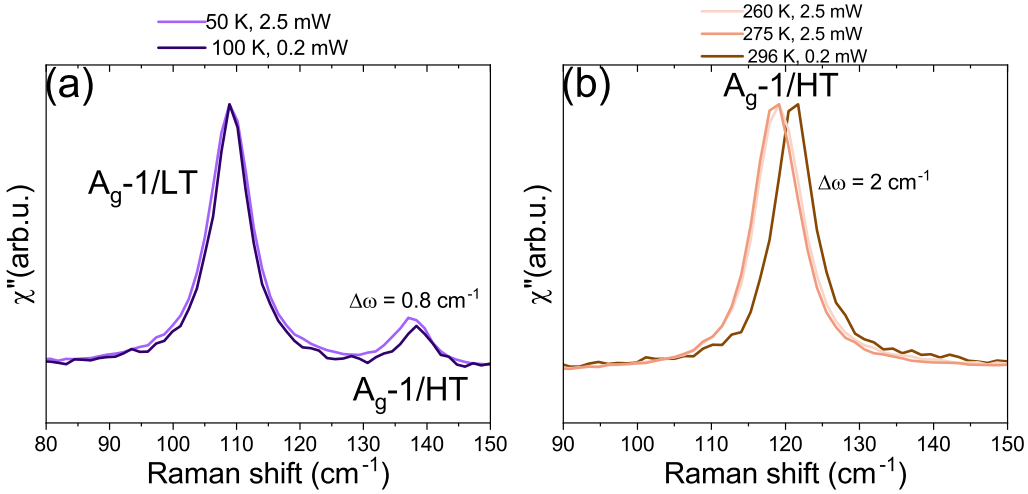

Figure C.23.: Comparison of Raman spectra focused on the A_g-1 phonon in the coexistence phase and HT phase of a $CrAs_{1-x}P_x$ single crystal with $x_{sur} \approx 0.6\%$. (a) Spectra measured at 50 K (2.5 mW) and 100 K (0.2 mW). (b) Spectra measured at 260 K (2.5 mW), 275 K (2.5 mW) and 296 K (0.2 mW). The extrapolation of the A_g-1 temperature dependence, for the 260 K and 275 K measurements, yields a local temperature increase of approximately 60 K. The frequency difference between the two spectra $\Delta\omega$, is obtained from the fitted A_g-1 peak positions and labeled alongside the spectra.

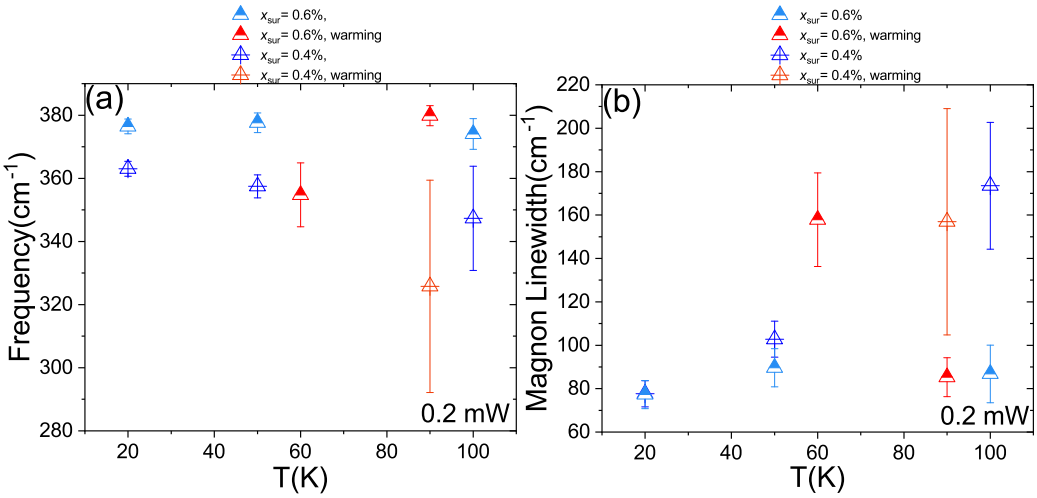

Figure C.24.: Temperature dependence of the low energy magnon in the $x_{sur} \approx 0.4\%$ and $x_{sur} \approx 0.6\%$ $CrAs_{1-x}P_x$ single crystal batches, measured upon cooling and warming with an incident laser power of 0.2 mW: (a) Frequency and (b) Linewidth.

C.3. Raman mapping and TEM on Phosphorus-doped samples

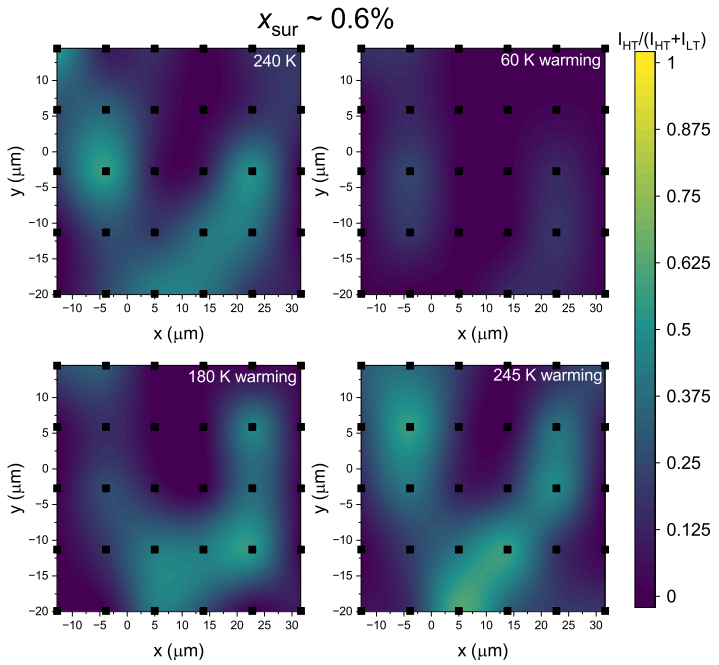

Figure C.25.: Raman mapping of the $x_{sur} \approx 0.6\%$ $CrAs_{1-x}P_x$ single crystal upon cooling and then warming, measured with an incident laser power of 0.2 mW. The selected temperatures at which the measurements were taken are indicated in each panel. Overlaid scatter symbols represent the measurement spots.

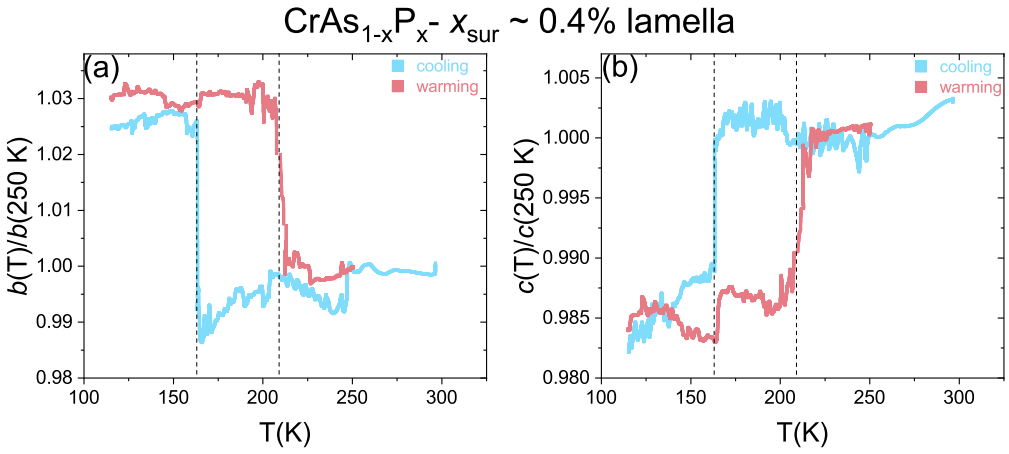

Figure C.26.: Temperature dependence of the (a) b lattice parameter and (b) c lattice parameters, normalized to their respective values at 250 K, for the $x_{eff} \approx 0.4\%$ doped lamella, upon cooling and warming. The dotted lines indicate the transition temperatures and the relative changes at the transition are annotated next to each curve.

$T(K)$	**Phase**	θ_b (°)	**Width** (nm)
296	HT		
220	HT + LT	70 ± 3	60 ± 10
215	HT + LT	54 ± 3/45 ± 3	50 ± 10/50 ± 10
213	HT + LT	62 ± 3/53 ± 3	270 ± 10/70 ± 10
204	HT + LT	65 ± 3/62 ± 3	35 ± 10/20 ± 10
200	HT + LT	64 ± 3/45 ± 3	40 ± 10/30 ± 10

Table C.8.: Summary of the average domain stripe orientation (θ_b) and widths determined from TEM mapping of the pure CrAs lamella for all measured temperatures. Coexisting HT phase domain orientations at the same temperature are separated by slashes.

$T(K)$	**Phase**	θ_b (°)	**HT Width** (nm)	**LT Width** (nm)
296	HT			
184	HT + LT	11 ± 3	20 ± 10	70 ± 10
175	HT + LT	40 ± 3	40 ± 10	70 ± 10
165	HT + LT	45 ± 3	45 ± 10	60 ± 10/35 ± 10
160	HT + LT	45 ± 3	40 ± 10	65 ± 10/30 ± 10
155	HT + LT	55 ± 3	20 ± 10	130 ± 10/30 ± 10
145	HT + LT	20 ± 3	25 ± 10	280 ± 10/60 ± 10
137.4	HT + LT	30 ± 3	40 ± 10	
136.8	HT + LT	30 ± 3	45 ± 10	
114	LT			
87	LT			

Table C.9.: Summary of both HT and LT domain stripe orientation (θ_b) and widths determined from TEM mapping of the $x_{sur} \approx 0.4\%$ $CrAs_{1-x}P_x$lamella at selected temperatures. Coexisting LT domain widths at the same temperature are separated by slashes.

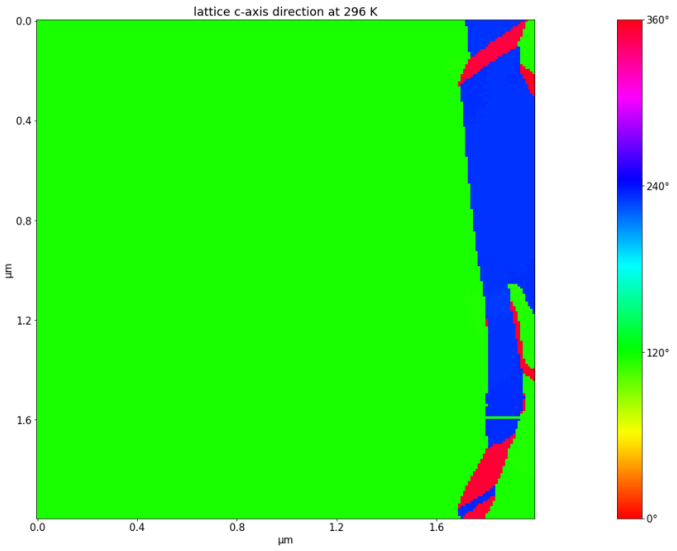

Figure C.27.: TEM mapping of the $x_{sur} \approx 0.4\%$ $CrAs_{1-x}P_x$lamella at room temperature, from Fig. 4.59, showing regions with different in plane rotations of the c lattice parameter.

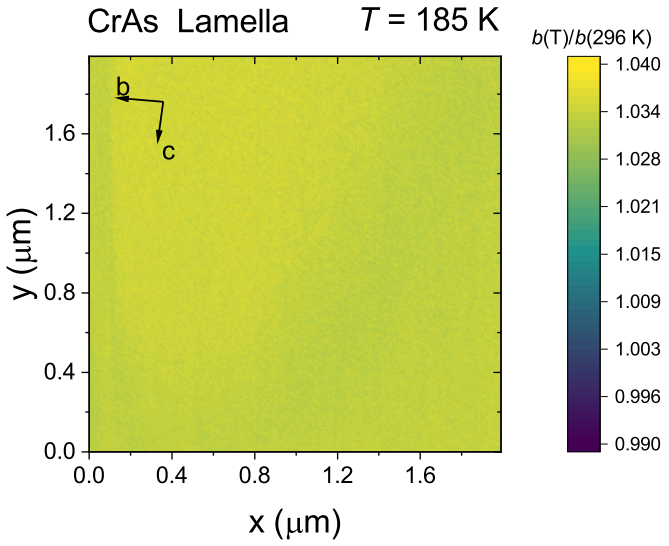

Figure C.28.: TEM mapping of the pure CrAs lamella, corresponding to the sample shown in Fig. 4.57, acquired at 185 K when the lamella is fully in the LT phase. The corresponding lattice parameter directions are indicated.

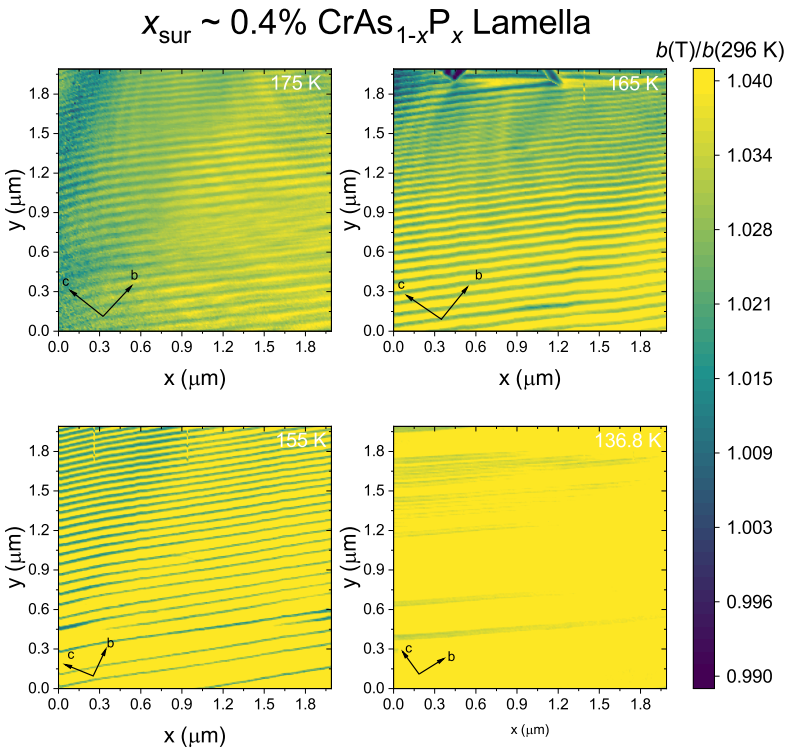

Figure C.29.: TEM mapping of the $x_{sur} \approx 0.4\%$ $CrAs_{1-x}P_x$ lamella upon cooling. The temperatures at which the measurements were acquired, as well as the corresponding lattice parameter directions, are indicated in each panel. The white arrows indicate the relative orientation of the domains with respect to the crystallographic axes.

Surface power density (mW/μm^2)	$\omega_{A_g-1}(cm^{-1})$	$\omega_{A_g-2}(cm^{-1})$	$\omega_{A_g-3}(cm^{-1})$	$\omega_{A_g-4}(cm^{-1})$
0.01	120.06 ± 0.06	178.57 ± 0.42	228.98 ± 1.04	
0.04	120.26 ± 0.01	178.94 ± 0.09	228.38 ± 0.22	265.71 ± 0.32
0.03	119.08 ± 0.15	177.64 ± 0.62	228.52 ± 0.76	
0.09	117.20 ± 0.08	177.83 ± 0.34	226.34 ± 0.77	

Table C.10.: Summary of the A_g phonon frequencies of CrAs extracted from fits as a function of surface power density, at room temperature. The upper half of the table shows data measured on single crystals, while the lower half contains measurements taken on the lamella. Data at 0.04 mW/μm^2 are from [8].

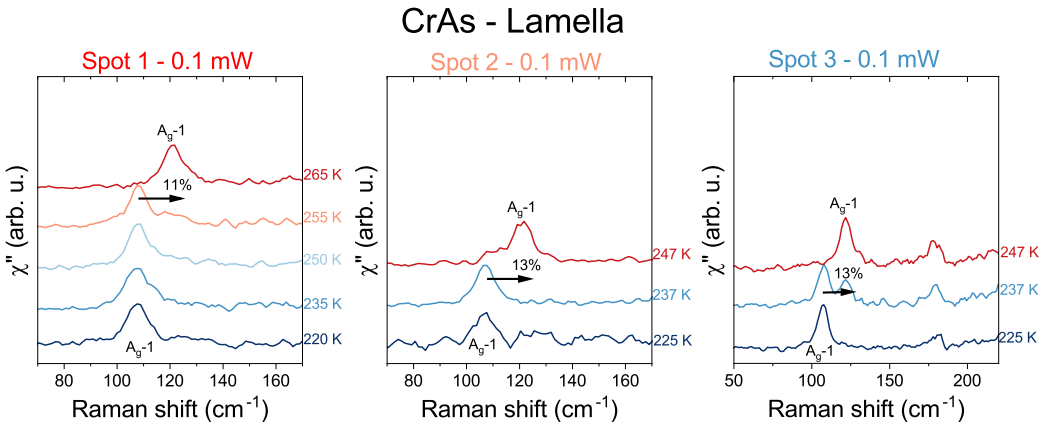

Figure C.30.: Selected region of the Raman spectra of the pure CrAs lamella, showing the evolution of the A_g-1 phonon mode at the three different spots, measured upon warming with 0.1 mW laser power. Spot 2 and Spot 3 were measured within the same thermal cycle, while Spot 1 was measured in a separate cycle. The corresponding temperatures are shown alongside the curves. Black arrows indicate the relative frequency shift $(\omega_{LT} - \omega_{HT})/\omega_{HT}$ at the onset of the transition or at the onset of the coexistence.

D. Appendix: Resonant Inelastic X-ray scattering on CrAs

In Sec. 4.1.3.2, it was discussed how Sen et al. [8] analyzed the two broad magnetic features observed in the Raman spectra of CrAs at 350 cm^{-1} and 1700 cm^{-1} by calculating the magnetic density of state (M-DOS) and the associated magnon dispersion. The model used was based on a predetermined set of exchange constant ratios derived by the work of Matsuda et al. on polycrystalline CrAs: : $J_{c2}/J_a = 7.1$, $J_{c1}/J_a = -0.5$ and $J_a/J_b = 1.3$ [7] .

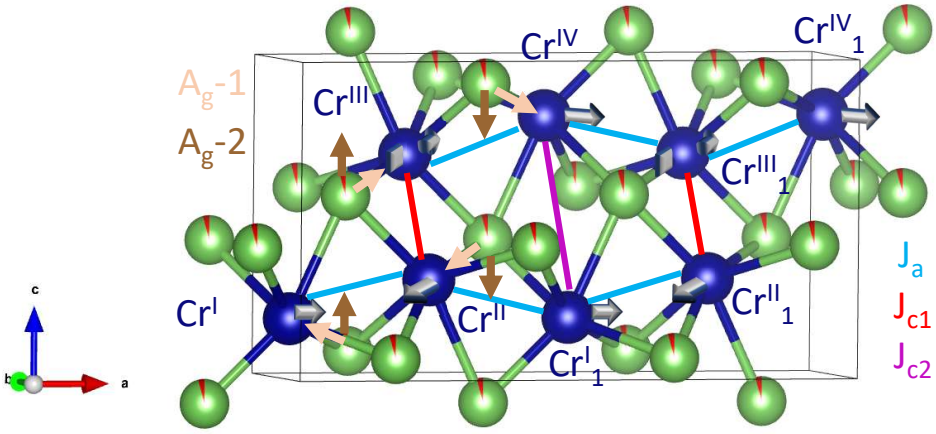

Figure D.1.: Extended view of $CrAs_{1-x}P_x$ structure along the a-axis, showing two consecutive unit cells. Cr atom labels and the color scheme for Cr,As,P follow from Fig. 3.19. Solid lines between Cr atoms indicate magnetic exchange couplings, following from [24]. Grey (metallic) arrows on Cr atoms represent spin orientations. Yellow and brown arrows on As/P atoms, shown on one side of the image, represent the eigendisplacements associated with A_g-1 and A_g-2 phonon modes, respectively, following from [52].

Within this framework, the resulting M-DOS exhibits a dominant feature whose associated two-magnon excitation energy is in reasonable agreement with the observed feature at 1700 cm^{-1}. However, this model fails to reproduce the additional excitation at 350 cm^{-1}, which led Sen et al. to suggest that a linear spin-wave Heisenberg description might be insufficient to describe the magnetic excitations of the double-helical state in CrAs [8]. Recent neutron scattering measurements on single crystal CrAs by Qin et al. revealed that that J_a and J_{c1} are in fact stronger than J_{c2} [24, 15]. Their work demonstrates that a linear spin-wave Heisenberg model provides a good description of the spin excitation spectrum, leading to a direct measurement of the exchange coupling constant and a revised ratios: $J_{c2}/J_a = -0.5$, $J_{c1}/J_a = 2.3$ and $J_a/J_b = 3.0$ [24].
While the symmetry based identification of the A_g-1 and A_g-2 modes as key phonons remains unchanged, using the exchange paths and coupling strenghts reported by Qin et al. leads to a revised interpretation. Once the updated directions and relative strenghts of the magnetic exchange paths are taken into account, the eigendisplacements of A_g-1 and A_g-2 point towards a modulation of J_a and J_{c1}, rather than J_{c2}, as shown in Fig. D.1.

Resonant Inelastic X-ray Scattering (RIXS) is a photon-in, photon-out spectroscopic technique that has become increasingly used for probing the electronic, magnetic and structural properties of solids. It operates by detecting the energy loss that occurs when an incident X-ray photon is resonantly absorbed, followed by the inelastic scattering and emission of a lower-energy photon [123]. Motivated by the need to directly access the magnetic excitation spectrum of CrAs and therefore to obtain experimental information on the exchange coupling constants, we performed RIXS measurements in addition to the Raman experiments discussed in the main text. These measurements were carried out at the I21 beamline of Diamond Light Source, with the suppor of our local contacts Dr. Stefano Agrestini and Dr. Mirian Garcia. While the measurements provide momentum dependent RIXS spectra of CrAs, the quantitative modeling required to determine the exchange interactions is still ongoing and will be reported in a forthcoming publication. The data are therefore presented here in their current form.

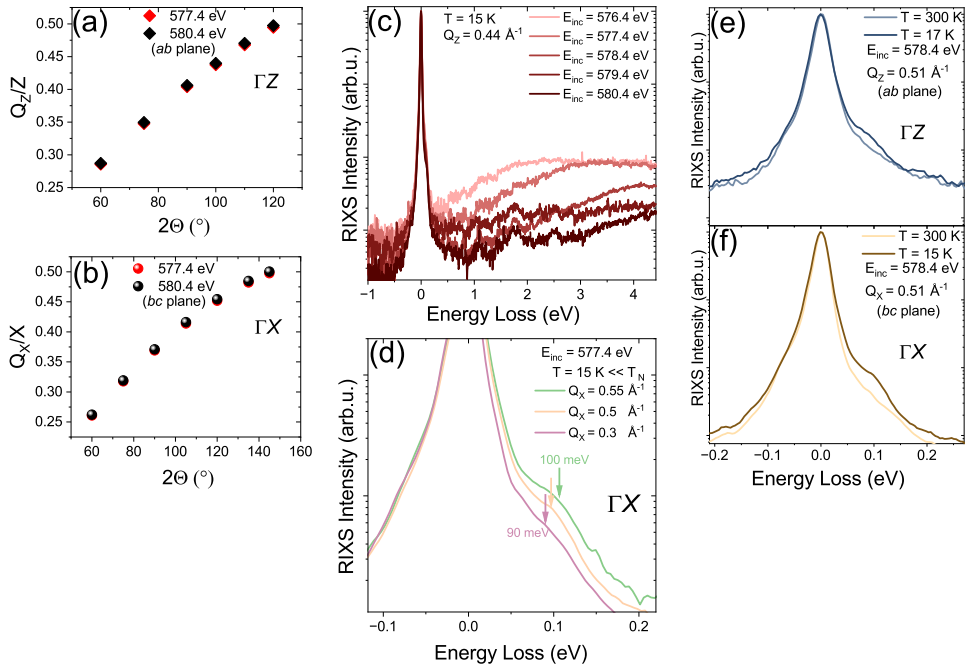

Figure D.2.: RIXS on CrAs: (a,b) High symmetry reciprocal space cuts investigate during the beamtime. (c) RIXS intensity as a function of transferred energy at $T = 15$ K., for different incident energies. (d,e) Comparison between RIXS spectra in the magnetically ordered and disordered state, at the indicated momentum in both the reciprocal lattice direction probed. (f) RIXS spectra for different transferred momentum as indicated, for $T = 15$K and $E_{inc} = 577.4$ eV. The arrows highlight the dispersing behavior of the anomaly in the elastic line tail. All the above spectra were measured in LV polarization and are plotted in log scale.

For this experiment, two CrAs single crystals were mounted on each sample holder using conductive epoxy and RIXS spectra were succesfully collected on all samples. Measurements were first perfomed at room temperature and then to 15 K, in order to minimize thermal cycling, as repeated crossing of T_N can induce cracking due to the large lattice expansion. From the XAS spectra, it was determined that an incident energy of 577.4 eV provides optimal sensitivity to the magnetic excitations of CrAs. At this energy, four 30-minutes RIXS spectra were acquired for each sample using both vertical and horizontal polarization and several 2θ scattering angles. Additional measurements were also performed at 580.4 eV for comparison. Because of a malfunction in the rotation stage, the continous 2θ scan was limited to a maximum angle of 145°.

Fig. D.2 a,b show the 2θ angles accessed at both 577.4 eV and 580.4 eV, from which approximately 50% of two high symmetry directions in reciprocal space ($\mathbf{\Gamma Z}, \mathbf{\Gamma X}$) were probed. Representative spectra recorded at 15 K are shown in Fig. D.2 c. The features at approximately 1.8 eV and 2.5 eV are attributed to *dd* excitations, while the increase in intensity at high energy loss arises from fluorescence. The main finding of this beamtime is displayed in Fig. D.2 (d-f). At an incident energy of 577.4 eV, a clear low energy anomaly appears around 100 meV, near the elastic line, within the magnetically ordered state, and is absent above T_N. This behavior is reproduced at other incident energies (e.g. 578.4 eV) and along all probed reciprocal space directions (the $\mathbf{\Gamma Z}$ cuts are not show), suggesting that this low energy anomaly originates from a magnon excitation. In summary, the RIXS measurements reveal a low energy magnetic excitation in CrAs and its dispersive character along different reciprocal lattice directions. These observation confirm the success of the experiment and can be used to corroborate the magnetic response reported in literature.

List of Figures

List of Tables

Bibliography

[1] L. N. Cooper. Bound electron pairs in a degenerate fermi gas. *Phys. Rev., 104*, 1956. doi:10.1103/PhysRev.104.1189.

[2] J. Bardeen, L. N. Cooper, and J. R. Schrieffer. Theory of superconductivity. *Phys. Rev., 108*, 1957. doi:10.1103/PhysRev.108.1175.

[3] M. R. Norman. The challenge of unconventional superconductivity. *Science, 332*, 2011. doi:10.1126/science.1200181.

[4] G. R. Stewart. Unconventional superconductivity. *Advances in Physics, 66*, 2017. doi:10.1080/00018732.2017.1331615.

[5] R. Fernandes, A. Chubukov, and J. Schmalian. What drives nematic order in iron-based superconductors? *Nature Phys, 10*, 2014. doi:10.1038/nphys2877.

[6] S. M. Souliou, F. Weber, and M. Le Tacon. Lattice dynamics signatures of competing orders in unconventional superconductors. *Synchrotron Radiation News, 36*, 2023. doi:10.1080/08940886.2023.2226045.

[7] M. Matsuda, F.K. Lin, J.-G. Cheng, W. Wu, J.P. Sun, J.H. Zhang, P.J. Sun, K. Matsubayashi, T. Miyake, T. Kato, J.-Q. Yan, M.B. Stone, Si Qimiao, J. L. Luo, and Y. Uwatoko. Evolution of magnetic double helix and quantum criticality near a dome of superconductivity in CrAs. *Physical Review X 8, no. 3*, 2018. doi:10.1103/PhysRevX.8.031017.

[8] K. Sen, Y. Yao, R. Heid, A. Omoumi, F. Hardy, K. Willa, M. Merz, A. A. Haghighirad, and M. Le Tacon. Raman Scattering Study of lattice and magnetic excitations in CrAs. *Physical Review B 100, no. 10*, 2019. doi:10.1103/PhysRevB.100.104301.

[9] W. Wu, J. Cheng, K. Matsubayashi, P. Kong, F. Lin, C. Jin, N. Wang, Y. Uwatoko, and J. Luo. Superconductivity in the vicinity of antiferromagnetic order in CrAs. *Nat. Commun., 5*, 2014. doi:10.1038/ncomms6508.

[10] R. Khasanov, Z. Guguchia, I. Eremin, H. Luetkens, A. Amato, P. K. Biswas, C. Rüegg, M. A. Susner, A. S. Sefat, N. D. Zhigadlo, and E. Morenzoni. Pressure-induced electronic phase separation of magnetism and superconductivity in CrAs. *Scientific Report, 5*, 2015. doi:10.1038/srep13788.

[11] K. Motizuki, H. Ido, T. Itoh, and M. Morifuji. *Electronic Structure and Magnetism of 3d-Transition Metal Pnictides. vol. 131.* Springer Berlin Heidelberg, 2010. doi:10.1007/978-3-642-03420-6.

[12] M. R. Norman. Superconductivity with a twist. *Physics, 8*, 2015. doi:10.1103/Physics.8.24.

[13] J. Cheng and J. Luo. Pressure-induced superconductivity in cras and mnp. *J. Phys.: Condens. Matter 29, 383003*, 2017. doi:10.1088/1361-648X/aa7b01.

[14] R. Y. Chen and N. L. Wang. Progress in Cr- and Mn- based superconductors: a key issure review. *Reports on Progress in Physics 82*, 2019. doi:10.1088/1361-6633/aaed0d.

[15] M. Matsuda, J. Cheng, and Y. Uwatoko. Pressure variation of magnetism in chromium and manganese mono-pnictide superconductors. *Journal of the Physical Society of Japan 94*, 2025. doi:10.7566/JPSJ.94.032001.

[16] Andreas Eich. *Crystal and Magnetic Structure of CrAs under Extreme Conditions*. PhD thesis, RWTH Aachen University, 2024.

[17] Z. Yu, W. Wu, H. Qingyang, Z. Jinggeng, L. Chunyu, Y. Ke, C. Jinguang, L. Jianlin, W. Lin, and M. Ho-kwang. Anomalous anisotropic compression behavior of superconducting CrAs under high pressure. *Proceedings of the National Academy of Sciences 112, no. 48*, 2015. doi:10.1073/pnas.1520570112.

[18] A. Eich, A. Grzechnik, C. Paulmann, Müller T., Y. Su, T. Wolf, and K. Friese. Comparison of the temperature- and pressure- dependent behavior of the crystal structure of CrAs. *Acta Crystallographica Section B Structural Science, Crystal Engineering and Materials 77, no. 4*, 2021. doi:10.1107/S2052520621005655.

[19] L. Keller, J. S. White, M. Frontzek, P. Babkevich, M.A. Susner, Z.C. Sims, A. S. Sefat, H. M. Rønnow, and Ch. Rüegg. Pressure dependence of the magnetic order in CrAs: A neutron diffraction investigation. *Physical Review B, 91*, 2015. doi:10.1103/PhysRevB.91.020409.

[20] Y. Shen, Q. Wang, Y. Hao, B. Pan, Y. Feng, Q. Huang, L.W. Harriger, J.B. Leao, Y. Zhao, R. M. Chisnell, J. W. Lynn, H. Cao, J. Hu, and J. Zhao. Structural and magnetic phase diagram of CrAs and its relationship with pressure-induced superconductivity. *Physical review B, 93*, 2016. doi:10.1103/PhysRevB.93.060503.

[21] K. Selte, A. Kjekshus, W. E. Jamison, A.F. Andresen, J. E. Engebretsen, and L. Ehrenberg. Magnetic structure and properties of CrAs. *Acta Chemica Scandinavica, 25*, 1971. doi:10.3891/acta.chem.scand.25-1703.

[22] H. Boller and A. Kallel. First order crystallographic and magnetic phase transition in CrAs. *Solid State Communications 9, no. 19*, 1971. doi:10.1016/0038-1098(71)90344-9.

[23] N. Kazama and H. Watanabe. Magnetic properties of $Cr_{1-x}Mn_xAs$ system. *J. Phys. Soc. Jpn., 30*, 1971. doi:10.1143/JPSJ.30.1319.

[24] Y. Qin, Y. Shen, Y. Hao, H. Wo, S. Shen, A. E. Russell, Y. Zhao, L. W. Harriger, J. W. Lynn, and J. Zhao. Frustrated magnetic interactions and quenched spin fluctuations in CrAs. *Chinese Physics Letters 39*, 2022. doi:10.1088/0256-307X/39/12/127501.

[25] B. Y. Pan, H.C. Xu, Y. Liu, R. Sutarto, F. He, Y. Shen, Y. Q. Hao, J. Zhao, L. Harriger, and D. L. Feng. Anomalous helimagnetic domain shrinkage due to the weakening of the Dzyaloshinskii-Moriya interaction in CrAs. *Physical Review B 102*, 2020. doi:10.1103/PhysRevB.102.104432.

[26] A. Eich, A. Grzechnik, Y. Su, B. Ouladdiaf, D. Sheptyakov, T. Wolf, V. Petricek, H. Shaded, and K. Friese. Incommensurate magnetic structure of CrAs at low temperatures and high pressures. *Acta Cryst., B79*, 2023. doi:10.1107/S205252062300817X.

[27] É. A. Zavadskiĭ and I. A. Sibarova. Some features of phase transition in chromium arsenide at high pressures. *Sov. Phys. JETP, 51*, 1980. doi:https://ui.adsabs.harvard.edu/abs/1980JETP...51..542Z.

[28] H. Kotegawa, S. Nakahara, R. Akamatsu, T. Hideki, H. Sugawara, and H. Harima. Detection of an unconventional superconducting phase in the vicinity of the strong first-order magnetic transition in CrAs using ^{75}As-nuclear quadruopole resonance. *Physical Review Letters, 114*, 2015. doi:10.1103/PhysRevLett.114.117002.

[29] H. Kotegawa, S. Nakahara, H. Tou, and H. Sugawara. Superconductivity of 2.2 k under pressure in helimagnet CrAs. *J. Phys. Soc. Jpn., 83*, 2014. doi:10.7566/JPSJ.83.093702.

[30] H. Kotegawa, K. Matsushima, S. Nakahara, H. Tou, J. Kaneyoshi, T. Nishiwaki, E. Matsuoka, H. Sugawara, and H. Harima. Superconductivity and magnetic fluctuations developing in the vicinity of strong first-order magnetic transition in cras. *Journal of Physics: Condensed Matter, 29*, 2017. doi:10.1088/1361-648X/aa6e7d.

[31] C. Y. Guo, M. Smidman, B. Shen, W. Wu, F. K. Lin, X. L. Han, Y. Chen, F. Wu, Y. F. Wang, W. B. Jiang, X. Lu, J. P. Hu, J. L. Luo, and H. Q Yuan. Evidence for triplet superconductivity near an antiferromagnetic instability in CrAs. *Phys. Rev. B, 98*, 2018. doi:10.1103/PhysRevB.98.024520.

[32] K. Selte, A. Kjekshus, P. G. Peterzéns, and A. F. Andresen. Magnetic structures and properties of $Mn_{1-t}Cr_tAs$ ($0 < t < 0.40$). *Acta Chemica Scandinavica, 32*, 1978. doi:10.3891/acta.chem.scand.32a-0653.

[33] H. Ido. Temperature-dependent magnetic moment in the MnAs-CrAs system. *Journal of Magnetism and Magnetic Materials, 70*, 1987. doi:10.1016/0304-8853(87)90408-2.

[34] T. Suzuki and H. Ido. 3d metal-substitution effects on magnetic and crystallographic properties of CrAs. *J. Appl. Phys. 69*, 1991. doi:10.1063/1.348302.

[35] S. Park, S. Shin, S. I. Kim, S. Kim, C. Park, J.D. Thompson, and T. Park. Tunable quantum critical point and detached superconductivity in Al-doped CrAs. *npj Quantum Materials, 4*, 2019. doi:10.1038/s41535-019-0188-6.

[36] K. Selte, H. Hjersing, A. Kjekshus, A. Andresen, and P. Fischer. Magnetic structures and properties of $CrP_{1-x}As_x$. *Acta Chemica Scandinavica 29a*, 1975. doi:10.3891/acta.chem.scand.29a-0695.

[37] T. Suzuki and H. Ido. Crystallographic and magnetic properties of $CrAs_{1-x}Sb_x$. *Journal of Magnetism and Magnetic Materials, 54*, 1986. doi:10.1016/0304-8853(86)90321-5.

[38] T. Suzuki and I. Hideaki. Magnetic-nonmagnetic transition in cras and the related compounds. *Journal of Applied Physics 73, no. 10*, 1993. doi:10.1063/1.353591.

[39] K. Kanaya, S. Abe, H. Yoshida, K. Kamigaki, and T. Kaneko. Magnetic and structural properties of pseudo-binary compounds $CrAs_{1-x}P_x$. *Journal of Alloys and Compounds, 6*, 2004. doi:10.1016/j.jallcom.2004.04.055.

[40] A. M. Aliev, L. N. Khanov, A. G. Gamzatov, A. B. Batdalov, D. R. Kurbanova, K. I. Yanushkevich, and G. A. Govor. Giant magnetocaloric effect in $MnAs_{1-x}P_x$ in a cyclic magnetic field: Lattice and magnetic contributions and degradation of the effect. *Applied Physics Letters, 118*, 2021. doi:10.1063/5.0038500.

[41] S. Reimers, L. Odenbreit, L. Šmejkal, V. N. Strocov, P. Costantinou, A. B. Hellenes, R. J. Ubiergo, W. H. Campos, V. K. Bharadwaj, A. Chakraborty, T. Denneulin, W. Shi, R. E. Dunin-Borkowski, S. Das, M. Kläui, J. Sinova, and M. Jourdan. Direct observation of altermagnetic band splitting in CrSb thin films. *Nature Communications, 15*, 2024. doi:10.1038/s41467-024-46476-5.

[42] A. Fakhredine, R. M. Sattigeri, G. Cuono, and C. Autieri. Interplay between altermagnetism and nonsymmorphic symmetries generating large anomalous hall conductivity by semi-Dirac points induced anticrossings. *Phys. Rev. B, 108*, 2023. doi:10.1103/PhysRevB.108.115138.

[43] W. Beida, E. Şaşioğlu, C. Friedrich, G. Bihlmayer, Y. Mokrousov, and S. Blügel. Chiral split magnons in metallic g-wave altermagnets: insights from many-body perturbation theory. *npj Quantum Mater., 10*, 2025. doi:10.1038/s41535-025-00818-8.

[44] T. Ito, H. Ido, and K. Motizuki. Electronic structure and magnetic properties in CrX (XP, As and Sb). *Journal of Magnetism and Magnetic Materials 310*, 2007. doi:10.1016/j.jmmm.2006.10.470.

[45] C. Autieri and C. Noce. First principles study of structural, magnetic and electronic properties of CrAs. *Philosophical Magazine 97*, 2017. doi:10.1080/14786435.2017.1375607.

[46] Z. Charifi, Dj. Guendouz, H. Baaziz, F. Soyalp, and B. Hamad. Ab-initio investigations of the structural, electronic, magnetic and mechanical properties of CrX (X = As, Sb, Se, and Te) transition metal pnictides and chalcogenides. *Physica Scripta 94*, 2019. doi:10.1088/1402-4896/aaece3.

[47] C. Autieri, G. Cuono, F. Forte, and C. Noce. Tight-binding calculation of the magnetic moment of CrAs under pressure. *Journal of Physics: Conference Series*, 2018. doi:10.1088/1742-6596/969/1/012106.

[48] P. Coleman and A. Schofield. Quantum criticality. *Nature, 433*, 2005. doi:10.1038/nature03279.

[49] T. Shibauchi, A. Carrington, and Y. Matsuda. A quantum critical point lying beneath the superconducting dome in iron pnictides. *Annu. Rev. Condens. Matter Phys., 5*, 2005. doi:10.1146/annurev-conmatphys-031113-133921.

[50] T. Oka, Z. Li, S. Kawasaki, G. F. Chen, N. L. Wang, and G. Zheng. Antiferromagnetic spin fluctuations above the dome-shaped and full-gap superconducting states of $LaFeAsO_{1-x}F_x$ revealed by ^{75}As-nuclear quadrupole resonance. *Phys. Rev. Lett., 108*, 2012. doi:10.1103/PhysRevLett.108.047001.

[51] Y. Hu, X. Zheng, G. Ma, H. Lu, L. Zhang, C. Zhang, Y. Xia, Y. Hao, L. He, J. Chen, F. Shen, S. Wang, C. Wang, D. Wang, and Y. Du. Giant negative thermal expansion in antiferromagnetic CrAs-based compounds. *Phys. Rev. App. , 12*, 2019. doi:10.1103/PhysRevApplied.12.034027.

[52] Yi Yao. *Study of lattice, spin and charge dynamics in Cr- and Ni-based pnictide superconductors*. PhD thesis, Karlsruher Institut für Technologie (KIT), 2021.

[53] W. Wu, Z. XiaoDong, Y. ZhiHua, Z. Ping, W. NanLin, and L. JianLin. Low temperature properties of pnictide cras single crystal. *Science China Physics, Mechanics and Astronomy 53, no. 7*, 2010. doi:10.1007/s11433-010-4006-1.

[54] Urs Strobel. Crystal growth and characterisation of helimagnetic mono-pnictide $CrAs_{1-x}P_x$. Master's thesis, Karlsruher Institut für Technologie (KIT), 2020.

[55] K. N. Subramanian. *Lead-Free Electronic Solders*. Springer New York, 2007. doi:10.1007/978-0-387-48433-4.

[56] M. Takibana. *Beginner's Guide to Flux Crystal Growth*. Springer Japan, 2017. doi:10.1007/978-4-431-56587-1.

[57] M. Venktatraman and J. P. Neumann. The As-Cr (arsenic-chromium) system. *Journal of Phase Equilibria 11, no. 5*, 1990. doi:10.1007/BF02898253.

[58] A. Grzechnik, V. Dmitriev, M. Hanfland, T. Geise, H. Shahed, and Friese K. Anti-isostructural phase transition and twinning in CrAs at low temperatures and high pressures. *Journal of Physics and Chemistry of Solids 180*, 2023. doi:10.1016/j.jpcs.2023.111436.

[59] K. Selte, A. Kjekshus, A. Andresen, A. Pilotti, S. Svensson, and Swahn C.G. On phase transitions between the MnP and NiAs type structures. *Acta Chemica Scandinavica 27*, 1973. doi:10.3891/acta.chem.scand.27-3195.

[60] V. K. Pecharsky and P. Y. Zavalij. *Fundamentals of Powder Diffraction and Structural Characterization of Materials, Second Edition.* Springer New York, NY, 2008. doi:10.1007/978-0-387-09579-0.

[61] B. H. Toby and R. B. Von Dreele. GSAS-II: the genesis of a modern open-source all purpose crystallography software package. *J. Appl. Cryst. 46 544-549*, 2013. doi:10.1107/S0021889813003531.

[62] D. Zagorac, H. Müller, S. Ruehl, J. Zagorac, and S. Rehme. Recent developments in the Inorganic Crystal Structure Database: theoretical crystal structure data and related features. *J. Appl. Cryst. 52 918-925*, 2019. doi:10.1107/S160057671900997X.

[63] P. Benzi, E. Bottizzo, and N. Rizzi. Oxygen determination from cell dimensions in YBCO superconductors. *Journal of Crystal Growth 269, no. 2–4*, 2004. doi:10.1016/j.jcrysgro.2004.05.082.

[64] S. Griffitt, M. Spaić, J. Joe, Z. W. Anderson, D. Zhai, M. J. Krogstad, R. Osborn, D. Pelc, and M. Greven. Local inversion-symmetry breaking in a Bismuthate high-T_c superconductor. *Nature Communications 14, no. 1*, 2023. doi:10.1038/s41467-023-36348-9.

[65] L. Vegard. Die konstitution der mischkristalle und die raumfüllung der atome. *Z. Physik 5, 17–26*, 1921. doi:10.1007/BF01349680.

[66] D. Shindo and T. Oikawa. *Energy Dispersive X-ray Spectroscopy. In: Analytical Electron Microscopy for Materials Science.* Springer, Tokyo, 2002. doi:10.1007/978-4-431-66988-3_4.

[67] S. Foner. Versatile and sensitive vibrating-sample magnetometer. *Rev. Sci. Instrument. 30*, 1959. doi:10.1063/1.1716679.

[68] J.-Q. Yan, A. Kreyssig, S. Nandi, N. Ni, L. Bud'ko, A. Kracher, R.J. McQueeney, R. W. McCallum, T. A. Lograsso, A. I. Goldman, and Canfield P. C. Structural transition and anisotropic properties of single-crystalline $SrFe_2As_2$. *Physical Review B 78, no. 2*, 2008. doi:10.1103/PhysRevB.78.024516.

[69] N. Kumar, R. Nagalakshmi, R. Kulkarni, P.L. Paulose, A. K. Nigam, S. K. Dhar, and A. Thamizhavel. Anisotropic magnetic and superconducting properties of $CaFe_{2-x}Co_xAs_2$ ($x = 0, 0.06$) single crystals. *Physical Review B 79, no. 1*, 2009. doi:10.1103/PhysRevB.79.012504.

[70] X. F. Wang, T. Wu, G. Wu, H. Chen, Y. L. Xie, J. J. Ying, Y. J. Yan, R. H. Liu, and X. H. Chen. Anisotropy in the electrical resitivity and susceptibility of superconducting $BaFe_2As_2$ single crystals. *Physical Review Letters 102, no. 11*, 2009. doi:10.1103/PhysRevLett.102.117005.

[71] R. Klingeler, N. Leps, I. Hellmann, A. Popa, U. Stockert, C. Hess, V. Kataev, H.-J. Grafe, F. Hammerath, G. Lang, S. Wurmhel, G. Behr, L. Harnagea, S. Singh, and B. Büchner. Local antiferromagnetic correlations in the iron pnictide superconductors $LaFeAsO_{1-x}F_x$ and $Ca(Fe_{1-x}Co_x)_2As_2$ as seen via normal-state susceptibility. *Physical Review B 81, no. 2*, 2010. doi:10.1103/PhysRevB.81.024506.

[72] P. J. Hirschfeld, M. M. Korshunov, and I. I. Mazin. Gap symmetry and structure of Fe-based superconductors. *Rep. Prog. Phys. 74*, 2011. doi:10.1088/0034-4885/74/12/124508.

[73] Andrei Chubukov. Pairing mechanism in Fe-based superconductors. *Annu. Rev. Condens. Matter Phys. 3:57–92*, 2012. doi:10.1146/annurev-conmatphys-020911-125055.

[74] K. Momma and F. Izumi. VESTA 3 for three-dimensional visualization of crystal, volumetric and morphology data. *J. Appl. Cryst., 44*, 2011. doi:10.1107/S0021889811038970.

[75] A. Kallel, H. Boller, and E.F. Bertaut. Helimagnetism in MnP-type compounds: MnP, FeP, CrAs and $CrAs_{1-x}Sb_x$ mixed crystals. *Journal of Physics and Chemistry of Solids 35*, 1974. doi:10.1016/S0022-3697(74)80132-0.

[76] M. Cardona. *Light Scattering in Solids. Vol. 8.* Springer Berlin Heidelberg, 1975. doi:10.1007/978-3-540-37568-5.

[77] E. Smith and G. Dent. *Modern Raman Spectroscopy: A Practical Approach.* John Wiley and Sons, 2005. doi:10.1002/0470011831.

[78] E. Strelcov, A. Levlev, A. Belianinov, A. Tselev, A. Kolmakov, and S. V. Kalinin. Local coexistence of VO_2 phases revealed by deep data analysis. *Scientific Report, 6*, 2016. doi:10.1038/srep29216.

[79] Y. Kim, H. Park, and C. Yang. Raman imaging of ferroelastically configurable jahn–teller domains in $LaMnO_3$. *npj Quantum Mater., 6*, 2021. doi:10.1038/s41535-021-00361-2.

[80] Thomas Strohm. *Electronic Raman scattering in high-temperature superconductors.* PhD thesis, Universität Stuttgart, 1999.

[81] Kretzschmar Florian. *Nematic Fluctuations, Fermiology and the Pairing Po- tential in Iron-based Superconductors.* PhD thesis, Technische Universität München, 2015.

[82] T. P. Devereaux and R. Hackl. Inelastic light scattering from correlated electrons. *Rev. Mod. Phys., 79*, 2007. doi:10.1103/RevModPhys.79.175.

[83] K. Sen, D. Fuchs, R. Heid, K. Wolff, J. Schmalian, and M. Le Tacon. Strange semimetal dynamics in $SrIrO_3$. *Nat. Comm., 11*, 2020. doi:10.1038/s41467-020-18092-6.

[84] J. Toporski, T. Dieing, and O. Hollricher. *Confocal Raman Microscopy.* Springer Series in Surface Sciences, 2018. doi:10.1007/978-3-319-75380-5.

[85] Romain Grasset. *Supraconductivité et ordres exotiques : à la recherche du Boson de Higgs.* PhD thesis, Université Sorbonne Paris Cité, 2017.

[86] Antoine Baron. Spectroscopy under constraint of highly correlated materials. Master's thesis, École Normale Supérieure, 2022.

[87] G. Shen, Y. Wang, A. Dewaele, C. Wu, D.E. Fratanduono, J. Eggert, S. Klotz, K. F. Dziubek, P. Loubeyre, O. V. Fat'yanov, P. D. Asimow, T. Mashimo, and R. M. M. Wentzcovitch. Toward an international practical pressure scale: A proposal for an ipps ruby gauge (IPPS-Ruby2020). *High Pressure Research, 40*, 2020. doi:10.1080/08957959.2020.1791107.

[88] P. G. Klemens. Anharmonic decay of optical phonons. *Physical Review 148, no. 2*, 1966. doi:10.1103/physrev.148.845.

[89] X. Huang, Y. Gao, T. Yang, W. Ren, H.M. Cheng, and T. Lai. Quantitative analysis of temperature dependence of raman shift of monolayer WS_2. *Scientific Reports 6, no. 1*, 2016. doi:10.1038/srep32236.

[90] N. W. Ashcroft and D. Mermin. *Solid state physics.* Saunders College Publishing, 1976.

[91] M. Ye, T. Lacmann, M. Frachet, I. Vinograd, G. Garbarino, N. Maraytta, M. Merz, R. Heid, A.A. Haghighirad, and M. Le Tacon. Anomalous phonon grüneisen parameters in the semiconductor Ta_2NiS_5. *Physical Review B 110, no. 3*, 2024. doi:10.1103/PhysRevB.110.035120.

[92] L. Lazewski, P. Piekarz, J. Tobola, B. Wiendlocha, P. T. Jochym, M. Sternik, and K. Parlinski. Phonon mechanism of the magnetostructural phase transition in MnAs. *Physical Review Letters, 104*, 2010. doi:10.1103/PhysRevLett.104.147205.

[93] W.Z. Hu, J. Dong, G. Li, P. Zheng, G. F. Chen, J. L. Luo, and N. L. Wang. Origin of the spin density wave instability in AFe_2As_2 (A = Ba, Sr) as Revealed by Optical Spectroscopy. *Physical Review Letters, 101*, 2008. doi:10.1103/PhysRevLett.101.257005.

[94] J. Jaramillo-Fernandez, E. Chavez-Angel, and C. M. Sotomayor-Torres. Raman thermometry analysis: Modelling assumptions revisited. *Applied Thermal Engineering, 130*, 2018. doi:10.1016/j.applthermaleng.2017.11.033.

[95] C. Fangcheng and H. Zhen. Determination of thermal conductivity using micro-Raman spectroscopy with a three-dimensional heating model. *J Raman Spectrosc., 50*, 2019. doi:10.1002/jrs.5725.

[96] W. T. Riffe, S. Zare, K. D. Ardrey, V. K. Champagne, M. Milich, K. Lee, M. Jassas, S. Makarem, E. J. Opila, D. R. Clarke, P. V. Balachandran, and P. E. Hopkins. Broadband optical phonon scattering reduces the thermal conductivity of multi-cation oxides. *Nat. Commun., 16*, 2025. doi:10.1038/s41467-025-58345-w.

[97] Q. Xie, L. Xu, C. Hu, L. Chen, J. Zheng, W. Wang, H. Yin, G. Cheng, and X. Ai. Phonon anharmonicity of thermoelectric material $HfTe_5$ studied by raman spectroscopy. *J Raman Spectrosc., 52*, 2020. doi:10.1002/jrs.6090.

[98] A. Togo and I. Tanaka. First principles phonon calculations in materials science. *Scripta Materialia, 108*, 2015. doi:10.1016/j.scriptamat.2015.07.021.

[99] M. Yang, X. Cheng, Y. Li, Y. Ren, M. Liu, and Z. Qi. Anharmonicity of monolayer MoS_2, $MoSe_2$, and WSe_2: A raman study under high pressure and elevated temperature. *Appl. Phys. Lett. 27*, 2017. doi:10.1063/1.4977877.

[100] R. G. Greene, H. Luo, and A. L. Ruoff. High pressure x-ray and raman study of ZnSe. *Journal of Physics and Chemistry of Solids, 56*, 1995. doi:10.1016/0022-3697(95)80020-4.

[101] R. Mittal, R. Heid, A. Bosak, T. R. Forrest, S. L. Chaplot, D. Lamago, D. Reznik, K.-P. Bohnen, Y. Su, N. Kumar, S. K. Dhar, A. Thamizhavel, Ch. Rüegg, M. Krisch, D. F. McMorrow, Th. Brueckel, and L. Pintschovius. Pressure dependence of phonon modes across the tetragonal to collapsed-tetragonal phase transition in $CaFe_2As_2$. *Phys. Rev. B, 81*, 2010. doi:10.1103/PhysRevB.81.144502.

[102] L. Chauvière, Y. Gallais, M. Cazayous, M. A. Méasson, A. Sacuto, D. Colson, and A. Forget. Raman scattering study of spin-density-wave order and electron-phonon coupling in $Ba(Fe_{1-x}Co_x)_2As_2$. *Phys. Rev. B, 84*, 2011. doi:10.1103/PhysRevB.84.104508.

[103] X. Zhou, T. Dierke, W. Mingjian, Y. Shengbo, K. Götz, T. Unruh, P. Pelz, J. Will, J. Maultzsch, and E. Spiecker. Identification of polytypism and their dislocations in bilayer MoS_2 using correlative transmission electron microscopy and Raman spectroscopy. *npj 2D Mater. Appl., 9*, 2025. doi:10.1038/s41699-025-00575-z.

[104] B. J. Saikia, G. Parthasarathy, B. K. Saikia, P. Bordoloi, and R. R. Borah. First observation of coexisting crystalline and amorphous mineral phases in the Bhawad LL6 chondrite: Evidence from micro-raman spectroscopic studies. *Geoscience Frontiers, 17*, 2026. doi:10.1016/j.gsf.2025.102236.

[105] M. Qiu, W. Yang, P. Xu, T. Huang, X. Chen, and N. Dai. Coexistent VO_2 (m) and VO_2 (b) polymorphous thin films with multiphase-driven insulator-metal transition. *Nanomaterials, 9*, 2023. doi:10.3390/nano13091514.

[106] G. Zhang, X. Wang, Q. Sun, Y. Wang, and Q. Zhang. Phase transition and morphology evolution of superfine $NaNbO_3$ particles synthesized by the hydrothermal method with the assistance of K+. *Ceramics International, 48*, 2022. doi:10.1016/j.ceramint.2022.05.279.

[107] J. Warmuth, M. Bremholm, P. Hofmann, J. Wiebe, and R. Wiesendanger. Domain imaging across the magneto-structural phase transitions in $Fe_{1+y}Te$. *npj Quantum Materials, 3*, 2018. doi:10.1038/s41535-018-0096-1.

[108] L. A. Giannuzzi and F. A. Stevie. *Introduction to Focused Ion Beams.* Springer New York, NY, 2005. doi:10.1007/b101190.

[109] P. J. W. Moll. Focused ion beam microstructuring of quantum matter. *npj Quantum Materials, 4*, 2018. doi:10.1146/annurev-conmatphys-033117-054021.

[110] S. J. Pennycook and P. D. Nellist. *Scanning Transmission Electron Microscopy.* Springer New York, NY, 2011. doi:10.1007/978-1-4419-7200-2.

[111] R. Skrotzki, J. Fiedler, T. Herrmannsdörfer, V. Heera, M. Voelskow, A. Mücklich, B. Schmidt, W. Skorupa, G. Gobsch, M. Helm, and J. Wosnitza. On-chip superconductivity via gallium overdoping of silicon. *Applied Physics Letters, 97*, 2010. doi:10.1063/1.3509411.

[112] K. Aikoh, S. Kosugi, T. Matsui, and A. Iwase. Quantitative control of magnetic ordering in FeRh thin films using 30 keV Ga ion irradiation from a focused ion beam system. *Journal of Applied Physics, 109*, 2011. doi:10.1063/1.3549440.

[113] K. Pandey, K. Paredis, T. Hantschel, C. Drijbooms, and W. Vandervost. The impact of focused ion beam induced damage on scanning spreading resistance microscopy measurements. *Sci Rep, 10*, 2020. doi:10.1038/s41598-020-71826-w.

[114] R. F. Egerton, P. Li, and M. Malac. Radiation damage in the tem and sem. *Micron, 35*, 2004. doi:10.1016/j.micron.2004.02.003.

[115] J. Park, K. Bae, T. R. Kim, C. Perez, A. Sood, M. Asheghi, K. E. Goodson, and W. Park. Direct quantification of heat generation due to inelastic scattering of electrons using a nanocalorimeter. *Adv. Sci., 8*, 2021. doi:10.1002/advs.202002876.

[116] B. Gao, E. Nikbin, G. Johnstone, Z. Shi, C. Heath, N. Appathurai, B. D. Moreno, A. Rahemtulla, G. D. Gu, J. M. Tranquada, J. Y. Howe, and Y.J. Kim. Structural phase separation and enhanced superconductivity in $La_{1.875}Ba_{0.125}CuO_4$ under uniaxial strain. *Adv. Mat. , e09308*, 2025. doi:10.1002/adma.202509308.

[117] J. C. Loudon. Antiferromagnetism in NiO observed by transmission electron diffraction. *Phys. Rev. Lett. , 109*, 2012. doi:10.1103/PhysRevLett.109.267204.

[118] K. Lyon, A. Bergman, P. Zeiger, D. Kepaptsogou, J. C. Ramasse, Q. M.and Idrobo, and J. Rusz. Theory of magnon diffuse scattering in scanning transmission electron microscopy. *Phys. Rev. B , 104*, 2021. doi:10.1103/PhysRevB.104.214418.

[119] M. Uchida, N. Nagaosa, J. P. He, Y. Kaneko, S. Iguchi, Y. Matsui, and Y. Tokura. Topological spin textures in the helimagnet FeGe. *Phys. Rev. B, 77*, 2008. doi:10.1103/PhysRevB.77.184402.

[120] R. Hovden, A.W. Tsen, P. Liu, B.H. Savitzky, I. El Baggari, Y. Liu, W. Lu, Y. Sun, P. Kim, A. N. Pasupathy, and Kourkoutis L.F. Atomic lattice disorder in charge-density-wave phases of exfoliated dichalcogenides (1T-TaS_2). *PNAS, 113 (41)*, 2016. doi:10.1073/pnas.1606044113.

[121] B.H. Savitzky, I. El Baggari, A.S. Admasu, J. Kim, S.W. Cheong, R. Hovden, and L.F. Kourkoutis. Bending and breaking of stripes in a charge ordered manganite. *Nat. Comm., 8*, 2017. doi:10.1038/s41467-017-02156-1.

[122] J.L. Hart, H. Pan, S. Siddique, N. Schnitzer, K. Mallayya, S. Xu, L.F. Kourkoutis, E.A. Kim, and J.J. Cha. Real-space visualization of a defect-mediated charge density wave transition. *PNAS, 121 (33)*, 2024. doi:10.1073/pnas.2402129121.

[123] A. Kotani and S. Shik. Resonant inelastic x-ray scattering spectra for electrons in solids. *Reviews of Modern Physics 73, no. 1, 203-46*, 2001. doi:10.1103/RevModPhys.73.203.